AntennaLab

UNIVERSITAT POLITÈCNICA DE CATALUNYA
BARCELONATECH

Department of Signal Theory and Communications

PhD Thesis Dissertation

Multifunctional Metamaterial Designs for Antenna Applications

PhD Thesis Author

Pere Josep Ferrer González

AntennaLab - TSC

Universitat Politècnica de Catalunya

E-mail: pj.ferrer@tsc.upc.edu

PhD Thesis Advisors

José María González Arbesú

and

Jordi Romeu Robert

AntennaLab - TSC

Universitat Politècnica de Catalunya

E-mail: [jmgonzalez, romeu]@tsc.upc.edu

Thesis submitted for the degree of *Doctor of Phylosophy*
from the Universitat Politècnica de Catalunya

Barcelona, June 2015

Multifunctional Metamaterial Designs for Antenna Applications

Pere Josep Ferrer González

Ph.D. program on Signal Theory and Communications (TSC). Universitat Politècnica de Catalunya (UPC). Barcelona (Spain)

Als meus pares
Francisco i Francisca.

Abstract

Over the last decades, Metamaterials (MTMs) have caught the attention of the scientific community. Metamaterials are basically artificially engineered materials which can provide unusual electromagnetic properties not present in nature. Among other novel and special EM applications, such as the negative refraction index (NRI) application, Metamaterials allow the realisation of perfect magnetic conductors (PMCs), which are of interest in the development of smaller and more compact antenna systems composed of one or more antennas.

In this context, this thesis is focused on investigating the feasibility of using metamaterial structures to improve the performance of antennas operating at the microwave frequencies. The metamaterial design process is challenging because metamaterials are primarily composed of resonant particles, and hence, their response is frequency dependent due to the dispersive behaviour of their effective medium properties. However, one can take advantage of this situation by exploiting those strange properties while finding other antenna applications for such metamaterial designs. For the case of the PMC applications, the relative magnetic permeability values are negative, because they are found just above the resonance of the metamaterial.

This thesis investigates several antenna applications of artificial magnetic materials (AMMs). The initial work is devoted to the design of a spiral resonator (SR) AMM slab to realise a low profile reflector dipole antenna by taking advantage of its PMC response. The spiral resonator has been used due to its reduced unit cell size when compared to other metamaterial resonators, leading to a more homogeneous metamaterial structure. In addition, a bidirectional PMC spacer has been applied to produce a small and compact antenna system composed of two monopole antennas, although the concept may be applied to other antenna types. A third application as an AMC reflector are the transpolarising surfaces, where the incident electric field plane wave is reflected at a polarisation rotation angle of 90 degrees. Such surfaces may be of interest to produce high cross-polar response reflecting devices, like the modified trihedral corner reflector that has been tested for polarimetric synthetic aperture radar (PolSAR) purposes.

Another application of the SR AMM metamaterial is the patch antenna with a magneto-dielectric loading. The relative magnetic permeability of the AMM meta-

material has values over the unity in the frequency band below the resonance. As a consequence, the patch antenna can be miniaturised without reducing its bandwidth of operation, in contrast to a typical high dielectric permittivity substrate.

Finally, the SR AMM metamaterial also presents values of relative magnetic permeability between zero and the unity (MNZ). In such a case, the SR AMM metamaterial has been applied as an MNZ cover of a slot antenna, devoted to increasing the broadside radiated power and directivity of the antenna.

Contents

Chapter 1

Introduction

1.1 Motivation and thesis objectives

Since the end of the twentieth-century, the development of mobile communication systems has grown together with the increasing demand for Internet and localisation services (VoIP, messaging, browsing, streaming, GPS). Year by year, the electronics systems design industry has become increasingly focused on realising smaller mobile transmitting/receiving (Tx/Rx) devices, while maintaining or increasing data capacity and signal coverage. Consequently, miniaturised antennas are in increasing demand. In addition, multiple antenna systems (MIMO), which traditionally suffer from couplings between the antenna elements, are often used to improve the signal quality and coverage in complex propagation scenarios such as urban or indoor environments. Therefore, the antenna design strategies have become more complex.

On the other hand, over the last decades, Metamaterials (MTMs) have caught the attention of the scientific community [1–16]. Metamaterials are basically artificially engineered materials which can provide unusual electromagnetic properties not present in nature. The first theoretical study was carried out by the Russian physicist V.G. Veselago in 1968 [17], introducing the possibility of left-handed media (LHM). In the late-90's, the British physicist J.B. Pendry investigated the feasibility of fabricating those metamaterials proposed 30 years before [18] from the combination of different

types of electric conductors. Finally, the American physicist D.R. Smith and co-workers demonstrated experimentally the LHM behaviour [19, 20]. In the mid 2000's, the project Metamorphose NoE, funded by the European Commission through the FP6 programme, led to the creation of a European scientific community network among electrical engineers and physicists working with Metamaterials.

In terms of Electromagnetics (EM), metamaterial properties can be applied from Microwave frequencies (MHz-GHz) to Optics (THz), continuously leading to new discoveries and applications, such as later metamaterial applications found in Acoustics [21, 22]. Among other novel and special EM applications, such as the negative refraction index (NRI) application [19], Metamaterials allow the realisation of perfect magnetic conductors (PMCs) [8], which are of interest in the development of smaller and more compact antenna systems composed of one or more antennas. The antenna system can be miniaturised when using metamaterials, because they are able to overcome and reduce the $\lambda/4$ distance requirement of a linear antenna placed above (or opposite) a perfect electric conductor (PEC), that is, a reflecting metallic surface. PMCs are theoretically predicted in the Image Current Theory [23], but very little attention has been reported by the scientific community to the proper realisation of such structures at microwave frequencies (MHz-GHz). One drawback of metamaterials is that the resulting PMC condition in the designed metamaterials may only be achieved within a narrow frequency bandwidth of operation.

In this context, the thesis is focused on investigating the feasibility of different metamaterial designs devoted to improve the performance of antennas operating at the GHz frequencies, like the artificial PMCs (AMCs) for compact and low profile antenna applications. The metamaterial design process is challenging because metamaterials are primarily composed of resonant particles, and hence, their response is frequency dependent due to the dispersive behaviour of their effective medium properties. However, one can take advantage of this situation by exploiting those strange properties while finding other antenna applications for such metamaterial designs.

1.2   Thesis outline

This thesis is organised as follows. Chapter 2 introduces the basics of metamaterials, as well as a compilation of metamaterials applied to antennas. Chapter 3 presents the properties study of spiral and loop-like magnetic metamaterial inclusions, where the spiral resonator (SR) is chosen as the artificial magnetic material (AMM) to be used as artificial PMC, as well as, in other antenna applications that will be discussed in the following chapters. Chapter 4 focuses on the low profile dipole reflector design and a compact two-antenna system using the SR AMMs. Chapter 5 introduces a

polarisation conversion property of a metamaterial reflector, which is also applied to polarimetric synthetic aperture radar (PolSAR) calibration with a modified trihedral corner reflector (TCR). Chapter 6 studies the bandwidth and patch antenna miniaturisation possibilities when using magneto-dielectric (MD) metamaterial and SR AMM substrates. Chapter 7 presents a broadside power and directivity increase study when using a SR AMM cover of a slot antenna. Finally, Chapter 8 concludes this thesis and gives some suggestions for further research lines in AMM metamaterials for antenna applications.

Chapter 2

Metamaterials in Antenna Engineering

2.1 Introduction to Metamaterials

Metamaterials (MTMs) were first introduced by Veselago [17], who considered that the constitutive values ε (electric permittivity) and μ (magnetic permeability) of an effectively homogeneous material could take simultaneously negative values. As a consequence of that, several physical phenomena could change their natural behaviour, such as the reversal of Snell's law, the reversal of Doppler shift, the reversal of Čerenkov effect, among others. The constitutive material parameters ε and μ, are related to the refractive index n as:

$$n = \pm\sqrt{\varepsilon_r \mu_r} \tag{2.1}$$

where ε_r and μ_r are the relative permittivity and permeability related to the free space permittivity $\varepsilon_0 = \varepsilon/\varepsilon_r \approx 8.85 \cdot 10^{-12}$ F/m and permeability $\mu_0 = \mu/\mu_r = 4\pi \cdot 10^{-7}$ H/m.

Then, four possible regions appear depending on the sign combinations of (ε, μ); since ε_0 and μ_0 are positive fundamental constants, negative values in $\varepsilon = \varepsilon_0\varepsilon_r$ and

$\mu = \mu_0 \mu_r$ are due to the sign of the relative parameters ε_r and μ_r, respectively. An $\varepsilon-\mu$ diagram has been depicted in Figure 2.1 representing the possible materials arising from the four sign combinations of (ε, μ).
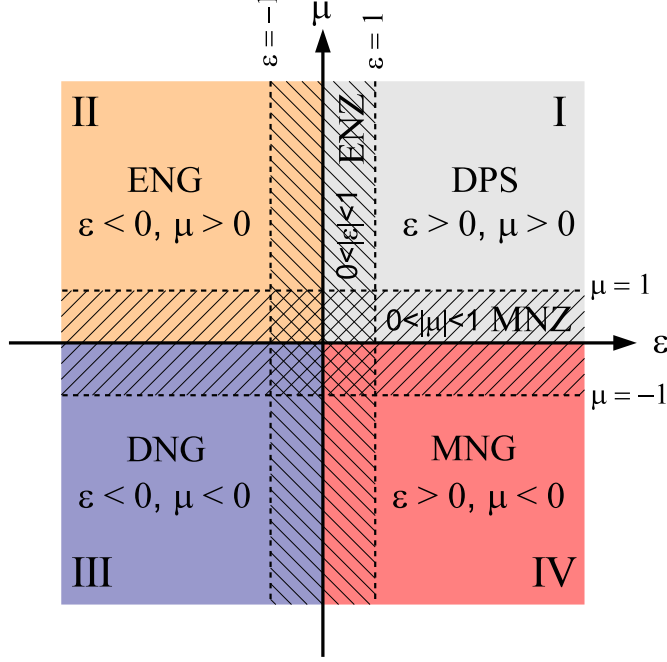
Figure 2.1: $\varepsilon - \mu$ diagram. In this graph, $\varepsilon = \varepsilon_0 \varepsilon_r$ and $\mu = \mu_0 \mu_r$.

Waves can only propagate in materials from regions I and III, where ε and μ parameters are both positive (double positive, DPS, or right-handed medium, RHM) or both negative (double-negative, DNG, or left-handed medium, LHM). Non propagating evanescent waves are found in regions II and IV, where $\varepsilon < 0$ (epsilon negative, ENG) or $\mu < 0$ (mu negative, MNG). Finally, some other regions of interest might also be considered, such as the epsilon-near-zero (ENZ) where $0 < |\varepsilon| < 1$, and the mu-near-zero (MNZ) where $0 < |\mu| < 1$.

Double negative metamaterials (DNG) are characterised by their simultaneous $\varepsilon < 0$ and $\mu < 0$ values. This fact also affects the field equations in Maxwell's formulas. A general definition of the Poynting vector $\vec{S}$ in a phasor notation is (2.2), where a time dependence $e^{+j\omega t}$ and a space dependence e^{-jkr} are assumed:

$$\vec{S} = \frac{1}{2}\vec{E} \times \vec{H}^* \tag{2.2}$$

where the electric field $\vec{E}$ and the magnetic field $\vec{H}$ are defined by:

$$\vec{\beta} \times \vec{E} = \omega\mu\vec{H}$$
$$\tag{2.3}$$
$$\vec{\beta} \times \vec{H} = -\omega\varepsilon\vec{E}$$

Therefore, for an isotropic and homogeneous medium with $\varepsilon > 0$ and $\mu > 0$, the electric field $\vec{E}$, the magnetic field $\vec{H}$ and the propagation vector $\vec{\beta}$ form a right-handed triplet, which is the origin of the right-handed medium (RHM) definition. However, by considering a medium with $\varepsilon < 0$ and $\mu < 0$, the previous equations can be rewritten as:

$$\vec{\beta} \times \vec{E} = -\omega \left| \mu \right| \vec{H}$$

$$\vec{\beta} \times \vec{H} = \omega \left| \varepsilon \right| \vec{E} \tag{2.4}$$

showing that the $\vec{E} - \vec{H} - \vec{\beta}$ forms a left-handed triplet. This medium is referred to as left-handed medium (LHM), and supports backward waves, because the Poynting vector $\vec{S}$ is opposite the propagation vector $\vec{\beta}$, that is, the energy and wavefronts travel in opposite directions. This fact is reflected in the RHM and LHM $\vec{E} - \vec{H} - \vec{\beta}$ triplets depicted in Figure 2.2.
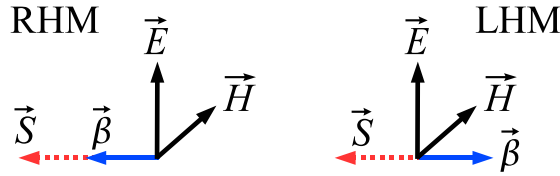
Figure 2.2: $\vec{E} - \vec{H} - \vec{\beta}$ triplets for right-handed and left-handed media.

The DNG behaviour was first achieved by combining two single negative materials, this is, a wire/rodded medium (introduced in 1962 by W. Rotman [24] as artificial dielectrics) which provides the required $\varepsilon < 0$, and a split ring resonator (SRR) medium (introduced in 1999 by J.B. Pendry [18]) which provides the required $\mu < 0$. The SRRs were initially realized as cylindrical conducting structures with longitudinal gaps [18], although first metamaterial prototypes were fabricated from the combination of planar SRRs, etched on a thin dielectric layer, and metallic rods [19]. In addition, a two-dimensional metamaterial design was also presented taking advantage of the two sides of the dielectric layers, this is, by etching the SRRs on one side of the dielectric layer, and the planar strips (equivalent to the wires) on the opposite one [20]. Some of the first fabricated metamaterial samples are shown in Figure 2.3.

However, the wire medium and the SRRs medium are frequency dependent due to their strong resonant behaviour (Drude-Lorentz models), and hence, DNG metamaterials are also frequency dependent. For this reason, the refraction index n is reformulated as:

$$n \equiv n_{eff}(\omega) = \sqrt{\varepsilon_{eff}(\omega)\mu_{eff}(\omega)} \tag{2.5}$$

(a) 1D design

(b) 2D design
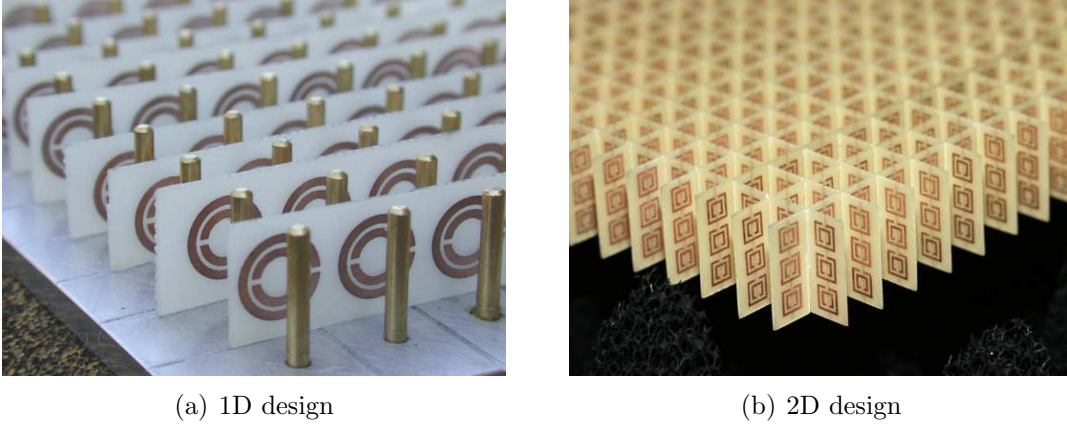
Figure 2.3: First fabricated metamaterial designs composed of SRRs and rods/strips
[19, 20].

where $\varepsilon_{eff}(\omega)$ and $\mu_{eff}(\omega)$ are the frequency dependent effective permittivity and the effective permeability, respectively. These effective material parameters are characterised by their Drude-Lorentz dispersion models, and have the form described in (2.6).

$$\varepsilon_{eff}(\omega) = 1 - \frac{\omega_{ep}^2 - \omega_{e0}^2}{\omega^2 - \omega_{e0}^2 + j\omega\nu_c}$$

$$\mu_{eff}(\omega) = 1 - \frac{F\omega^2}{\omega^2 - \omega_{m0}^2 + j\omega\Gamma}$$

(2.6)

where ω_{ep} and ω_{mp} are the electric and magnetic plasma frequencies, ω_{e0} and ω_{m0} are the electric and magnetic resonant frequencies, ν_c is the collision frequency, F is an amplitude factor and Γ is a damping factor. These expressions have been plotted in Figure 2.4.

(a) Effective permittivity

(b) Effective permeability
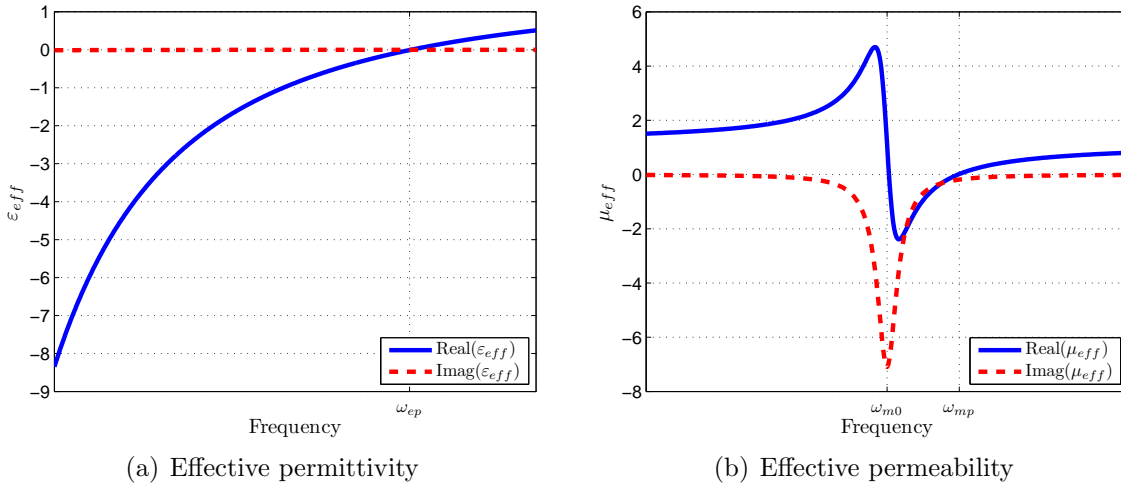
Figure 2.4: Effective material functions for a DNG metamaterial.

The negative parameter frequency bands are located above the resonant frequency

but below the correspondent plasma frequency. Then, the ENG region is found for $\omega_{e0} < \omega < \omega_{ep}$, and the MNG region for $\omega_{m0} < \omega < \omega_{mp}$. Note that if the wires are electrically continuous, their resonant frequency is 0 ($\omega_{e0} \approx 0$). In order to have a DNG metamaterial, both negative regions ENG and MNG must coincide. Consequently, since the MNG region is narrower compared to the ENG region, the magnetic resonator metamaterial limits the DNG performance when assembled together with an electric resonator metamaterial.

Novel DNG metamaterials are designed in planar dielectric layer technology and they do not use wires. They are either composed of paired resonators etched on both sides of the dielectric layer [25], or coplanar electric and magnetic resonators printed on the same side of the dielectric layer [26]. Some examples are shown in Figure 2.5.

(a) Planar 2-D bilayer design [25]

(b) Coplanar electric and magnetic reso-
nators design [26]
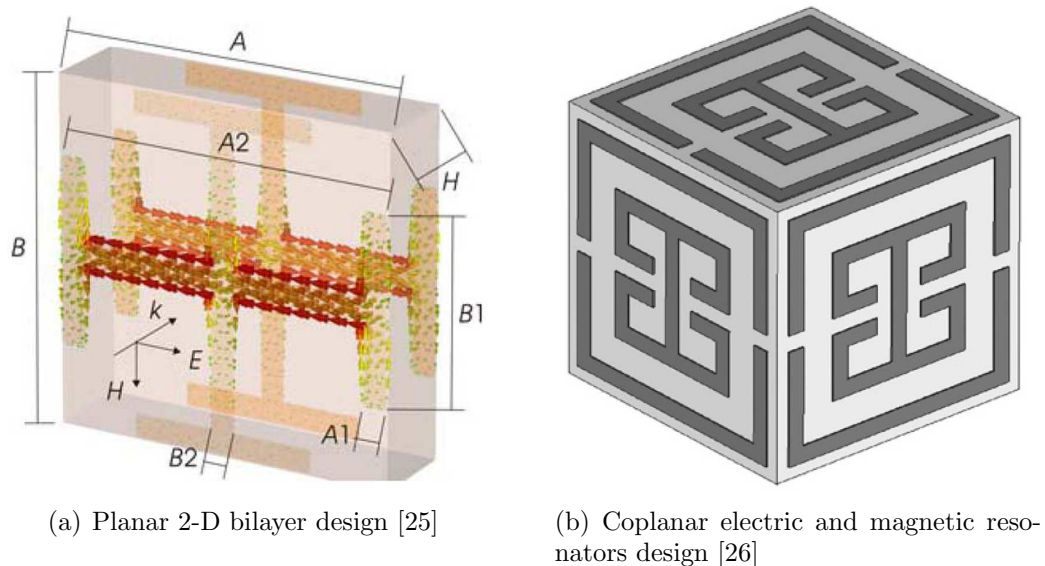
Figure 2.5: Novel planar DNG metamaterial designs.

2.2   Metamaterials Applications

Although DNG materials seem to be the most interesting to be realised due to their novel backward-wave propagation and other related properties, the use of SNG metamaterials, either ENG or MNG, may offer some additional worthy applications. Some remarkable applications based on metamaterials are:

- Negative refraction index (NRI) [27]. A double negative medium is characterised by its negative index of refraction ($\varepsilon < 0, \mu < 0$). This fact affects Snell's law by producing a negative angle of refraction, when a plane wave going from a right-handed medium impinges onto a left-handed medium.

- Perfect flat lens [28]. A direct result arsing from the NRI is the perfect flat lens. Lenses are used to focus or shape radiation beams, but they present several limitations due to the wavelength limit. Normal lenses are typically convex, and they need a wide aperture to achieve good resolution; in addition, the details of the image are contained in the near field which decays exponentially (evanescent waves), thus having no contribution to the final image. Negative index lenses might be concave or even flat, and they are able not only to focus the image, but also to amplify the evanescent waves which positively contribute to the final image while overcoming the wavelength limitation.

- High impedance surface (HISs) [31] and artificial magnetic conductors (AMC) [32,34]. Metamaterials can be used to realise novel types of surfaces or reflectors which behave like perfect magnetic conductors (PMCs). This might be of interest for the design of low profile, compact and isolated antenna systems comprised of one or more antennas.

- Electromagnetic cloak [29,30]. Three-dimensional metallic objects can be made invisible by using an electromagnetic cloak. Cloaking enables control of the paths of electromagnetic waves within a metamaterial by introducing a required spatial variation in its constitutive parameters. This might be of interest for stealth applications.

2.3   Metamaterials Applied to Antennas

Among the metamaterial applications, high impedance surfaces (HISs) and artificial magnetic conductors (AMCs) are the ones which are most related to antenna applications, since they can lead to the design of compact and low profile antenna systems. In such a case, metamaterial designs are placed around or close to the antennas, although metamaterials could also be used in the feeding part of the antenna system, or even as a part of the antenna structure.

2.3.1   Metamaterials in the Antenna Environment

Due to radiating requirements, antennas might often be placed in front of a reflector in order to radiate in one direction only, while reducing the back-radiation. In this case, the antennas should be placed at a minimum $\lambda/4$ distance above the metal surface, which acts as a reflector, in order to properly enhance radiation. This fact can be explained by means of the Image Theory for either electric or magnetic currents. As explained in [23], when a charge $\rho(\vec{r})$ or current $\vec{J}(\vec{r})$ distribution is close to a conductor,

several charges and currents appear on the surface which contribute to the radiation. These image currents appear for both perfect electric conductor (PEC) and perfect magnetic conductor (PMC) boundary conditions (BCs), although the images of the electric or magnetic currents change depending on the type of reflector. This fact is illustrated in Figure 2.6 for the case of electric currents (e.g. dipole antennas) placed above a PEC and a PMC boundary condition (surface or reflector).
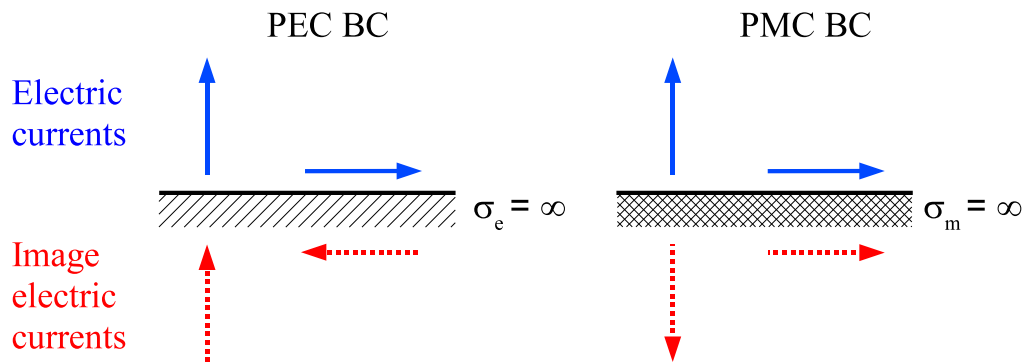
Figure 2.6: Electric image currents due to a PEC or a PMC boundary condition (BC).

As seen in Figure 2.6, a reflected electrical vertical current from a PEC positively contributes to the radiation; this is the case of a monopole antenna, where half of the antenna is above the metal reflector, whereas the other half is obtained by the reflected image. However, the impinging and reflected electric currents parallel to a PEC cancel each other out. This fact is evidenced when a dipole antenna placed parallel and close to a metal reflector is short-circuited (unmatched and not radiating). On the other hand, an electric current can be placed close and parallel to a PMC surface, where an in-phase image is created, thus enhancing broadside radiation, leading to a low profile antenna system. Contrary to the PEC surfaces which can be made from any conventional metal sheet, these PMC surfaces do not exist in nature, although they are feasible with metamaterials. Therefore, the fabricated PMC surfaces are usually named artificial magnetic conductors (AMCs) or reflectors (AMRs).

One of the first AMC surfaces was the electromagnetic band-gap (EBG) surface, which was introduced by D.F. Sievenpiper in 1999 [31]. The so called mushroom-like surface is composed of a ground plane loaded with a lattice of square patches which are connected to the ground plane through metallic vias, as shown in Figure 2.7.

This reflecting surface combines two different electromagnetic phenomena, that is, the PMC response (where the phase of the reflection coefficient of the electric field crosses the 0° axis, contrary to a PEC phase of 180°), and the EBG response (surface waves are suppressed in the band-gap region enhancing broadside radiation). These behaviours are shown in Figure 2.8 (a) and Figure 2.8 (b), respectively.

(a)

(b)
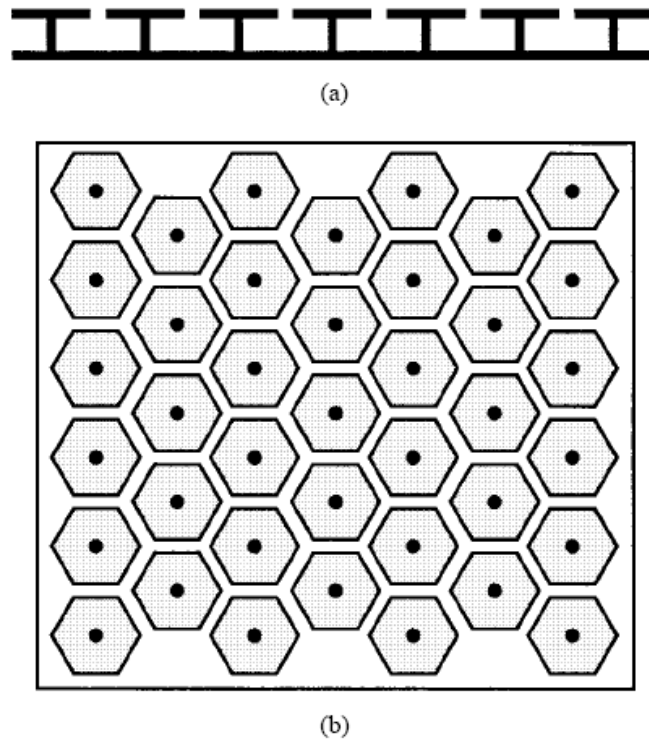
Figure 2.7: Mushroom-like surface design [31].
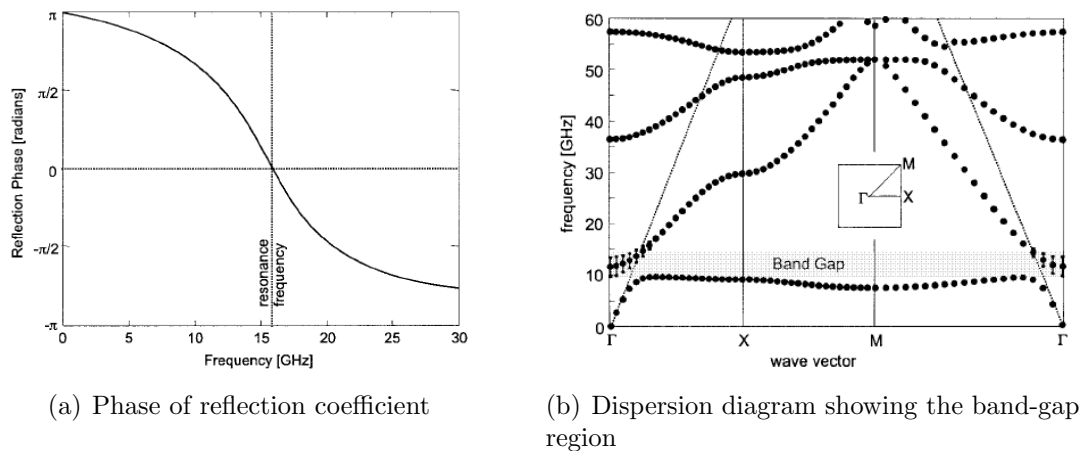
(a) Phase of reflection coefficient

(b) Dispersion diagram showing the band-gap region

Figure 2.8: Mushroom-like surface design and main characteristic results [31].

The previous AMC surface can be easily fabricated using a planar dielectric substrate, where the patches (or the correspondent resonators) are etched on one side, whereas the opposite side remains as ground plane. On the other hand, a possible insertion of metallic vias is more complicated and needs to be mechanised. However, it also possible to design AMCs composed of square patches over a ground plane but without the use of vias [32], although the EBG response would be null or weak, and the reflecting response of this via-less AMC would be slightly different, mostly when reflecting high oblique incident angles [33].

Other AMC designs do not require backing ground plane for reflection purposes [34]. In this case, the magnetic resonators are printed on dielectric strips forming a volumetric AMC. One layer with capacitively-loaded loops (CLLs) of the volumetric AMC is seen in Figure 2.9 (a). An electric field plane wave linearly polarised along the y-axis impinges the volumetric CLL metamaterial block along the $+z$ direction (port 1), or along the $-z$ direction (port 2). In such a case, the phase of the reflection coefficient S_{11} in Figure 2.9 (b) shows a PMC response (phase(S_{11}) = 0°) around 10 GHz. It is also interesting that the phase of S_{22} remains around $\pm180°$. This results in a dual PMC/PEC property for such AMC surfaces; they behave as PMC in reflection when one side of the AMC is illuminated, and as PEC when the opposite side is illuminated. In this case, the PMC side is often referred to as artificial magnetic conductor (AMC) or reflector (AMR), as already commented, and the PEC side as artificial electric conductor (AEC) or reflector (AER).

(a) One layer of CLL resonators   (b) Phase of the reflection coefficients S_{11} and S_{22}
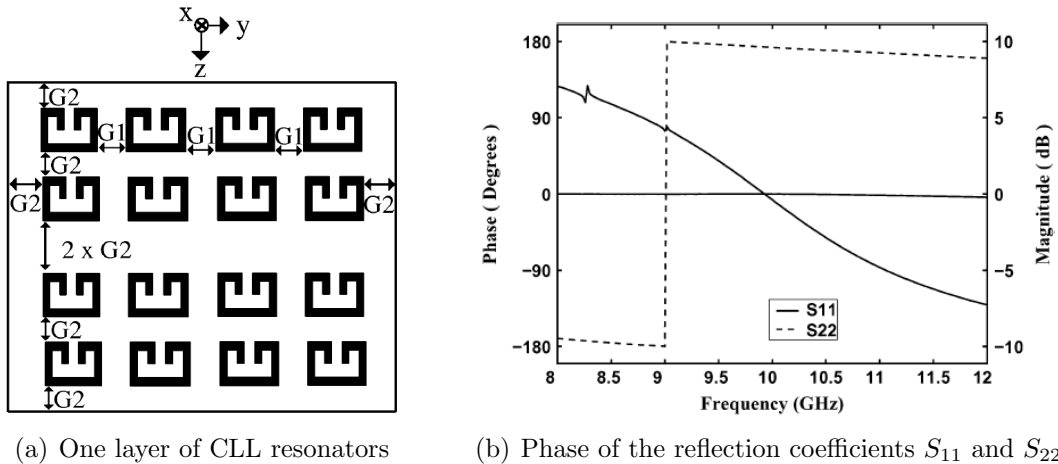
Figure 2.9: Detail of one layer of the AMC surface composed of CLLs and reflection results [34].

One possible drawback of these layered AMCs remains in the fabrication process, since the layers with magnetic resonators are designed to be separated by a certain distance, by filling the gap between the strips with air. For this reason, an external spacer or support like Styrofoam is required, in order to keep the strips with the magnetic resonators at the requested separation, while providing robustness to the design. Other fabricated designs may present the metamaterial strips placed together with no air gaps, by using the dielectric strips, where the magnetic resonators are etched, as spacer, forming a packed metamaterial block.

Previous examples of AMCs are related to artificial ground planes for dipole/planar antennas to enhance broadside radiation. Another way to improve this broadside radiation relies on the use of a metamaterial transmitting superstrate, as stated in [35]. A LH superstrate can increase radiation to the boresight of a dipole antenna. This design

is shown in Figure 2.10, where radiation is enhanced about 3 dB around 11 GHz, at
the expense of a narrow bandwidth response.

(a) Enhanced radiation along frequency   (b) Radiation diagrams with and with-
                                             out superstrate at 11 GHz
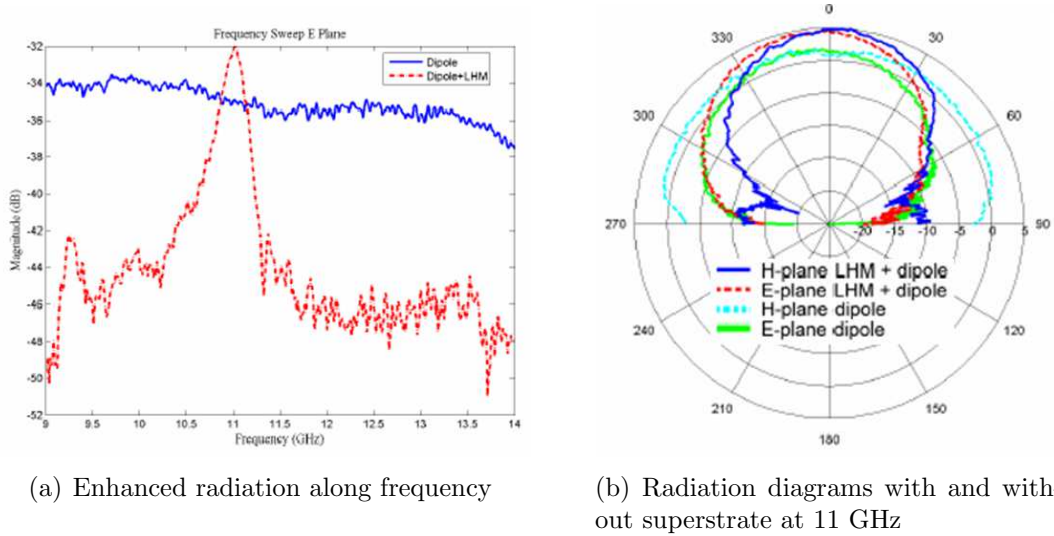
Figure 2.10: Power enhancement of a dipole by a left-handed (LH) superstrate [35].

Another application of AMCs (both planar or volumetric metamaterials) is the
isolation improvement between two close antennas [36], as can be seen in Figure 2.11.
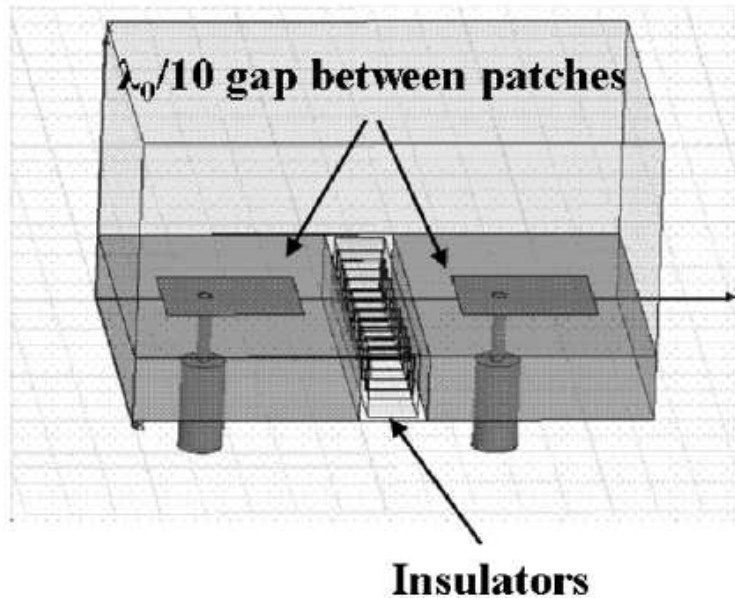
Figure 2.11: Metamaterial insulator used to increase isolation between close patch
            antennas [36].

Measured S_{21} results with and without the metamaterial insulator are plotted in
Figure 2.12. The isolation is improved in more than 15 dB when the AMC surface
is inserted between two close antennas, although the frequency response is slightly

shifted. This can lead to the design of compact antenna systems composed of two or more antennas.

(a) S_{11}-S_{21} without insulator   (b) S_{11}-S_{21} with AMC insulator
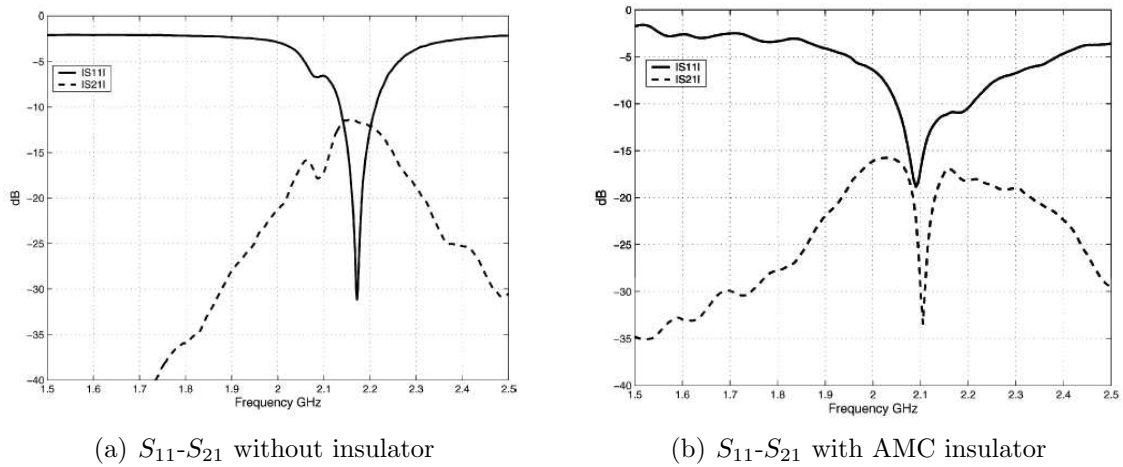
Figure 2.12: S_{21} results with and without the use of a metamaterial insulator [36].

Electrically small antennas can be covered by a metamaterial shell that makes the antenna resonant [37]- [38]. An infinitesimal dipole is covered by an ENG ($\varepsilon < 0$) shell that enhances radiation, as shown in Figure 2.13. Nevertheless, when taking into account the losses in the design, the performance level decreases. The dual case of this property includes a loop antenna covered by a MNG ($\mu < 0$) shell, while matching the antenna, the radiation is also enhanced [39].

(a)   (b)
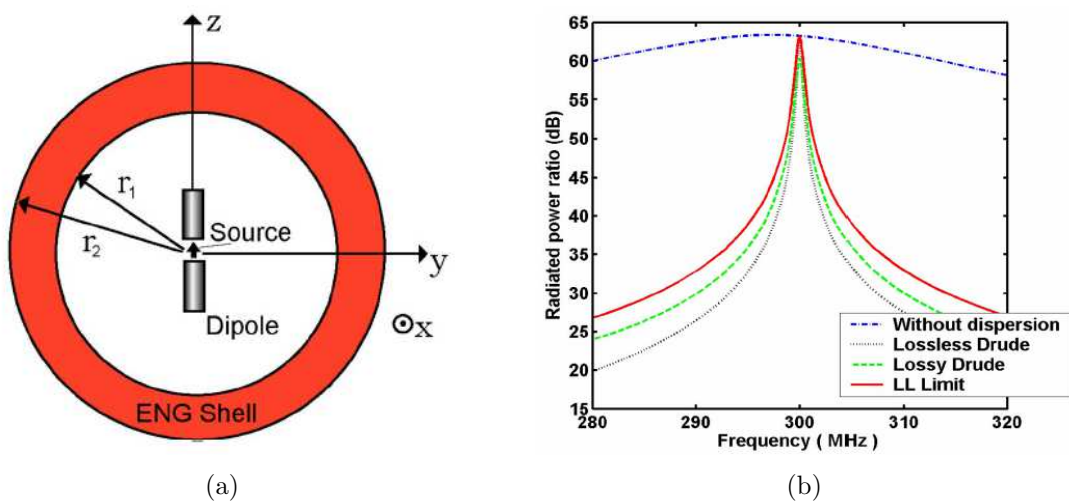
Figure 2.13: Infinitesimal dipole enclosed by an ENG shell (left) and ratio between radiated powers (right). [37]- [38].

A similar application involves a leaky wave antenna composed of a grounded meta-material slab excited by a line source, which can produce highly directive beams [40]. The metamaterial slab is made of homogeneous ε-dispersive material. For low values

of permittivity $0 < \varepsilon < 1$ (ENZ), the leaky modes supported by the slab are excited, and hence, directive beams pointing at broadside are obtained, as seen in Figure 2.14.

(a) Metamaterial slab composed of wires

(b) Radiation patterns showing a highly directive beam at 20.155 GHz
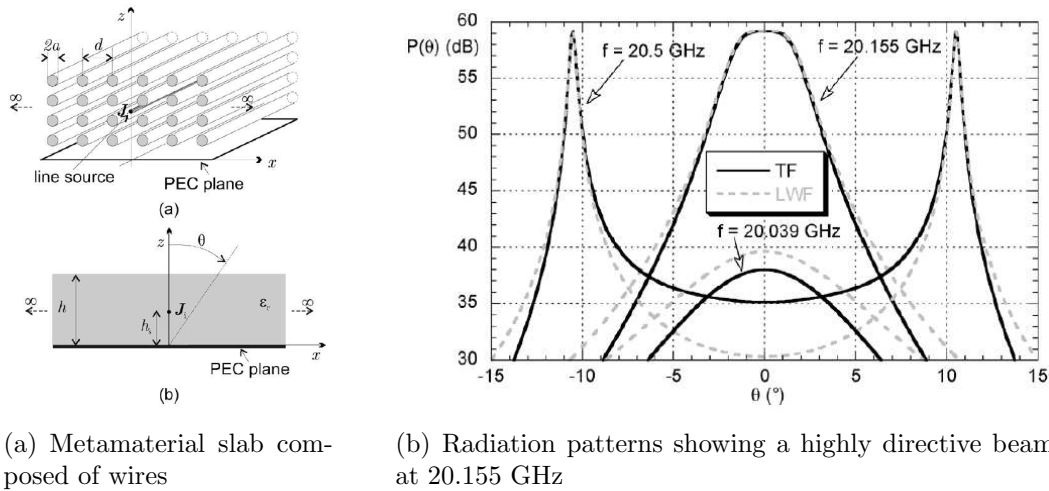
Figure 2.14: Grounded metamaterial slab achieving highly directive beams [40].

2.3.2   Metamaterials in the Antenna Structure

Metamaterials can be part of the antenna structure. One application is to use a metamaterial with high permeability values ($\mu >> 1$) such as a magneto-dielectric (MD) substrate of patch antennas [41]. In this configuration, antenna size can be significantly reduced without the use of high permittivity ($\varepsilon >> 1$) dielectric substrates. Results proving this patch antenna miniaturisation technique are shown in Figure 2.15, where the frequency of operation is reduced from 2.15 GHz (patch filled with air) down to 1.3 GHz (patch antenna filled with MD substrate).
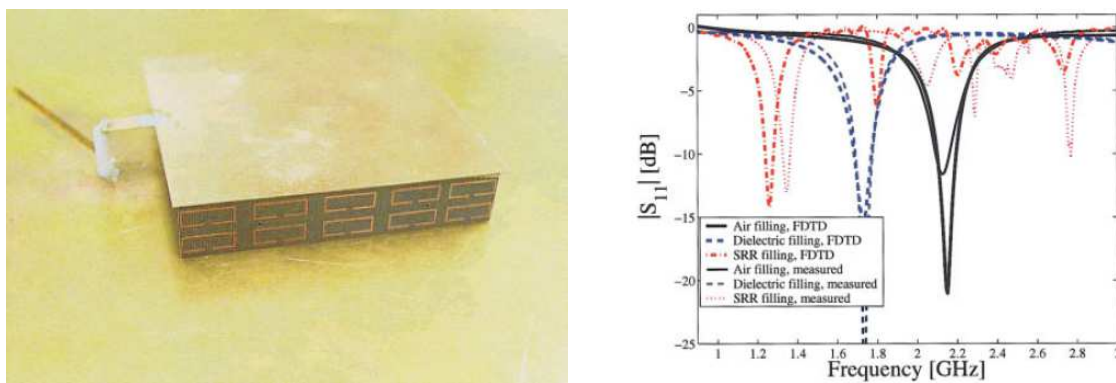
(a) Patch antenna with high-μ metamaterial substrate

(b) Input impedance results comparing different substrates: air, dielectric and magneto-dielectric

Figure 2.15: Fabricated patch antenna with magneto-dielectric substrate [41].

Moreover, some novel antenna designs come from the application of left-handed transmission line (LH-TL) properties. A dipole antenna, made of shunt inductors and series capacitors forming a LH-TL [42], achieves a high miniaturisation factor $\lambda/5.55$ (compared to the typical $\lambda/2$), as shown in Figure 2.16.

(a) LH dipole antenna design   (b) Measured radiation pattern at 547 MHz
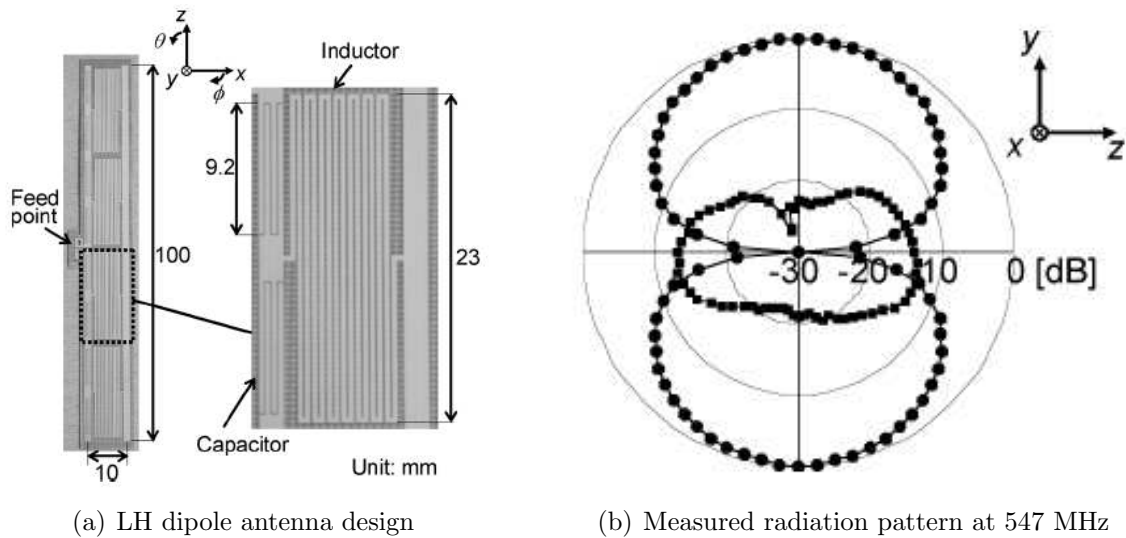
Figure 2.16: Detail of the LH dipole antenna and radiation results [42].

Another LH-TL application is related with leaky wave antennas (LWAs) [43]. This LWA design is a 1-port transmission line composed of right-handed and left-handed components, the so-called composite right-left-handed transmission line (CRLH-TL), and it is ended with a matched load in order to avoid undesired reflections, as shown in Figure 2.17.
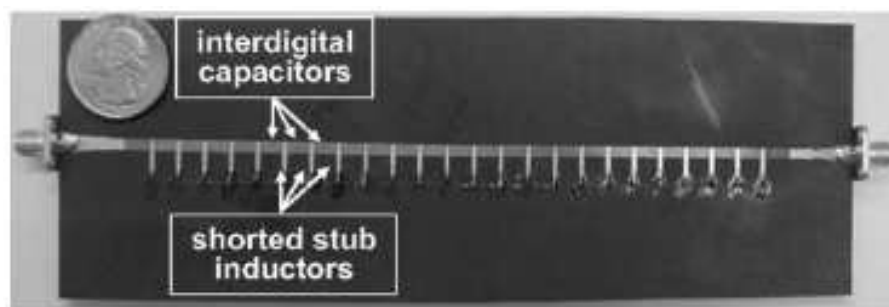
Figure 2.17: CRLH-TL leaky wave antenna design [43].

Such CRLH-TL radiates at broadside but with an angle that depends on the phase propagation β. In that case, steering arrays are feasible when changing the frequency of operation from backfire (LH contribution, $\beta < 0$) to endfire (RH contribution $\beta > 0$), as shown in Figure 2.18 for different frequencies.
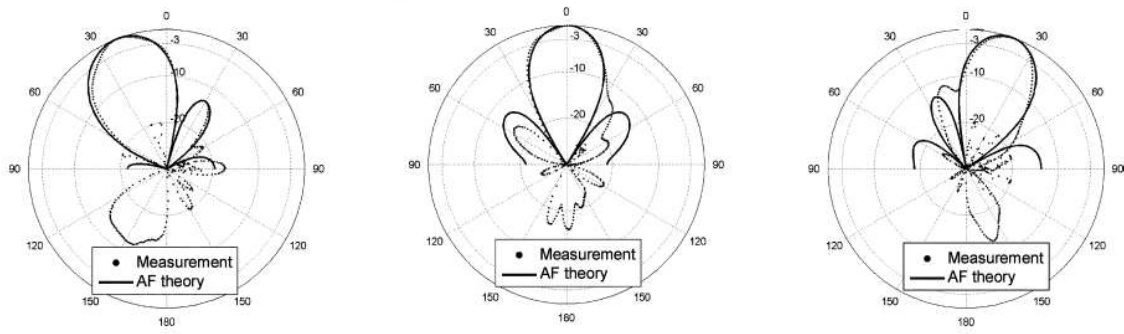
(a) Backward radiation ($\beta <$ 0) at 3.4 GHz

(b) Broadside radiation ($\beta =$ 0) at 3.9 GHz

(c) Forward radiation ($\beta < 0$) at 4.3 GHz

Figure 2.18: Steerable radiation patterns when changing the frequency of operation of the CRLH-TL leaky wave antenna [43].

2.3.3   Metamaterials in the Antenna Feeding Network

The antenna feeding is usually composed of a transmission line, and some filters devoted to avoiding unwanted frequencies being radiated through the antenna. Many microwave devices can be implemented applying left-handed metamaterials, while reducing the circuit size/length when compared to conventional devices. For instance, a series fed power divider that uses zero-degree phase shifting transmission lines is presented in [44], and provides an increase of 165% in the input return loss bandwidth. It is also remarkable that the divider itself occupies only 2.6% of the area that the conventional transmission line divider (made of meander lines) occupies, as shown in Figure 2.19.
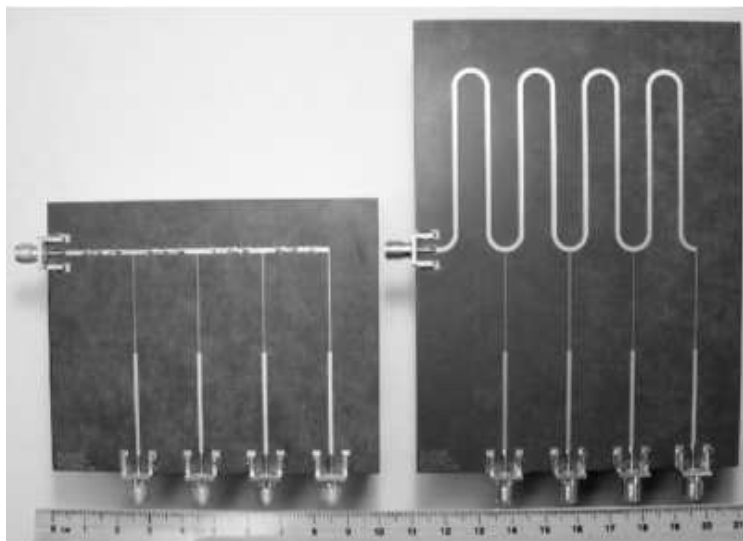
Figure 2.19: Zero-degree metamaterial phase shifter (left) and conventional design (right) [44].

A coupled-line coupler composed of a microstrip line edge-coupled to a LH line is presented in [45], exhibiting co-directional phase and counter-directional Poynting vectors on the lines, which leads to a backward-wave coupling. The fabricated prototype is shown in Figure 2.20.
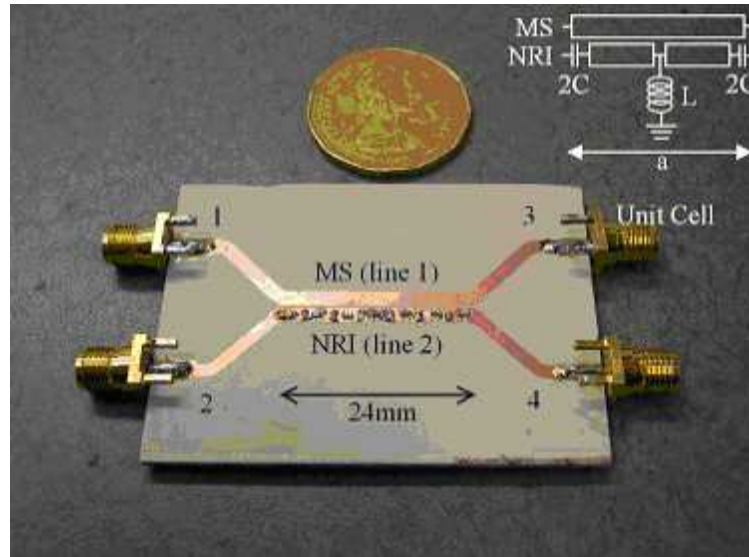
Figure 2.20: Metamaterial coupler [45].

Many authors have reported the use of split ring resonators (SRRs) or spiral resonators (SRs) to design miniaturised coplanar waveguide (CPW) transmission lines and microstrip filters [46–50]. In addition, it is possible to produce tunable band-pass or rejected-band filters by simply adding varactors to the SRRs that form the filter [51], as shown in Figure 2.21.
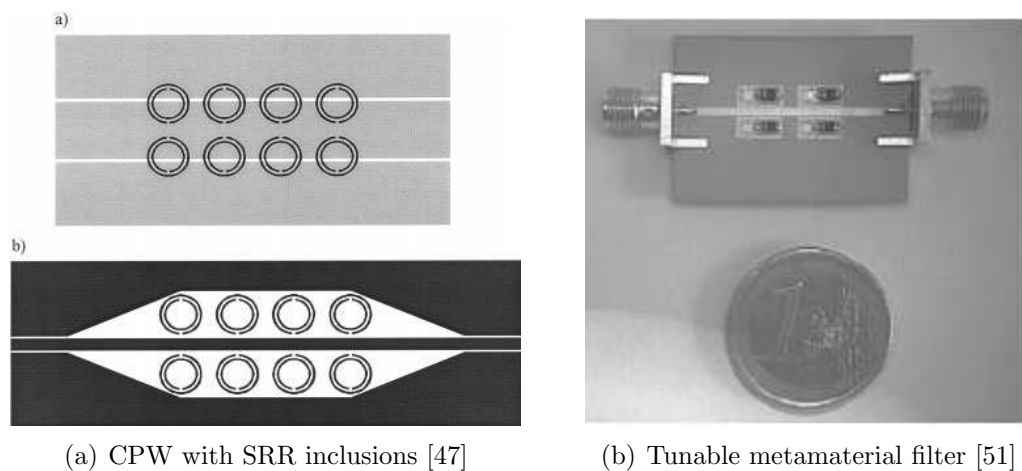
(a) CPW with SRR inclusions [47]   (b) Tunable metamaterial filter [51]

Figure 2.21: Transmission lines and filters with metamaterials.

2.4   Chapter Conclusions

Metamaterials can be used in many different antenna applications. Some interesting applications have been presented by taking advantage of metamaterial properties, such as the artificial magnetic conductors (AMCs), the magneto-dielectric patch antenna substrates, or the CRLH transmission lines with the zero phase shift. However, the metamaterials may introduce some losses (material losses and dispersion losses), and they also provide a narrow bandwidth of operation with the desired properties. Such disadvantages have to be considered in order to optimise the future metamaterial antenna designs.

Chapter 3

Spiral Resonators as Artificial Magnetic Materials

3.1 Introduction

Artificial magnetic materials (AMMs) are composed of metallic inclusions showing a high magnetic polarisability (μ-dispersive behaviour), hence, they are usually referred to as magnetic resonators. Split-ring resonators (SRRs) were first introduced by Pendry [18] as they provide the required MNG behaviour to realise DNG metamaterials. However, other well known magnetic resonators are the spiral resonators (SRs) [18,52,53]. Additional geometries can also be found in the literature such as the capacitively loaded loops (CLLs) [34], and the omega particles (Ω) [54]. Some examples of magnetic resonators are depicted in Figure 3.1.

It is also interesting that some magnetic resonators like the SRRs introduce undesired cross polarisation or bianisotropic effects, that is, an electric polarisation may be created when a magnetic field is applied, and vice versa. Bianisotropy is characterised by different forward and backward reflected powers (or different reflection S-parameters), wider stop-band in transmission, and the presence of a magneto-electric coupling coefficient (ξ_0) [9]. The bianisotropy present in the SRRs comes from the different dimensions of the internal and external rings; this results in an additional electric

(a) SRR [18]   (b) SR [53]   (c) CLL [34]   (d) Ω particle [54]
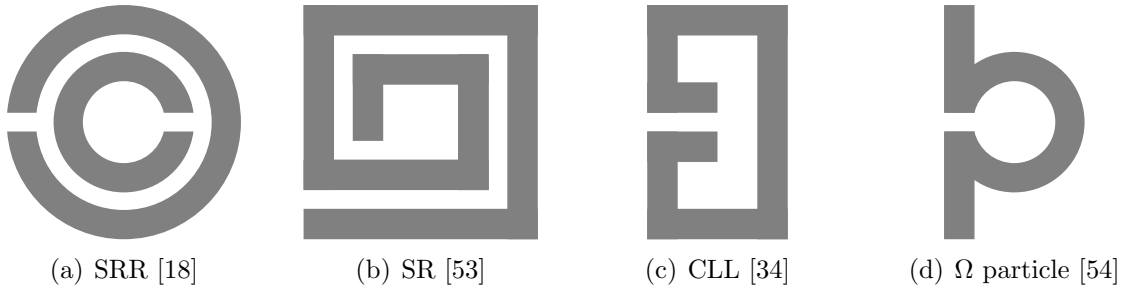
Figure 3.1: Examples of magnetic inclusions to realize AMMs.

polarisability. A modified SRR was proposed in [55] to avoid the bianisotropy present in the typical SRRs. This was the so-called broadside-coupled SRR (BC-SRR), and it consists of two identical rings placed on both sides of the dielectric substrate that cancel the magneto-electric coefficient, and hence, there is no bianisotropy in this magnetic resonator. Moreover, other magnetic particles can also be designed in a broadside-coupled geometry: BC-SR (or DSR) [56], BC-Ω-particle [54] or BC-S-particle [57].

This chapter is organised as follows. Several SR AMM designs are numerically and experimentally characterised, and their properties are compared to other types of AMMs. A miniaturised square SR AMM printed on Rogers RO4003C substrate is presented as a candidate for different metamaterial applications, taking advantage of the μ-dispersive behaviour of AMMs.

3.2 AMM Characterisation

Artificial magnetic materials can be characterised in different ways. Among them, S-parameters are the most commonly used, due to their ease of retrieval, either by numerical simulation or by measurement, while offering reflection (S_{11}) and transmission (S_{21}) responses across a frequency range. Once the S-parameters are obtained, an effective material extraction method can be applied to estimate the effective relative permittivity (ε_r) and permeability (μ_r) values.

3.2.1 Simplified modelling

Artificial magnetic materials (AMMs) are typically large screens in terms of operational wavelength λ_0, composed of a periodic arrangement of magnetic resonators. This fact makes a complete numerical analysis difficult, due to the large amount of required memory and computing time resources. However, periodic boundary conditions (PBCs) can be applied to a single unit cell, leading to an infinite two-dimensional array approach. This methodology has been widely used to analyse metamaterials and metasurfaces (e.g. [58]), and in principle is not limited in thickness, that is, more than

one resonator could be inserted inside the unit cell along the incident propagation axis.

For instance, a circular Archimedean spiral resonator printed on dielectric strips has been designed and simulated as AMM with the help of Ansoft HFSS [59]. In this case, PBCs have been applied to a unit cell comprising only one spiral resonator, having two sides of the unit cell (along y axis) with perfect electric conductor (PEC) as boundary condition, and the other two (along x axis) with perfect magnetic conductor (PMC), as can be seen in Figure 3.2. In addition, the spiral resonator is considered as a perfect magnetic conductor strip with zero thickness in order to simplify the simulations, and it is etched on a FR4 epoxy ($\varepsilon_r = 4.4$, and $\tan\delta = 0.02$) with a dielectric thickness of 0.27 mm. The unit cell of the metamaterial slab is cube-shaped with a side width of 8 mm.
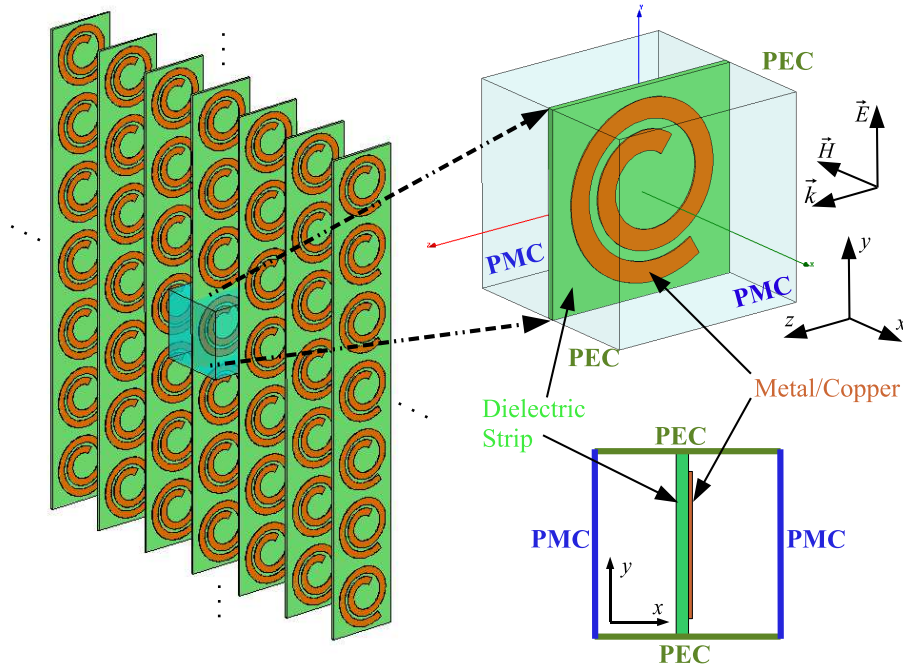
Figure 3.2: Infinite array approach by means of periodic boundary conditions (PBC) applied to a single unit cell (two sides as PEC and two sides as PMC).

The remaining two sides of the unit cell (along z axis) are used as waveports, for excitation and radiation purposes. Further details on boundary conditions and excitations assignment to a unit cell are shown in Figure 3.3. Note that, the waveport #1 will be used as the reference port #1 for the S-parameters; the same thing applies to waveport #2 for port #2.

Since the unit cell is surrounded by two PEC sides and two PMC sides, this method is also called PEC/PMC periodic boundary conditions. Moreover, Master/Slave boundary conditions, could also be used in Ansoft HFSS as PBC [60] instead of PEC/PMC ones. However, due to its increased computing time and set-up configuration complex-

(a) PEC Boundary Condition   (b) PMC Boundary Condition   (c) Waveports
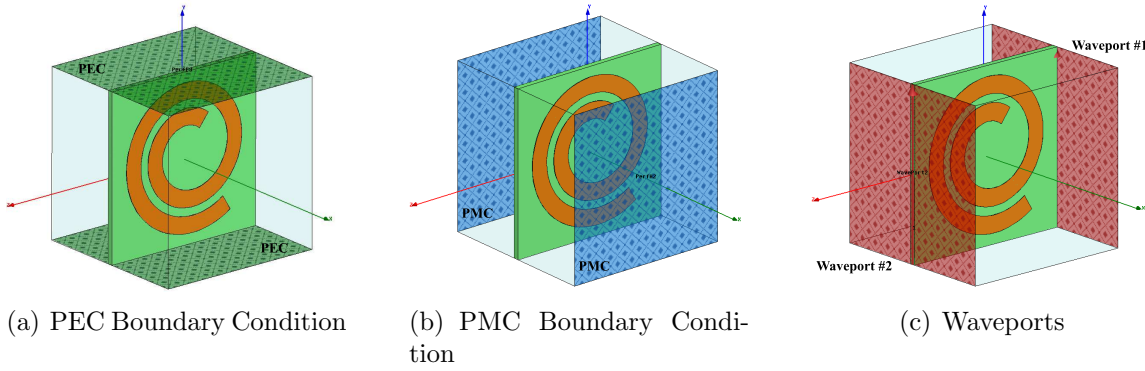
Figure 3.3: Boundary conditions and excitations applied to a single unit cell.

ity, they are mostly applied when dealing with oblique incidence and other EM fields computations.

An incident electric field $\vec{E}$ linearly polarised along $+y$ axis (parallel to the plane where the magnetic resonator is placed) is used to excite the SR AMM; the propagation vector $\vec{k}$ goes along the $+z$ axis; and the magnetic field $\vec{H}$ goes along $-x$ axis (along the axis of the spiral resonator), which could also be used to excite the magnetic inclusion. The S-parameters (S_{11}, S_{21} and S_{22}) as a function of the frequency (from 2 to 4 GHz) are obtained through HFSS simulations, as can be seen in Figure 3.4. The magnitude of the S-parameters is typically presented in logarithmic scale as $20log_{10}|S_{ij}|$, and the phase is often presented in degrees, ranging from -180° to 180°, or equivalently, from $-\pi$ to π radians. However, the phase is sometimes presented unwrapped, that is, as a continuous result with no 360° (or 2π) jumps.

(a) Magnitude of S_{ij} (b) Phase of S_{ij}
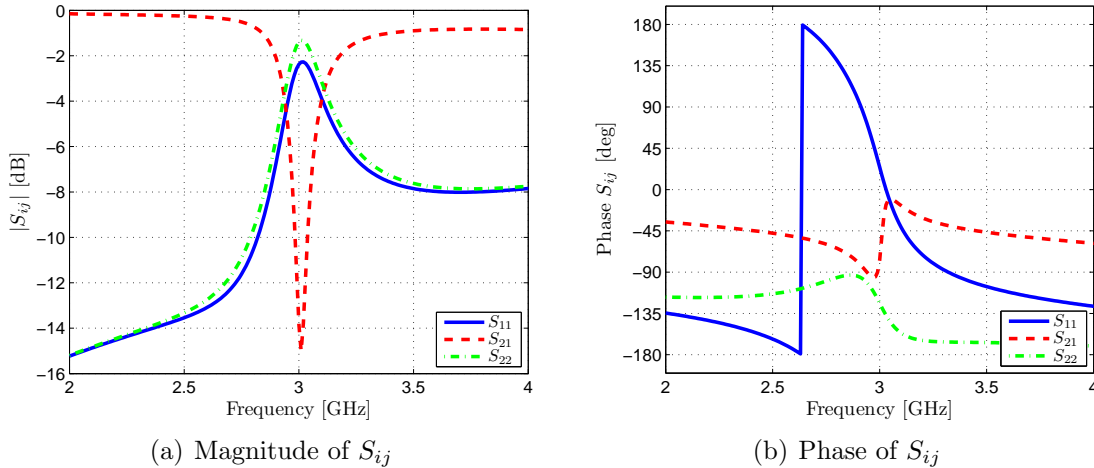
Figure 3.4: S-parameter results of the SR AMM.

From the S-parameter results, it is seen that the SR AMM is eminently a reflecting material around 3 GHz, since S_{11} and S_{22} have a high value around 3 GHz; at the same time, S_{21} presents a dip around 3 GHz, confirming the non-propagating property of the

typical AMMs around the resonant frequency, as already seen in Figure 2.1 for the case of MNG ($\mu_r < 0$) metamaterials. Moreover, the phase behaviour of the S-parameters reveals an asymmetry (or anisotropy), since the phase behaviours of S_{11} and S_{22} are different. However, the phase of S_{11} decreases from 180° to -180° while crossing the 0° axis around 3 GHz. Regarding the image theory of electric currents, a 0° phase behaviour is equivalent to the perfect magnetic conductor (PMC) property, and it may lead to the design of artificial magnetic conductors/reflectors (AMCs/AMRs). On the other hand, the phase of S_{22} remains around -135°, which is closer to $-180°$, the phase defined for the perfect electric conductor (PEC) property. In this case, the anisotropy that arises from S_{11} and S_{22} leads to a dual PEC/PMC behaviour of such AMMs.

Regarding the magnitude of the S-parameters, the maximum of S_{11}-S_{22} and the minimum of S_{21} occur around 3 GHz, which could be considered as the resonant frequency (f_0) of the SR AMM. However, taking advantage of the PMC property of these AMMs, another definition for resonant frequency comes from the frequency at which the phase of S_{11} crosses the 0° axis ($f_0 = f|_{phase(S_{11}) = 0°}$). Once defined f_0, the fractional bandwidth (FBW) comes from the relation between f_0, f_1 and f_2, given a bandwidth level (e.g. $\pm 45°$ or $\pm 90°$). For the case of a $\pm 45°$ FBW, it is defined as:

$$FBW_{\pm 45°}[\%] = \frac{f_2 - f_1}{f_0} 100\%$$

$$f_1 \equiv f|_{phase(S_{11})=45°} \tag{3.1}$$

$$f_2 \equiv f|_{phase(S_{11})=-45°}$$

Other parameters could be found from the S_{11}-S_{22} results to characterise the AMMs, like the electrical thickness (or electrical size), which is defined as the ratio between the physical thickness of the AMM surface/slab t, that is, the thickness of the unit cell in which the metamaterial resonator is embedded, and the wavelength at the resonance λ_0 in free space, as indicated in (3.2).

$$Electrical\ Thickness\ [\lambda] \equiv t\frac{f_0}{c} = \frac{t}{\lambda_0} \tag{3.2}$$

Another important parameter is related with the losses. It has been seen that the AMMs are mainly reflecting materials at f_0, although the reflected power may suffer from material losses, absorption, or cross-polarisation effects. Thus, the losses L of a metamaterial slab (or metamaterial resonator) are defined as the level of S_{11} (or S_{22}) at the resonant frequency f_0, as indicated in (3.3).

$$L\ [dB] = 20log_{10}|S_{ii}|_{f=f_0} \tag{3.3}$$

The losses L and the fractional bandwidth FBW at f_0 of the previous spiral resonator are depicted in Figure 3.5, according to the S_{11} results extracted from Figure 3.4. In this case, the losses are about -2.34 dB, the FBW$_{\pm 45°}$ is 4.44%, and the electric thickness is $\lambda/12.4$.

(a) Losses at f_0 (b) $\pm 45°$ FBW definition at f_0
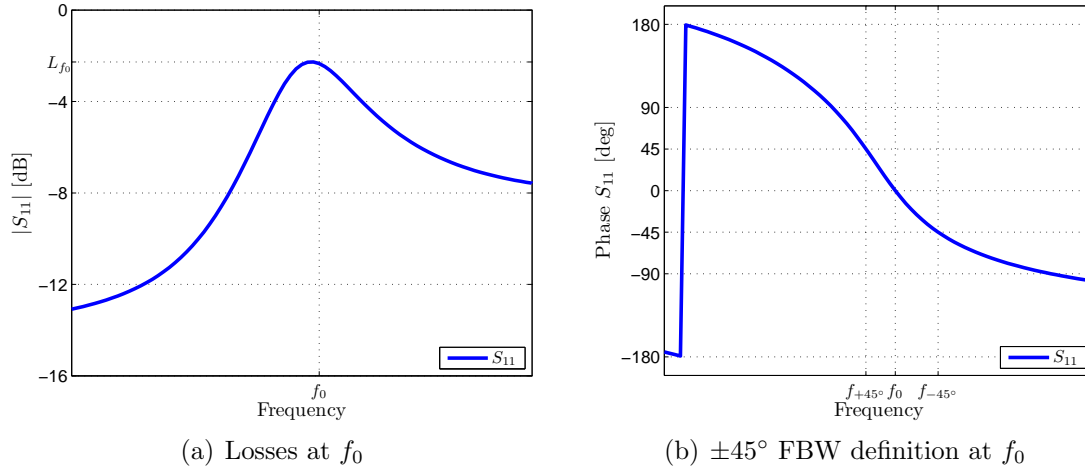
Figure 3.5: Definition of losses and FBW at the resonant frequency f_0 of a generic AMM.

In principle, the S_{21} results do not provide characteristic parameters of the AMMs, although the magnitude of S_{21} might become important when dealing with EM blocking applications around f_0 (minimum S_{21} is desired), or when dealing with a propagation response (maximum S_{21} is desired) of the metamaterial slab.

3.2.2   MNG Measurement Setup

The waveguide MNG behaviour assessment could be used as a method to characterise the AMMs, assuming the μ-dispersive property of the AMMs, which implies different frequency bands of interest depending on the values of the relative magnetic permeability (μ_r). Considering the resonant frequency f_0 of the previous spiral resonator slab as a reference, the MNG band ($\mu_r < 0$) is expected just above f_0, that is, for $f > 3$ GHz.

The existence of a MNG band above the resonant frequency f_0 is assessed by putting several layers of spiral resonators inside a non-propagating waveguide, and finding a pass-band just above f_0. This measurement setup was initially proposed by Marqués for the case of SRRs [61], and it was also applied to the case of SRs [52]. The key point of this measurement procedure is to assume that a hollow metallic waveguide can produce a negative electric permittivity (ENG, or $\varepsilon_r < 0$) behaviour along the axial direction, when the operational frequency is below the cut-off frequency of its dominant mode [61]. Then, some magnetic resonators (e.g. spiral resonators) are

placed inside the waveguide in order to produce the MNG behaviour necessary to obtain a left-handed transmission band. So, this left-handed transmission band (or pass-band) denotes the frequency band at which the electric permittivity and magnetic permeability are both negative, thus showing the MNG frequency band produced by the magnetic resonators placed inside the waveguide when operating below the cut-off frequency of the waveguide.

The measurement kit is composed of different interconnected metallic waveguides, as can be seen in Figure 3.6. A hollow square waveguide is inserted between two N-to-WR340 transitions, which will be connected to a vector network analyser (VNA) through the N-to-SMA transitions. Notice that the square waveguide will be the host medium for the metamaterial samples under test.
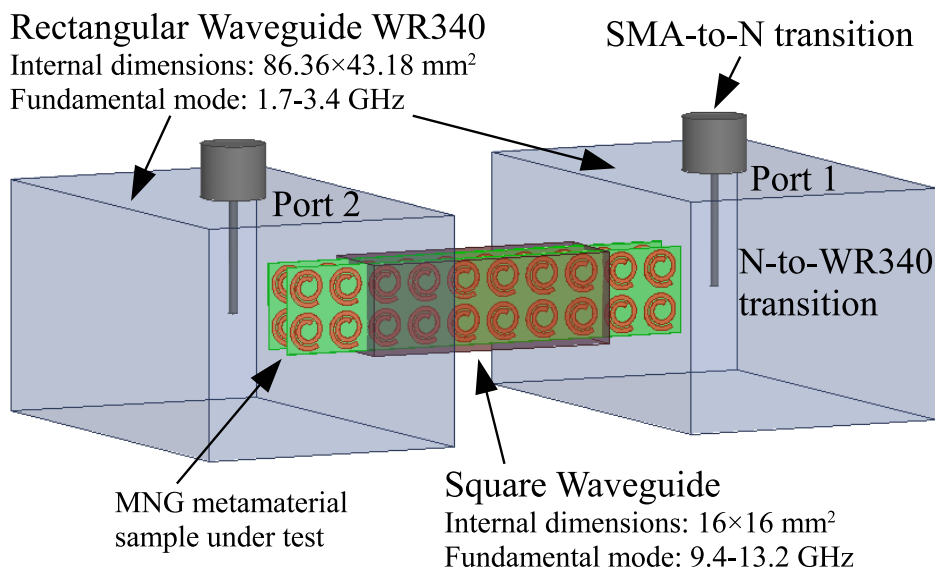
Figure 3.6: Sketch of the measurement kit composed of different interconnected wave-
guides, and how the metamaterial samples are placed inside the hollow
square waveguide.

The complete measurement setup can be observed in Figure 3.7, showing the measurement kit connected to the HP8510C network analyser, as well as a detail of the metamaterial samples under test placed inside the square waveguide. The propagation in the fundamental mode of the WR340 waveguide sections is found between 1.7-3.4 GHz, which will be used to excite the metamaterial samples. This fundamental mode is significantly lower than the cut-off frequency of the square waveguide, which propagates only in its fundamental mode between 9.4-13.2 GHz.

The circular spiral resonator samples have been printed on a FR4 substrate using standard photo-etching techniques. The dimensions of the spiral resonators are the same as the ones used before in the numerical simulations. And then, two rows with
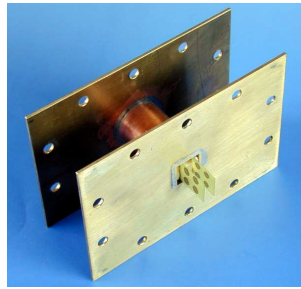
(a) Metamaterial samples placed inside the square waveguide
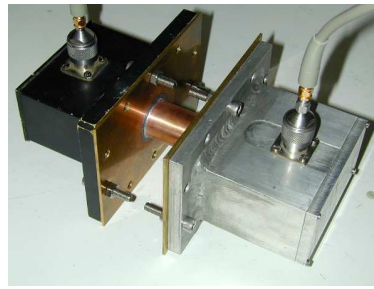
(b) Measurement waveguide setup

(c) Complete measurement setup including the HP8510C network analyser

Figure 3.7: Photographs of the measurement setup composed of two coax-to-WR340 waveguide transitions and a square waveguide connecting both transitions, and a detail of the metamaterial samples placed inside the square waveguide.

ten spiral resonators have been printed in each dielectric strip, as can be seen in Figure 3.8.

Once fabricated, the circular spiral resonator samples were inserted inside the square waveguide. Since the cross-section dimensions of the square waveguide are $16{\times}16$ mm^2, the two strips containing the spiral resonators completely fill the square waveguide (in height and width), while maintaining a gap of 8 mm between adjacent layers of resonators, the same unit cell width used in the simulations. However, taking into account that the length of the square waveguide is 50 mm, only six spiral resonator layers completely fit inside the waveguide, whereas two spiral resonator layers are placed outside each end of the square waveguide.

The HP8510C network analyser has been used to measure the transmission coeffi-
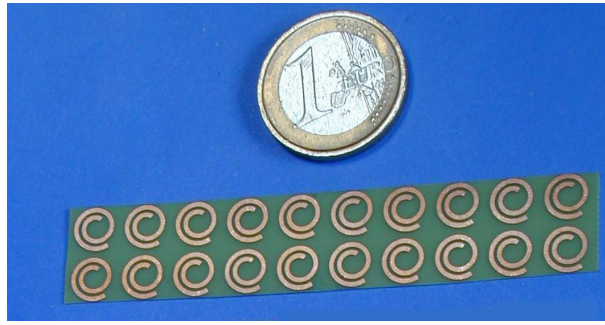
Figure 3.8: Fabricated circular spiral resonators on FR4 substrate to be placed inside the waveguide.

cient S_{12} between the two ports of the WR340 waveguides, with the SR-loaded square waveguide in between. The measured results are plotted in Figure 3.9, where a pass-band appears above 3.2 GHz for the circular spiral resonator. The pass-band provides a neat transmission region of more than 70 dB above the noise level. This result may also be useful for waveguide miniaturisation applications, at the expense of non-negligible insertion losses. In other words, insertion losses of more than 15 dB are observed in each pass-band and they may be due to the mismatch between the waveguide transitions and the WR340 waveguide section. Multi-pass-band results with very low insertion losses have subsequently been achieved in [62], identifying the mismatch between waveguide sections as the source of the insertion losses in the pass-bands.
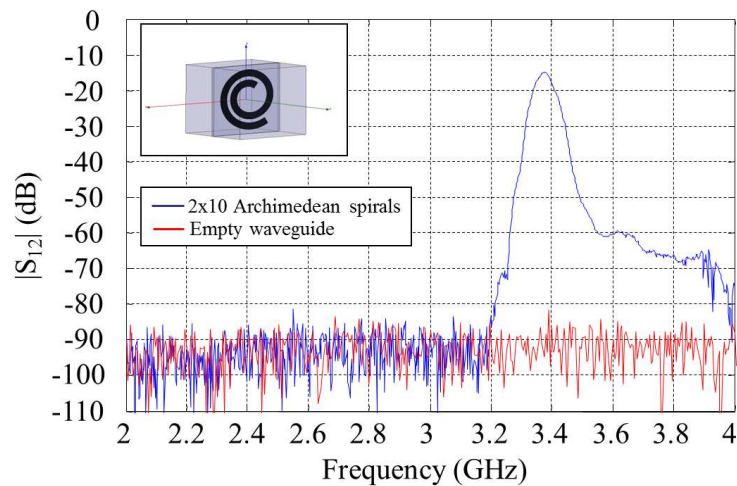
Figure 3.9: Measured transmission coefficient S_{12} of the circular SR loaded waveguide. This result is compared with the empty waveguide case.

3.3   Why Spiral Resonators as AMMs?

One fundamental property of the spiral resonators (SRs) is their smaller electrical size with respect to the SRRs and single loop SRRs (open loops), yielding to a higher degree of material homogenisation [53], at the expense of a smaller fractional bandwidth. This fact is confirmed when simulating different types of AMMs, that is, a single loop SRR, a SRR and a SR, all of them having the same dimensions. The unit cell dimensions along the xyz axes are 8×8×8 mm³. being 0.8 mm the width of the the metal strips (lw), and 0.4 mm the width of gaps (lg) that form each magnetic resonator. In addition, the metal strips are considered as PEC and they have been etched on FR4 ($\varepsilon_r = 4.4$, $\tan \delta = 0.02$) dielectric layers, with a thickness of 0.27 mm. In all cases, the reference port #1 has been considered on the side of the aperture (for the SR) or the gap (for the SRRs) of the magnetic inclusions. The S_{11} and S_{21} results for the three magnetic inclusions are plotted in Figure 3.10.

(a) Magnitude of S_{11} and S_{21} (b) Phase of S_{11}
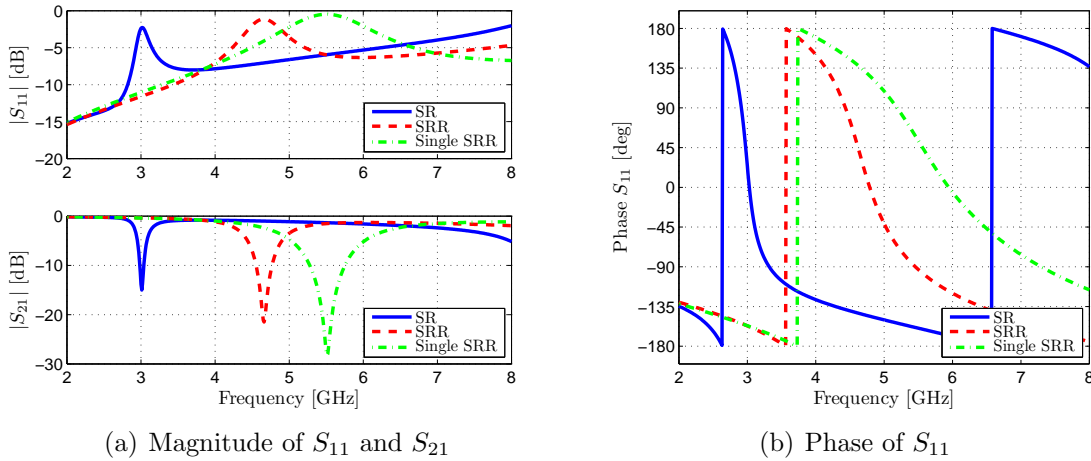
Figure 3.10: Simulated S_{11} and S_{21} results of the Single SRR, the SRR and the SR.

It is confirmed from the figure that higher miniaturisation is achieved with the use of an SR AMM, when compared with the SRR and the single loop SRR cases, at the expense of a decreased $\pm45°$FBW and slightly higher losses at f_0. Thus, a trade-off between miniaturisation of magnetic resonators and achievable FBW is established for AMMs. Some of the characteristic parameters of these magnetic resonators are listed in Table 3.1.

Besides the miniaturisation property, spiral resonators offer an ease of operational frequency tunability, by simply changing the number of turns of the spiral resonator given a maximum external radius. Note that fractional number of turns are also allowed. In fact, the spiral resonator presented before has 1.7 turns. Given the external radius of a spiral resonator ($lx/2$), the maximum number of turns N_{max}^{SR} is given by

AMM type	AMM geometry	f_0	Electrical Thickness	FBW$_{\pm 45°}$	Losses at f_0
Single SRR		5.95 GHz	$\lambda/6.3$	15.43%	-1.83 dB
SRR		4.79 GHz	$\lambda/7.83$	8.52%	-1.71 dB
SR		3.03 GHz	$\lambda/12.38$	4.44%	-2.34 dB

Table 3.1: Parameter comparison of SR, SRR and Single SRR AMMs.

(3.4) [63], where lw is the metal strip width, and lg the gap between adjacent strips. SRRs could also be miniaturised by adding internal split rings, defined as multiple split rings resonators (MSRRs), although the achievable miniaturisation factor is always lower than the one for spiral resonators [63].

$$N_{max}^{SR} \approx \text{Integer Part} \left[\frac{lx - (lw + lg)}{2(lw + lg)} \right] \tag{3.4}$$

The SR AMM presented before could be studied in terms of arm length variation, from 1 to 2.5 turns (previous design was 1.7 turns long), while keeping the other dimensions lx, lw and lg with the same initial values. The simulated S-parameter results are presented in Figure 3.11.

(a) Magnitude of S_{11} and S_{21} (b) Phase of S_{11}
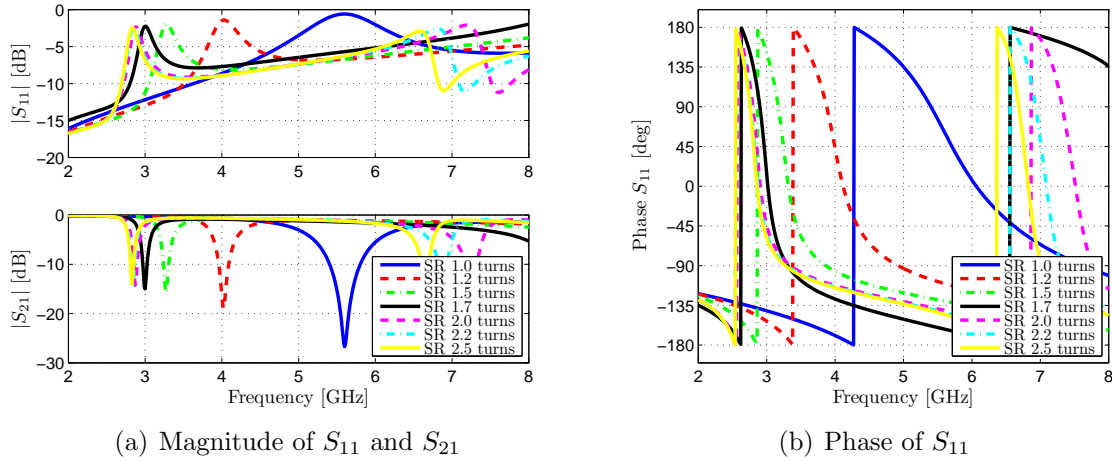
Figure 3.11: Simulated S_{11} and S_{21} results of the SR when increasing the spiral arm length.

A miniaturisation from about 6 GHz to 2.9 GHz has been achieved when increasing the number of turns from 1 to 2.5. A saturation in terms of resonant frequency is appreciated for a spiral arm length greater than 2 turns. This fact is also seen in Figure 3.12 (a), where the resonant frequency f_0 is plotted as a function of the spiral arm length. The highest miniaturisation increment is achieved from 1 to 1.2 turns, reaching the saturation above 2 turns. Moreover, higher miniaturisation (lower f_0)

also means lower FBW, as confirmed in Figure 3.12 (b), where the FBW decreases from about 15% to 4%. Finally, the level of S_{11} losses at f_0 remains almost constant (around -2.5 dB) when increasing the spiral arm length, as shown in Figure 3.12 (c), although the maximum S_{11} level slightly decreases as the miniaturisation is increased. Note that some variations in the S-parameter results (observed both in the magnitude and in the phase) appear above 6 GHz, although they correspond to superior resonances of the SR AMMs due to the increased miniaturisation factor when the spiral arm length is greater than 1.7 turns.

(a) Resonant frequency f_0 (b) $FBW_{\pm 45°}$ at f_0 (c) S_{11} losses at f_0
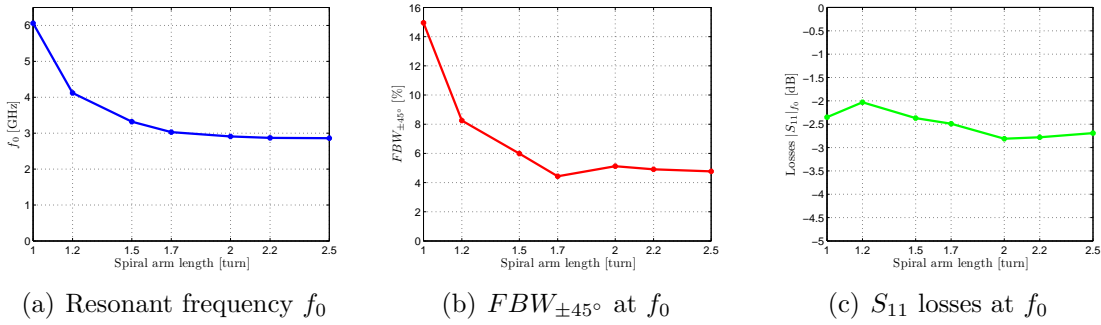
Figure 3.12: Resonant frequency f_0, FBW and losses results as a function of number of turns of the spiral arm.

Characteristic parameters of the spiral resonators simulations for different spiral arm lengths are listed in Table 3.2.

SR arm length [turn]	SR AMM geometry	f_0	Electrical Thickness	FBW$_{\pm 45°}$	Losses at f_0
1.0		6.06 GHz	$\lambda/6.18$	14.95%	-2.35 dB
1.2		4.12 GHz	$\lambda/9.1$	8.25%	-2.03 dB
1.5		3.32 GHz	$\lambda/11.3$	5.99%	-2.37 dB
1.7		3.03 GHz	$\lambda/12.38$	4.44%	-2.49 dB
2.0		2.91 GHz	$\lambda/12.89$	5.12%	-2.81 dB
2.2		2.87 GHz	$\lambda/13.07$	4.91%	-2.78 dB
2.5		2.86 GHz	$\lambda/13.11$	4.77%	-2.69 dB

Table 3.2: Parameter comparison of the SR AMM when changing the spiral arm length.

Another property of the (circular) spiral resonator is that it can be rotated around its own axis producing different responses. In fact, the previously analysed magnetic resonators are considered to have no rotation (or 0°). For the case of an SR AMM (and other types of AMMs), a PMC response is obtained at the resonance in S_{11}, (phase(S_{11})

$= 0°$), and a PEC response in S_{22} (phase(S_{22}) $\approx \pm 180°$). Taking into account the PEC/PMC property of the SR AMMs, different responses between the PMC and the PEC behaviours may be expected when rotating the spiral resonator around its axis. Simulated S-parameter results of the SR AMM when the spiral resonator is rotated from $0°$ to $330°$ are presented in Figure 3.13.

(a) Magnitude of S_{11} and S_{21} (b) Phase of S_{11}
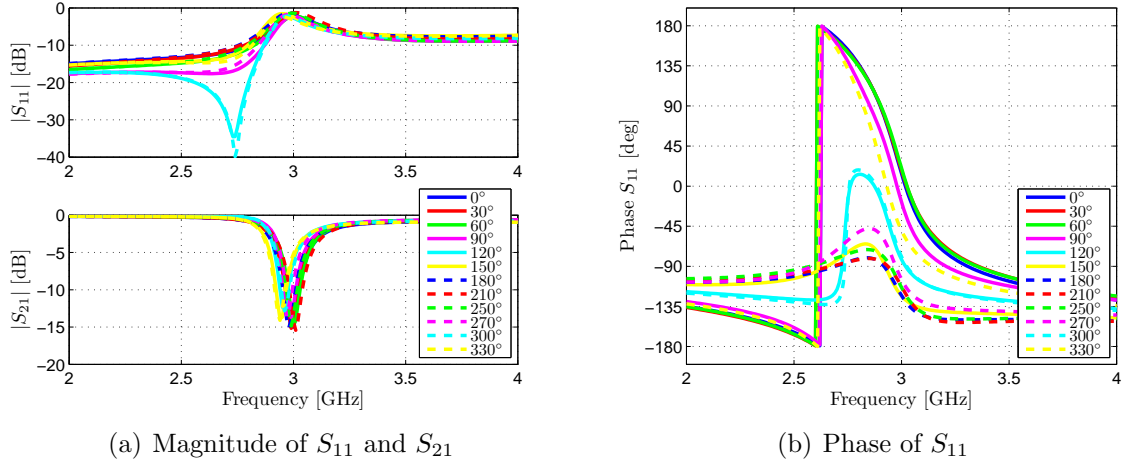
Figure 3.13: Simulated S_{11} and S_{21} results of the SR when rotating the spiral.

Simulated results confirm that the rotation of the spiral resonator around its axis mainly affects the phase behaviour of S_{11}, showing PMC-like responses for SR rotations of $0°$, $30°$, $60°$, $90°$ and $330°$. Note that these PMC-like results are obtained when the aperture of the spiral resonator is facing the illuminating electric field. On the other hand, PEC-like responses (or a phase at the resonance very different to $0°$) are obtained for the other values of SR rotation. In addition, some other results also cross the $0°$ axis, although the phase behaviour is bizarre, making the $FBW_{\pm 45°}$ calculation not possible (e.g. $120°$ and $300°$ cases). Moreover, those results present high S_{11} losses at their correspondent f_0. In general, magnitudes of S_{11} and S_{21} remain practically insensitive to the SR rotation angle. The characteristic parameters of the spiral resonator simulations when changing the angle of rotation are listed in Table 3.3.

In this case, although the $0°$ SR AMM seems to produce a PMC like response with almost the best FBW and lower S_{11} losses at f_0, some other rotation angle cases might be considered for PMC purposes like $30°$, $60°$ and $330°$, providing a certain rotation angle tolerance while achieving the PMC response.

On the other hand, square spiral resonators are also feasible as SR AMMs [53, 63]. They are of interest because they occupy more space given a square (or rectangular) shaped unit cell, and they also restrict the angular rotation of the spiral resonator to only four angles ($0°$, $90°$, $180°$ and $270°$). Thus, a square shaped spiral resonator has been designed as AMM. Fiberglass FR4 ($\varepsilon_r = 4.4$, tan $\delta = 0.02$) has been used as

SR rotation [deg]	SR AMM geometry	f_0	Electrical Thickness	FBW$_{\pm 45°}$	Losses at f_0
0		3.02 GHz	$\lambda/12.42$	4.46%	-2.34 dB
30		3.02 GHz	$\lambda/12.42$	4.79%	-2.41 dB
60		3.03 GHz	$\lambda/12.38$	4.78%	-2.41 dB
90		2.98 GHz	$\lambda/12.58$	3.84%	-2.52 dB
120		2.87 GHz	$\lambda/13.06$	-	-9.61 dB
150		-	-	-	-
180		-	-	-	-
210		-	-	-	-
240		-	-	-	-
270		-	-	-	-
300		2.88 GHz	$\lambda/13.02$	-	-9.12 dB
330		2.93 GHz	$\lambda/12.8$	3.70%	-2.58 dB

Table 3.3: Parameter comparison of the SR AMM when changing the SR rotation angle around its axis.

the dielectric substrate in the previous simulations, although it has important dielectric losses, which produced S_{11} losses at f_0 of about -2.4 dB. For this reason, Rogers RO4003C ($\varepsilon_r = 3.38$, $\tan \delta = 0.0027$) is a good alternative to FR4 as a practical low loss dielectric substrate for AMMs.

The unit cell dimensions of the square SR AMM are $6 \times 4 \times 6$ mm^3 along the xyz axes, that is, the $t \times g \times h$ factor, as indicated in Figure 3.14. The dielectric substrate is Rogers RO4003C, with a dielectric strip thickness of 0.8 mm, and a copper thickness of 18 μm. The spiral resonator has 2 turns and its major size lz is 5.6 mm, with a spiral arm width lw of 0.6 mm and the internal gap lg is 0.4 mm.

Note that the spiral resonator is placed in a plane parallel to the xz plane, and when applying periodic boundary conditions, the periodicity is established in the yz plane. An incident electric field $\vec{E}$ linearly polarised along the $+z$ axis is used to excite the square SR AMM, and the propagation vector $\vec{k}$ goes along the $+x$ axis, whereas the magnetic field $\vec{H}$ oriented along $-y$ axis. The simulated S-parameters are plotted in Figure 3.15 for a frequency range from 2 to 8 GHz. The reference port #1 for the S-parameters goes along the $+x$ axis, whereas the port #2 goes along the $-x$ axis.

The response of this 2-turn square SR AMM is similar to that of the 1.7-turn circular SR AMM presented before. The phase of the reflection coefficient S_{11} crosses the 0° axis at 2.6 GHz, producing a PMC-like response with a $FBW_{\pm 45°}$ of 5.86% and losses at
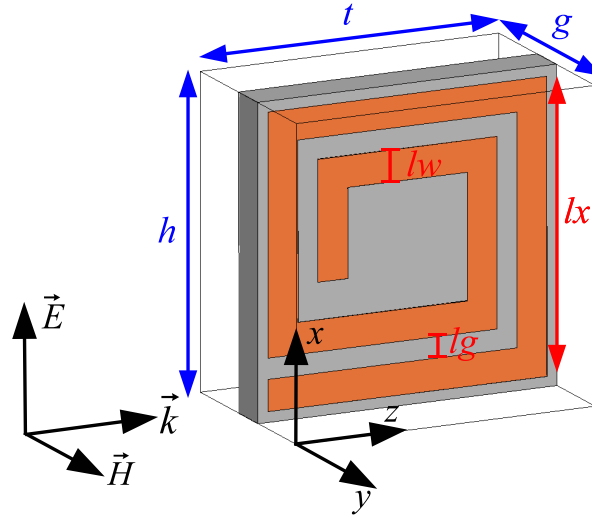
Figure 3.14: Detail of the unit cell of the square spiral resonator printed on Rogers RO4003C substrate. In this design, $h = t = 6$ mm, $g = 4$ mm, $lz = 5.6$ mm, $lw = 0.6$ mm and $lg = 0.4$ mm. The characteristics of RO4003C substrate are thickness $= 0.8$ mm, copper thickness $= 18$ μm, $\varepsilon_r = 3.38$, and $\tan \delta = 0.0027$.

(a) Magnitude of S_{ij}

(b) Phase of S_{ij}
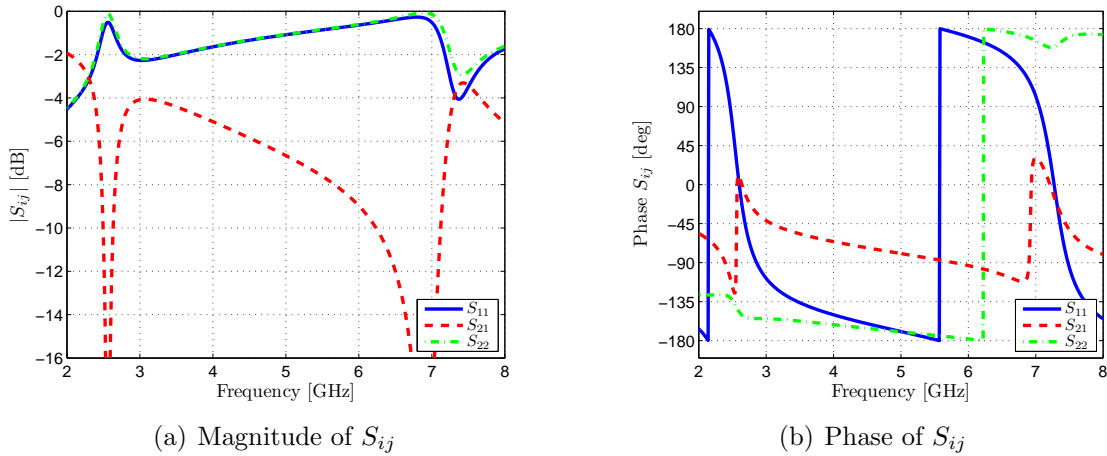
Figure 3.15: Simulated S-parameter results of the square SR AMM printed on RO4003C dielectric substrate.

f_0 of only -0.64 dB. On the other hand, the S_{22} results have a PEC-like response with a phase around f_0 of about -147°, and losses of -0.26 dB. Again, the anisotropic behaviour ($S_{11} \neq S_{22}$) is obtained due to the non-symmetric shape of the square SR along the propagation direction. In this case, the reflected PMC-like response is obtained when the aperture of the spiral resonator is illuminated, whereas the reflected PEC-like response is obtained when the opposite side of the spiral resonator (no aperture) is illuminated. In transmission, the S_{21} results show a dip in magnitude of more than 30 dB at f_0, as expected for this kind of magnetic inclusions. Hence, with this design

not only the losses have been reduced (due to the use of the RO4003C as dielectric substrate which has lower losses than the FR4), but also the electric thickness has been improved to $\lambda/19.2$. Note that the variations above 6 GHz in the S-parameter results correspond to a second resonance of the spiral resonator, although it is not practical due to its higher magnitude losses.

3.4   Effective Medium Approach

The effective medium approach of a metamaterial is directly linked to miniaturisation and homogenisation. An effectively homogeneous material is a structure whose unit cell size p is much smaller than the guided wavelength λ_g [3]. It is well known that metamaterials are composed of periodic arrangements of electric/magnetic resonators. Then, if the the unit cell size is equal to or smaller than the guided wavelength $p \leq \lambda_g/4$, the effective-homogeneity property is satisfied. Therefore, the structure behaves as a real material with effective constitutive parameters, that is, the electric permittivity ε_{eff} or ε_r, the magnetic permeability μ_{eff} or μ_r, and hence, the refraction index n_{eff}.

The effective material parameters of a composite slab are mainly retrieved from plane-wave reflection (R) and transmission (T) parameters, i.e. S_{11} and S_{21}, assuming the slab as a continuous and uniform medium. In this way, the effective parameters can be obtained from simulations or measurements of the S-parameters [58, 64–70]. Other retrieval methods use the impedance z and the refraction index n definitions in terms of S-parameters; then, considering the dispersive models of the electric permittivity and the magnetic permeability, the effective parameters are obtained through optimisation algorithms [71–73]. Another practical methodology relies on the combination of the equivalent circuit model of the electric/magnetic resonator (in terms of capacitances and inductances) and the electric/magnetic polarisabilities through the Clausius-Mossoti formulation [1], thus obtaining the effective parameters [74–78]. Finally, a field summation technique could also be used [79], where the effective parameters are obtained from the field averaging through the number of unit cells along the direction of propagation.

Taking into account that the study of effective material parameter extraction methods is not the purpose of this dissertation, R-T extraction methods are of interest due to their simplicity and general problem application. The initial point is to have a metamaterial slab (ε_r, μ_r) with a thickness d embedded in free space (ε_0, μ_0). The S-parameters are defined outside the metamaterial slab representing the correspondent reflected (R) and transmitted (T) waves. A sketch of this configuration is shown in Figure 3.16.
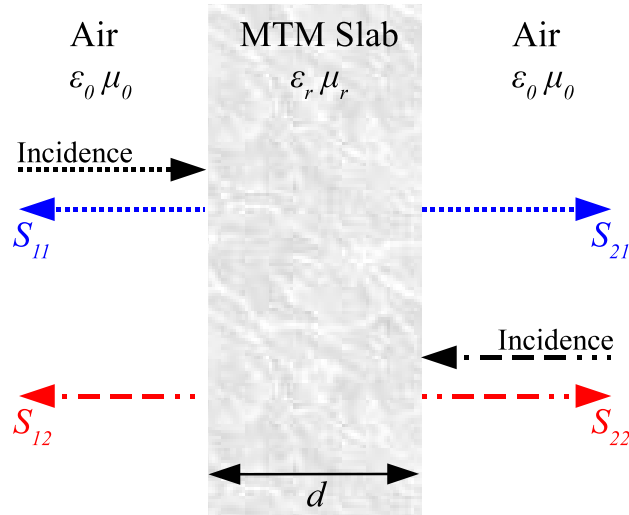
Figure 3.16: Sketch of the S-parameters definition for a metamaterial slab embedded in free space.

The simplest *R-T* extraction method is referred as the Nicolson-Ross-Weir (NRW) approach, introduced for AMMs in [58]. Two composite terms V_1 and V_2 are introduced from the combination of S_{11} and S_{21}:

$$V_1 = S_{21} + S_{11}$$

$$V_2 = S_{21} - S_{11}$$

(3.5)

After some derivations and assuming $k_0 d \leq 1$ (this stands for electrically thin layers of metamaterials), where k_0 is the free space wavenumber and d the metamaterial slab thickness, the relative permittivity and permeability are obtained as:

$$\varepsilon_r \approx \frac{2}{jk_0 d}\frac{1 - V_1}{1 + V_1}$$

$$\mu_r \approx \frac{2}{jk_0 d}\frac{1 - V_2}{1 + V_2}$$

(3.6)

The effective material parameters of the aforementioned square spiral resonator have been retrieved from the S-parameters (see Figure 3.15). The real and imaginary parts of the relative electric permittivity ε_r and magnetic permeability μ_r using NRW method are plotted in Figure 3.17.

The results retrieved confirm the μ-dispersive behaviour of the square spiral AMM slabs. Two resonances appear in the μ_r results (around 2.6 and 7.3 GHz), which correspond to the frequencies at which the phase(S_{11}) = 0°. Two resonances appear in the ε_r results (at 2.45 and 6.3 GHz), which in principle correspond to frequencies at which the phase(S_{11}) $\approx$ 180°. The imaginary parts of ε_r and μ_r are considered as

(a) Relative electric permittivity ε_r (b) Relative magnetic permeability μ_r
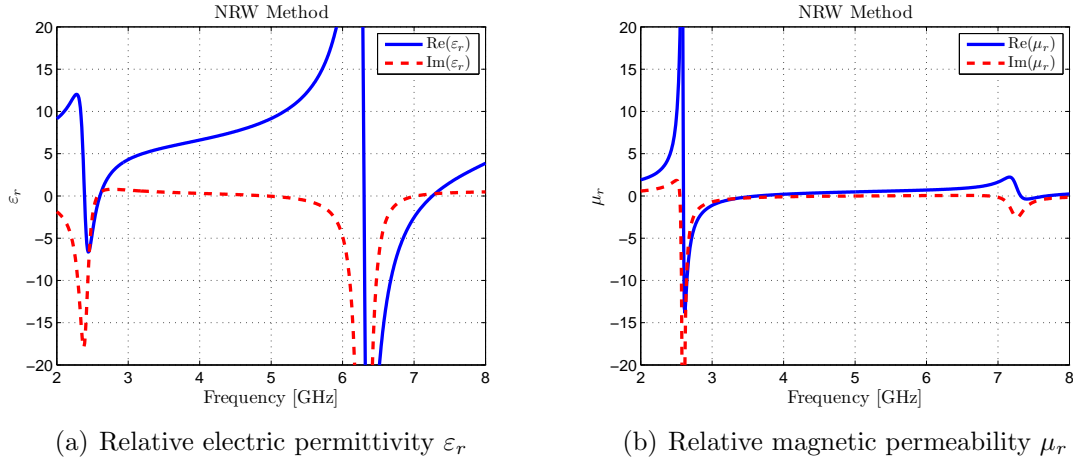
Figure 3.17: Effective material parameters of the square SR extracted applying the NRW method.

material losses when they are different than 0. In addition, the imaginary parts of ε_r and μ_r shown in Figure 3.17 are mainly negative. This fact is due to a $e^{j\omega t}$ time dependence assumption. Thus, positive imaginary values are considered non-physical.

However, most metamaterial slabs are often inhomogeneous, that is, they are composed of non symmetric resonators, which present different reflection parameters when illuminating the slab on one side or on the another, showing an anisotropic behaviour ($S_{11} \neq S_{22}$). In [65], Smith fails to provide a closed procedure to retrieve the effective material parameters of inhomogeneous metamaterial slabs; an average reflection coefficient is then considered, $S_{avg} = \sqrt{S_{11}S_{22}}$, although the value of z is still ambiguous, and hence, ε_r and μ_r could not be properly determined.

In this way, metamaterial slabs which are composed of ring shaped resonators (like the SRR or the SR) are often anisotropic because of the orientations and apertures of the rings, and they may also present bianisotropic behaviour due to the specific properties of the rings. Remember, that bianisotropy in magnetic resonators was studied in [55] for the case of SRRs and in [52] for the case of SRs. Considering the resonator orientation shown in Figure 3.14, and supposing a reciprocal and bianisotropic metamaterial medium, the constitutive relationships are written as [68]:

$$\bar{D} = \bar{\bar{\varepsilon}} \cdot \bar{E} + \bar{\bar{\xi}} \cdot \bar{H}$$

$$\bar{B} = \bar{\bar{\mu}} \cdot \bar{H} + \bar{\bar{\zeta}} \cdot \bar{E}$$

(3.7)

being $\bar{\bar{\varepsilon}}$ the permittivity tensor, $\bar{\bar{\mu}}$ the permeability tensor, and $\bar{\bar{\xi}}$ and $\bar{\bar{\zeta}}$ the magneto-electric coupling tensors, which have the following form:

$$\bar{\bar{\varepsilon}} = \varepsilon_0 \begin{pmatrix} \varepsilon_x & 0 & 0 \\ 0 & \varepsilon_y & 0 \\ 0 & 0 & \varepsilon_z \end{pmatrix} \quad \bar{\bar{\mu}} = \mu_0 \begin{pmatrix} \mu_x & 0 & 0 \\ 0 & \mu_y & 0 \\ 0 & 0 & \mu_z \end{pmatrix}$$

$$\bar{\bar{\xi}} = \frac{1}{c} \begin{pmatrix} 0 & 0 & 0 \\ 0 & 0 & 0 \\ 0 & -j\xi_0 & 0 \end{pmatrix} \quad \bar{\bar{\zeta}} = \frac{1}{c} \begin{pmatrix} 0 & 0 & 0 \\ 0 & 0 & j\xi_0 \\ 0 & 0 & 0 \end{pmatrix}$$

$$(3.8)$$

where ε_0 and μ_0 are the permittivity and permeability of free space respectively, c the speed of light in free space. There are seven complex unknowns to be determined: ε_x, ε_y, ε_z, μ_x, μ_y, μ_z, and ξ_0. Thus, at least seven complex equations are required. This fact is fulfilled by illuminating the unit cell with different incidences (e.g. TE1, TM1, TE2, TM2, TE3, and TM3) [68], where each incidence gives two complex equations, one for reflection (S_{11}) and the other one for transmission (S_{21}). The use of the bianisotropic term ξ_0 in the retrieval method is justified to explain the differences between this method and the isotropic one.

But when a plane wave that is polarised in the z direction (propagation along x axis), only three parameters (ε_z, μ_y, and ξ_0) are active, while the other four (ε_x, ε_y, μ_x, and μ_z) are not involved in the bianisotropic behaviour. Note that the reference impedance of a bianisotropic material has different values depending on the direction of propagation in the x axis:

$$z^+ = \frac{\mu_y}{n + j\xi_o}$$

$$z^- = \frac{\mu_y}{n - j\xi_o}$$

$$(3.9)$$

where the refractive index n is now defined as:

$$n = \pm\sqrt{\varepsilon_z \mu_y - \xi_o^2} \tag{3.10}$$

Three complex equations are derived having the S-parameters as a function of the constitutive parameters (ε_z, μ_y, and ξ_0). After some derivations, the constitutive parameters are easily obtained:

$$\xi_0 = \left(\frac{n}{-2sin(nk_0 d)} \right) \left(\frac{S_{11} - S_{22}}{S_{21}} \right)$$

$$\mu_y = \left(\frac{jn}{sin(nk_0 d)} \right) \left(\frac{2 + S_{11} - S_{22}}{2S_{21}} - cos(nk_0 d) \right) \qquad (3.11)$$

$$\varepsilon_z = \frac{n^2 + \xi_0^2}{\mu_y}$$

This procedure is referred as the Li method [70], and improves the method presented in [68] by using S_{11} and S_{22} in the complex equations and the magneto-electric coupling coefficient ξ_0 (or bianisotropic term), which enables proper retrieval of the constitutive parameters of a bianisotropic inhomogeneous ($S_{11} \neq S_{22}$) metamaterial slab. The retrieved material parameters of the square spiral AMM slab using Li method are plotted in Figure 3.18 and in Figure 3.19.

(a) Relative electric permittivity ε_r　　　　　(b) Relative magnetic permeability μ_r
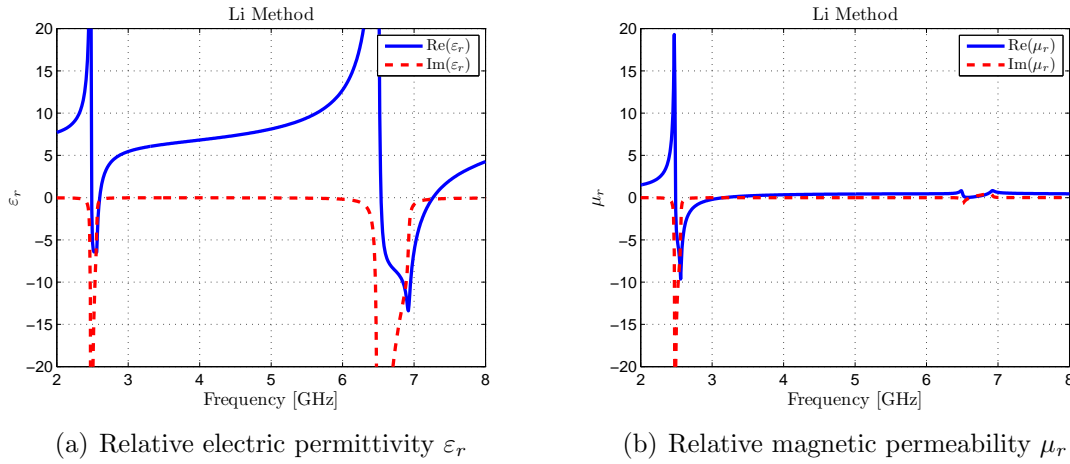
Figure 3.18: Effective material parameters extracted applying the Li method.

Note that with the Li method, the retrieved relative electric permittivity ε_r corresponds to the ε_z component of $\bar{\bar{\varepsilon}}$, and the relative magnetic permeability μ_r corresponds to the μ_y component of $\bar{\bar{\mu}}$. So, for any loop-like magnetic resonator and despite the bianisotropic effects, the μ_r enhancement is achieved along its axis (the direction normal to the surface of the magnetic resonator), whereas the ε_r enhancement is achieved along the direction of the polarisation of the incident electric field. Note that some authors also consider a ε_r enhancement along the direction of propagation (e.g. ε_x for the case of the square spiral AMM slab), thus having ε_r enhancement along two orthogonal directions of the plane where the magnetic resonator is laid ($\varepsilon_r \equiv \varepsilon_z = \varepsilon_x$). In fact, and following the same principle, the constitutive parameters ε_r and μ_r retrieved with the NRW method are also equivalent to ε_z and μ_y. In such a case, and considering the same orientation used in the retrieval methods, the permittivity $\bar{\bar{\varepsilon}}$ and the permeability
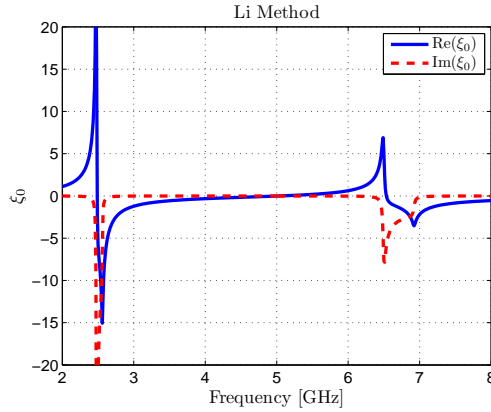
Figure 3.19: Magneto-electric coupling coefficient of the bianisotropic metamaterial slab extracted applying Li method.

$\bar{\bar{\mu}}$ tensors in (3.8) could be simplified to (3.12), confirming the anisotropic behaviour of the square spiral AMM slab:

$$\bar{\bar{\varepsilon}} = \varepsilon_0 \begin{pmatrix} \varepsilon_x & 0 & 0 \\ 0 & 1 & 0 \\ 0 & 0 & \varepsilon_z \end{pmatrix} \quad \bar{\bar{\mu}} = \mu_0 \begin{pmatrix} 1 & 0 & 0 \\ 0 & \mu_y & 0 \\ 0 & 0 & 1 \end{pmatrix} \tag{3.12}$$

It seems that the Li method has a broad application, since not only deals with inhomogeneous metamaterial slabs, but also with bianisotropic ones. The results obtained with the Li method are similar to those retrieved with the NRW method, finding the resonances at almost the same positions, with the exception of the correction introduced in the refraction index due to the magneto-electric factor xi_0.

These reflection and transmission methods are mainly used to determine the effective parameters, due to their simple formulation and general scope of application. In principle, they are valid for all types of electric/magnetic metamaterials, although the results may not be reliable in some cases, due to the isotropic, homogeneous, and non-bianisotropic approximations considered in the metamaterial slab. Sometimes, the wrong approximation relies in using the effective parameters retrieved from a single-layer metamaterial (the so called meta-surface) to be applied to synthesise a whole thicker metamaterial. Moreover, several critical papers are found in literature showing the limitations of the extraction methods when trying to fully describe the properties/behaviours of the metamaterial media [80–82].

Finally, the use of effective material parameters may be of interest not only to better describe the metamaterial phenomena, but also to be used in the numerical simulations. The simulation time of large metamaterial structures dramatically increases, as well as the computing and memory requirements. However, and depending on the complexity of the metamaterial design, only full-wave simulation results may be comparable to

measured results [83].

3.5   Chapter Conclusions

Circular and square spiral resonator AMMs present a higher degree of miniaturisation when compared with other magnetic resonators like the SRRs, despite their intrinsic anisotropic behaviour, due to their non-symmetric shape.

The 2-turn square SR AMM design printed on RO4003C substrate has been chosen among all other SR designs due to their higher miniaturisation degree ($\lambda/19.2$). The resonant frequency f_0 is found at 2.6 GHz, producing a reflected PMC-like response with a $FBW_{\pm 45°}$ of 5.86% and -0.64 dB of magnitude losses on one side, and a reflected PEC-like response on the opposite side, with magnitude losses of -0.23 dB, and a phase of -147° at f_0. In transmission, a dip of about -30 dB is found around f_0.

Potential applications of the square SR AMM design may be initially focused on the design of artificial magnetic conductors/reflectors (AMCs/AMRs), exploiting the PMC-like response obtained in reflection. This may lead to the design of low profile antenna systems, reducing the minimum $\lambda/4$ of the metallic reflectors. Moreover, the dip around f_0 obtained in transmission may block electromagnetic waves, thus improving the isolation if this AMM is placed between two antennas. However, other applications may arise from the μ-dispersive behaviour of this AMM design, when operating out of the resonance.

Finally, the use of effective material parameters may be of interest to better describe the metamaterial phenomena, mostly when properly applied to simulate complex metamaterial designs. However, since the retrieval methods mentioned do not always yield similar results, the retrieved effective material parameters should be taken for reference purposes only.

Chapter 4

AMMs for Low Profile and Compact Antenna Systems

4.1 Introduction

A straightforward application of the artificial magnetic materials (AMMs) is to perform as artificial magnetic conductors/reflectors (AMC/AMR), leading to low profile antenna systems. Therefore, in this chapter, the single layer square spiral resonator (SR) AMM presented in Chapter 3 (Figure 3.14) is applied as a reflector of a dipole antenna. In addition, the special properties of the two layer AMM slabs are applied to decouple two close antennas.

4.1.1 Single and double layer AMCs characterisation

The feasibility of SR AMMs as AMCs has been reported in Section 3.3. The square SR AMM presented in Figure 3.14 has two resonances in the 2-8 GHz frequency band. Focusing in the 2-4 GHz band, the resonance is found around 2.6 GHz, where the phase of S_{11} crosses the 0° axis, where the PMC condition is satisfied, as it is shown in Figure 4.1. The phase of S_{22} remains around -150° and it could be considered as a PEC response. Therefore, a dual PMC/PEC ($\equiv$ AMC/AEC) property arises for this

type of AMM due to the anisotropy (non-symmetric shape) of the magnetic resonator along the direction of propagation.

(a) Magnitude of S_{ij} (b) Phase of S_{ij}
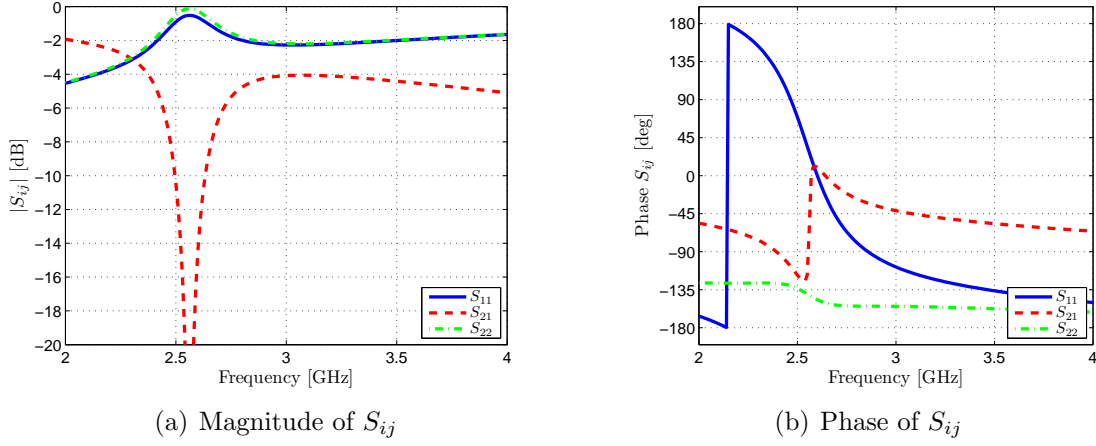
Figure 4.1: Simulated S-parameter results of the square SR AMM.

Moreover, S_{21} is minimised around f_0, where S_{11} is maximum. For this reason, and considering energy conservation ($|S_{11}|^2 + |S_{21}|^2 = 1$), (lossless) AMM slabs are often characterised by their S_{11}/S_{22} results only, because they are mainly reflecting materials due to their intrinsic non-propagating MNG property.

The previous design is only 1 layer thick, although more layers could be added to the SR AMM slab, forming multilayer AMM slabs. The S_{11}/S_{22} results for the case of 2 and 3 layers are plotted in Figure 4.2 and Figure 4.3. These multi-layer designs have been simulated with the same conditions as the single layer SR AMM design. The only change in dimensions relies on the thickness of the metamaterial slab along the direction of propagation; in the case of 2 layers, the thickness is simply $2 \times t$ (where t is equal to 6 mm), and for the 3 layers, the thickness is $3 \times t$.

(a) Magnitude of S_{ij} (b) Phase of S_{ij}
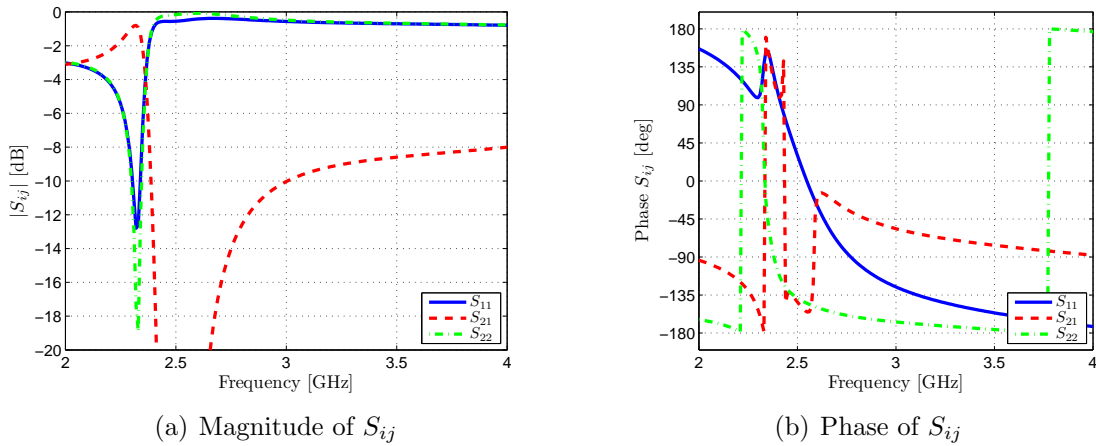
Figure 4.2: Simulated S-parameter results of the square SR AMM with 2 layers.

(a) Magnitude of S_{ij} (b) Phase of S_{ij}
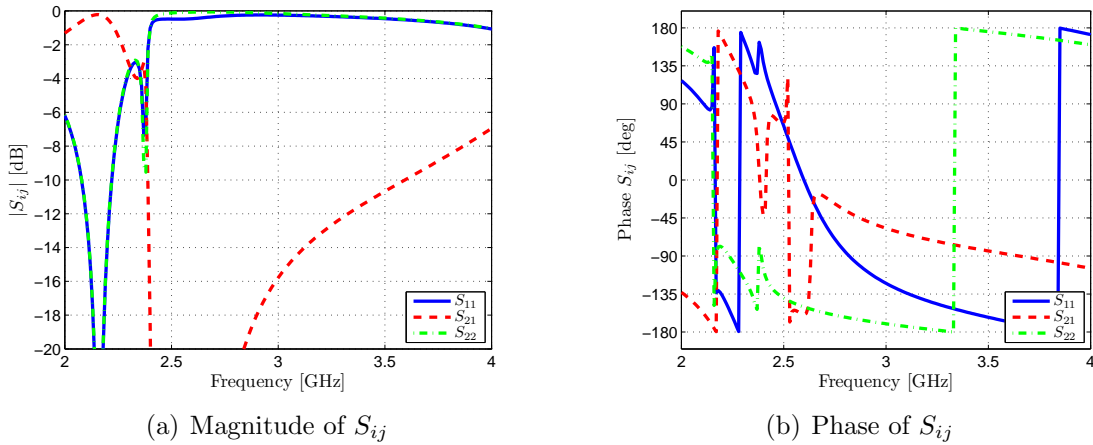
Figure 4.3: Simulated S-parameter results of the square SR AMM with 3 layers.

It is seen that the magnitude of S_{11} is improved around the resonance when adding more square SR layers, but the PMC condition is still found approximately at the same frequency. This result means that enhanced AMC surfaces can be realised when adding more layers, in spite of an increase in the (electrical) thickness. Similar conclusions could also be stated for the case of S_{22} and S_{21}. For a better comparison, the main parameters of the 1, 2 and 3 layers square SR AMM designs are listed in Table 4.1. From the results, it is seen that the resonant frequency f_0 and the fractional bandwidth $FBW_{\pm 45°}$ are not affected by the increase in number of layers of the square SR AMM slab. The losses of S_{11} at f_0 are slightly reduced, although the improvement in the magnitude of S_{11} is mainly observed over a wide frequency band after the resonance.

Layers	AMM geometry	f_0	Electrical Thickness	FBW$_{\pm 45°}$	Losses at f_0
1		2.60 GHz	$\lambda/19.2$	5.86%	-0.64 dB
2		2.55 GHz	$\lambda/9.8$	6.07%	-0.48 dB
3		2.60 GHz	$\lambda/6.4$	6.03%	-0.46 dB

Table 4.1: Parameter comparison of the SR AMM when increasing the number of layers.

However, what could be of interest due to its novelty is the smart combination of two single layer AMM slabs with their respective PMC sides facing outwards, thus resulting in a bidirectional (or double sided) AMC slab. Two single layer square SR AMM slabs are combined forming a bidirectional PMC response, as is shown in Figure 4.4. The dimensions of the spiral resonators are the same as those used in previous designs. The overall thickness t of the bidirectional AMC slab is 13 mm, considering an additional gap ls of 1 mm between spiral resonators.
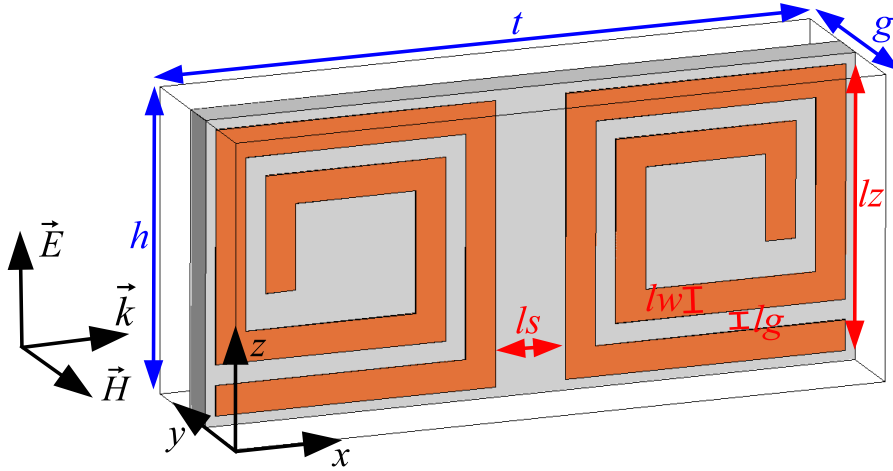
Figure 4.4: Detail of the unit cell of the bidirectional square spiral resonator printed on Rogers RO4003C substrate. In this design, $h = 6$ mm, $t = 13$ mm, $g = 4$ mm, $lz = 5.6$ mm, $lw = 0.6$ mm, $lg = 0.4$ mm and $ls = 1$ mm. The characteristics of RO4003C substrate are thickness = 0.8 mm, copper thickness = 18 μm, $\varepsilon_r = 3.38$, and $\tan \delta = 0.0027$.

Simulated S-parameter results for this design from 2 to 4 GHz are plotted in Figure 4.5. The resonant frequency is 2.61 GHz, with a $FBW_{\pm 45°}$ of 5.05% and the S_{11} losses at f_0 of -0.55 dB. Note that $S_{11} = S_{22}$ as expected from the proper combination of single layer SR AMM slabs, and hence, the PMC response is obtained in reflection on both sides of the metamaterial slab. Moreover, the S_{21} is strongly minimised around f_0, thus providing enhanced isolation if this bidirectional AMC is used as an insulator between two close antennas.

(a) Magnitude of S_{ij}

(b) Phase of S_{ij}
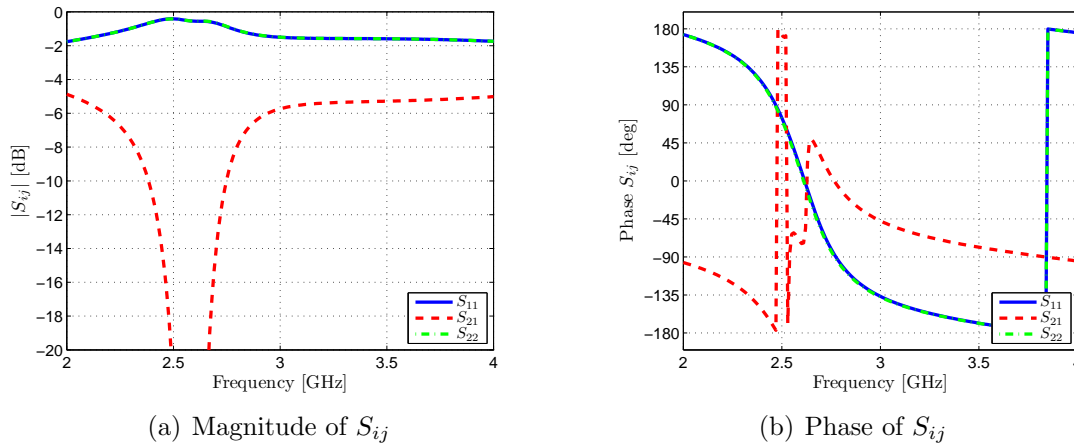
Figure 4.5: S-parameter results of the bidirectional square SR AMC.

More layers of spirals could be added to produce enhanced bidirectional AMC slabs, although the thickness will be dramatically increased. Note that the bidirectional PEC surface, which could be considered as the analogous case in electromagnetism,

is obtained with a simple and thin metal sheet. Therefore, the objective should be oriented to reduce the physical/electrical thickness of the bidirectional AMC. Then, capacitively-loaded loops (CLL) [34] designed with a smaller width than the SRs could also perform as a bidirectional AMC. The width lx of the CLLs is 4.5 mm, although lz is increased up to 13.5 mm, as it is shown in Figure 4.6. The total thickness t of the slab is reduced from 13 to 10.5 mm (when compared to the bidirectional SR AMC).
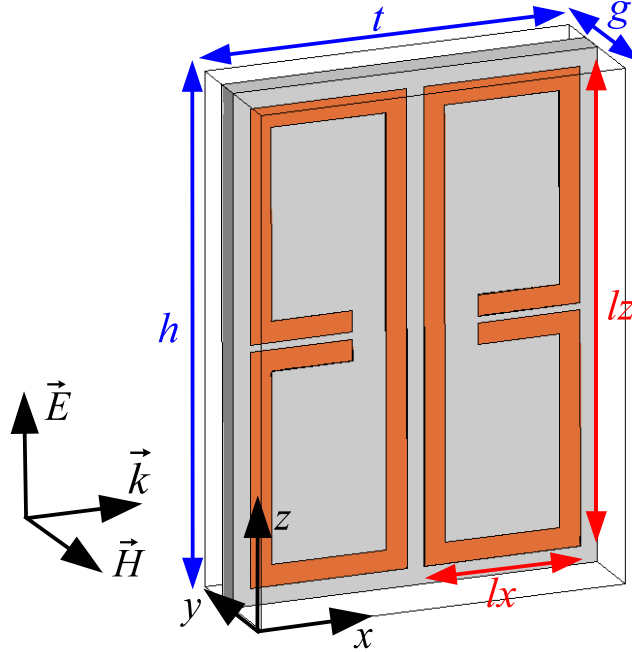
Figure 4.6: Detail of the unit cell of the bidirectional CLL resonator printed on Rogers RO4003C substrate. In this design, $h = 14.5$ mm, $t = 10.5$ mm, $g = 4$ mm, $lx = 4.5$ mm, $lz = 13.5$ mm, $lw = 0.6$ mm, and $lg = 0.2$ mm. The characteristics of RO4003C substrate are thickness = 0.8 mm, copper thickness = 18 μm, $\varepsilon_r = 3.38$, and $\tan \delta = 0.0027$.

Simulated S-parameter results for the bidirectional CLL AMC design from 2 to 4 GHz are plotted in Figure 4.7. The resonant frequency is 2.61 GHz, with a $FBW_{\pm 45°}$ of 5.55% and the S_{11} losses at f_0 of -0.6 dB. Note that, $S_{11} = S_{22}$ and S_{21} is strongly minimised around f_0, as expected from previous results. In addition, the magnitude of S_{11} decays in about 2 dB after the resonance, making it sensitive to the frequency variations of the impinging waves.

The main parameters of the bidirectional SR and CLL AMC designs are listed in Table 4.2. It is significant that the CLL design offers a slightly higher $FBW_{\pm 45°}$ and a smaller electrical length. In addition, although the S_{11} losses at f_0 of the bidirectional SR and CLL designs are quite similar, the shape of S_{11} around f_0 is not symmetrical for the CLL case, presenting a decay of more than 2 dB after f_0.

(a) Magnitude of S_{ij} (b) Phase of S_{ij}
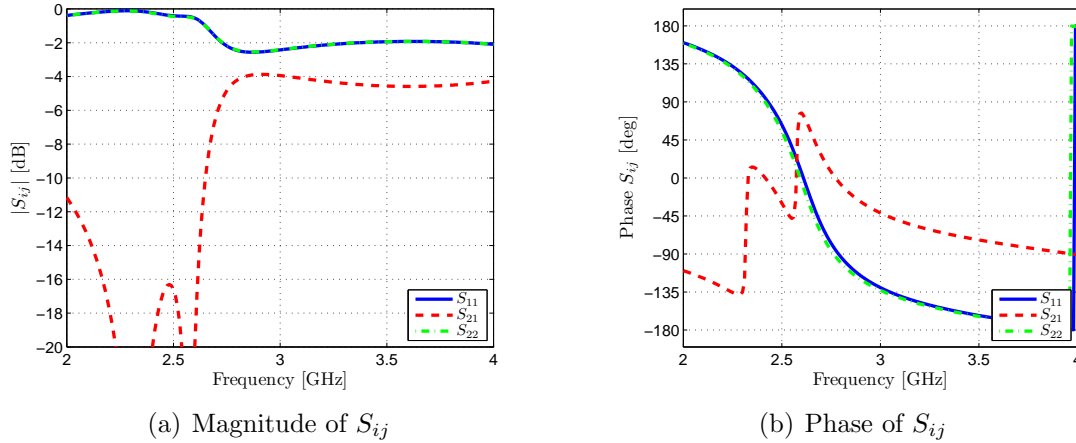
Figure 4.7: S-parameter results of the bidirectional CLL AMC.

Layers	AMM geometry	f_0	Electrical Thickness	FBW$_{\pm 45°}$	Losses at f_0
1		2.60 GHz	$\lambda/19.2$	5.86%	-0.64 dB
2		2.61 GHz	$\lambda/8.84$	5.05%	-0.55 dB
2		2.61 GHz	$\lambda/10.95$	5.55%	-0.6 dB

Table 4.2: Parameter comparison of the single layer SR AMM with the two layer bidirectional AMM slabs.

4.1.2 Fabrication of the prototypes

The single layer SR AMC, and bidirectional SR and CLL AMC slabs have been fabricated at our facilities using standard photo-etching techniques, in order to assess the results obtained from HFSS simulations. The fabricated single layer SR AMC design is composed of 22 transversal strips which are 60 mm long, containing 10 square spirals etched on a Rogers RO4003C substrate ($\varepsilon_r = 3.38$, $\tan \delta = 0.0027$), and using the same dimensions as used before in the numerical simulations. Styrofoam has been used as supporting board where the strips are laid, because there is an air gap between adjacent strips with magnetic resonators. The use of Styrofoam is remarkable because this material behaves like air (almost transparent) at microwave frequencies and it provides the required robustness to fabricate solid-like metamaterial slabs. The single layer SR AMC is shown in Figure 4.8.

The bidirectional AMC designs are composed of 8 SRs and 4 CLLs, respectively, fitted in each layer of the dielectric strips which are 60 mm long. The fabricated prototypes are shown in Figure 4.9.

Figure 4.8: Fabricated single layer SR AMC on a Styrofoam board.

(a) SR design
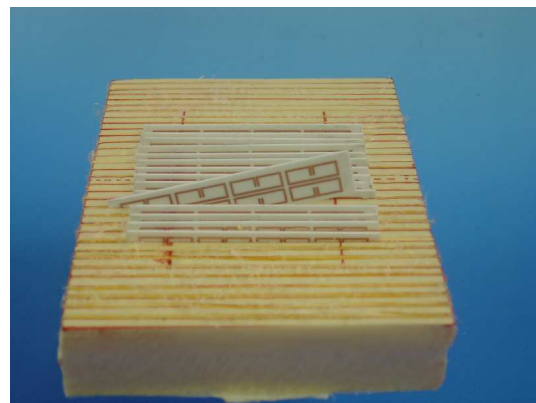
(b) CLL design

Figure 4.9: Fabricated bidirectional AMC designs

4.1.3   S-parameter Measurement

The fabricated AMC slabs have been measured with an HP8510C network analyser and an open waveguide setup (WR340) as shown in Figure 4.10.

A full two-port calibration has been performed using the standard short-open-load-thru (SOLT) technique between 1.8 and 3.4 GHz for 801 points. The AMC slab under test is placed between the waveguide ports like a transition. Note that in the band of interest, only the TE10 mode is propagating, which will be used to excite the AMC slab under test. Thus, the S-parameters can be easily found with the help of the network analyser. The complete scheme of the waveguide setup and all the connections involved is depicted in Figure 4.11.

The one layer SR AMC slab has been measured using the aforementioned setup. The

Figure 4.10: Open waveguide setup for S-parameter measurement.

S_{11} and S_{22} results have been plotted in Figure 4.12. From the results, the magnitude of S_{11} is -1.08 dB at the resonant frequency 2.67 GHz, where its phase crosses the $0°$ axis. The $FBW_{\pm45°}$ is 4.6%, and the electrical thickness is $\lambda/18.7$. Moreover, the magnitude of S_{22} is about -0.2 dB around the resonance, with a phase of about -150° across the whole frequency range. Compared to the simulated results, the resonant frequency is found at a slightly higher frequency. However, the dual PMC/PEC behaviour is experimentally assessed.

The measurement results for the bidirectional SR AMC are shown in Figure 4.13. The resonant frequency is 2.64 GHz ($\lambda/8.7$), with a S_{11} magnitude at f_0 of -1.66 dB and a $FBW_{\pm45°}$ of 3.83%. Note that $S_{11} = S_{22}$, as expected for a bidirectional metamaterial slab.

The measurement results for the bidirectional CLL slab are shown in Figure 4.14, obtaining a resonant frequency of 2.61 GHz ($\lambda/11$), a S_{11} magnitude at f_0 of -1.48 dB, and a $FBW_{\pm45°}$ of 4.18%.

When comparing simulated and measured results of the three metamaterial slabs under study, the resonant frequency is practically the same (a small shift from 2.6 to 2.67 GHz is observed in f_0), although there is a 1 dB increase in the losses of S_{11} around f_0. These discrepancies are mainly due to some fabrication tolerances in the photo-etching process, and to the measurements carried out to a finite structure (contrary to the infinite metamaterial slab approach taken in the HFSS simulations), where the effect of the array truncation and the edges become more important. In this way, some
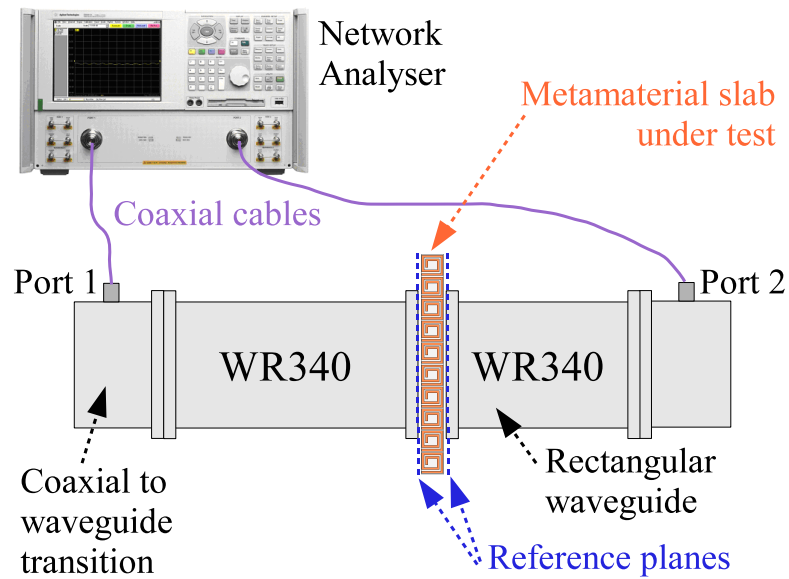
Figure 4.11: Scheme of the WR340 measurement setup.

(a) Magnitude of S_{ij}

(b) Phase of S_{ij}
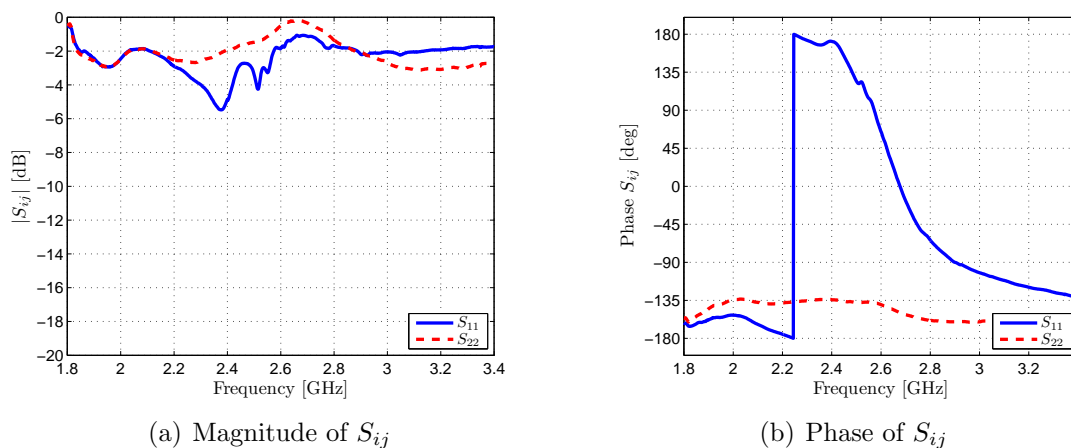
Figure 4.12: Measured S-parameter results of the single layer square SR AMC.

energy leakage can be expected due to the fact that the metamaterial samples have been measured with an open waveguide setup for practical purposes. In addition, the fabricated AMC slabs were excited using the TE10 mode in an S-band waveguide, although the simulated AMCs had been excited with a TEM mode when the periodic boundary conditions were applied to the numerical simulations.

Moreover, regarding the previous results, it is seen that losses along the operational frequency band are mainly due to the substrate itself and to the aforementioned energy leakage due to the open waveguide measurement setup, because the magnitude of the reflection coefficient remains constant even when placing a metallic plate on the outward surface of the material, to try to force a full reflection towards the excitation waveguide port. This effect is seen in Figure 4.15, where the magnitude and phase of

(a) Magnitude of S_{ij} (b) Phase of S_{ij}
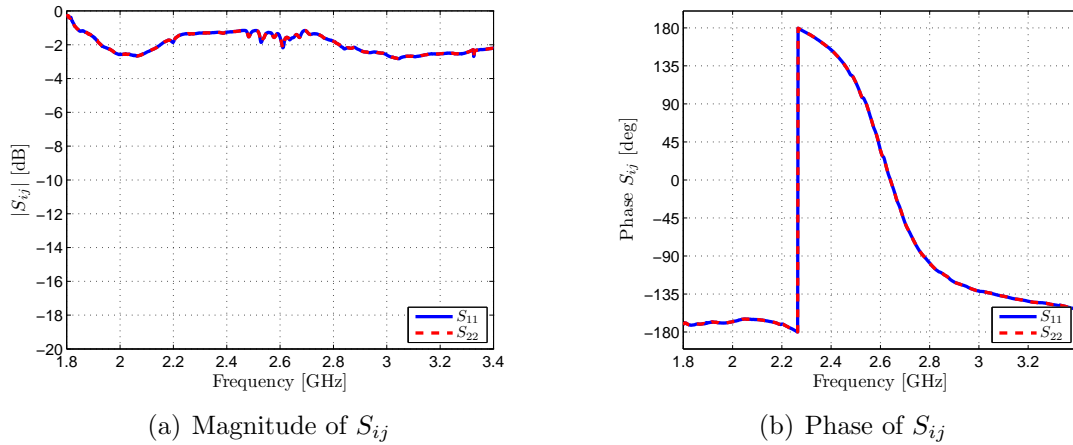
Figure 4.13: Measured S-parameter results of the bidirectional square SR AMC.

(a) Magnitude of S_{ij} (b) Phase of S_{ij}
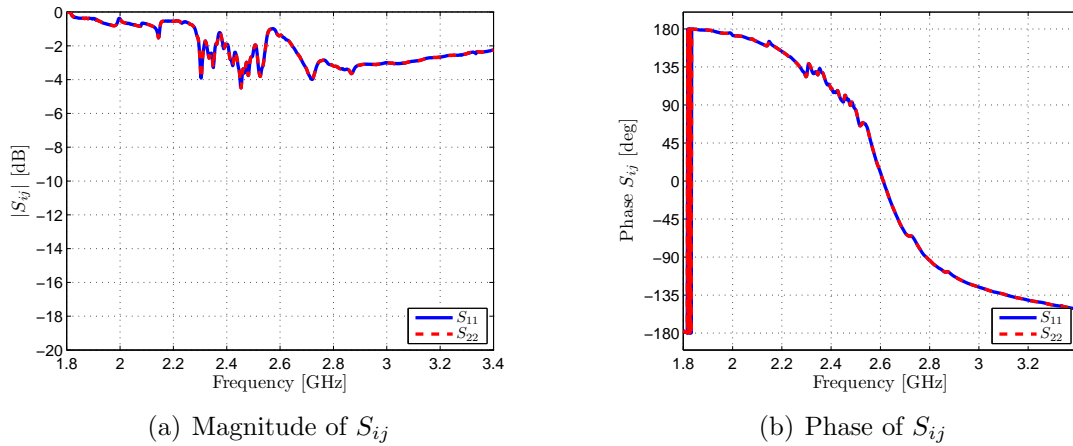
Figure 4.14: Measured S-parameter results of the bidirectional CLL AMC.

S_{11} of the bidirectional SR AMC with and without a backing metallic plate (PEC) is compared. Therefore, no change is seen either in the magnitude of S_{11} or in its phase around the central frequency 2.64 GHz. This result is obtained within a fractional bandwidth of 8.9%. This result also confirms the usefulness of this bidirectional AMC slab to design compact antenna systems, where two (or more) antennas are put close to a common reflecting surface for isolation purposes, as stated in 4.1.1 due to the strong dip found in S_{21} results at f_0 for bidirectional AMC designs.

4.2   Single layer SR AMC as Antenna Reflector

The design of low profile antennas/reflectors with AMCs has been widely studied for the case of mushroom-type AMCs [31, 84], square patch AMCs [32], and other types of AMCs with backing ground plane [85]. The use of a volumetric metamaterial composed of CLLs (without the use of a backing ground plane) as AMC for reflecting

(a) Magnitude of S_{ij} (b) Phase of S_{ij}
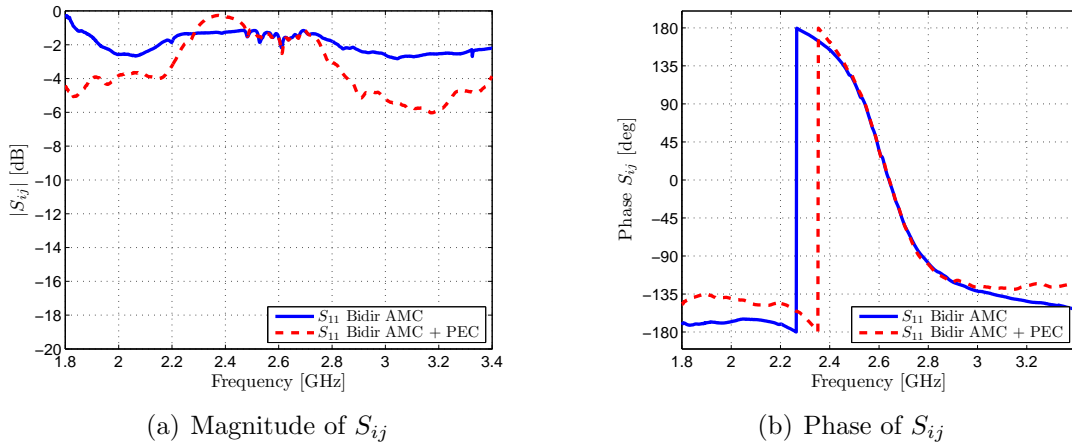
Figure 4.15: Measured S-parameter results of the bidirectional square SR AMC with and without a metallic sheet placed in the opposite side of the metamaterial slab.

purposes was proposed in [34] and confirmed in [86]. In that case, although the CLL metamaterial block had a resonant frequency at 10 GHz, the introduction of the printed dipole antenna shifts the resonance to slightly lower frequencies (around 9.45 GHz), where an in-phase reflection occurs. Besides some possible restrictions, it seems possible to use the SR AMC slab to design low profile antennas.

4.2.1   Input Impedance

A printed folded dipole antenna has been fabricated in order to assess the validity of the single layer SR AMC for low profile antenna applications. The antenna is coaxially fed, so a microstrip balun is needed to reduce antenna mismatch while enhancing radiation. A sketch of the folded dipole and the SR AMC slab is depicted in Figure 4.16.

The folded dipole antenna is placed at a certain distance above the single layer SR AMC slab, testing the PMC (AMC) and PEC (AEC) sides of the AMM slab. Measured results are also compared with a conventional metal surface (PEC). From Image Theory (see Figure 2.6), test distances are set to 1 mm ($\equiv 0$) and 29 mm ($\equiv \lambda/4$), where the PEC reflector works properly. Therefore, the input reflection coefficient S_{11} of the folded dipole above a PEC and AMC reflectors at 1 mm are plotted in Figure 4.17.

The folded dipole in free space presents a matched response ($S_{11} <$ -10 dB) from 2.18 to 2.71 GHz. But the insertion of a backing reflector dramatically reduces the frequency band of operation. For a dipole height of 1 mm, it is observed that the dipole is completely mismatched when using a PEC reflector, as expected from Image Theory. Two matched bands, 2.25 and 2.55 GHz, appear when using the SR AMC
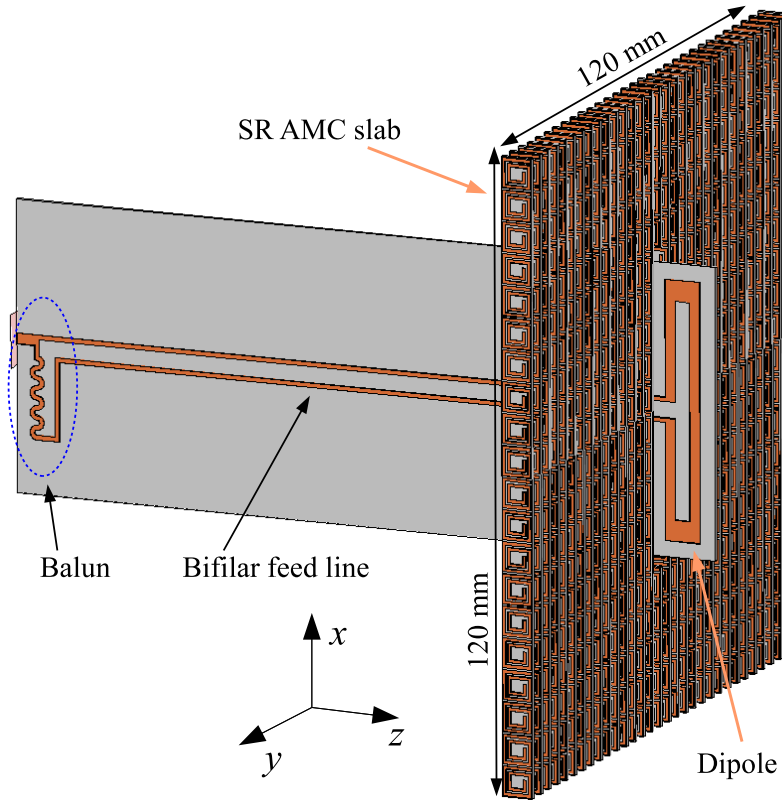
Figure 4.16: Fabricated folded dipole antenna and the SR AMC reflector.

reflector. Note that the resonance of the SR AMC has been shifted from 2.67 down to 2.55 GHz; this reduction may be due to the interactions of the dipole and the SRs, and to the fact that a lower impedance is found out of the resonance of the SR AMC, where antenna matching becomes easier, as stated in [86]. Moreover, regarding the SR AEC surface results, it is observed that there are two matching regions, around 2.38 and 2.61 GHz. This fact confirms that the AEC SR could not actually be considered as a PEC-like surface because the antenna is not completely unmatched (as compared to the conventional metal sheet); in addition, the matched two frequency regions are complementary to the matching regions obtained with the AMC surface. On the other hand, the results for a dipole height of 29 mm ($\equiv \lambda/4$) are reversed with respect to the case of 1 mm. In such a situation, the antenna is matched with a conventional metal sheet (PEC) around 2.18 and 2.58 GHz ($\lambda/4$). The results for the AEC are more similar to those of the PEC reflector, whereas the AMC reflector presents complementary results to those of the AEC case, with two matching regions around 2.42 and 2.71 GHz.

The PMC behaviour of the SR AMC is clearly seen in the input impedance of the folded dipole, which is plotted in Figure 4.18. For a dipole height of 1 mm, there is a matching region for the AMC case around 2.55 GHz, which is confirmed with

(a) Dipole at a height of 1 mm

(b) Dipole at a height of 29 mm
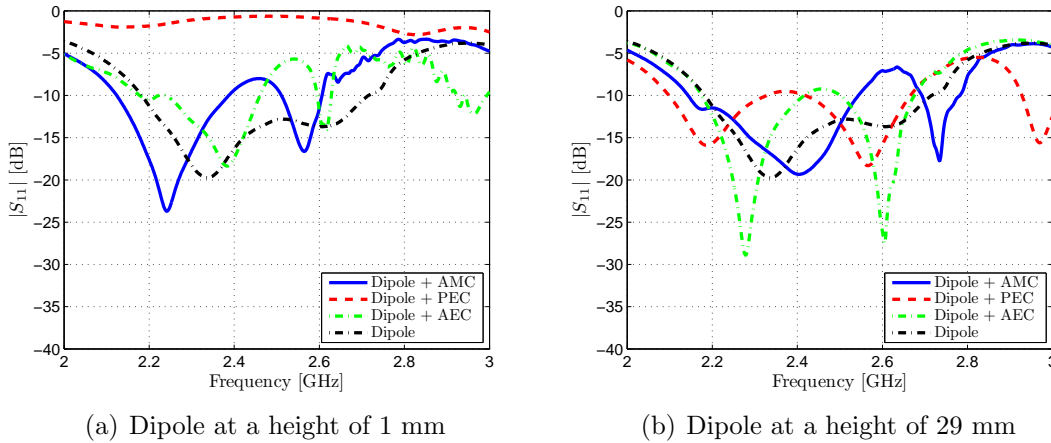
Figure 4.17: Measured S_{11} results of a folded dipole antenna placed at a certain distance above different types of reflectors.

$\text{Im}(Z_{AMC}) = 0$. It is observed that the $\text{Re}(Z_{free-space}) = 36 \ \Omega$ at 2.55 GHz. However, when using a PEC reflector, $\text{Re}(Z_{PEC}) = 3.2 \ \Omega \ (\approx 0 \ \Omega)$, as expected. On the other hand, $\text{Re}(Z_{AMC}) = 69.6 \ \Omega$ (almost doubling the $\text{Re}(Z_{free-space})$), which is a typical result for dipole antennas above PMC surfaces [101].

(a) Real part of Z_{in}

(b) Imaginary part of Z_{in}
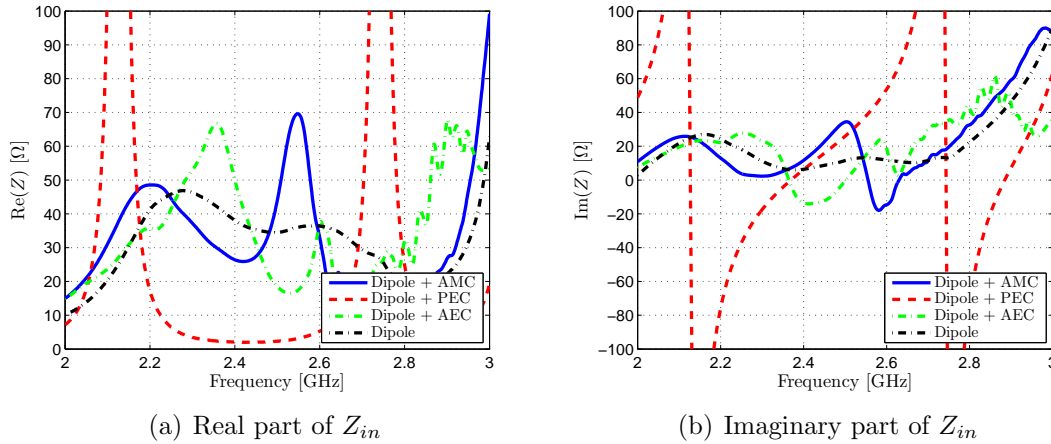
Figure 4.18: Measured input impedance Z of the folded dipole placed 1 mm above different reflectors.

4.2.2   Radiation Patterns

The radiation patterns of the folded dipole above a SR AMC surface have been measured in the UPC anechoic chamber. Results for the AMC case are compared to those obtained with a PEC and a AEC reflector, as is shown in Figure 4.19.

Radiation patterns have been measured at 2.55 GHz, where the dipole antenna is matched when it is placed 1 mm above the SR AMC surface, and 29 mm above the PEC

(a) SR AMC reflector   (b) Conventional PEC reflector
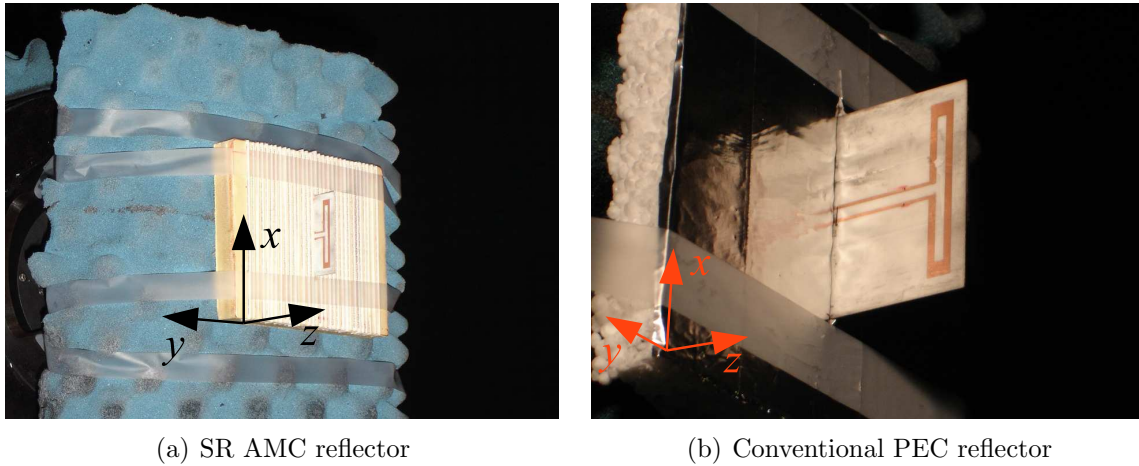
Figure 4.19: Fabricated folded dipole antenna placed above two different reflectors.

surface. Measured E-plane (xz-cut, $\phi = 0°$) and H-plane (yz-cut, $\phi = 90°$) radiation patterns are plotted in Figure 4.20, for a dipole height of 1 mm and 29 mm over AMC, PEC and AEC reflectors, as well as the results of the dipole in free-space (with no reflector).

The insertion of a backing reflector clearly redirects the back-radiation of the dipole antenna towards broadside. For a dipole height of 29 mm with respect to the reflecting surface, best results are obtained for the PEC and AEC cases, as a direct consequence of the Image Theory, which provides a good performance of an antenna placed at $\lambda/4$ of a metal surface. In that case, the PEC outperforms the AMC and free-space cases in about 5 dB. However, when reducing the dipole height to 1 mm, the behaviour is reversed, thus obtaining the best result for the AMC case, outperforming the free-space case in about 3 dB, and the PEC case in about 9 dB. Despite the wider pattern obtained in the E-plane for a dipole height of 1 mm, it can be concluded that a low profile antenna system (reflector) has been obtained with a SR AMC surface.

Moreover, besides the dipole dimensions, the dipole height over the SR AMC reflector has been reduced from 29 mm ($\lambda/4$) to 1 mm ($\lambda/117.6$). However, the use of a SR AMC increases the reflector thickness by up to 6 mm, a fact that should be taken into account, especially when compared to the almost negligible thickness of a typical PEC surface. In that case, the antenna profile is reduced from 29 mm ($\lambda/4$) to 7 mm ($\lambda/16.8$), which includes the thickness of the SR AMC (6 mm) and the height of the dipole (1 mm). This situation is depicted in Figure 4.21.

(a) E-plane (xz-cut) @ 1 mm

(b) H-plane (yz-cut) @ 1 mm

(c) E-plane (xz-cut) @ 29 mm

(d) H-plane (yz-cut) @ 29 mm
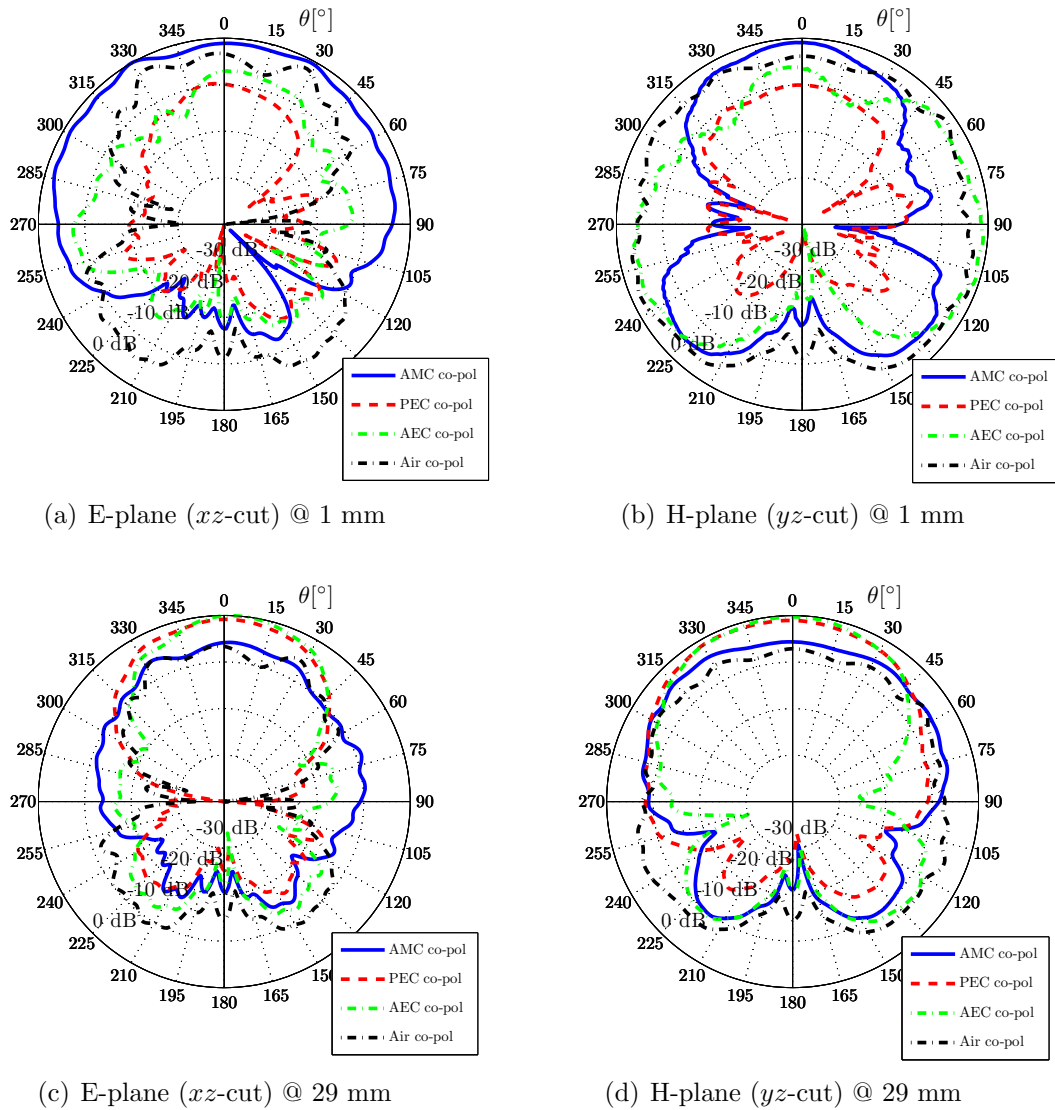
Figure 4.20: Measured radiation patterns at 2.55 GHz of the folded dipole placed 1 mm and 29 mm above an AMC, PEC and AEC reflectors, as well as the free-space case (no reflector).

(a) Dipole + PEC reflector

(b) Dipole + SR AMC reflector
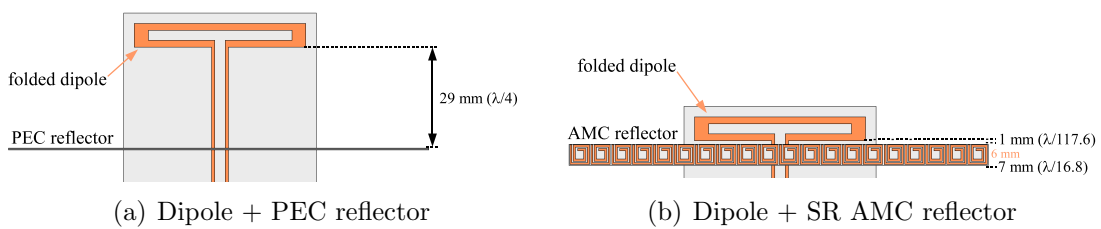
Figure 4.21: Profile comparison of the dipole antenna placed above a conventional PEC and a SR AMC reflectors.

4.3   Bidirectional AMCs for Compact Antenna Systems

It has been seen how the bidirectional AMCs provide good stability in terms of resonant frequency and magnitude of S_{11} against possible perturbations in the opposite side of the metamaterial slab. So, two antennas with a bidirectional AMC slab in between would improve their isolation. In this section, the bidirectional CLL metamaterial design is used to enhance the decorrelation between two closely-spaced antennas.

4.3.1   Spatial Diversity Antenna Systems

One implementation of multiple antenna wireless systems (MIMO) is to take advantage of the spatial diversity by combining multiple signals, and consequently, improving the signal quality at the receiver, and the system capacity. The performance of such antenna systems is degraded by the mutual coupling between the antennas [88]. For a multiple element antenna (MEA), the S-parameter matrix $[S]$ can be defined at the MEA ports, as seen in Figure 4.22:
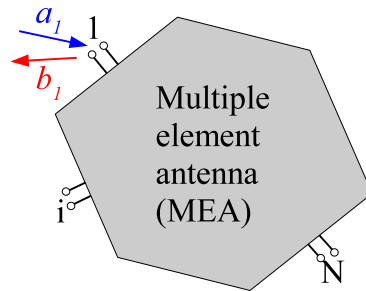
Figure 4.22: Scattering Matrix $[S]$ at the MEA ports.

The system performance is in part determined by the correlation matrix. For a rich scattering environment, the correlation matrix $[C]$ is related with the S-parameter matrix $[S]$ of a multiple-antenna system as:

$$[C] = [I] - [S]^H[S] \tag{4.1}$$

where $[I]$ stands for the identity matrix, and $[S]^H$ for the Hermitian matrix of $[S]$. The elements C_{ii} and C_{ij} of the matrix $[C]$ are referred to as the autocorrelation and the cross-correlation parameters respectively.

The envelope correlation ρ_e can also be used to measure the performance of a spatial diversity system [89]. For a reciprocal and symmetrical two-antenna system, the envelope correlation is defined:

$$\rho_e = \frac{C_{12}C_{21}}{C_{11}C_{22}} \tag{4.2}$$

where C_{11} and C_{12} are defined as:

$$C_{11} \equiv C_{22} = 1 - |S_{11}|^2 - |S_{12}|^2$$
$$\tag{4.3}$$
$$C_{12} \equiv C_{21} = |2Re(S_{11}S_{12}^*)|$$

Minimising the envelope correlation (4.2) implies, for a lossless antenna system, increasing the radiated power for a given available power. Different solutions were proposed in [90,91] using lossless matching and decoupling networks, in order to impose orthogonality between the antenna patterns to reduce the cross-correlation between the antennas. A different approach is considered when using a bidirectional AMC slab (spacer) inserted between two closely-spaced antennas. To demonstrate the advantages of this approach, the results obtained with the metamaterial spacer are compared with a conventional metal sheet (PEC) and with the case of air (no spacer).

4.3.2 Two-Antenna System Design and Fabrication

The antenna system is composed of two closely-spaced monopoles over a metallic ground plane. Monopole antennas have been chosen due to their simplicity, although the concept could be extended to other antenna types. The monopoles have been designed to be matched at 2.6 GHz, so their dimensions are: wire length l_{dip} is 27.8 mm and wire diameter is 0.8 mm. The ground plane is made of aluminium and has a side dimensions l_{gp} of 230 mm, equivalent to $2\lambda \times 2\lambda$ at the working frequency. The separation between the monopoles d is 18 mm (0.156λ). The antenna system is depicted in Figure 4.23.
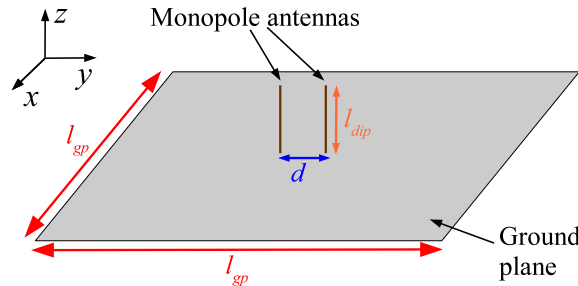
Figure 4.23: Two-antenna system design.

The metamaterial spacer made from a bidirectional CLL AMC, already presented in Section 4.1.1, has the following width-height-thickness dimensions: 46 mm $\times$ 33 mm $\times$ 10.5 mm ($0.4\lambda \times 0.29\lambda \times 0.09\lambda$). The bidirectional CLL AMC slab is composed

of 10 bidirectional strips embedded in a piece of Styrofoam. The PEC spacer is made
from a thin aluminium sheet attached to a piece of Styrofoam, whereas its width-height
dimensions are equal to the those of the AMC spacer: 46 mm × 33 mm. Moreover,
due to the different thickness of the spacers, the distance between a monopole PEC
spacer d_{PEC} is 9 mm (0.078λ), and the distance between the a monopole and the AMC
spacer d_{AMC} is 3.75 mm (0.033λ). A cross-section of the antenna system focusing on
the different distances is shown in Figure 4.24.

(a) PEC spacer   (b) AMC spacer
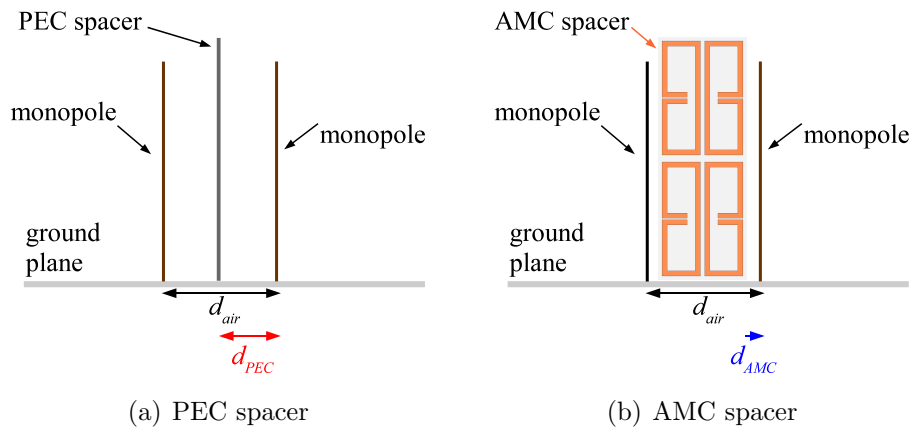
Figure 4.24: Two-antenna system cross-section, and detail of distances between an-
tennas and spacers.

The fabricated antenna system and a detail of the AMC and PEC spacers which is
used in the measurements is shown in Figure 4.25.
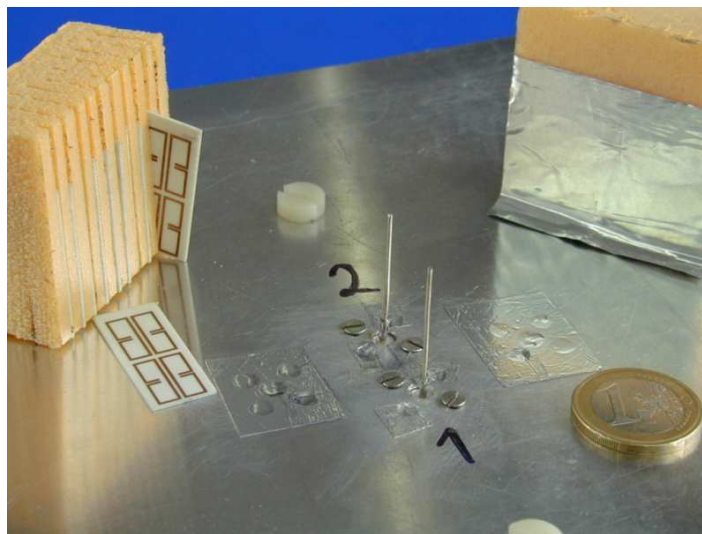
Figure 4.25: Fabricated two-antenna system with a detail of the AMC and PEC spac-
ers.

4.3.3   Two-Antenna System Measurements

The performance of the two-antenna system is based on the S-parameters and the computation of the C-parameters and the envelope correlation. Moreover, the radiation pattern will provide us with additional information in terms of orthogonality between the antenna diagrams.

4.3.3.1   S-parameters

The S-parameter measurements have been performed with an Agilent E8362 vector network analyser from 2 to 3 GHz, as shown in Figure 4.26. Note that each monopole antenna is connected to a different measurement port of the VNA; in this way, due to the symmetry of the antenna system, the return loss of the two monopoles should be similar, that is, $S_{11} = S_{22}$.
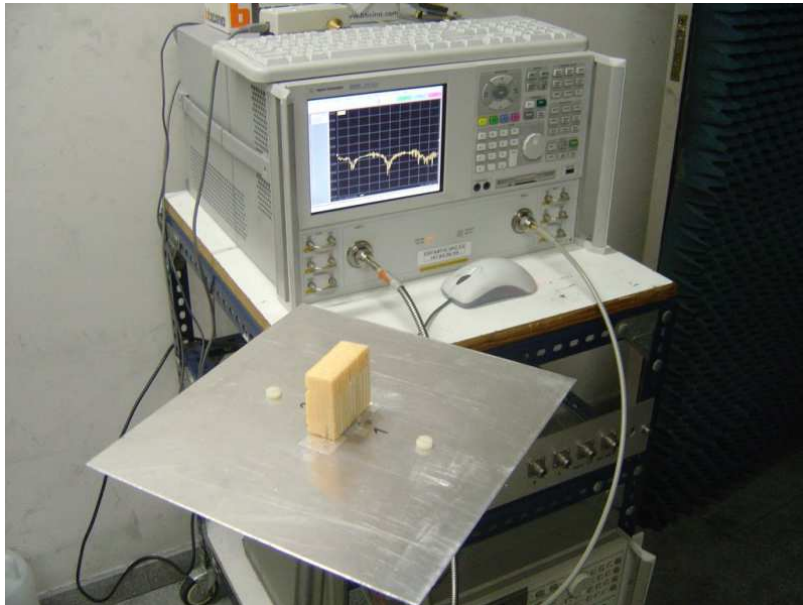
Figure 4.26: Two-antenna system S-parameter measurement setup.

The magnitude of S_{11} and S_{21} is plotted in Figure 4.27, for the cases of air (no spacer), PEC and AMC spacers between the two monopoles. From the results, it is shown that, in the air case, the monopoles are matched (S_{11} < -10 dB) around 2.6 GHz, although there is a high mutual coupling between the antennas (S_{21} > -10 dB). The PEC spacer improves the decoupling (S_{21} < -10 dB) between the monopoles, although they are practically non-radiating because they are unmatched ($S_{11} > -2dB$). However, matching and decoupling is achieved when using the AMC spacer over a practically wide frequency band (from 2.3 to 2.87 GHz).

In addition, the PEC spacer has been considered as a single centred metal layer between the monopoles that provides an antenna matching of -2 dB around 2.6 GHz.

(a) Matching S_{11} (b) Isolation S_{21}
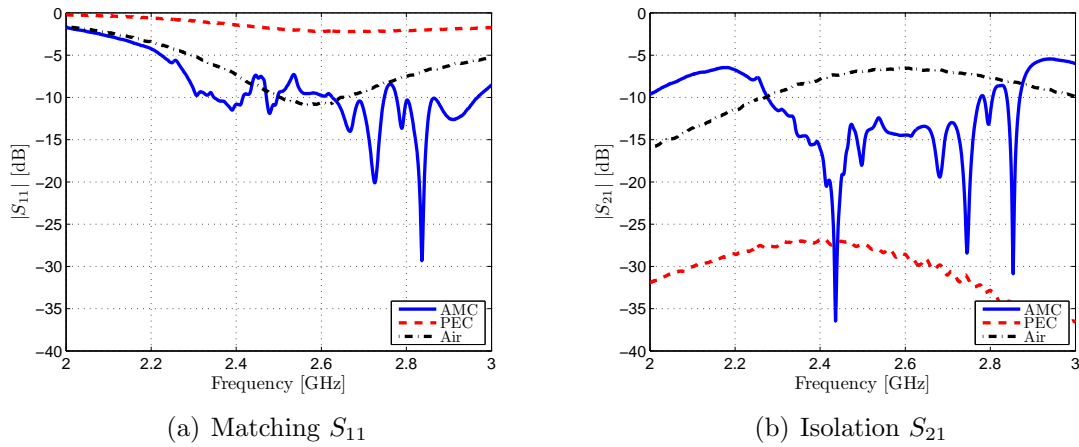
Figure 4.27: Measured S-parameter of the two-antenna system.

However, this antenna matching would be even worse ($S_{11} \approx 0$ dB) if the PEC spacer had the same thickness as the AMC spacer (13.5mm), yielding an effective distance between a monopole and the PEC spacer d_{PEC} of 3.75 mm.

4.3.3.2   Envelope Correlation

In order to verify the performance of the antenna system and the spatial diversity, the envelope correlation ρ_e (4.2) has been computed from the S-parameters, and the results are plotted in Figure 4.28. A minimum 3 dB of correlation envelope is required for a proper spatial diversity performance. From the results, it is seen how this minimum requirement is fulfilled with the three cases across the whole frequency band, although the best results are obtained with the AMC spacer, achieving $\rho_e < $ -30 dB around 2.7 GHz.
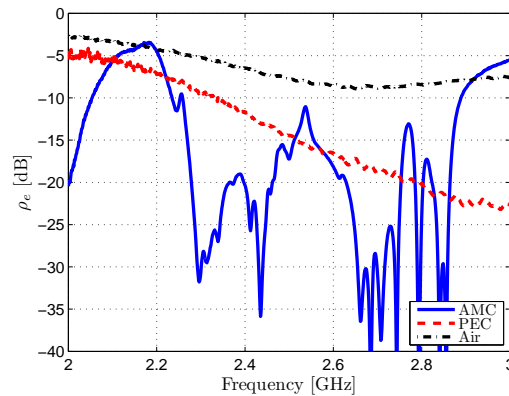
Figure 4.28: Computed envelope correlation of the two-antenna system.

4.3.3.3   C-parameters

Nevertheless, the C-parameters are required for a more precise analysis, since the envelope correlation results are reasonably good for the three cases over the whole frequency band. The C-parameter results are plotted in Figure 4.29. An autocorrelation $C_{11} \approx 0$ dB, as well as a low cross-correlation level $C_{12} <$ -10 dB, is required to produce decorrelated antennas. For the air case, the C_{11} does not reach the 0 dB because the monopoles are coupled. In this way the AMC spacer improves the performance with a higher autocorrelation (≈ 0 dB) from 2.25 to 2.9 GHz. For the PEC spacer, C_{11} is lower because the monopoles in that case are mismatched; again, this result would be worse if a thicker PEC spacer had been used between the monopoles. Moreover, in terms of the cross-correlation C_{12}, both the PEC and the AMC spacers improve the results obtained in the air case (levels below -12 dB). Therefore, the AMC spacer is able to properly decorrelate the monopole antennas around the frequency of interest, because not only does it improve the decoupling between the antennas, it also keeps them matched.

(a) Auto-correlation C_{11} (b) Cross-correlation C_{12}
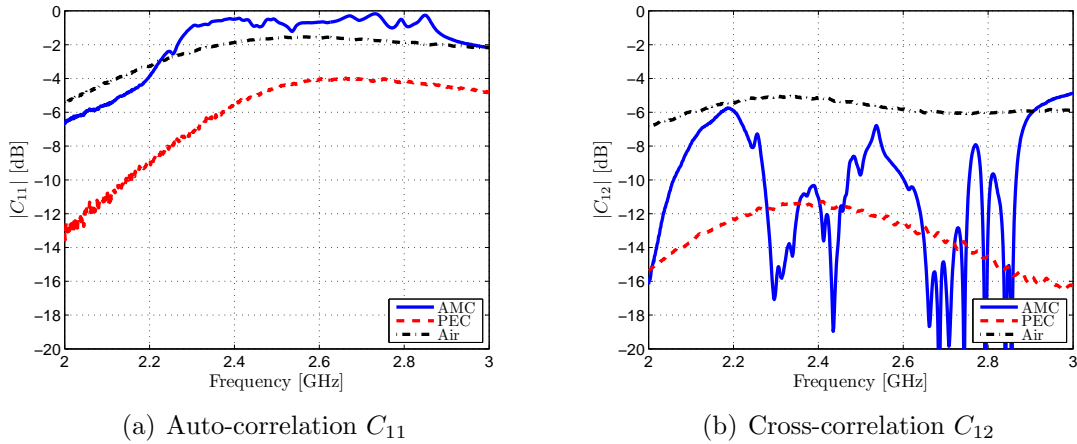
Figure 4.29: Computed C-parameters of the two-antenna system.

4.3.3.4   Radiation Patterns

Decorrelated antennas are also characterised by their orthogonal radiation patterns. Therefore, complete radiation patterns ($0 \leq \theta \leq 180°$, $0 \leq \phi \leq 360°$) have been measured in the D3-UPC anechoic chamber, at the frequency of 2.68 GHz, where the performance with the AMC spacer were optimal. Due to the antenna system symmetries, only one monopole has been measured for the radiation patterns, whereas the other one has been loaded with a characteristic impedance (50 Ω). Measured radiation patterns for the three cases are plotted in a three-dimensional representation in Figure

4.30. The results have been normalised to the maximum value of the electric field considering the three cases. It is seen how for the air case the pattern is omnidirectional, as expected of a monopole over a ground plane, and slightly affected by the presence of the parasitic dipole. The presence of the spacers is clearly evidenced in the radiation patterns, because the PEC and the AMC spacers tend to concentrate radiation into one half-space (improving the orthogonality of the diagrams).

(a) Air (no spacer)   (b) PEC spacer

(c) AMC spacer
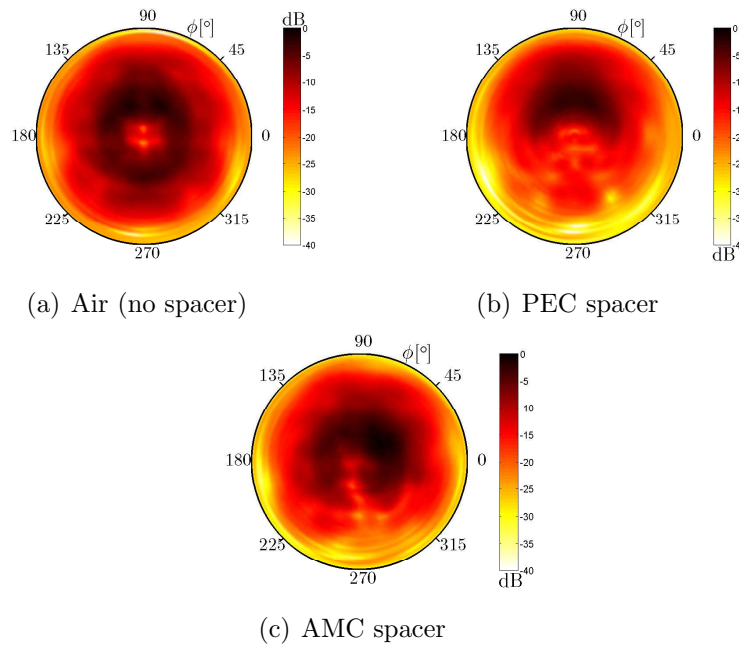
Figure 4.30: Complete measured radiation patterns of the two-antenna system for the three cases at 2.68 GHz.

In addition, The E-plane and H-plane cuts are plotted in Figure 4.31 for a better performance comparison. From these results, it is clearly seen in the H-plane that the case of no spacer results in an omnidirectional pattern, as expected, whereas the presence of the PEC and the AMC spacers tend to concentrate the radiation into a half-space, thus obtaining quasi-orthogonal patterns. The AMC spacer outperforms the back-radiation with respect to the air case in about 17 dB, and the PEC spacer in about 10 dB.

The total radiated power has been computed from the measured radiation patterns in order to asses the effect of losses. Note that the air case losses are essentially due to power dissipated in the load of the coupled antenna, whereas losses in the AMC case are mainly due to the spacer material losses. However, losses for the AMC case with respect to the air case are estimated to be lower than 0.6 dB.

(a) E plane   (b) H plane
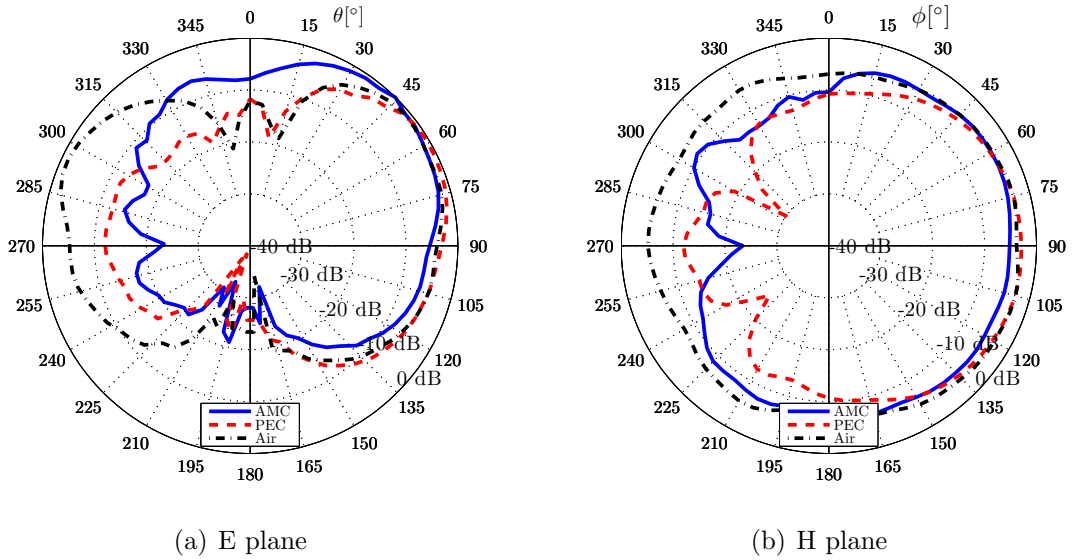
Figure 4.31: Measured E-plane and H-plane radiation patterns of the two-antenna system for the three cases at 2.68 GHz.

4.4 Chapter Conclusions

The spiral resonator AMM slab has been fabricated, and the simulated results have been experimentally assessed, confirming the feasibility of this metamaterial as AMC around the resonant frequency of 2.6 GHz. In addition, the SR AMM slab has been tested as AMC reflector for a dipole antenna, achieving a broadside directed beam with a profile of $\lambda/117.6$ ($\lambda/16.8$ when considering the SR AMC thickness).

On the other hand, the smart combination of two single layer AMC slabs leads to the design of bidirectional AMC slabs, showing a PMC response when an incident wave impinges on any or both sides of the slab. Two bidirectional AMC designs have been presented, one composed of SR AMMs, and a narrower one composed of CLL AMMs. This bidirectional AMC material has been applied to decouple and decorrelate two close antennas, while taking advantage of the high isolation of such AMM material, as well as the PMC response which allows a dipole/monopole antenna to be placed very close to this slab, thus leading to compact antenna systems. High decorrelation between two monopoles has been experimentally verified by means of the correlation $[C]$-parameters (high auto-correlation and low cross-correlation are of interest), and by the quasi-orthogonal radiation patterns. The separation between monopoles is $\lambda/6.4$, a result that is still improvable if the AMM slab is composed of thinner bidirectional AMM resonators, such as the broadside-coupled SRRs (BC-SRRs).

Chapter 5

AMMs for Low Profile Transpolarising Surfaces

5.1 Introduction

Transpolarising surfaces are basically passive transmitting or reflecting devices that can rotate the polarisation plane of an incident wave at a certain angle, typically 90°. In literature, such surfaces are also referred as to cross-polarising surfaces or twist polarisers/reflectors [118].

In this chapter, the design of a low profile and broadband transpolarising reflector is developed. The first design uses a combination of the square SR AMM slab presented in Chapter 3 (Figure 3.14) and metallic strips, whereas the second design is fully implemented in planar technology from a dielectric substrate. This latter design has been then applied to the design of a transpolarising trihedral corner reflector (TTCR), which is able to provide a high back-scattered cross-polar response.

5.1.1 Principle of Operation

Transpolarisation is achievable in reflection by taking advantage of the different reflection responses that a surface may present along two orthogonal axes [119–121].

In particular, a combination of perfect magnetic conductor (PMC) and perfect electric conductor (PEC) responses and the choice of the incident polarisation angle may result in a transpolarising surface. This is the case of the strip-type artificial magnetic conductor (AMC) surface, which is composed of a unidirectional periodic metallic grating placed above a metallic ground plane, resulting in one of the simplest transpolarising surface designs. This surface behaves like a PMC in the direction of the periodicity, and like a PEC in the direction of the strips. Transpolarisation is then obtained when the incident electric field is oriented at 45° with respect to the strips, as shown in Figure 5.1. In such a situation, the incident electric field E_i linearly polarised and tilted 45° with respect to the strips is decomposed into two components: $E_i^{\parallel}$ and $E_i^{\perp}$, which correspond to the parallel and orthogonal electric field components, respectively. Upon reflection, the electric field component in the direction of the periodicity $E_i^{\perp}$ is reflected as a PMC with a reflection phase of 0°, whereas the field component parallel to the strips $E_i^{\parallel}$ is reflected as a PEC with a reflection phase of 180°, and the electric field component is then reversed. Therefore, the resulting reflected electric field E_r is rotated by 90° with respect to the incident electric field E_i. In this case, E_i is referred to as the co-polar component and E_r as the cross-polar component, due to the 90° rotation between them.
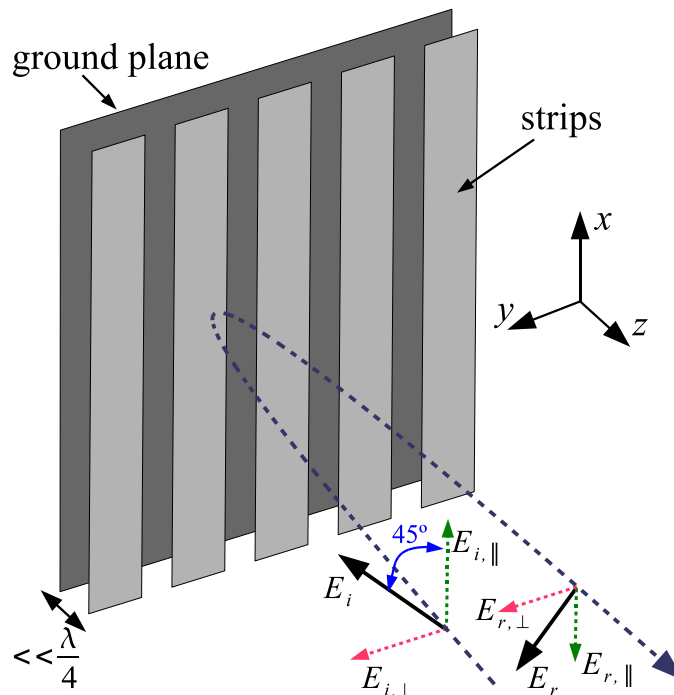
Figure 5.1: Basic principle of operation of a strip grating transpolarising surface.

The principle of operation of such transpolarising surfaces is formulated as follows:

$$
\begin{aligned}
E_i &= E_i^{\parallel} + E_i^{\perp} \\
E_r^{\parallel} &= E_i^{\parallel} e^{j180^\circ} = -E_i^{\parallel} \\
E_r^{\perp} &= E_i^{\perp} e^{j0^\circ} = E_i^{\perp} \\
E_r &= E_r^{\parallel} + E_r^{\perp} = -E_i^{\parallel} + E_i^{\perp} \\
E_r &\perp E_i
\end{aligned}
\tag{5.1}
$$

However, transpolarisation is a frequency dependent phenomenon because the width and gap dimensions of the periodic elements are related with the operational wavelength. In such a case, the transpolarisation may be found around the frequency of operation of the PMC response. Thus, the transpolarising surface not only reflects the cross-polar component E_{cross} around the frequency of operation, but it also reflects the co-polar component E_{cop} in the frequency range where there is no transpolarisation.

5.1.2   Potential Applications

Most applications of the transpolarising surfaces are devoted to taking advantage of the polarisation conversion they produce, since the principle of operation of such surfaces implies the decrease of the reflected co-polar component and the consequent increase of the cross-polar component around the frequency of operation.

- Polarisation conversion surface

  Transpolarising surfaces typically convert from one polarisation (i.e., E_u) to the cross-polar one (E_v) around the frequency range of operation; this corresponds to a linear-to-linear polarisation conversion. Historically, this property has been applied to reduce the blockage effect of a sub-reflector in Cassegrain antenna systems [121–123], as shown in Figure 5.2. In addition, the radar cross section (RCS) of a target when using single polarisation monostatic radar systems could be reduced by taking advantage of the co-polar response decrease around the frequency of operation. Another characteristic property of transpolarising surfaces is that an incident circular polarised wave is reflected preserving its handedness [124–126], contrary to the response of a typical metallic reflector. This feature can also be applied to generate a circularly polarised wave from a linearly polarised one, by placing a dipole antenna above a transpolarising surface, oriented 45° with respect to the direction of the periodicity [127, 128], as presented in Figure 5.3.

- Polarimetric radar calibration

  Trihedral corner reflectors (TCRs) are often used for radar calibrating purposes
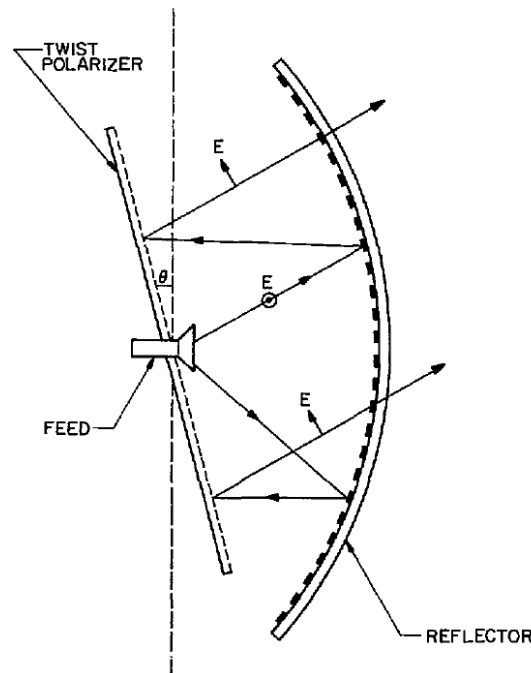
Figure 5.2: Transpolarising/twist reflector antenna system [121].
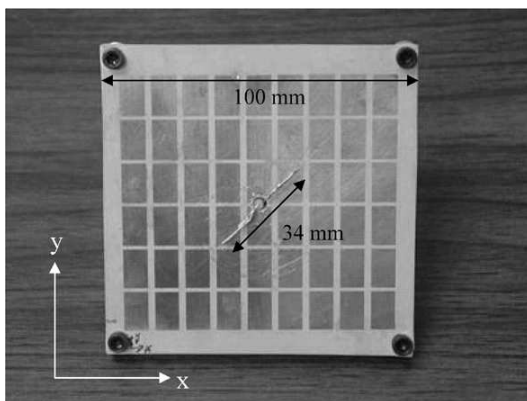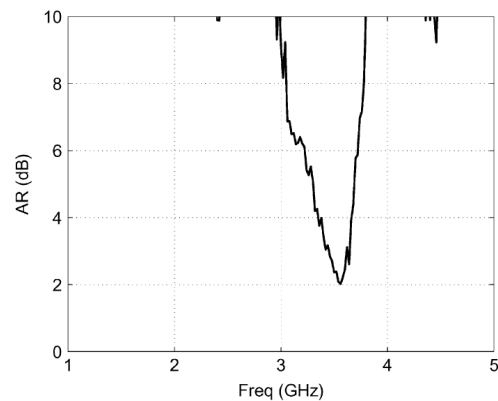
(a) CP dipole [127]   (b) Measured Axial Ratio [127]

Figure 5.3: Linear to circular polarisation conversion by placing a dipole antenna tilted 45° above a rectangular patches transpolarising surface.

although they can not provide a cross-polar response. Yet, if a transpolarising surface is placed on one side of a trihedral corner reflector, the transpolarising-TCR (TTCR) may produce a back-scattered cross-polar response [130, 131]. However, transpolarising surface designs comprising corrugations are bulky and heavy because they are made directly from a metal piece and they need a minimum thickness of about $\lambda/4$, as it is seen in Figure 5.4.
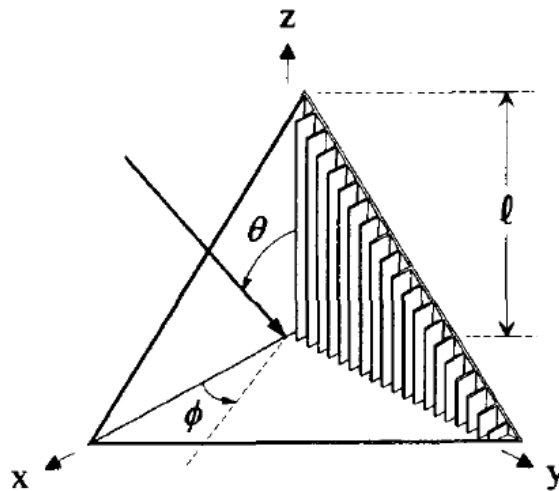
Figure 5.4: Trihedral corner reflector with conducting fins or corrugations on one of its interior sides [131].

5.1.3   Transpolarising surface examples

Transpolarising surface designs can present other geometries different from the periodic arrangement of strips, fins or corrugations above a metallic ground plane. Several examples of transpolarising surfaces are found in literature, such as AMC surfaces composed of rectangular patches [124, 127, 128], or even rectangular patches with slots [124, 126]. Other designs take advantage of an EBG surface [31] but with offset vias [124, 125]. Some unit cell examples of the aforementioned transpolarising surfaces are shown in Figure 5.5.

(a) Diagonal strips

(b) Patches with offset vias [125]

(c) Patches with diagonal slots [126]
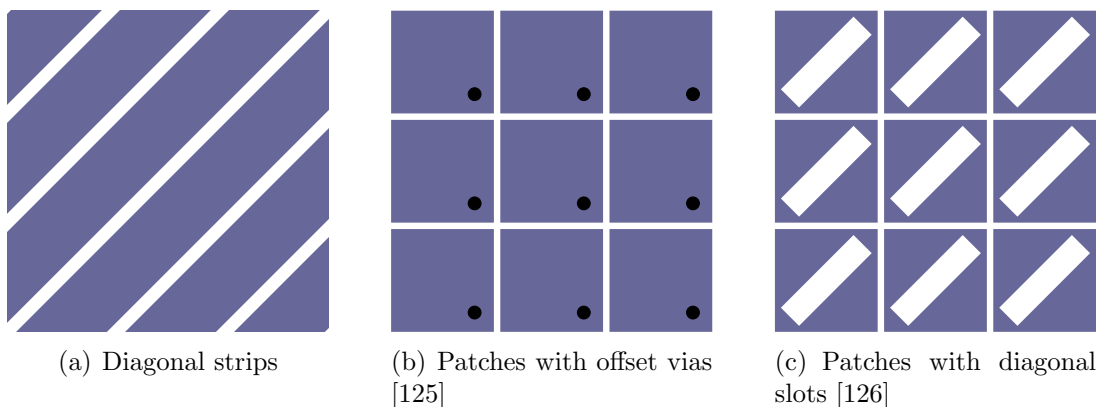
Figure 5.5: Examples of transpolarising surfaces.

Note that all these transpolarising surface designs are characterised by the asymmetry between the incident electric field polarisation and the direction of the periodic grating, resulting in a tilt angle of 45°, which is the principal factor in the fulfilment of the transpolarisation. In fact, any reflecting surface that orthogonally combines

PEC/PMC responses will produce transpolarisation at a given frequency when the incident wave polarisation is tilted 45° with respect to PEC/PMC axes. This PEC/PMC requirement is often referred as the 180° phase property due to the phase difference $\Delta\varphi$ between the PEC and the PMC responses,

$$\Delta\varphi[deg] = |\varphi_{PEC} - \varphi_{PMC}| = |180° - 0°| = 180° \tag{5.2}$$

In addition, this 180° phase requirement would also be valid for a surface with 90° and -90° phase responses along two orthogonal directions,

$$\Delta\varphi[deg] = |\varphi_1 - \varphi_2| = |90° - (-90°)| = 180° \tag{5.3}$$

5.2 Transpolarisation with a SR AMM slab

5.2.1 Design and simulation of a transpolarising SR surface

It seems possible to design a transpolarising surface by properly combining the SR AMM slab presented in Section 3.3, which provides a PMC response (0° in reflection) around 2.6 GHz, and a PEC reflector. Since the SR AMM slab provides the PMC response for the co-polar polarisation, the required 180° phase difference (5.2) to produce transpolarisation could be obtained by orthogonally placing a periodic arrangement of narrow metallic strips behaving as a PEC above the SR AMM slab. Thus, the resulting transpolarising SR surface is expected to operate around 2.6 GHz, because the SR AMM slab limits the frequency response of the overall design. The unit cell of the transpolarising SR surface is depicted in Figure 5.6. The SR AMM slab has the same dimensions as the one presented in Section 3.3, that is, 120 mm × 120 mm × 6 mm. Regarding the PEC reflector, the width of a metallic strip *gstrip* is 1 mm, whereas the length of the metallic strips is equal to the length of the whole SR AMM slab, that is, 120 mm, although *lstrip* is equal to 4 mm within the unit cell. An incident electric field linearly polarised along the x and y axis, that is, oriented at $\phi = 45°$ with respect to the strips, is used to properly produce the transpolarisation. The simulations have been carried out with Ansoft HFSS [59]. In this case, master/slave boundary conditions [60] have been applied to the unit cell, because with such a simulation setup the polarisation of the incident wave can be arbitrarily defined. Some views of the simulated transpolarising SR surface are depicted in Figure 5.7. Although not shown in these figures, a 0.5 mm thin layer of RO4003C substrate has been used to hold the metallic strips above the SR AMM slab.

The simulated magnitude and phase of the reflected E_x and E_y components of the transpolarising SR surface have been plotted in Figure 5.8 from 2 to 4 GHz. The
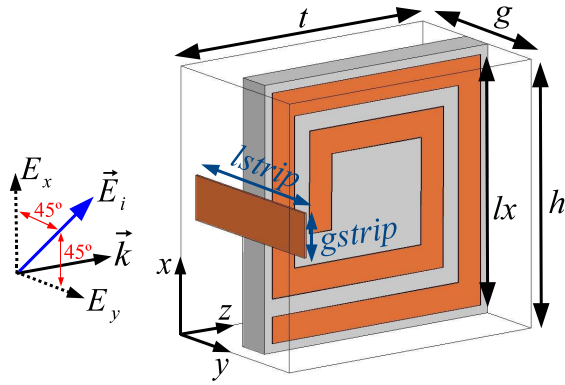
Figure 5.6: Detail of the unit cell of the SR AMM combined with a metal strip to produce a transpolarising SR AMM surface. In this design, $h = t = 6$ mm, $g = 4$ mm, $lx = 5.6$ mm, $lw = 0.6$ mm, $lg = 0.4$ mm, $lstrip = 1$ mm, and $gstrip = g = 4$ mm. The characteristics of the RO4003C substrate are, thickness = 0.8 mm, copper thickness = 0.018 mm, $\varepsilon_r = 3.38$, and tan δ = 0.0027.

(a)   (b)
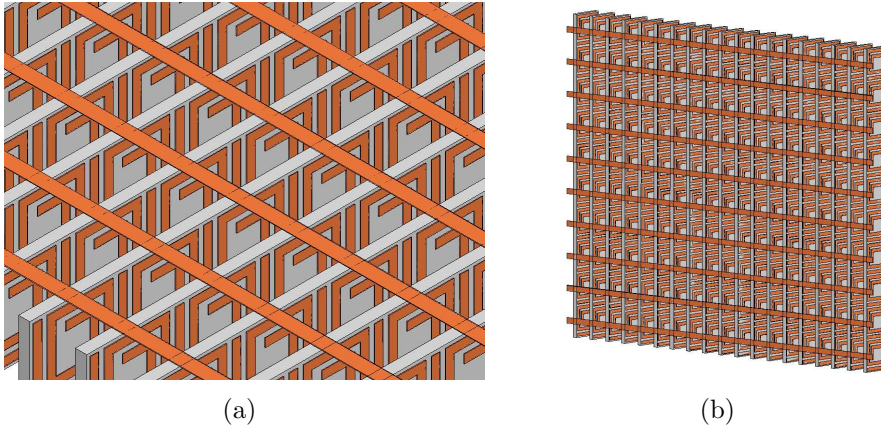
Figure 5.7: Two views of the transpolarising SR surface.

PMC-like response (0° phase condition) is achieved at 2.64 GHz for the E_x component, as expected. On the other hand, the PEC-like response (180° phase behaviour) is obtained for the E_y component across the whole frequency range. Note that, in terms of magnitude, the maximum is apparently limited to -3 dB (0.7 V/m in linear scale) because the magnitude of the incident wave is decomposed into E_x and E_y components. This fact could be overcome by carrying out two simulations, one with the incident polarisation along x, and the other with an incident polarisation along y.

Based on the principle of operation of a transpolarising surface presented in Section 5.1.1, the transpolarisation components E_u and E_v have been retrieved from the combination of the E_x and E_y results as follows:

$$E_u = E_x + E_y$$
$$E_v = E_x - E_y$$

(5.4)
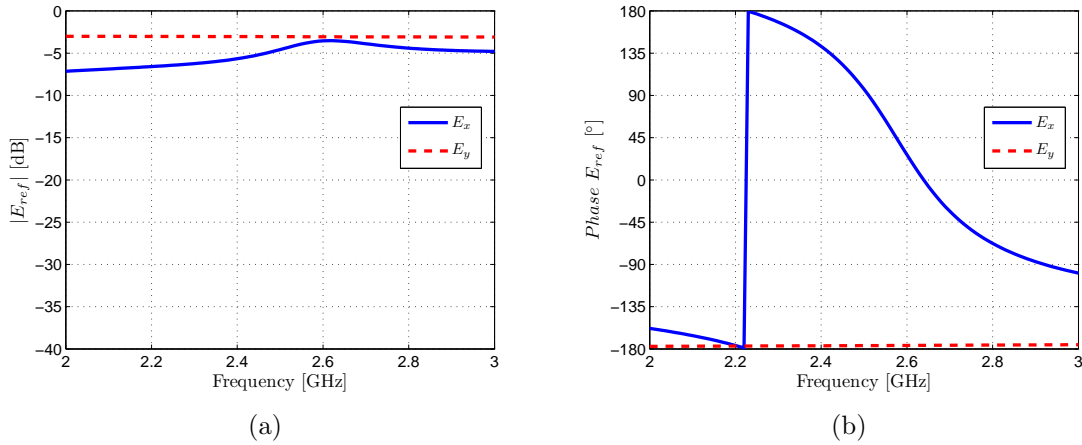
Figure 5.8: Simulated E_x and E_y components of the transpolarising SR surface.

The E_u and E_v results have been plotted in Figure 5.9. The co-polar component E_u has a decrease in magnitude around 2.64 GHz, whereas the cross-polar component E_v has its maximum at the same frequency. This result confirms that a phase difference of 180° between E_x and E_y components is needed to produce a transpolarisation response. Since the metallic strips provide 180° along the whole frequency range, the transpolarisation is found at the frequency where the 0° phase response of the SR AMM occurs. At 2.64 GHz, a transpolarisation ratio of about 30 dB has been obtained, whereas the cross-polarisation losses are only -0.3 dB. However, 20 dB transpolarisation bandwidth is only 1.33% due to the narrow band response of the SR AMM slab.
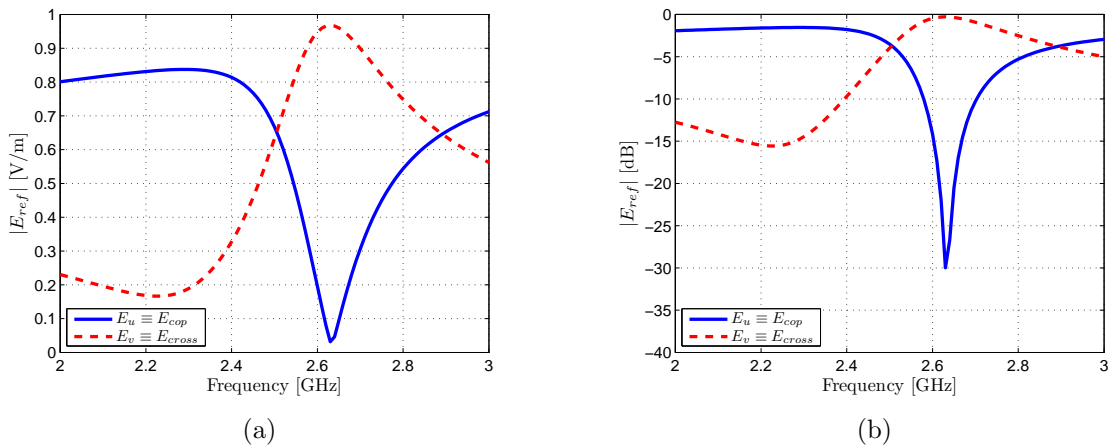
Figure 5.9: Computed co-polar E_u and cross-polar E_v components of the transpolarising SR surface.

5.2.2 Fabrication and measurement of a transpolarising SR surface

The transpolarising SR surface has been fabricated from the combination of a single layer SR AMM slab, which has been also used in previous chapters, and a periodic arrangement of metallic strips, which have been etched on a RO4003C substrate with a thickness of 0.5 mm. Therefore, the overall thickness of the transpolarising SR surface is 6.5 mm. The fabricated design is presented in Figure 5.10.

(a)   (b)
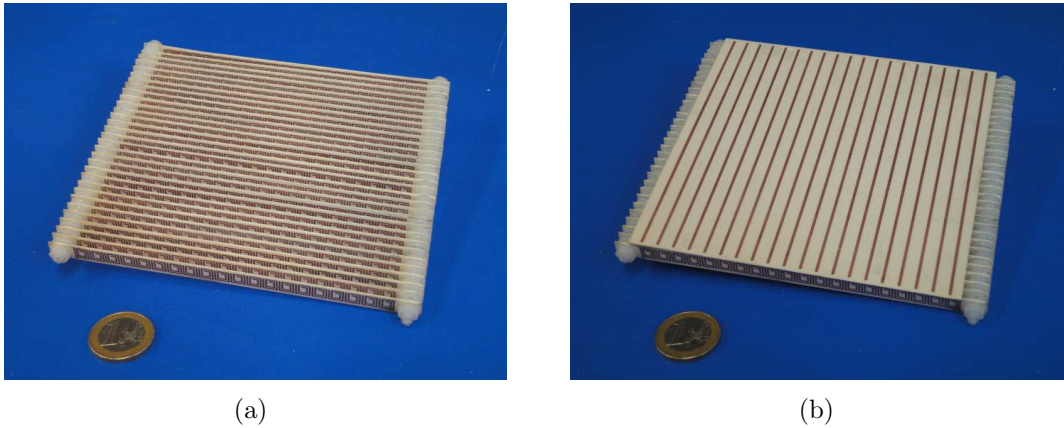
Figure 5.10: Fabricated transpolarising SR surface composed of a single layer SR AMM slab and a periodic arrangement of metallic strips printed on a RO4003C substrate.

Once fabricated, monostatic RCS measurements were carried out in the UPC anechoic chamber. In this configuration, two single polarisation measurements were carried out. The x polarisation corresponds to PMC-like response of the SR AMM slab, whereas the y polarisation corresponds to the PEC-like response of the metallic strips. A time domain gating method [133, 134] has been applied to the measurements in order to avoid undesired couplings and reflections. The whole process is explained in detail in Appendix A. In addition, a metallic surface with the same dimensions as the transpolarising SR surface has been used to normalise the measured results. The measured magnitude and the phase of the E_x and E_y components are plotted in Figure 5.11. The $0°$ phase condition is achieved at 2.61 GHz for the E_x component and, as expected, the $180°$ phase behaviour is obtained for the E_y component over the whole frequency band. Note that, the measured magnitude of the E_x and E_y components presents some small insertion losses, which may be due to the precision of the time gating method and to the small electrical dimensions of the transpolarising surface, which is only 1.3 $\lambda \times 1.3\lambda$.

The transpolarisation components E_u and E_v have been computed from the measured E_x and E_y results according to (5.4), and they are plotted in Figure 5.12. The
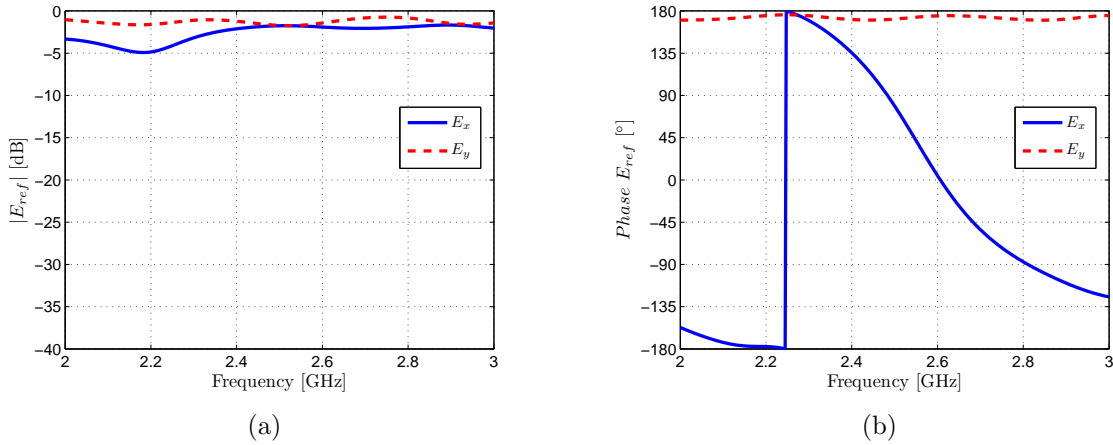
Figure 5.11: Measured E_x and E_y components of the fabricated transpolarising SR surface.

co-polar component E_u has a decrease in magnitude around 2.61 GHz, as expected from the 0° phase behaviour of the E_x component, whereas the cross-polar component E_v has its maximum at the same frequency. At 2.61 GHz, a transpolarisation ratio of about 29 dB has been obtained, whereas the cross-polarisation losses are -1.6 dB. Taking into account that the overall thickness of this design is 6.5 mm, this design can be considered as low profile, with an electrical thickness of $\lambda/17.45$, much smaller than the $\lambda/4$ of the designs involving fins and corrugations. Therefore, these results confirm the feasibility of the transpolarising SR surface.
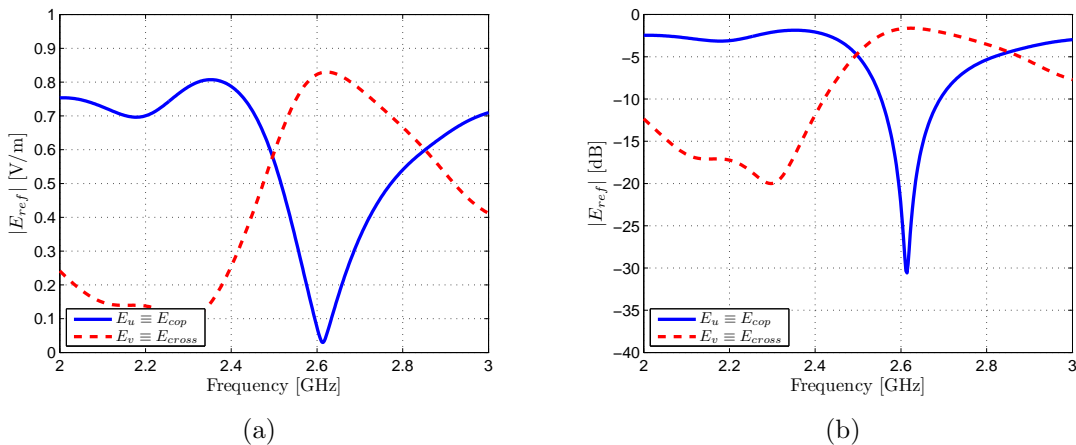
Figure 5.12: Computed co-polar E_u and cross-polar E_v components of the transpolarising SR surface from the measured E_x and E_y components.

5.3 Design of a broadband and low profile transpo- larising surface

The design presented in [126] has been chosen to produce a broadband and low profile transpolarising surface. This design is composed of a periodic arrangement of metallic square patches with a wide diagonal slot in the centre of each patch, above a conducting ground plane. Although the transpolarisation is achieved over a wide frequency range, this design has several fabrication issues. Air is used as spacer between the patches and the ground plane, leading to proper height selection to optimise transpolarising performance. However, a commercial dielectric substrate is preferred as spacer, taking advantage of the photo-etching techniques to be applied to one side of the dielectric board to produce the metal square patches with diagonal slots. Ansoft HFSS [59] has been used to carry out the numerical simulations of the transpolarising surface. Master/Slave periodic boundary conditions [60] have been applied to a single unit cell to simulate an infinite array approach, while avoiding memory and computing time limitations of an entire design simulation. The transpolarising surface has been designed to operate around 9.65 GHz, following the design guidelines presented in [126]. The square patch width lx is 4.8 mm, and the unit cell width lxx is 5.8 mm, with a gap lg of 1 mm between adjacent patches. The diagonal slot starts at 0.25 mm from the edge of the patch and $lx/4$ from its corner. Rogers RO4003C has been considered to simulate a real dielectric substrate. The dielectric thickness lh is 1.52 mm, the electric permittivity ε_r is 3.38, the loss tangent $\tan\delta$ is 0.0027, and the copper thickness lc is 0.018 mm. A sketch of a unit cell is depicted in Figure 5.13.

(a) Unit cell   (b) Transpolarising surface
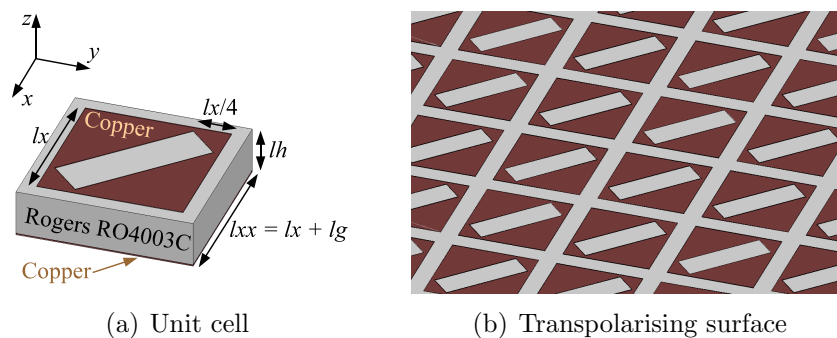
Figure 5.13: Transpolarising surface composed of square patches and diagonal slots printed on RO4003C substrate. In this design, $lx = 4.8$ mm, $lg = 1$ mm, $lxx = lx + lg = 5.8$ mm, $lh = 1.52$ mm, $\varepsilon_r = 3.38$, $\tan\delta = 0.0027$, and $lc = 0.018$ mm.

The simulated reflection results have been plotted in Figure 5.14 (a), for a linear incident electric field polarised along the x axis (E_x) with a magnitude of 1 V/m from 6 to 14 GHz. It can be seen that the magnitude of the co-polar component E_x

varies across the whole frequency band, having a minimum value of 0.026 V/m around
9.7 GHz. It is also remarkable how the cross-polar component E_y appears, having a
maximum value of 0.985 V/m where the co-polar component had its minimum value,
thus producing the polarisation conversion from x to y around 9.7 GHz. Therefore, the
overall thickness of the transpolarising surface is $\lambda/20.34$. Moreover, the E_z component
remains close to 0 V/m along the whole frequency range as expected, because surface
currents lack a vertical component.

(a) Linear scale   (b) Logarithmic scale
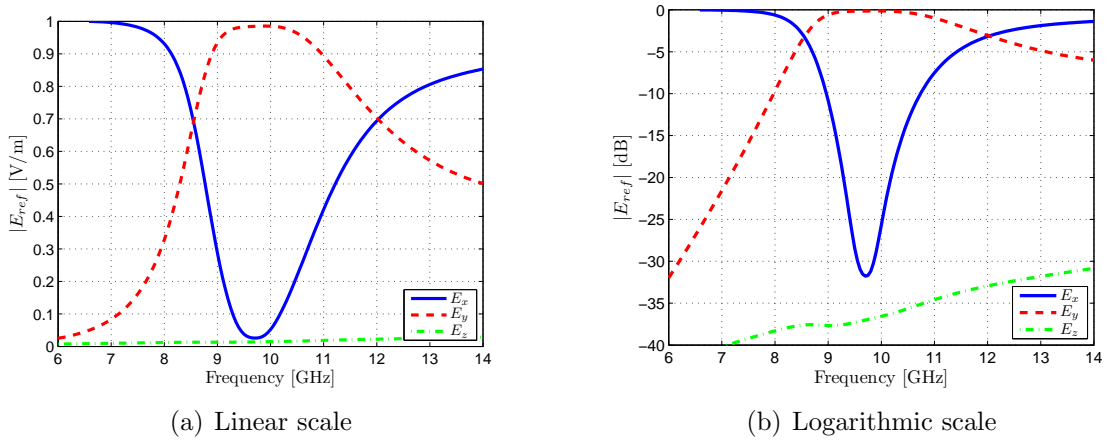
Figure 5.14: Simulated reflected co-polar (E_x) and cross-polar (E_y) components for
normal incidence in linear and logarithmic scale.

Previous results have also been plotted in Figure 5.14 (b) in logarithmic scale. At
the operational frequency, the minimum value of the co-polar component is -31.8 dB,
and the maximum value of the cross-polar component is -0.13 dB, which implies very
low cross-polar reflection losses. A 20 dB transpolarisation level is achieved for normal
incidence over a bandwidth of 9.83%. In addition, in [126] it was demonstrated that the
phase difference between co-polar and cross-polar components remains around $\pm 90°$
along the whole frequency band. This fact is evidenced in Figure 5.15.

Previous results have been found for $\theta = 0°$ (normal incidence) and $\phi = 0°$ (x
polarisation). In this way, transpolarisation response is expected to be found around
9.65 GHz every 90°, that is, for $\phi = 0°$, 90°, 180° and 270° due to the symmetry of
the unit cell. Consequently, no transpolarisation would be found for $\phi = 45°$, 135°,
225° and 315°, because only the co-polar response would be reflected. This fact is
demonstrated in Figure 5.16, where the angular ϕ variation from 0° to 90° has been
plotted. From these results, transpolarisation is found at $\phi = 0°$ and $\phi = 90°$, as
expected, whereas only co-polar response, and hence, no transpolarisation is found at
$\phi = 45°$.

Moreover, transpolarising surfaces are also able to reflect oblique incident waves.
In this case, TE (transversal electric, with the E field parallel to the surface) and
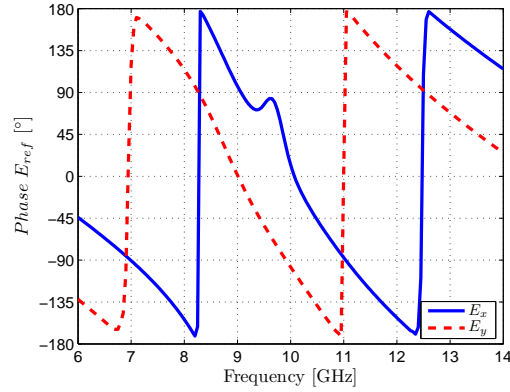
Figure 5.15: Simulated reflected co-polar (E_x) and cross-polar (E_y) phase components for normal incidence.
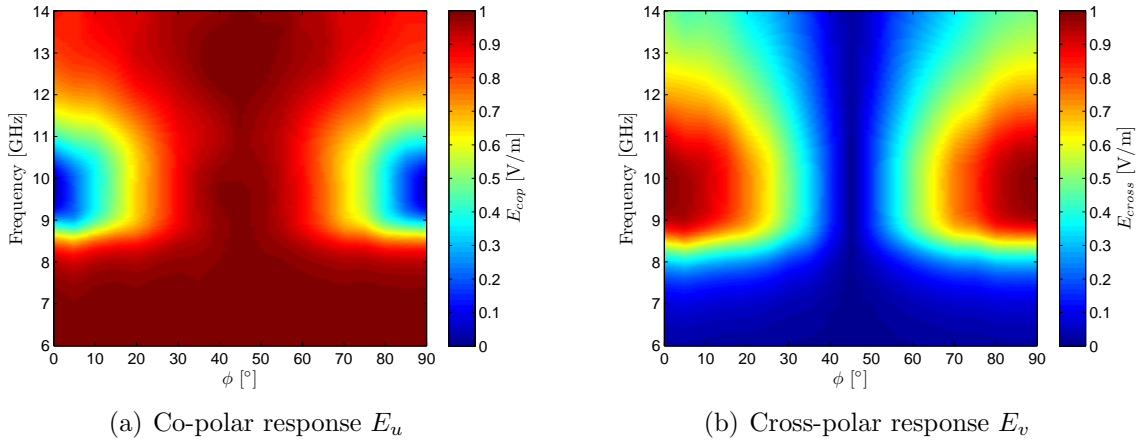
(a) Co-polar response E_u

(b) Cross-polar response E_v

Figure 5.16: Simulated normal incidence with ϕ angle variation from 0° to 90°.

TM (transversal magnetic, with the H field parallel to the surface) polarisation have been considered for oblique incidence for a θ angle variation from 0° to 45°. Simulated normal incidence (0°) and TE/TM oblique incidence (45°) results have been plotted in Figure 5.17.

From these results, it is concluded that, for 45° oblique incidence, the magnitude of the co-polar component is increased from 0.04 up to 0.24 V/m at 9.9 GHz, whereas the cross-polar response seems not to be affected along the whole frequency band. This fact reduces the transpolarisation ratio from 30 dB down to 12 dB. However, the operational bandwidth is slightly increased when considering a transpolarisation ratio of 12 dB at 9.9 GHz. It is also remarkable that a second resonance appears around 10.8 GHz for TE oblique incidence, although both TE and TM responses are quite similar before 9.9 GHz. This fact is evidenced when plotting the reflected co-polar and cross-polar responses while varying the incidence angle θ from 0° to 45°, as shown in Figure 5.18 for TE and in Figure 5.19 for TM oblique incidences.

(a) Linear scale

(b) Logarithmic scale
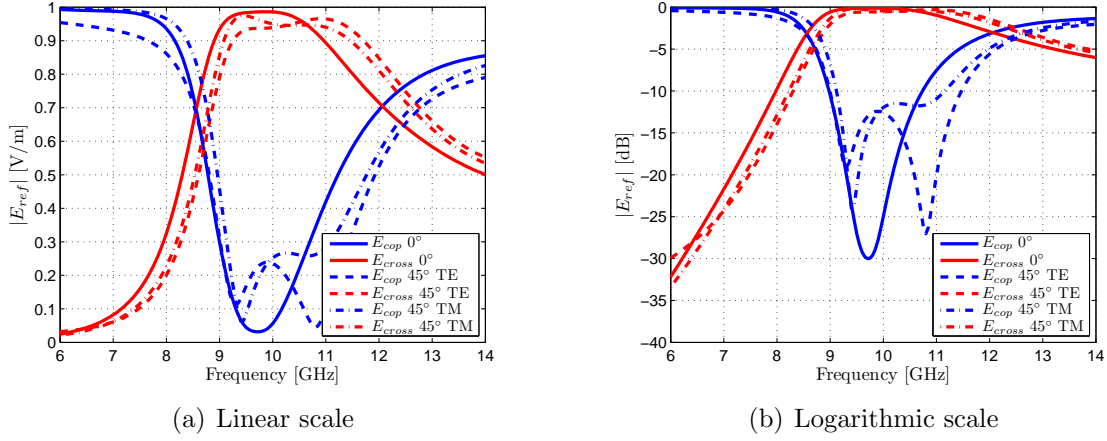
Figure 5.17: Simulated 0° normal incidence and 45° TE and TM oblique incidence for the transpolarising surface design.

(a) Co-polar response $E_{cop} = E_x$

(b) Cross-polar response $E_{cross} = E_y$
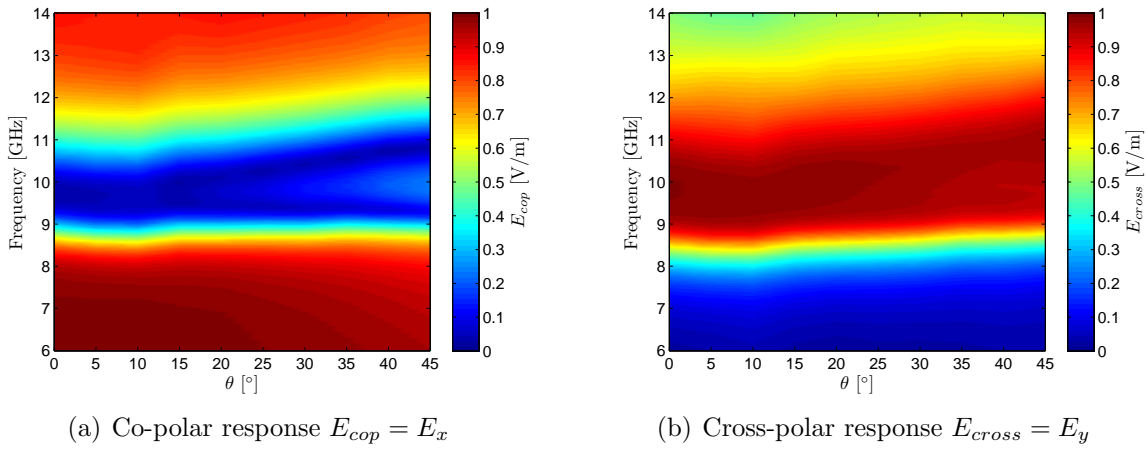
Figure 5.18: Simulated TE oblique incidence from 0° to 45°.

(a) Co-polar response $E_{cop} = E_x$

(b) Cross-polar response $E_{cross} = E_y$
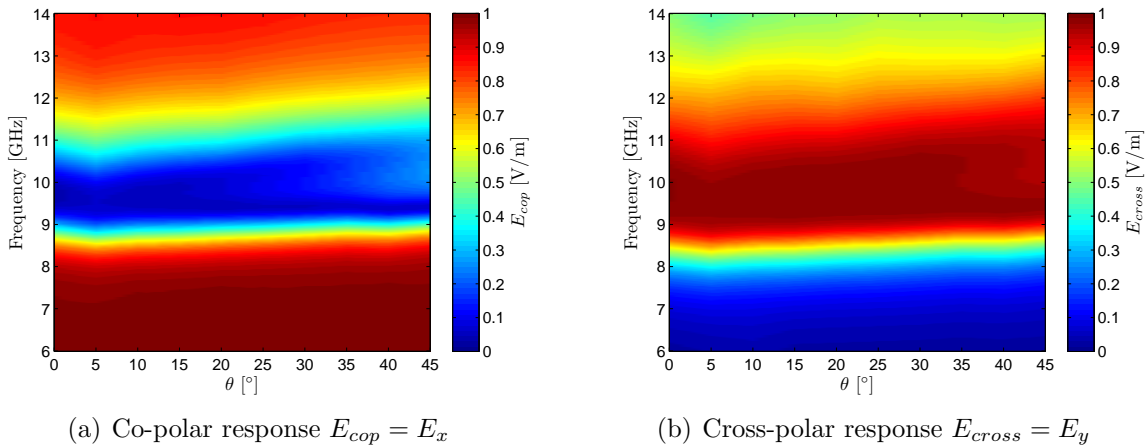
Figure 5.19: Simulated TM oblique incidence from 0° to 45°.

5.4   Fabrication and Measurement of a Low Profile Transpolarising Surface

The designed transpolarising surface has been fabricated and measured in order to assess the validity of the numerical characterisation. A 15 cm × 15 cm transpolarising surface has been fabricated using standard photo-etching techniques on a Rogers RO4003C substrate. The unit cell dimensions are the same as those previously used in the numerical simulations, which leads to a surface composed of 26×26 square patches with diagonal slots. The bottom side of the dielectric substrate remains as the backing ground plane. The fabricated design is shown in Figure 5.20. Once fabricated, the transpolarising surface has been mounted in the rotor of the D3 UPC anechoic chamber in order to carry out the measurements for normal and oblique incidence.

(a) Detail   (b) Full view
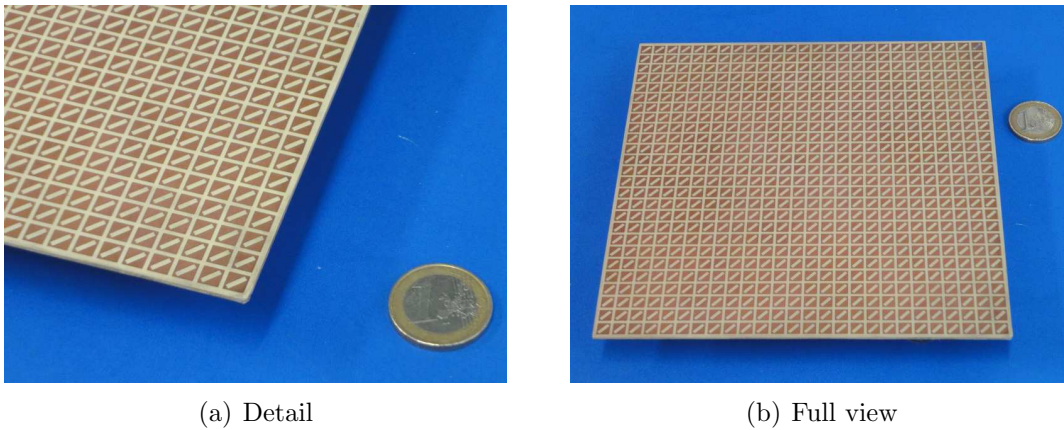
Figure 5.20: Fabricated 26×26 unit-cell transpolarising surface.

5.4.1   Normal Incidence Measurements

The transpolarising surface has been attached to the rotor by means of a support made of Rohacell foam, a material which behaves like air ($\varepsilon_r \approx 1$), as shown in Figure 5.21. This may reduce the reflections produced by the metallic parts of the rotor over the transpolarising surface.

On the other side of the anechoic chamber, two ridged horn antennas are placed as a probe in order to directly measure the co-polar (E_{cop}) and cross-polar (E_{cross}) response of the transpolarising surface, as shown in Figure 5.22. One antenna is used for transmitting and the other one for receiving purposes. This yields a bistatic RCS measurement setup.

A scheme of the whole measurement setup placed in the anechoic chamber is depicted in Figure 5.23.

(a) Rotor view   (b) Complete view
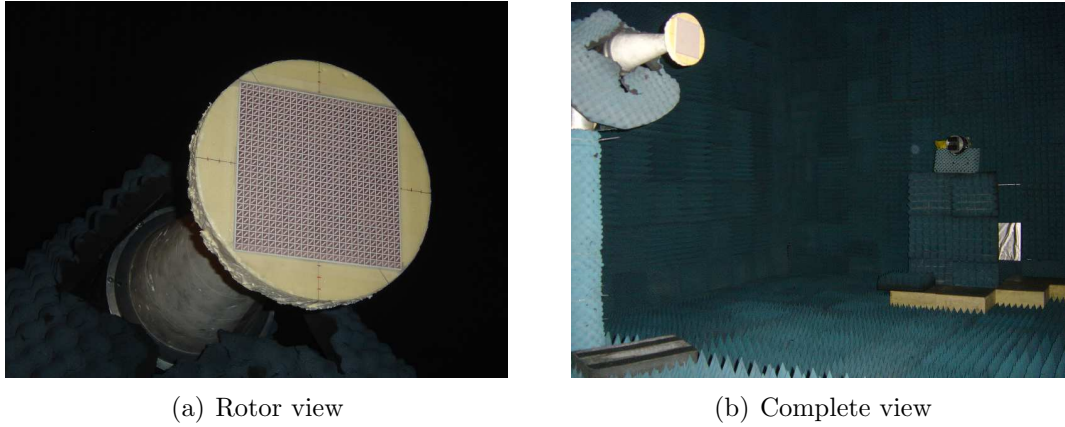
Figure 5.21: Transpolarising surface placed in the D3 UPC anechoic chamber.

(a) Co-polar configuration   (b) Cross-polar configuration
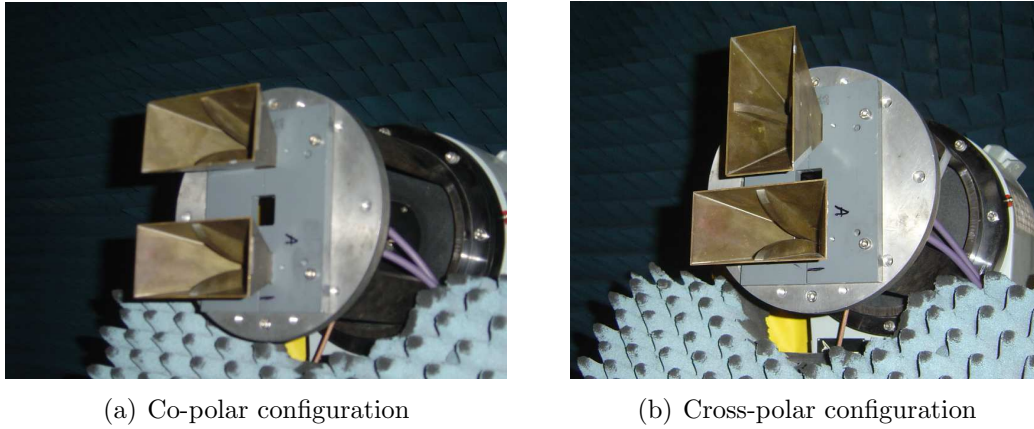
Figure 5.22: Ridged horn antennas used to carry out the bistatic RCS measurements
of the transpolarising surface.

The measured co-polar ($E_{cop}^{transpol}$) and cross-polar ($E_{cross}^{transpol}$) responses need to be
normalised by the co-polar (E_{cop}^{pec}) response of a metallic sheet of the same dimensions
placed at the same position, in order to compensate the propagation losses. For sim-
plicity, the opposite side of the transpolarising surface, which is a backing ground plane,
has been used as the reference metallic surface (PEC). In this case, E_{cop} and E_{cross} are
retrieved as (5.5):

$$E_{cop} = \frac{E_{cop}^{transpol}}{E_{cop}^{pec}}$$

(5.5)

$$E_{cross} = \frac{E_{cross}^{transpol}}{E_{cop}^{pec}}$$

Therefore, the co-polar and the cross-polar responses of the transpolarising surface
and the co-polar response of the metallic surface have been measured from 2 to 12 GHz.
The measured results have been plotted in Figure 5.24. The co-polar response of the
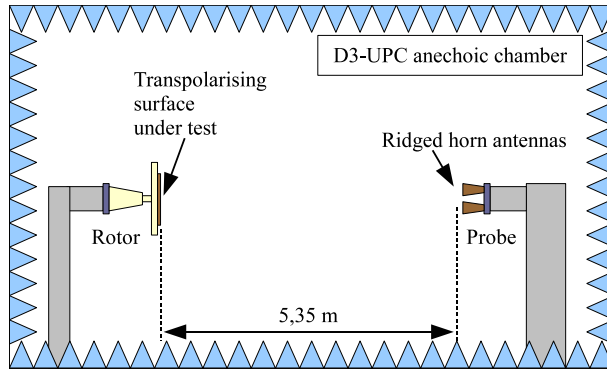
Figure 5.23: Scheme of the measurement setup placed in the anechoic chamber.

transpolarising surface and the metallic surface present a similar behaviour, whereas the cross-polar response of the transpolarising surface is found about 20 dB below the co-polar responses, as expected from polarisation mismatch.
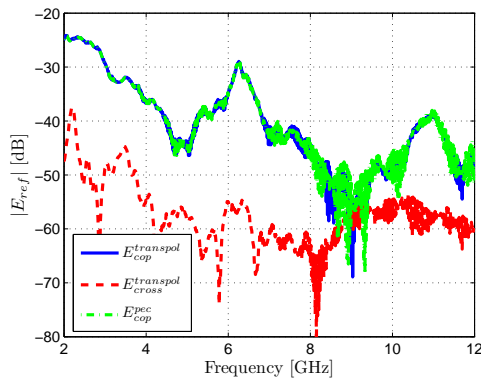
Figure 5.24: Measured reflected co-polar ($E_{cop}^{transpol} \equiv E_x$) and cross-polar ($E_{cross}^{transpol} \equiv E_y$) components of the transpolarising surface, and the co-polar (E_{cop}^{pec}) component of the metallic surface.

However, no transpolarisation response is apparently seen in the frequency range from 8 to 10 GHz, where it was expected from numerical simulations. Measured results may suffer from the strong coupling between the transmitting and receiving antennas and also from some reflections due to the environment (e.g., metallic parts of the rotor and the probe), thus masking the transpolarisation response. For this reason, a time domain gating method [133,134] may be applied to reduce these undesired effects. The key point is that all these couplings and reflections are measured with a sufficient delay with respect to the main signal, and they could be filtered in time domain, by using a gating window centred around the main response. Further details about the time-gating method are found in Appendix A. The application of the gating process results in cleaner and smoother measured results, as seen in Figure 5.25.

The co-polar and cross-polar results of the transpolarising surface are then nor-
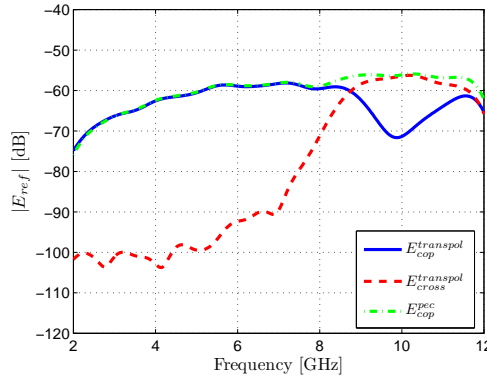
Figure 5.25: Measured data in frequency domain after applying the gating window.

malised by the co-polar result of the reference metallic surface, and they are plotted in
Figure 5.26.
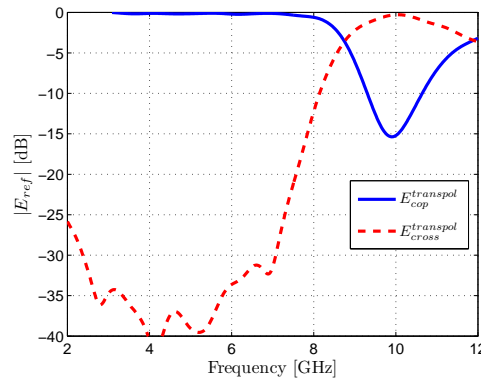
Figure 5.26: Measured data in frequency domain after applying the gating window
and metallic surface normalisation.

After the application of the time gating method, the transpolarisation response is
clearly revealed around 9.8 GHz. This operational frequency is slightly shifted from
9.7 to 9.8 GHz when compared with the numerical simulation. The transpolarisation
ratio at 9.8 GHz is about 15 dB, the insertion losses (maximum cross-polar value) is
about -0.4 dB, and the overall thickness of the surface is $\lambda/20.14$, which is five times
smaller than the required $\lambda/4$ for the transpolarising corrugated surfaces. Finally, the
magnitude and phase of the measured co-polar and cross-polar components is plotted
in Figure 5.27. The phase difference between both components is about $\pm 90°$ along
the whole frequency range, as pointed out in the numerical simulations.
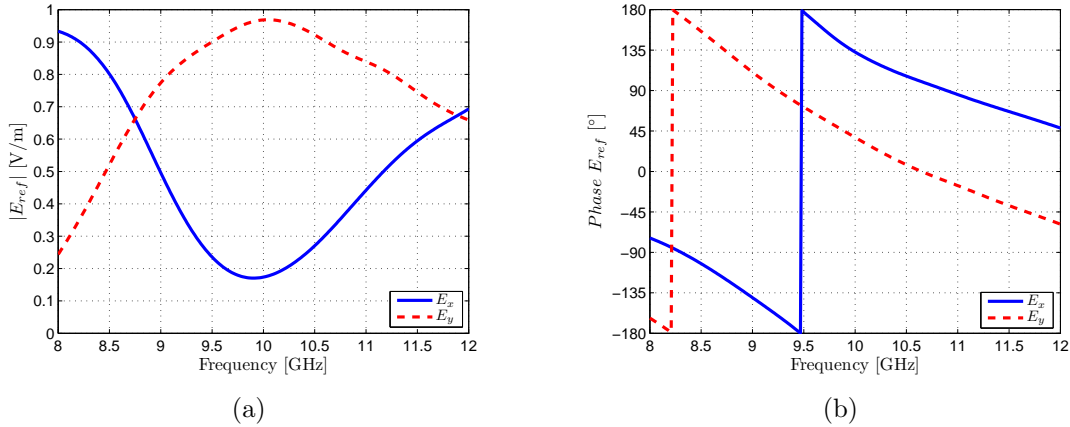
Figure 5.27: Measured magnitude and phase of the reflected co-polar (E_x) and cross-polar (E_y) components for normal incidence.

5.4.2   Oblique Incidence Measurements

Several methods could be used to measure the oblique incidence response of a reflecting surface. The most common procedure uses a transmitting antenna and a receiving antenna oriented at an angle θ with respect to the normal direction of the reflecting surface; in such a case, the angle θ can take values from $0°$ to $90°$. However, this measurement setup is inaccurate when no proper angular positioning system for the transmitting and receiving antennas with respect to the reflecting surface is used.

Another measurement method for oblique incidence requires the use of a dihedral corner reflector (DCR). DCRs are well known as radar calibrators, because they can provide reflected co-polar and cross-polar responses by simply rotating the DCR by $45°$ around its axis. In this method, the transpolarising surface would be placed on one side of the DCR, whereas the other side remains as a metallic surface; in this way, with the presence of a transpolarising surface, the performance of the DCR is expected to be reversed, leading to a transpolarising DCR (TDCR). However, DCRs have a narrow elevation angular response. Therefore, a trihedral corner reflector (TCR), another well known radar calibrator, could be used instead. TCRs provide a high backscattered co-polar response for a wide range of incident angles. In this case, a transpolarising surface would also be placed on one side of the TCR, whereas the other two sides remain as metallic surfaces. This configuration can lead to the design of a transpolarising TCR (TTCR). Although the internal oblique incidence angle of the TCR is fixed, the incidence angle to the TTCR could be even higher than $45°$ due to the geometry of the TCR and to the orientation with respect to probe antennas. Thus, if the performance of the TTCR is successfully verified, this measurement setup could be considered as an application of the transpolarising surfaces.

For simplicity, the latter method has been chosen to test the oblique incidence

performance of the designed transpolarising surface. Then, a triangular transpolarising surface has been fabricated to be placed inside the TTCR, as it is shown in Figure 5.28. The standard trihedral corner reflector is made of aluminium, with a major dimension of 32 cm.
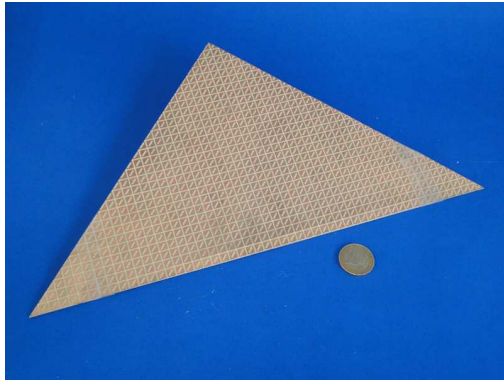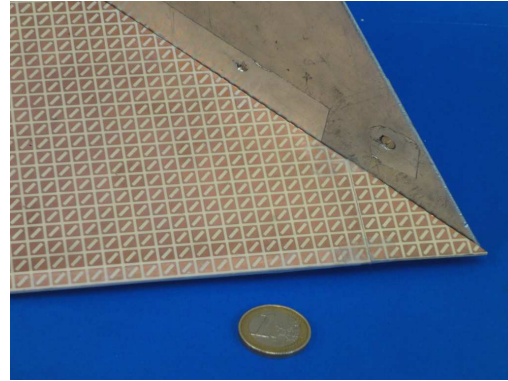
(a) Transpolarising surface   (b) Transpolarising TCR

Figure 5.28: Fabricated triangular transpolarising surface to be placed inside the trihedral corner reflector (TCR) forming a transpolarising TCR (TTCR).

Once fabricated, the TTCR has been placed in the anechoic chamber in order to proceed to the bistatic RCS measurements, with the same configuration as used before for the normal incidence measurements, as shown in Figure 5.29. The reflected co-polar
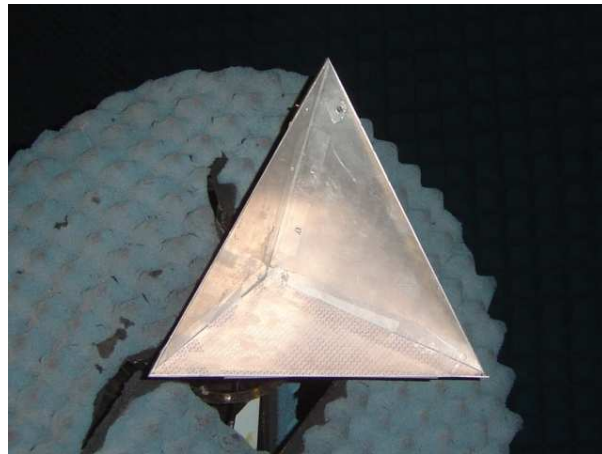
Figure 5.29: Fabricated transpolarising trihedral corner reflector (TTCR) placed in the D3 UPC anechoic chamber.

and cross-polar responses of the TTCR have been plotted in Figure 5.30. Although the oblique incidence angle is supposed to be higher than 45°, a transpolarisation behaviour is still obtained. A transpolarisation ratio of about 12 dB has been obtained around 10.1 GHz. The cross-polarisation losses at the operational frequency are -1.5 dB.

(a) Linear scale   (b) Logarithmic scale
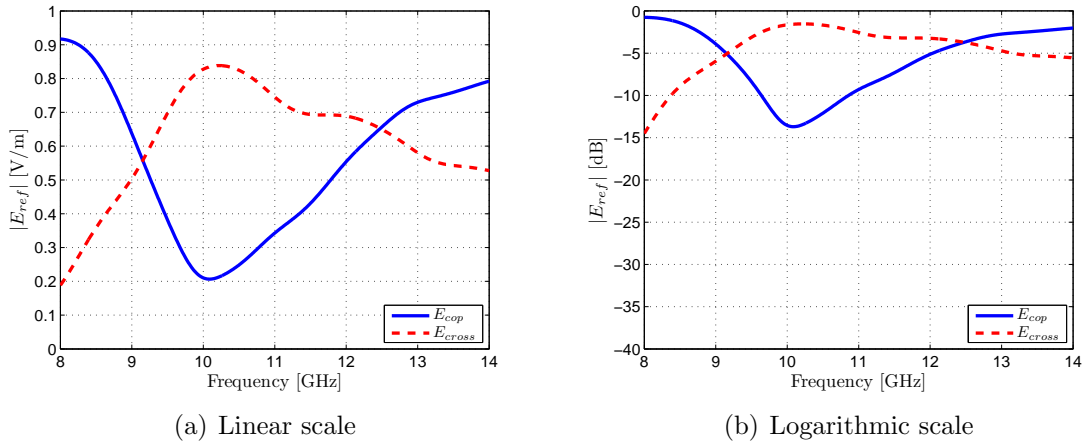
Figure 5.30: Measured reflected co-polar and cross-polar response of the transpolarising surface placed inside a trihedral corner reflector as TTCR.

5.5   Application of a Transpolarising Surface to a Polarimetric Radar Calibrator

5.5.1   Introduction to Polarimetric Radar Calibration

Polarimetric SAR (PolSAR) systems have caught the interest of the research community since they are able to provide much more information than conventional single polarisation SAR systems. This interest will gradually increase since several spaceborne PolSAR missions have been launched in the recent years: ALOS-PALSAR, RADARSAT 2 and TERRASAR-X. Thus, reliable polarimetric calibration procedures and techniques are mandatory.

Trihedral corner reflectors (TCRs) are commonly employed to calibrate SAR data, as they provide a high backscattering RCS response for a wide range of incident angles. Nevertheless, the TCRs lack a cross-polar response, making them limited for full polarimetric calibration, as stated in the scattering matrix of a TCR (5.6):

$$S_{TCR} = \left[\begin{array}{cc} S_{HH} & S_{HV} \\ S_{VH} & S_{VV} \end{array} \right] = \left[\begin{array}{cc} -1 & 0 \\ 0 & -1 \end{array} \right] \tag{5.6}$$

In the 90's, different solutions appeared to realise TCRs providing cross-polar response taking advantage of transpolarising surfaces composed of fins or corrugations [129–131], as presented before in Section 5.1.2. Such transpolarising surfaces (or twist reflectors) are placed on one side of the TCR, with the corrugations aligned at 45° with respect to the incident electric field polarisation. However, these corrugations have to be designed with a depth of at least $\lambda/4$ (the wavelength λ is referred to as the

operational frequency). Although the corrugations are metallic, which is interesting for weatherproof applications, one drawback is the requirement of a heavy and bulky piece of metal to realise the corrugations, which makes the fabrication process more difficult.

A low profile transpolarising surface was presented in [126]. This transpolarising surface is composed of a periodic arrangement of metallic square patches with a diagonal slot over a metal ground plane. The advantages of this transpolarising surface applied to polarimetric SAR calibrators were discussed in [132], although measurement results were not achieved. An ideal transpolarising trihedral corner reflector (TTCR) would be characterised by the scattering matrix (5.7):

$$S_{TTCR} = \left[\begin{array}{cc} S_{HH} & S_{HV} \\ S_{VH} & S_{VV} \end{array} \right] = \left[\begin{array}{cc} 0 & 1 \\ 1 & 0 \end{array} \right] \tag{5.7}$$

In this section, the performance of the proposed low profile transpolarising surface placed on one side of a TCR, that is, as a TTCR designed for polarimetric calibration purposes will be experimentally assessed by using a ground-based SAR (GB-SAR) system [135], operating at 9.65 GHz (X-band).

5.5.2   Transpolarising Surface Design

A triangular transpolarising surface has been fabricated according to design guidelines presented in Section 5.3. The transpolarising surface is mainly composed of square patches and diagonal slots over a ground plane. The square patches have a width of 4.8 mm, with a gap of 1 mm between adjacent patches. The diagonal slot has a length of 4.8 mm and a width of 1.4 mm. A Rogers RO4003C ($\varepsilon_r = 3.38$, $\tan \delta = 0.0027$) has been used as dielectric substrate. The overall thickness of the transpolarising surface is 1.52 mm ($\lambda/20$), much smaller than the $\lambda/4$ thickness required for the fabrication of the corrugations [131]. This triangular transpolarising surface is then placed on the bottom side of the TCR, as shown in Figure 5.31.

The co-polar and cross-polar responses of the standard TCR and the TTCR have been measured in the D3 UPC anechoic chamber and they are shown in Figure 5.32. The standard TCR shows a broadband response with a co-polar to cross-polar ratio of more than 30 dB. The transpolarising TCR produces a high cross-polar response around 10 GHz with a cross-polar ratio of more than 14 dB. Note that the cross-polar ratio around 9.65 GHz is only about 8 dB, although this result may vary slightly depending on the parameters of the time-gating method used in the retrieval of the measured results.
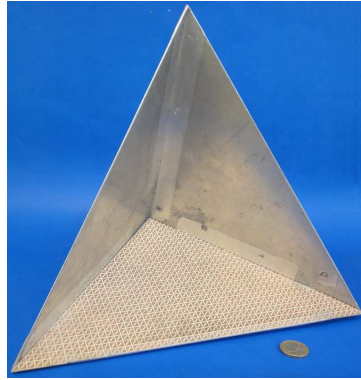
Figure 5.31: Fabricated transpolarising trihedral corner reflector (TTCR).
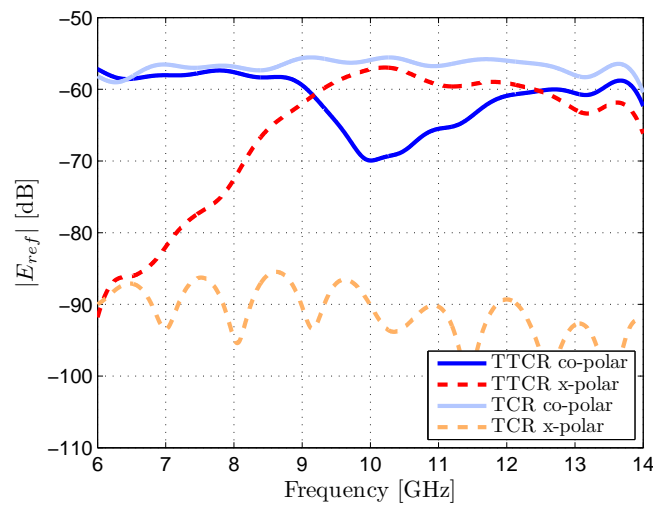
Figure 5.32: Measured RCS response of the TCR and TTCR.

5.5.3   Field Measurement Results of the Transpolarising TCR

Full polarimetric field measurements at 9.65 GHz (X-band) have been carried out with a GB-SAR system to assess the performance of the designed TTCR.

5.5.3.1   Measurement Setup

The measurements were carried out from an elevated part of the Campus Nord UPC (Barcelona, Spain) facing towards a flat square with some small trees, as shown in Figure 5.33. The trihedral under test (TUT) was placed in the middle of the measurement scenario, which is also complemented with some different reference point scatters: four conventional TCRs, which provide a pure co-polar response; one bruderhedral (B) [136], tilted 45 degrees, which provides a passive pure cross-polar response; and a polarimetric active radar calibrator (PARC) [137], that is, an active system that also provides a pure cross-polar response. However, the PARC is also tilted 45 degrees,

thus producing co-polar and cross-polar responses, making its signature present in the results for the four polarimetric components.
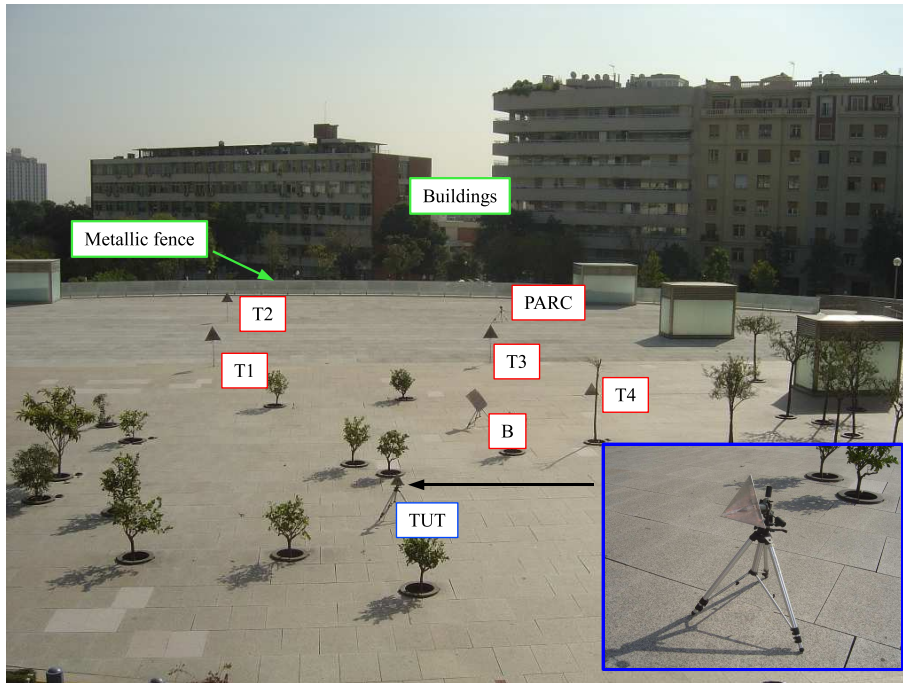
Figure 5.33: Measurement scenario.

The GB-SAR system is mounted on the top of a terrace facing the measurement scenario, as shown in Figure 5.34. The measurement parameters of the UPC GB-SAR are listed in Table 5.1. Further details about the UPC GB-SAR system can be found in [138].

(a) GB-SAR system (top view)

(b) GB-SAR system (bottom view)

Figure 5.34: Measurement scenario system.

UPC X-Band GB-SAR	
f_0	9.65 GHz
PRF	20 KHz
Chirp BW	120 MHz
Base-band BW	40 MHz
A/D Sampling Rate	100 Msamples/sec
Transmitted Power	27 dBm
Time AVG	128 samples
Horn Antennas 3 dB Beamwidth	30°
Azimuth Sampling	1 cm
Aperture Length	2 m
PolSAR (Stop&Go)	2 min 20 sec

Table 5.1: UPC X-Band GB-SAR system measurement parameters.

5.5.3.2   Measured Results

The measured HH component of the complete scenario is plotted in Figure 5.35. The maximum range in the measurements is about 250 m, although the trihedral under test (TUT) and the reference scatters, both passive trihedral corner reflectors (T1-T4) and bruderhedral (B), as well as the active PARC system, are located at a range below 70 m. The buildings and the metallic fence are easily identified. In addition, note that the nearest region to the UPC GB-SAR system is strongly amplified; this fact dramatically increases the floor level of the backscattered signals while masking the results of the TUT and the reference scatters.
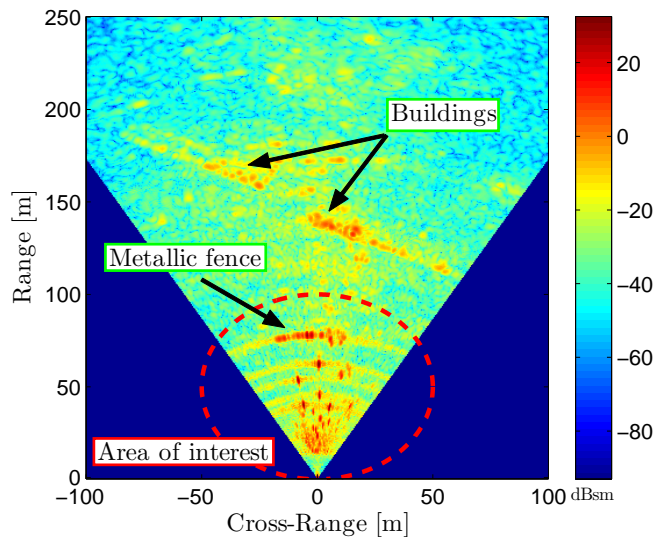
Figure 5.35: Measured HH component of the complete scenario at full range. The scatters, the buildings and the metallic fence are easily identified.

The measured results are plotted in Figure 5.36 and Figure 5.37 for a maximum

range of 80 m, that is, zooming into the area of interest. The measured results for the case of a conventional TCR as trihedral under test (TUT) for co-polar (HH, VV) and cross-polar (HV, VH) components are plotted in Figure 5.36. It can be seen that the TUT presents a high backscattered level in the co-polar components, while its level is reduced in the cross-polar ones, as expected for a conventional TCR. This is confirmed as well with the ackscattered signal of the reference TCRs (T1-T4). Note that the bruderhedral (B) is only present in the cross-polar components, as expected from a cross-polarising device. This is not the case of the PARC, which is clearly identified in all polarisations, due to its 45° tilt. It is worth noticing that the amplification, mainly due to the proximity to the GB-SAR system, increases the floor level in the surroundings of the trihedral under test, slightly masking its polarimetric signature.

The same measurements have been carried out for the case of a transpolarising TCR (TTCR) as TUT. The co-polar (HH, VV) and the cross-polar (HV, VH) components are plotted in Figure 5.37. The reference TCRs are clearly identified in the co-polar results, as expected. However contrary to the case of a standard TCR as TUT, it can be seen that the TTCR presents a high cross-polar response, in the same way as the bruderhedral and the PARC system. Moreover, although not completely vanished, the TTCR presents a lower level in the co-polar results, comparable to the cross-polar level found in the reference TCRs positions.

The measured backscattered cross-range cuts for the four polarimetric components at the TUT position are plotted in Figure 5.38. The maxima are well identified, and the cross-polar enhancement of the TTCR is verified.

The backscattered amplitude A_{TCR} and A_{TTCR} results for the case of a conventional TCR and a TTCR are listed in Table 5.2. Except for the case of vertical co-polar polarisation (VV), a difference of about 15 dB is obtained for each polarimetric component when using a TTCR compared to a standard TCR. In the worst case, the cross-polarisation ratio is about 7 dB for the TCR and 10 dB for the case of TTCR. Moreover, the maximum backscattering level with and without the transpolarising surface is slightly different. This fact may be due to a change in directivity suffered by the trihedral corner reflector when the transpolarising surface is placed inside it.

Polarimetric Component	VV	VH	HV	VV	x-pol ratio [dB]
A_{TCR} [dBsm]	21.8	6.2	10.6	21.5	10.9
A_{TTCR} [dBsm]	14.8	26.8	27.9	7.8	12.0
$|\Delta| = |A_{TCR} - A_{TTCR}|$ [dB]	7.0	20.6	17.3	13.7	

Table 5.2: Measured polarimetric components at the location of the trihedral under test (TUT), for the cases of conventional TCR and for a TTCR.

(a) TCR HH

(b) TCR HV

(c) TCR VH

(d) TCR VV
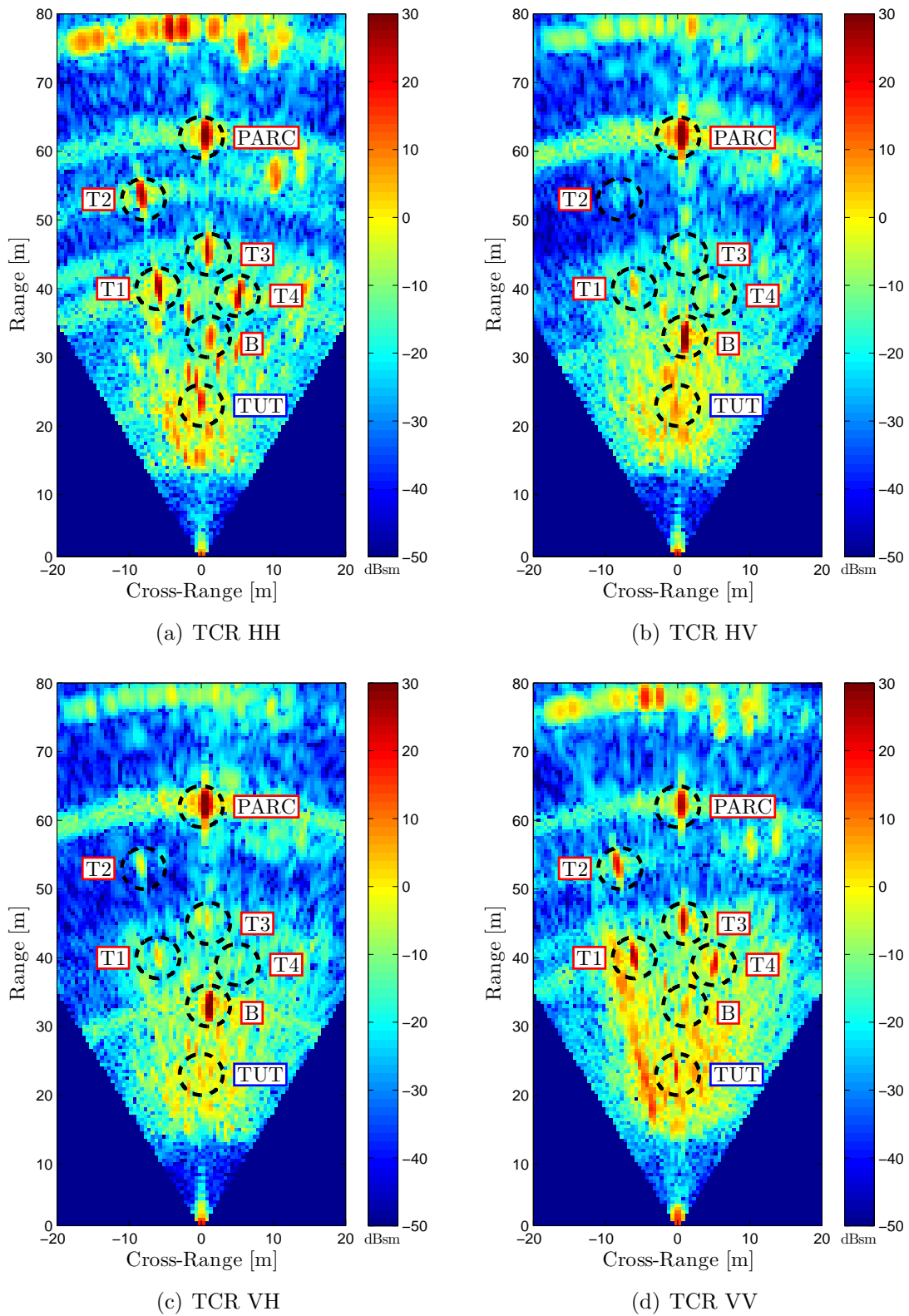
Figure 5.36: Measured HH, HV, VH and VV components of the scenario with a TCR as TUT.

(a) TTCR HH

(b) TTCR HV

(c) TTCR VH

(d) TTCR VV
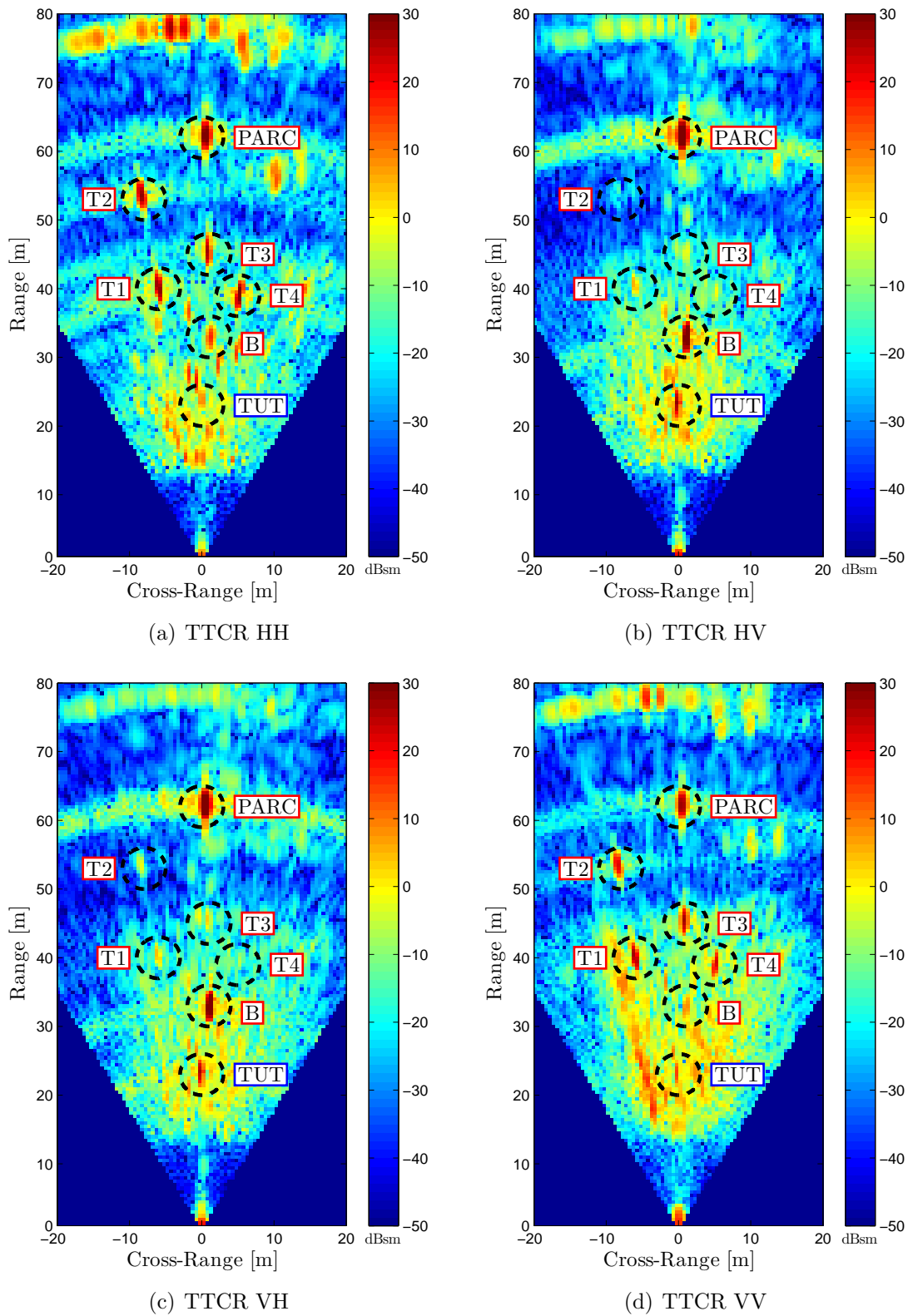
Figure 5.37: Measured HH, HV, VH and VV components of the scenario with a TTCR as TUT.

(a) Cross-range cut for TCR)

(b) Cross-range cut for TTCR
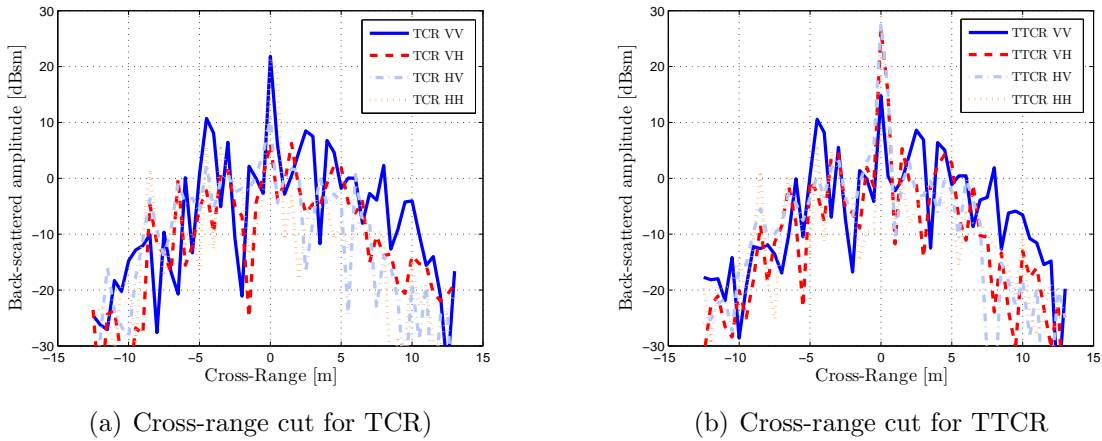
Figure 5.38: Measurement cross-range cuts for the TCR and TTCR at the TUT position.

5.6   Chapter Conclusions

The transpolarisation phenomenon has been verified by means of different low profile reflecting surfaces. The SR AMM slab, when properly combined with a metal strip reflector, presents the transpolarisation at 2.61 GHz, where the PMC response of the metamaterial slab was previously achieved. The overall thickness of this design is $\lambda/17.45$.

An AMC surface composed of metallic square patches and diagonal slots over a ground plane has been designed as transpolarising surface to operate around 9.65 GHz, with an overall thickness of $\lambda/20.34$, which is five times smaller than the required $\lambda/4$ for the transpolarising corrugated surfaces. This surface is also suitable for oblique incidence, where the transpolarisation is found for $\theta > 45°$. A good agreement is achieved between measured and simulated results.

Therefore, this transpolarising surface has been successfully applied as a passive polarimetric radar calibrator. Contrary to a conventional trihedral corner reflector, a transpolarising trihedral corner reflector (TTCR) is able to produce a backscattered cross-polar response. The performance of the TTCR has been measured with a ground based synthetic aperture radar (GB-SAR) operating at 9.65 GHz (X-band), showing a high backscattered level in the cross-polar channels.

Chapter 6

Patch Antenna Miniaturisation with AMM Loadings

6.1 Introduction

Patch antennas (PAs) have been widely used in modern communication systems due to their low profile, low cost and ease of fabrication. Square patch antennas are fabricated in a simple way by etching an effective half-wavelength long square patch on the top side of a dielectric substrate, while the opposite side remains as the ground plane. Such antennas are usually fed by a coaxial probe, although they could also be fed by a microstrip line, or by a slot in the ground plane. An example of a microstrip square patch antenna is shown in Figure 6.1.

The length L of a patch antenna is related to its frequency of operation f_0 and the index of refraction n_r of the antenna substrate, as stated in [98]:

$$L \approx \frac{c_0}{f_0}\frac{1}{2n} = \frac{\lambda_0}{2n_r} = \frac{\lambda_0}{2\sqrt{\varepsilon_r\mu_r}},\tag{6.1}$$

97

(a) Top view   (b) Bottom view
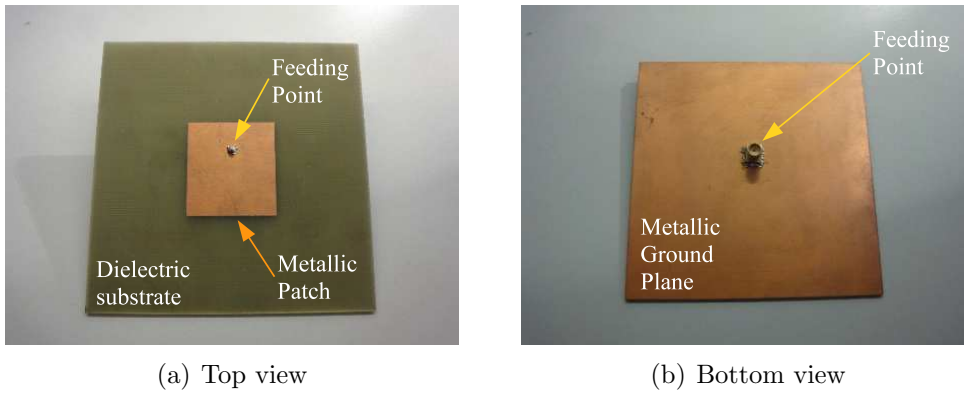
Figure 6.1: Example of microstrip patch antenna (MPA).

where ε_r and μ_r are the aforementioned relative electric permittivity and magnetic permeability, respectively. For the air case, where $\varepsilon_r = \mu_r = 1$, the patch antenna length is simply:

$$L_{air} \approx \frac{\lambda_0}{2}. \tag{6.2}$$

From (6.1), it is derived that when the index of refraction n_r increases ($n_r > 1$), the size of the patch antenna is reduced, enabling the patch antenna to be miniaturised. Therefore, n_r is also referred as the patch antenna miniaturisation factor n. High permittivity dielectrics ($\varepsilon_r >> 1, \mu_r = 1$) have been widely used to miniaturise patch antennas, although their performance is considerably degraded (reduced bandwidth of operation), as ε_r increases [99]. Recently, the use of magneto-dielectric (MD) patch antenna substrates has presented a possibility to overcome this issue [99–101]. Therefore, by choosing moderate values of ε_r and μ_r the same miniaturisation factor $n = \sqrt{\varepsilon_r \mu_r}$ could be achieved while improving the antenna bandwidth performance. However, potentials and limitations of magneto-dielectric patch antennas (MDMPA) are still under discussion [102, 103].

In this chapter, the use of metamaterial loaded patch antennas, the so called meta-substrates, is investigated. Size reduction, bandwidth, and losses are studied for non-dispersive homogeneous substrates, as well as for dispersive fabricated magneto-dielectric substrates, such as the SRR AMM slab presented in Chapter 3.

6.2   FBW computation techniques

It is known that a matched antenna has maximum return loss RL, or minimum reflection coefficient Γ or S_{11}, at the frequency of operation f_0. The return loss and

the reflection coefficient are related through (6.3):

$$RL = -\Gamma|_{dB} \tag{6.3}$$

and Γ is defined in (6.4) (expressed in dB):

$$\Gamma|_{dB} \equiv S_{11}|_{dB} = 20log_{10}\left|\frac{Z_a - Z_{ref}}{Z_a + Z_{ref}}\right| \tag{6.4}$$

being Z_a the antenna impedance and $Z_{ref} = Z_s = R_s$ the characteristic impedance (Z_s) of the source, generator, or feeding network at which the antenna is connected, as depicted in Figure 6.2.
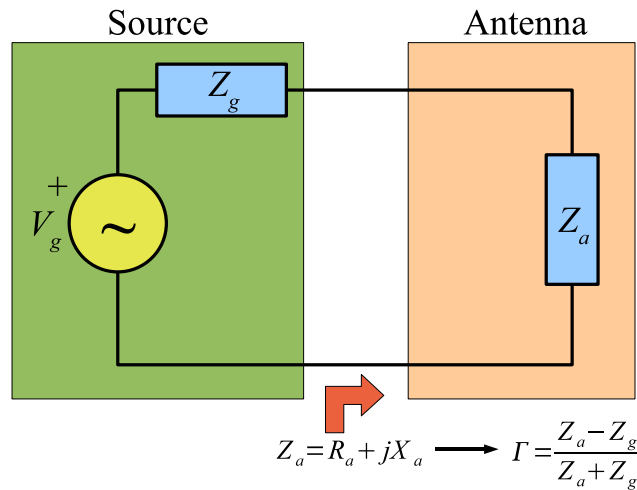
Figure 6.2: Sketch of an antenna system.

The reflection coefficient should ideally be equal to 0 (or $-\infty$ in logarithmic scale) when perfect matching between the antenna and the source is achieved. The antenna is considered to be properly matched when the reflection coefficient is under a threshold of $-L_{dB}$ at the frequency of operation. This fact is depicted in Figure 6.3, where the reflection coefficient S_{11} of a generic antenna is plotted as a function of the frequency.

Therefore, the fractional bandwidth (FBW) of an antenna for a given matching level $-L_{dB}$ is defined at the frequency of operation f_0 (or ω_0) as the relation between the frequencies f_1 and f_2, where $-L_{dB}$ cuts S_{11}, and f_0 as follows:
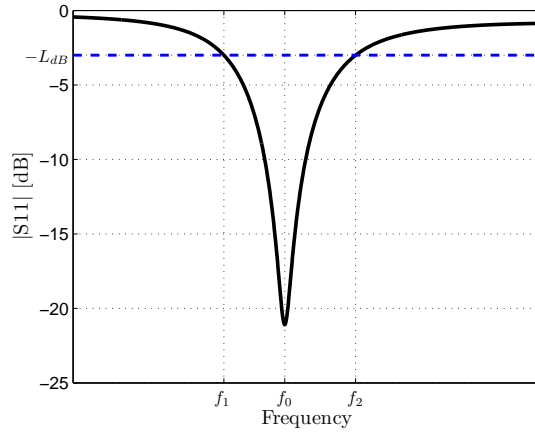
Figure 6.3: Direct FBW measurement.

$$FBW[\%] = \frac{f_2 - f_1}{f_0} 100$$

$$f_1 \equiv f|_{|S_{11}|_{dB}=-L_{dB}}, \ \ f_1 < f_0 \tag{6.5}$$

$$f_2 \equiv f|_{|S_{11}|_{dB}=-L_{dB}}, \ \ f_2 > f_0$$

This method to retrieve the FBW is referred to as the direct method (DM). However, if the antenna is not properly matched at the frequency of operation f_0, a matching network could be used to tune the antenna at f_0. In this way, the antenna could be simply tuned at a frequency ω_0 with a series reactance $X_s(\omega)$ as:

$$X_0(\omega) = X_a(\omega) + X_s(\omega), \tag{6.6}$$

where the series reactance $X_s(\omega)$ is comprised of either a series inductance L_s or a series capacitance C_s with a value of:

$$X_s(\omega) = \begin{cases} \omega L_s & \text{if } X_a(\omega_0) < 0 \\ -1/(\omega C_s) & \text{if } X_a(\omega_0) > 0 \\ 0 & \text{if } X_a(\omega_0) = 0 \end{cases} \tag{6.7}$$

to make the total reactance $X_0(\omega)$ equal 0 as:

$$X_0(\omega_0) = X_a(\omega_0) + X_s(\omega_0) = 0, \tag{6.8}$$

where $X_a(\omega)$ is the antenna reactance. This situation is depicted in Figure 6.4.

Once the antenna is made resonant $X_0(\omega_0) = 0$, the maximum Fractional Bandwidth (FBW) for ω_0 is directly computed using (6.5). This matching process is only valid at the tuned frequency ω_0. In this way, to retrieve the FBW over an entire frequency
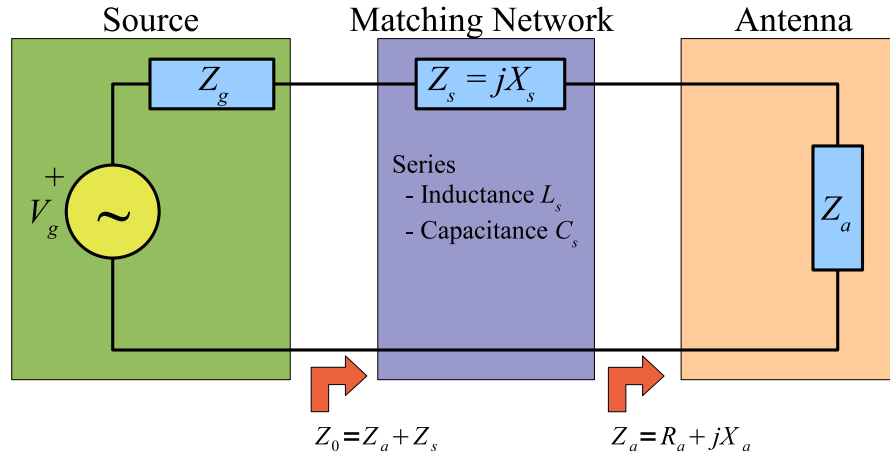
Figure 6.4: Sketch of an antenna system with a matching network.

band, this procedure needs to be applied to every single frequency value contained in the frequency band.

Furthermore, Yaghjian and Best [104] introduced a compact formulation for the calculation of the maximum fractional bandwidth FBW_{max} of single port antennas. This formulation is referred as the Yaghjian and Best method (YBM) and it is introduced in (6.9):

$$FBW_{max}(\omega_0) \equiv FBW(\omega_0) \approx \frac{4\sqrt{\beta}R_0(\omega_0)}{\omega_0|Z_0'(\omega_0)|}, \quad \text{with } \sqrt{\beta} = \frac{S-1}{2\sqrt{S}} \leq 1 \qquad (6.9)$$

where S is the desired $VSWR$ value (equivalent to the desired matching level $-L_{dB}$), R_0 is the antenna input resistance after tuning ($R_0 = R_a$), Z_0' is the first derivative with respect to frequency of the antenna input impedance after tuning, and ω_0 is the frequency at which the antenna is being tuned. Equation (6.9) holds for tuned antennas under the sufficient conditions that $X_0'(\omega)$ and $R_0'(\omega)$ do not change greatly over the bandwidth. One advantage of this formulation is that the FBW_{max} can be obtained even at frequencies where the antenna is not actually matched. One limitation of this formulation is that the reference impedance of the source Z_g needs to be changed to $Z_g(\omega_0) = R_0(\omega_0)$ at each frequency ω_0. However, this could be done with the inclusion of a matching network between the antenna and the source.

This formulation could be applied to retrieve the FBW_{max} across a frequency band by simply tuning the antenna at each frequency ω_0 in the frequency band of interest. This methodology is equivalent to directly retrieving the FBW from the reflection coefficient S_{11} after tuning the antenna at ω_0, as in the Direct Maximum FBW Method, while using the antenna resistance R_a as reference impedance $Z_{ref}(\omega_0) = R_0(\omega_0) = R_a(\omega_0)$, and repeating the process for each frequency across the frequency band. A

sketch showing these two procedures is depicted in Figure 6.5.
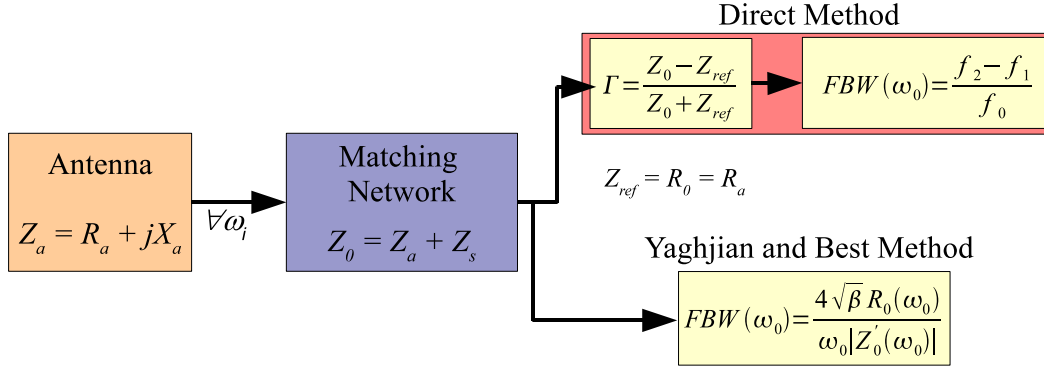
Figure 6.5: Direct and Yaghjian and Best methods to retrieve the maximum FBW of an antenna.

6.3 Homogeneous Substrate Patch Antenna Analysis

A patch antenna operating around $f_0 = 2.45$ GHz (ISM band) is used as reference to compare the FBW_{max} and the antenna miniaturisation factor when using homogeneous magneto-dielectric substrates. The patch antenna has a square shape $L = W = 53.7$ mm, and the size of the ground plane is $\lambda_0 \times \lambda_0$, being $L_{gp} = W_{gp} = \lambda_0 = 122.5$ mm. The patch antenna substrate has the same dimensions as the patch, with a height $h = 3$ mm over the ground plane. The patch antenna is fed through a coaxial probe placed at a certain distance $x_0 = 10.1$ mm from the centre of the patch. A sketch of the designed patch antenna for the HFSS simulations is shown in Figure 6.6, where the main dimension parameters are indicated.

The simulated reflection coefficient and input impedance results of the patch antenna for the air case ($\varepsilon_r = \mu_r = 1$) operating at 2.45 GHz are plotted in Figure 6.7. The reference impedance for the S_{11} plot is $Z_{ref} = 50\Omega$.

The FBW can be retrieved simply with the use of (6.5) because the antenna is tuned at 2.45 GHz, that is, $X_0(2.45 \text{ GHz}) = 0$. Retrieved values of FBW are presented in Table 6.1 applying different matching levels $-L_{dB}$. It is derived that the FBW decreases as the matching level increases, as expected.

Matching level $-L_{dB}$	$f_0[GHz]$	$f_1[GHz]$	$f_2[GHz]$	FBW[%]
-3	2.45	2.32	2.60	11.43
-6	2.45	2.37	2.54	6.94
-10	2.45	2.41	2.49	3.26

Table 6.1: FBW of the reference antenna for different values of matching level $-L_{dB}$.
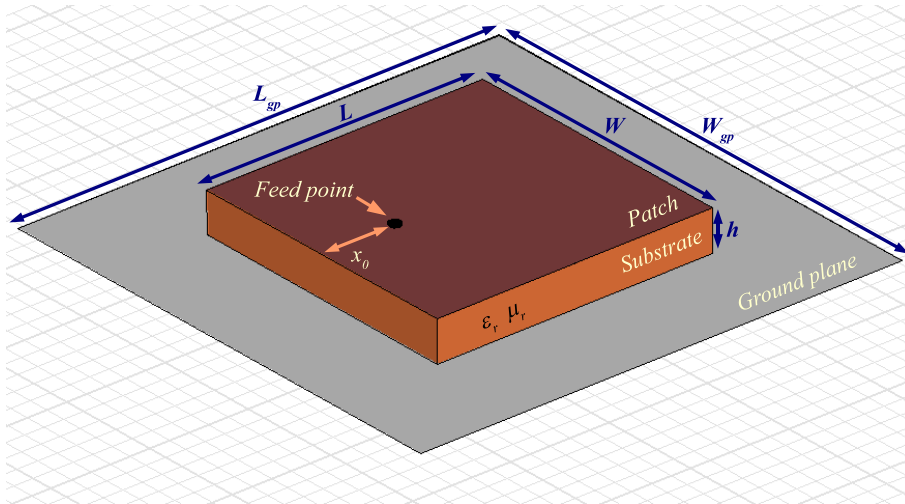
Figure 6.6: Sketch of a square microstrip patch antenna.
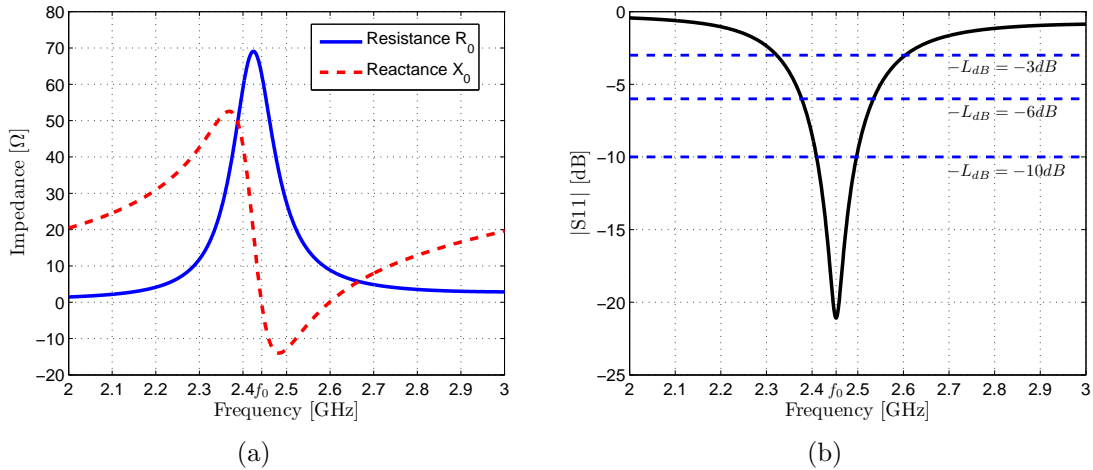
Figure 6.7: Input impedance Z_0 (left) and reflection coefficient S_{11} (right) for the
2.45GHz patch antenna. The patch antenna dimensions are: patch length
$L = 53.7$mm, substrate height $h = 3$ mm, probe position at $x_0 = 10.1$ mm,
and ground plane length $L_{gp} = 122.5$mm.

The two FBW retrieval methods presented before are applied to check for the maximum FBW at and around 2.45 GHz. The direct method (DM) and Yaghjian and Best method (YBM) are compared for three different patch antenna substrates: air ($\varepsilon_r = \mu_r = 1$), dielectric material ($\varepsilon_r = 3, \mu_r = 1$) and magnetic material ($\varepsilon_r = 1, \mu_r = 3$). In [104], they state that the YBM properly works given a minimum matching level of -3 dB. The FBW results for two different matching levels, -3 dB and -10 dB, are presented in Figure 6.8.

Some small disagreements appear between both methods, mostly for a matching level of -3 dB for all three different substrates. In general, the Yaghjian and Best method provides a FBW value slightly lower than the direct method. Therefore, from
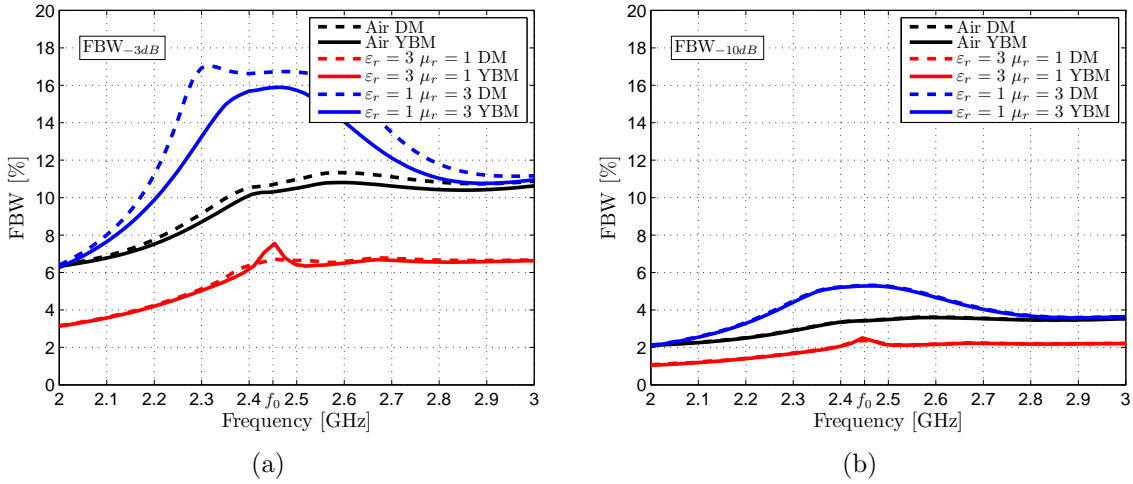
Figure 6.8: Comparison between direct (dashed line) and Yaghjian and Best (solid line) maximum FBW methods. Two matching levels are used: -3 dB (left) and -10 dB (right). DM denotes direct method, and YBM denotes Yaghjian and Best method.

now on the Yaghjian and Best FBW method will be used to retrieve the FBW of patch antennas due to its simplicity, while considering as well a matching level of -10 dB.

6.3.1 Substrate parameters variation

The patch antenna substrate material parameters, that is, the relative electric permittivity ε_r and the relative magnetic permeability μ_r, are swept between 0 and 10 within the product factor $n^2 = \varepsilon_r \mu_r$ in three different ways: ε_r variation only, μ_r variation only, and both. The FBW results computed for three cases are presented in the following subsections.

6.3.1.1 Electric permittivity variation

High permittivity (high-ε_r) materials are easily found in nature, such as glass or water. However, many high-ε_r present high losses at microwave frequencies. In this way, low loss laminates with moderate permittivity values are widely used for high frequency applications (e.g. Rogers Corporation laminates). A list of different dielectric materials is presented in Table 6.2, showing their relative permittivity value ε_r and their losses in terms of $tan\, \delta_e$.

On the other hand, materials with permittivity values close to 0, the so called epsilon-near-zero (ENZ) materials with $0 < \varepsilon_r < 1$, are hard to find in nature. Metamaterials composed of metallic wires embedded in a host medium offer negative and near-zero permittivity values, although they suffer from frequency dispersion [1].

The reference patch antenna is simulated with HFSS, by varying the substrate di-

Material	ε_r	$\tan \delta_e$
Air	1.0006	-
Dry wood	1.5-4	0.01
Teflon	2.1	0.0003
Rogers RT/Duroid 5880	2.2	0.001
Paper	3	0.008
Rogers RO4003C	3.38	0.0027
Fiberglass FR4	4.4	0.02
Porcelain	6	0.0014
Rogers RO3010	10.2	0.0023
Distilled Water	80	0.04
Sea Water	81	4.64

Table 6.2: Dielectric constants of typical dielectric materials.

electric constant $0 < \varepsilon_r < 10$ while maintaining $\mu_r = 1$. Simulated results of S_{11} and computed FBW_{max} are plotted in Figure 6.9.

Figure 6.9: Simulated reflection coefficient S_{11} and computed FBW_{-10dB} for a patch antenna substrate permittivity variation $0 < \varepsilon_r < 10$.

When increasing the ε_r value from 1 to 10, the bandwidth is dramatically decreased, as expected [99]. This fact is seen in the narrower dips in S_{11} results. However, better FBW results are obtained with $0 < \varepsilon_r < 1$, which improve the result for the air case, at the cost of increasing the patch antenna size. At 2.45GHz, the FBW for the air case is about 3.3%, whereas it is only 1.1% for $\varepsilon_r = 9$ and about 6.7% for $\varepsilon_r = 0.25$. A list with the FBW value and the patch antenna size at 2.45GHz for all cases is listed in Table 6.3.

ε_r	FBW$_{-10dB}$(2.45GHz)[%]	L[mm]
0.25	6.7	80.85
0.5	4.6	67.53
0.75	3.7	59.37
1	3.3	53.71
2	2.5	41.75
3	2.1	35.40
4	1.8	31.32
5	1.6	28.50
9	1.1	22.08

Table 6.3: Computed FBW$_{-10dB}$ at $f_0 = 2.45$GHz for $0 < \varepsilon_r < 10$ ($\mu_r = 1$).

6.3.1.2   Magnetic permeability variation

The study of the FBW of a patch antenna loaded with high-μ_r might be interesting due to the high FBW reported [99], although materials having a μ_r value different to unity (non-magnetic) at microwave frequencies are not naturally found in nature. Engineered magnetic metamaterial designs can offer $\mu_r \neq 1$, in spite of their dispersive behaviour and high losses at the resonance. Ferrites are one of the natural materials offering a high-μ_r property, although they are only useful when operating in MHz frequencies due to their high losses in GHz frequencies.

The reference patch antenna is simulated using HFSS, varying the substrate relative magnetic permeability constant $0 < \mu_r < 10$ while maintaining $\varepsilon_r = 1$. Simulated results of S_{11} and computed FBW$_{max}$ are plotted in Figure 6.10.

(a)   (b)
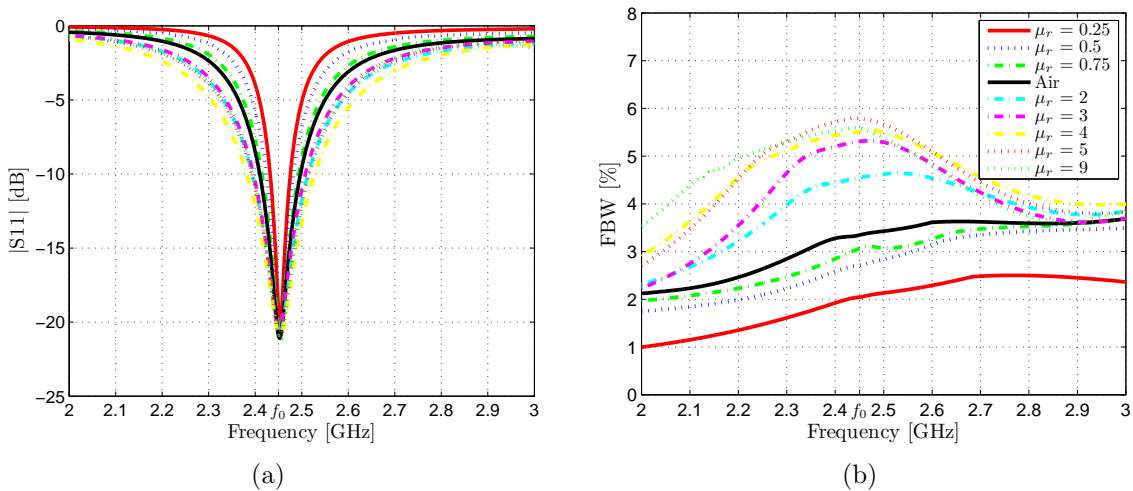
Figure 6.10: Simulated reflection coefficient S_{11} and computed FBW$_{-10dB}$ for a patch antenna substrate permittivity variation $0 < \mu_r < 10$.

From the simulated results, the FBW is generally increased for high-μ_r values, as expected, resulting in efficient patch antenna miniaturisation. Note that significant

FBW improvement is observed for moderate values of μ_r, and has its maximum level for $\mu_r \geq 4$. On the other hand, for $0 < \mu_r < 1$ values, whihc implies a larger patch antenna size, the FBW is lower than the air case. For $\mu_r = 9$, the FBW at 2.45GHz is about 5.5%, whereas for $\mu_r = 0.25$ is about 2%. A complete list of FBW and patch antenna size at 2.45GHz for all cases is presented in Table 6.4.

μ_r	FBW$_{-10dB}$(2.45GHz)[%]	L[mm]
0.25	2.0	108.70
0.5	2.7	74.43
0.75	3	60.80
1	3.3	53.71
2	4.4	41.25
3	5.3	35.92
4	5.5	34.05
5	5.8	31.70
9	5.6	28.65

Table 6.4: Computed FBW$_{-10dB}$ at $f_0 = 2.45$GHz for $0 < \mu_r < 10$ ($\varepsilon_r = 1$).

6.3.1.3 Electric permittivity and magnetic permeability variation

In most cases, a metamaterial substrate would present both ε_r and μ_r. For this reason, FBW analysis varying both material parameters is performed. In addition, if $\varepsilon_r = \mu_r$ condition is fulfilled, the antenna substrate would be matched to free space while reducing the reflections between the antenna substrate and the surrounding medium. Despite the losses at GHz frequencies, the $\varepsilon_r = \mu_r$ condition can be achieved by using ferrites [105]. Simulated S_{11} and computed FBW$_{max}$ results for $0 < \varepsilon_r \cdot \mu_r < 10$ with $\varepsilon_r = \mu_r$ are plotted in Figure 6.11.

From the results, it is extracted that the FBW has a similar value for all case, although the patch antenna size is miniaturised as the product $\varepsilon_r \cdot \mu_r$ increases, as expected. For $0.75 \leq \varepsilon_r \cdot \mu_r \leq 3$ the FBW at 2.45GHz is similar to the air case, and for $\varepsilon_r \cdot \mu_r = 0.25$ is slightly better than the air case. Although high-μ_r values might improve the FBW, its combination with high-ε_r leads to a moderate FBW reduction. A list of FBW and the patch antenna size at 2.45GHz is presented in Table 6.5.

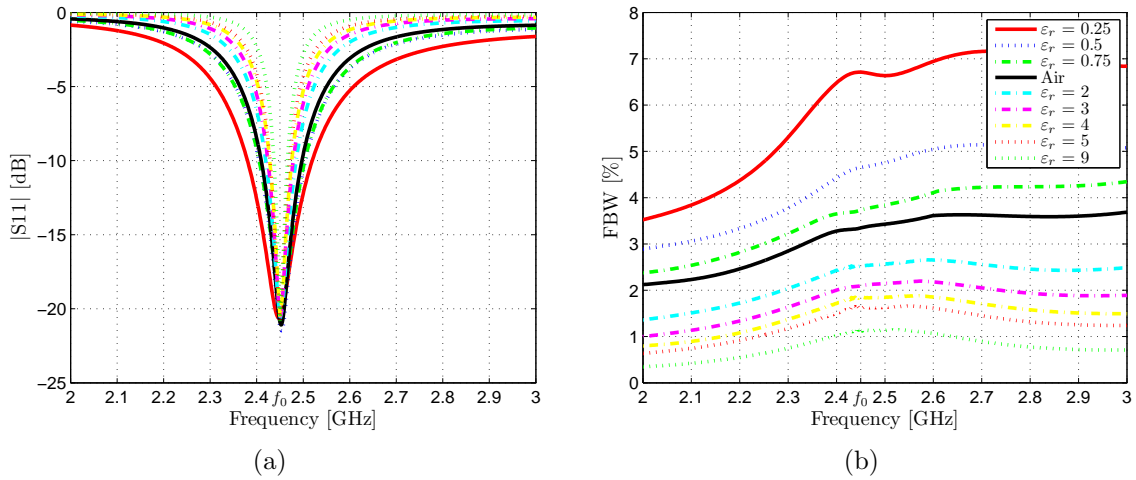(a)   (b)
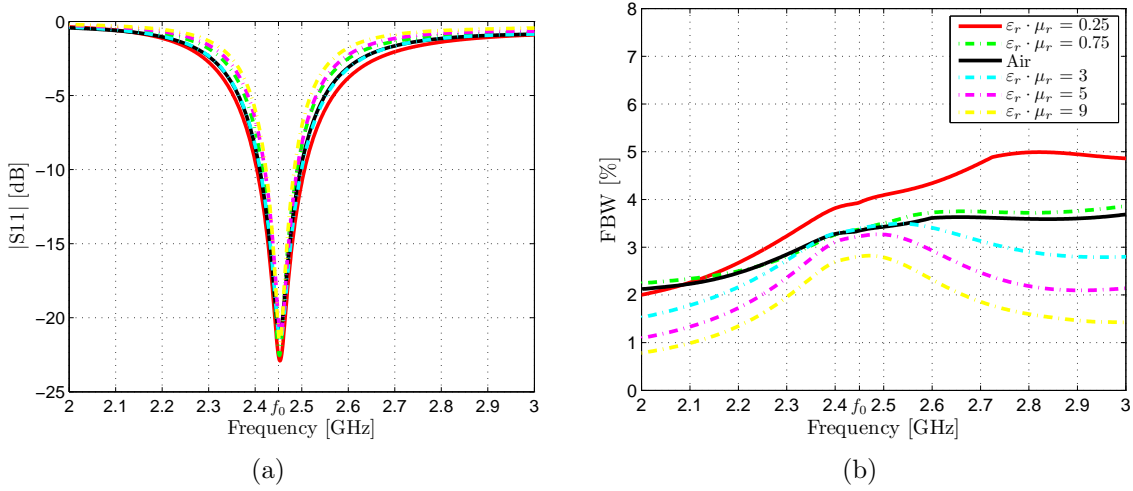
Figure 6.11: Simulated reflection coefficient S_{11} and computed FBW$_{-10dB}$ for a patch
              antenna substrate electric permittivity and magnetic permeability varia-
              tion $0 < \varepsilon_r \cdot \mu_r < 10$ with $\varepsilon_r = \mu_r$.

$\varepsilon_r \cdot \mu_r$	FBW$_{-10dB}$(2.45GHz)[%]	L[mm]
0.25	3.9	98.70
0.75	3.4	60.60
1	3.3	53.71
3	3.4	35.62
5	3.2	29.40
9	2.8	24.00

Table 6.5: Computed FBW$_{-10dB}$ at $f_0 = 2.45$GHz for $0 < \varepsilon \cdot \mu_r < 10$ ($\varepsilon_r = \mu_r$).

6.3.2   Losses in the Patch Antenna Substrate

Lossless material parameters have been used in the previous simulations, that is,
only the real parts of the relative electric permittivity $\varepsilon_r = Re\{\varepsilon_r\}$ and those of the
relative magnetic permeability $\mu_r = Re\{\mu_r\}$ have been considered in the patch an-
tenna substrate. Note that losses in the electric permittivity ε_r and in the magnetic
permeability μ_r are denoted as electric loss tangents $tan\,\delta_e$ and magnetic loss tangents
$tan\,\delta_m$, respectively. Therefore, the lossy material parameters should have the form of
equations (6.10) and (6.11).

$$\varepsilon_r \equiv Re\{\varepsilon_r\} + jIm\{\varepsilon_r\} = Re\{\varepsilon_r\}(1 + j\frac{Im\{\varepsilon_r\}}{Re\{\varepsilon_r\}}) = Re\{\varepsilon_r\}(1 + jtan\,\delta_e) \qquad (6.10)$$

$$\mu_r \equiv Re\{\mu_r\} + jIm\{\mu_r\} = Re\{\mu_r\}(1 + j\frac{Im\{\mu_r\}}{Re\{\mu_r\}}) = Re\{\mu_r\}(1 + jtan\,\delta_m) \qquad (6.11)$$

In order to study the effect of substrate losses in the computed FBW, two patch antennas with $Re\{\varepsilon_r\} = 2$ and $Re\{\mu_r\} = 2$ are considered for different values of $tan\,\delta_e$ and $tan\,\delta_m$. The simulated S_{11} and computed FBW results are plotted in Figure 6.12 for the electric loss tangent, and in Figure 6.13 for the magnetic loss tangent, while varying their values between 0 and 0.1.
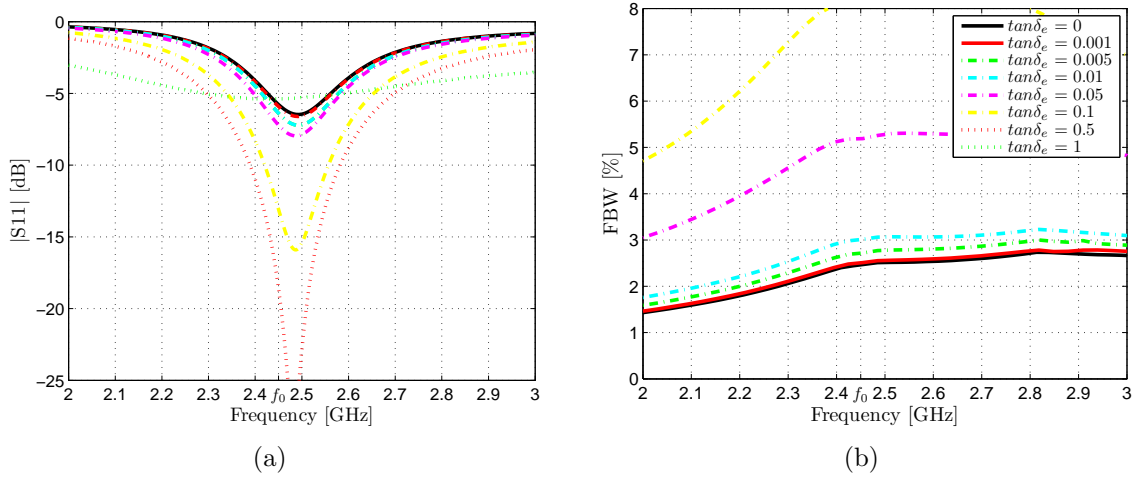
Figure 6.12: Simulated S_{11} (left) and computed FBW_{-10dB} (right), when varying $tan\,\delta_e$ between 0 and 1. $Re\{\varepsilon_r\} = 2$.
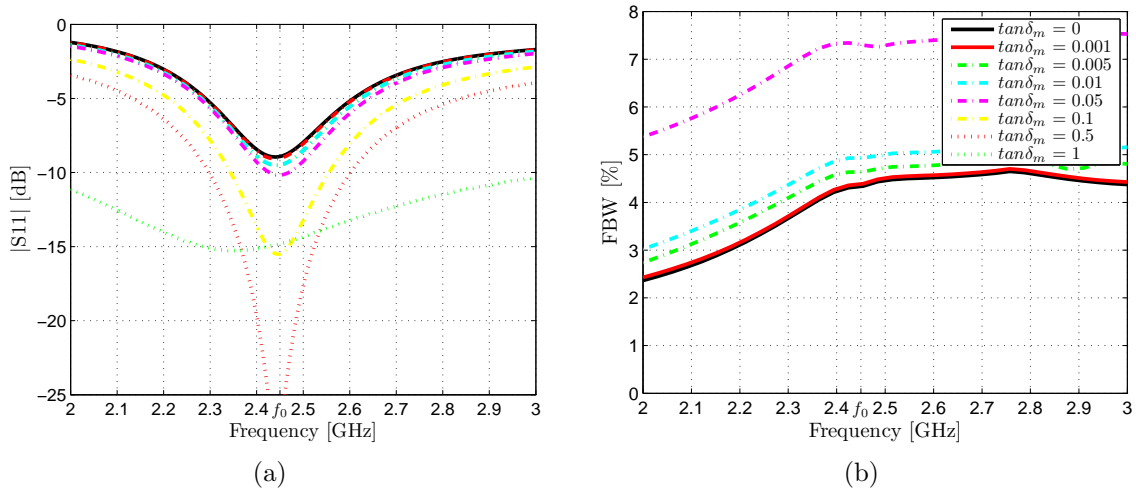
Figure 6.13: Simulated S_{11} (left) and computed FBW_{-10dB} (right), when varying $tan\,\delta_m$ between 0 and 1. $Re\{\mu_r\} = 2$.

These results clearly show that the FBW is higher when either the dielectric or magnetic losses are increased. The FBW is significantly increased when the loss tangent value is higher than 0.05 for both dielectric and magnetic cases. This is a common effect in all kind of antennas; when increasing the losses, the antenna is better matched, although the radiation efficiency may be decreased. In addition, a list with FBW results and radiation efficiencies η_{rad} is presented in Table 6.6. In both cases, it is

observed that the radiation efficiency decreases as the loss tangents ($tan\,\delta_e$, $tan\,\delta_m$) in the patch antenna substrate increase, although this also results in a higher FBW.

$tan\,\delta_e$	FBW$_{-10dB}$[%]	η_{rad}	$tan\,\delta_m$	FBW$_{-10dB}$[%]	η_{rad}
0	2.5	1.00	0	4.4	1.00
0.001	2.5	0.99	0.001	4.4	0.99
0.005	2.7	0.91	0.005	4.6	0.94
0.01	3	0.83	0.01	4.9	0.89
0.05	5.2	0.49	0.05	7.3	0.62
0.1	8.1	0.32	0.1	10.8	0.44

Table 6.6: Computed antenna FBW$_{-10dB}$ and radiation efficiencies (η_{rad}) for the electric (left) and magnetic (right) loss tangent variations.

6.3.3 Discussion on Bandwidth and Patch Antenna Miniaturisation

Besides the three cases under study, that is, ε_r variation, μ_r variation and $\varepsilon_r = \mu_r$ variation, the computed FBW results can be grouped into two categories, depending on the values of substrate parameters: near zero values ($0 < \varepsilon_r \cdot \mu_r \leq 1$) and high values ($1 < \varepsilon_r \cdot \mu_r < 10$). The FBW results plotted in Figure 6.14 confirm that high FBW values are obtained for $0 < \varepsilon_r < 1$ and for high-μ_r values, which are the maximum values for each category. In this way, the complementary FBW behaviour of ε_r and μ_r substrates depending on the $\varepsilon_r \cdot \mu_r$ values is clearly seen. Moreover, the use of magneto-dielectric substrates with $\varepsilon_r = \mu_r$ offers a moderate FBW increase with respect to the air case ($\varepsilon_r = \mu_r = 1$), although this case could be considered as a more realistic metamaterial substrate.

The FBW results at 2.45 GHz obtained when varying the substrate effective material parameters are summarised in Figure 6.15. The FBW results for the three cases are compared with the approximated FBW results obtained using the Hansen and Burke formula [99], which is defined as the zero-order Fractional Bandwidth of a patch antenna with a Magneto-Dielectric (MD) substrate with a thickness h, which is said to be valid for $1 \leq (\varepsilon_r, \mu_r) \leq 10$, and considering a $VSWR = 2$ ($\Gamma \approx -10$ dB):

$$FBW_{-10dB} \approx \frac{96\sqrt{\mu_r/\varepsilon_r}}{\sqrt{2}[4 + 17\sqrt{\varepsilon_r\mu_r}]}\frac{h}{\lambda_0} \tag{6.12}$$

It is seen that the simulated FBW results are lower than the FBW results obtained with (6.12), in particular for the Air case and for μ_r variation, and a good results agreement is only seen for high-ε_r and high $\varepsilon_r = \mu_r$ values. This may be due to the fact that the patch antenna substrate used in the simulations has the size of the patch
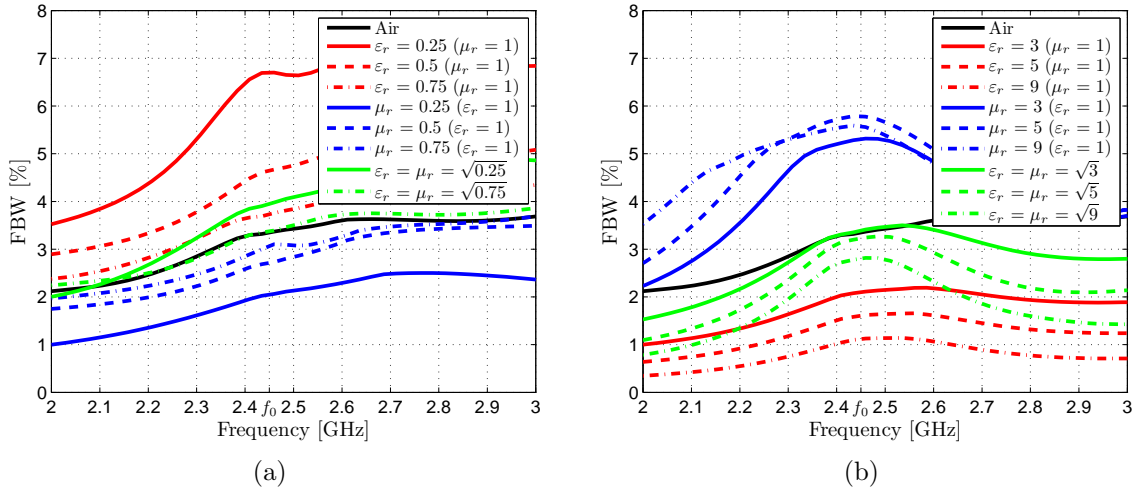
Figure 6.14: Computed FBW$_{-10dB}$ results for substrate parameters between $0 < \varepsilon_r \cdot \mu_r \leq 1$ (left) and $1 < \varepsilon_r \cdot \mu_r < 10$ (right).

antenna, which may lead to lower FBW results when compared with a ground plane sized substrate. However, this would not explain the discrepancy with the Air case, where the simulated and calculated FBWs are 3.4% and 8%, respectively.
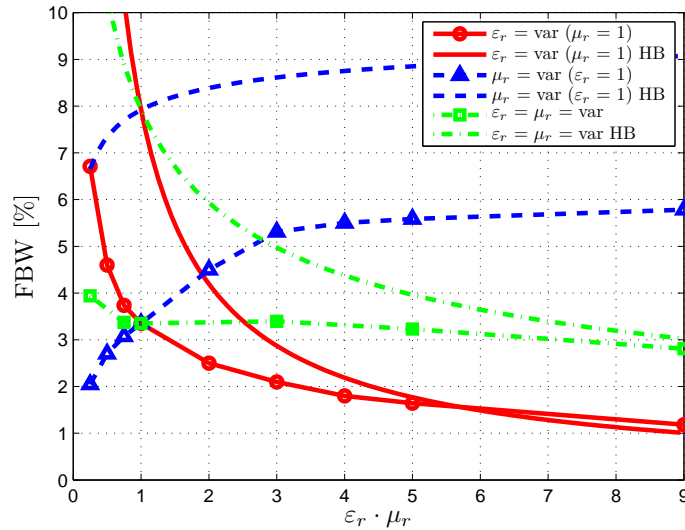
Figure 6.15: Computed FBW$_{-10dB}$ results as a function of $\varepsilon_r \cdot \mu_r$ values, and comparison with Hansen and Burke (HB) formula (6.12).

Despite the disagreements with the Hansen and Burke approximated FBW formula, high FBW values are achieved for high-μ_r values, as expected, and for $0 < \varepsilon_r < 1$ (ENZ) at the expense of an increase in the patch size. These high FBW values may be due to the high value of the substrate impedance, from which is derived that the FBW is proportional to the substrate impedance, as derived in (6.13). This fact has been also pointed out in [106], where it is concluded that the use of magnetic material substrates results in a smaller amplitude of the current induced to the antenna when

compared with dielectric substrates. This is equivalent to affirming that the antenna input impedance is bigger when using magnetic materials compared to dielectric materials, reducing the energy stored in the antenna and leading to a decreased quality factor, and therefore a higher FBW.

$$FBW_{-10dB} \propto Z_{substrate}/\eta_0 \approx \sqrt{\frac{\mu}{\varepsilon}}/\eta_0 = \sqrt{\frac{\mu_0\mu_r}{\varepsilon_0\varepsilon_r}}/\eta_0 = \sqrt{\frac{\mu_r}{\varepsilon_r}} \tag{6.13}$$

Moreover, a patch antenna is approximately miniaturised as the value of $n = \sqrt{\varepsilon_r\mu_r}$ increases, as stated in (6.1). This fact is confirmed when plotting the patch antenna size L when varying the substrate material parameters ε_r and μ_r. The patch antenna length L_{patch} results are compared with the patch antenna sizes obtained in the simulations for a matched antenna at 2.45 GHz by considering the effective material parameters variations reported for the patch antenna substrate. The results are presented in Figure 6.16.

(a) Linear scale   (b) Logarithmic scale
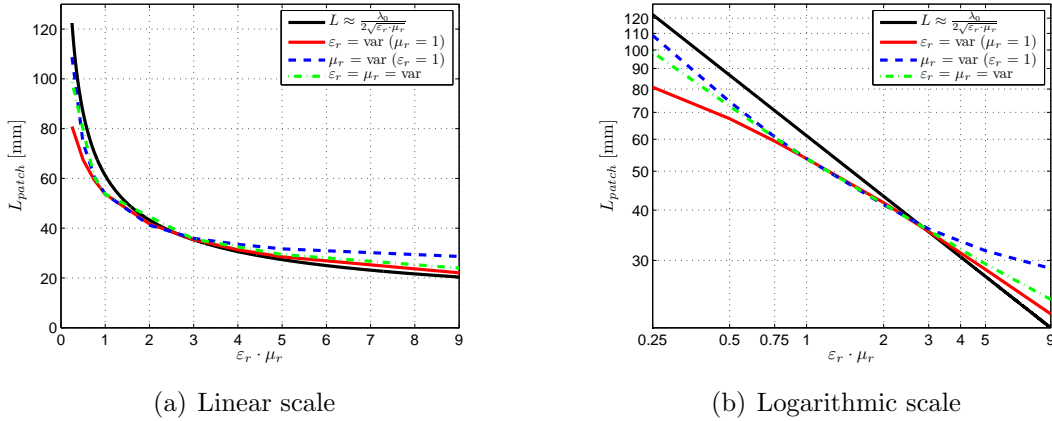
Figure 6.16: Patch size L_{patch} variation for different values of $n^2 = \varepsilon_r\mu_r$.

From these results, it is seen that the patch antenna size is reduced when increasing $\varepsilon_r \cdot \mu_r$ factor, although some discrepancies appear for very low and very high values with respect to the reference value given in (6.1). Even the Air case response is not well approximated with the reference patch size formulation; this fact is clearly seen in the logarithmic scale. A simple update of (6.1) is presented in (6.14), in order to better adjust the formula to the retrieved patch size responses when varying the patch antenna substrate:

$$L_{adjusted} \approx \frac{\lambda_0}{2.7\sqrt{\varepsilon_r\mu_r}} + 0.009 \tag{6.14}$$

As seen in Figure 6.17, previous results are now compared with the adjusted patch size reference $L_{adjusted}$. Although some disagreements are still observed for very low

values of electric permittivity ($\varepsilon_r < 0.75$) and for high values of magnetic permeability ($\mu_r > 3$), the reference patch size is better matched using the new approximated formula.

(a) Linear scale

(b) Logarithmic scale
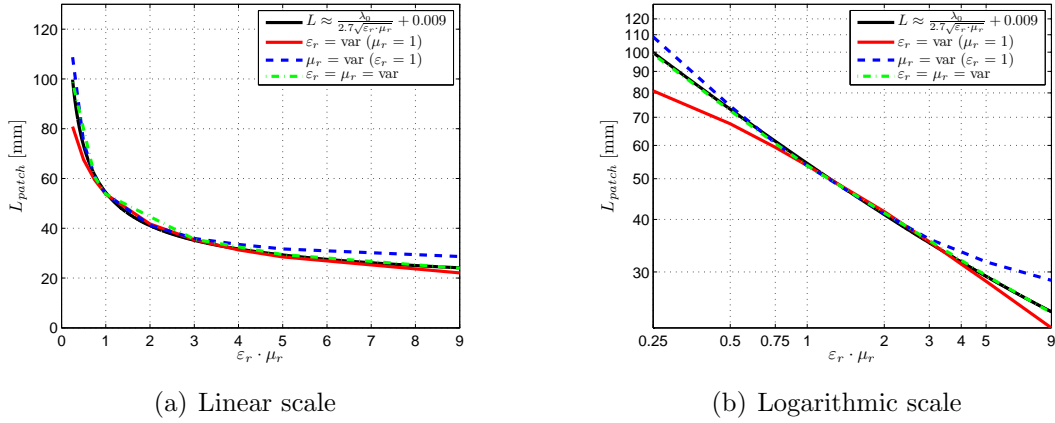
Figure 6.17: Adjusted patch size L_{patch} variation for different values of $\varepsilon_r \cdot \mu_r$.

6.4 Patch Antennas with Dispersive Metamaterial Loadings

In the previous section, the FBW of a patch antenna with an homogeneous and non-dispersive metamaterial substrate has been analysed, showing a FBW enhancement for $0 < \varepsilon_r < 1$ and for high-μ_r, although efficient antenna miniaturisation is only achievable with the latter patch antenna substrate.

Besides the dielectric only substrates, fabricated metamaterial substrates present a dispersive lossy magneto-dielectric behaviour. Different types of magneto-dielectric designs for patch antenna substrates, the so called metasubstrates, are found in literature such as the metasolenoid (composed of densely packed SRRs) [107,108], the spiral resonators (SRs) [109,110], the spiral Hilbert inclusions [111], the wire media embedded in a ferrite substrate [112], or the defected ground structure (DGS) composed of complementary SRRs [113].

The SR AMM slab presented in Chapter 3 will be used as a metasubstrate to miniaturise patch antennas by taking advantage of its μ-dispersive behaviour. Therefore, the design of a patch antenna with SR AMM metasubstrate and its performance as Magneto-Dielectric Patch Antenna will be numerically and experimentally assessed in this section.

6.4.1   SR AMM Design as a Metasubstrate

The SR AMM design that will be used as the patch antenna substrate is the same design as in Chapter 3, but with slightly enlarged unit cell dimensions along the xz-plane from 6 to 10 mm due to latter implementation purposes. The SR design and the main dimension parameters are shown in Figure 6.18. The spiral resonator width $lz2$ is 5.6 mm, the unit cell width $t2$ and height $h2$ are now 10 mm, and the remaining dimensions are the same as the former SR AMM design, which is also depicted in Figure 6.18. The former SR design is referred to as SR AMM, whereas the SR design with enlarged unit cell is referred to from now on as SR2 AMM.
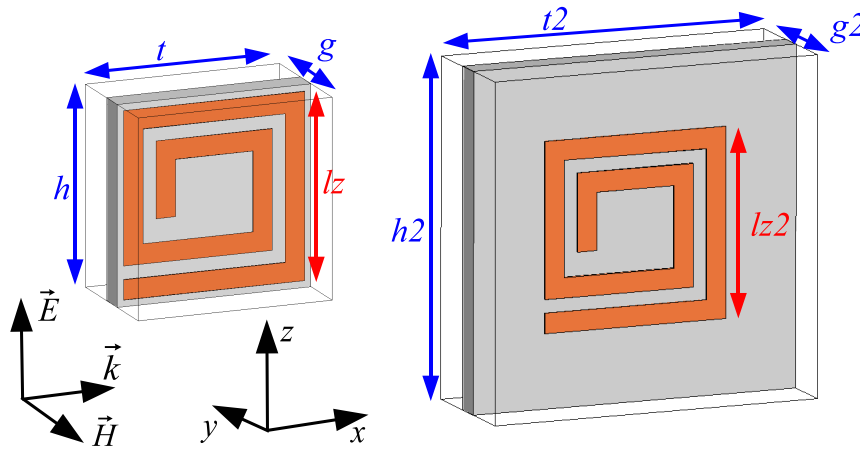
Figure 6.18: SR and SR2 AMM designs. The unit cell dimensions of the SR2 AMM design are: $t2 = h2 = 10$ mm, $g2 = g = 4$ mm, and $lz2 = lz = 5.6$ mm. The spiral width is $lw = 0.6$ mm, the spiral gap is $lg = 0.4$ mm, and the dielectric substrate is the 0.8 mm thick RO4003C, with electric permittivity $\varepsilon_r = 3.38$, loss tangent $\tan \delta = 0.0027$, and a copper thickness of 18 μm.

The simulated S-parameter results for the SR and SR2 AMM designs are plotted in Figure 6.19, yielding very similar results. Remarkable differences between both designs are only seen in the resonant frequency, where the phase of the S_{11} crosses the 0° axis, which is slightly shifted from 2.6 GHz down to 2.55 GHz, and in the narrower reflection frequency band. However, transmission is significantly enhanced over the whole frequency range, mostly below the resonance. This would result in a weaker attenuation in the frequency region before the resonance where the magnetic permeability is expected to be $\mu_r > 1$.

The effective material parameters for both designs have been retrieved applying the Li method [70], which has already been used to characterise the SR AMM. The retrieved relative electric permittivity ε_r and magnetic permeability μ_r results are plotted in Figure 6.20. From these results, it is seen that the amplitude of the electric per-

(a) Magnitude of S_{ij} (b) Phase of S_{ij}
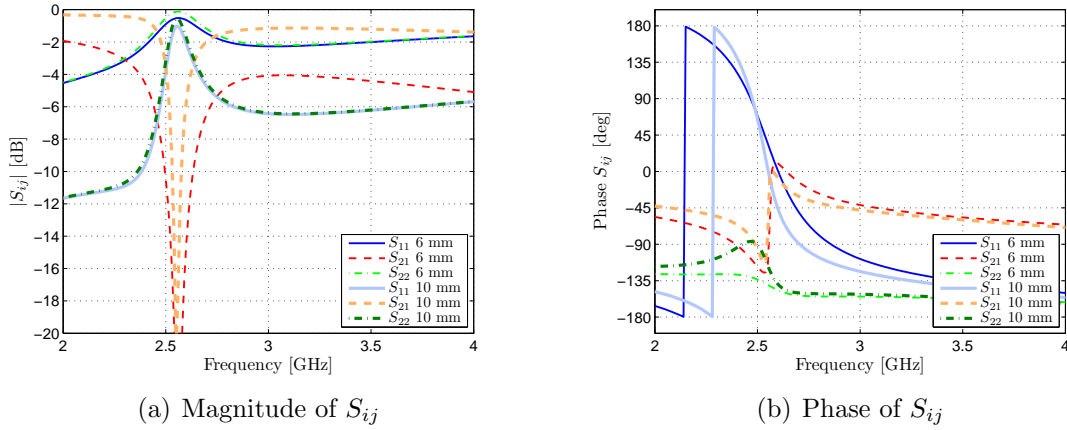
Figure 6.19: Simulated S-parameters for the SR and SR2 AMM designs.

mittivity resonance has been strongly reduced around 2.55 GHz, and the magnetic plasma frequency has been decreased from 3.1 GHz down to 2.7 GHz. However, the enlargement of the unit cell from 6 to 10 mm has little effect in the $\mu_r > 1$ region.

(a) Relative electric permittivity ε_r (b) Relative magnetic permeability μ_r
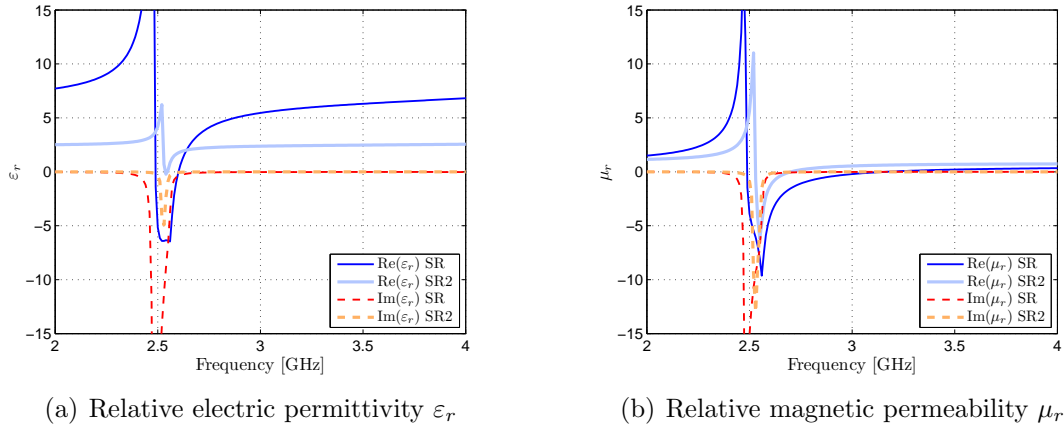
Figure 6.20: Retrieved relative electric permittivity ε_r and relative magnetic permeability μ_r results for the SR and SR2 AMM designs.

Moreover, the refraction index n_r and the magneto-electric coupling or bianisotropic parameter ξ_0, which is required to compute the refraction index as $n_r = \pm\sqrt{\varepsilon_r\mu_r - \xi_0^2}$, have been plotted in Figure 6.21. The decrease in magnetic plasma frequency produces a decrease in the frequency where the refraction index n_r is close to 0, from 3.3 GHz down to 2.74 GHz. Despite the slight differences between both designs, the SR2 AMM design preserves the $\mu_r > 1$ behaviour below the resonant frequency, that is, below 2.6 GHz.

(a) Magneto-electric coupling ξ_0 (b) Refraction index n_r
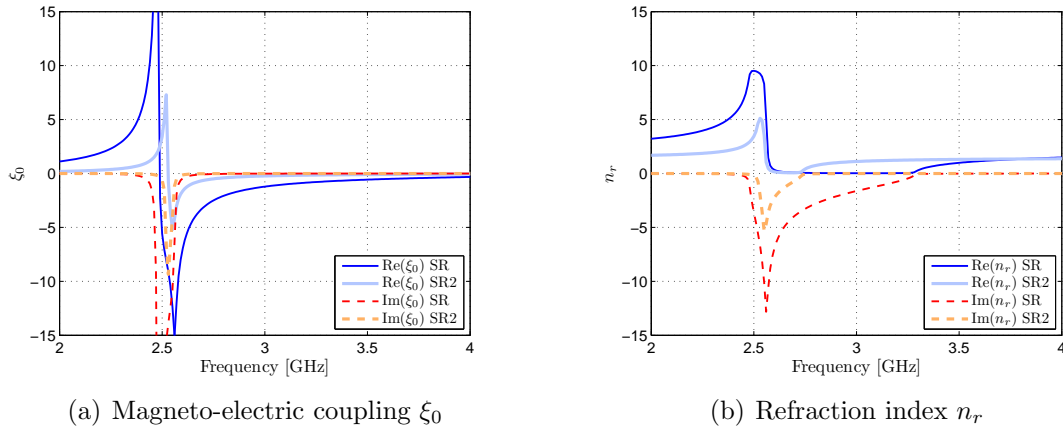
Figure 6.21: Retrieved magneto-electric coupling ξ_0 and refraction index n_r results for the SR and SR2 AMM designs.

6.4.2   Simulation of Patch Antennas with AMM Metasubstrates

A patch antenna with different metasubstrates has been designed and simulated with HFSS. The patch length L and width W are 40 mm, and the patch height h is 10 mm. The ground plane length L_{gp} and width W_{gp} are 250 mm. The patch antenna is coaxially fed through a metallic vias, and placed at several distances from the centre of patch: 1.5 mm, 6.5 mm, 11.5 mm and 16.5 mm; these feeding positions are named 1, 2, 3, and 4, respectively. A sketch of the designed patch antenna is presented in Figure 6.22.
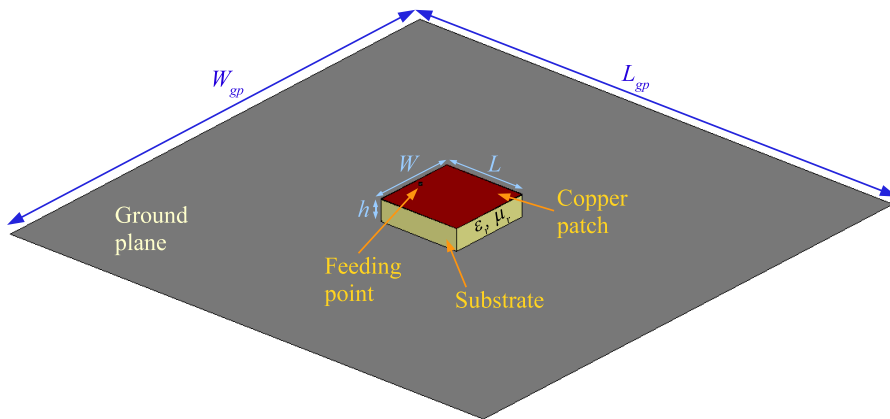
Figure 6.22: Sketch of the simulated patch antenna. The patch antenna dimensions are: $L_{gp} = W_{gp} = 250$ mm, $L = W = 40$ mm, $h = 10$ mm.

The simulated S_{11} results for the air ($\varepsilon_r = \mu_r = 1$) filled patch antenna are plotted in Figure 6.23. It is observed from the results that a poor matching is achieved for any feeding position; this may be due to the height of the patch antenna that makes the

coaxial vias take part in the input impedance of the patch antenna, thus increasing the antenna mismatch. The best result is found for the feeding position 4, yielding a matching level of -8 dB at 3.1 GHz.
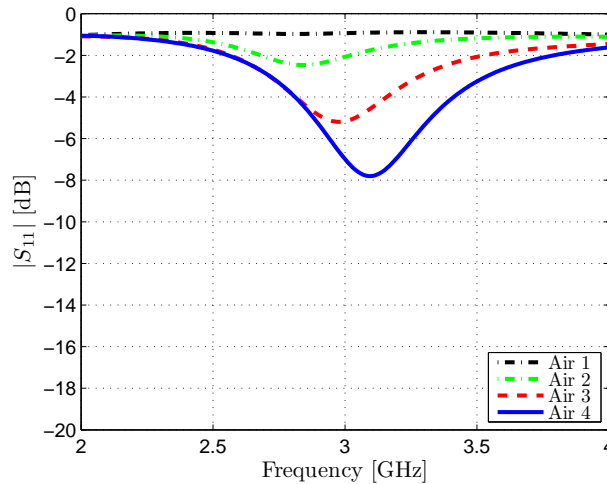
Figure 6.23: Simulated S_{11} results for the patch antenna filled with air, and for different feeding positions.

Then, the patch antenna is filled with a metasubstrate composed of 10 strips of SR2 AMM, forming a 40 mm $\times$ 40 mm metamaterial slab, as it is shown in Figure 6.24. Note that the gap between the metamaterial strips is filled with air.
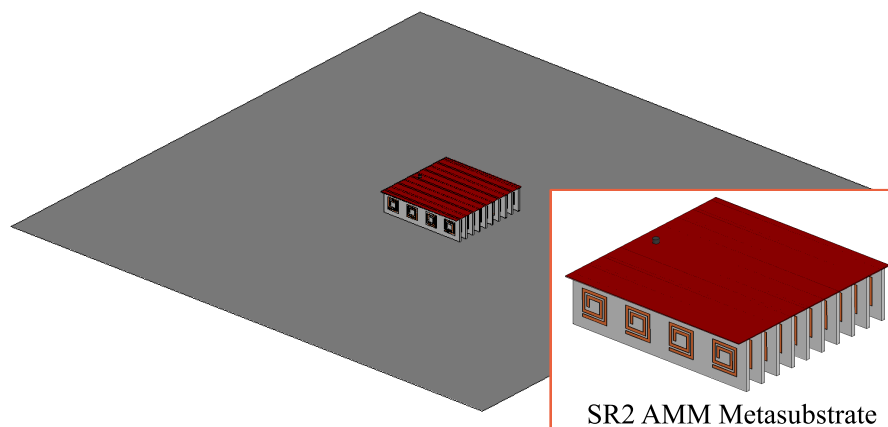
Figure 6.24: Sketch of the patch antenna with a SR2 AMM metasubstrate.

Simulated S_{11} results for the patch antenna filled with SR2 AMM using the feeding position 4 are plotted in Figure 6.25. This result is compared with other patch antenna fillings such as air, Rogers (only dielectric strips), and only SR2 resonators (embedded in air). The S_{11} results for the SR2 case present three different regions. There is a resonance of the patch antenna around 2.32 GHz, which corresponds with the $\mu_r >$

1 region of the SR2 AMM. Then, there is a noisy region around 2.6 GHz, which corresponds to the resonant behaviour of the SR2 AMM. Finally, there is a second resonance of the patch antenna around 3.1 GHz, which corresponds to the natural resonance of the patch antenna in air; this is probably due to the $n_r \approx 1$ of the SR2 AMM around 3.1 GHz.
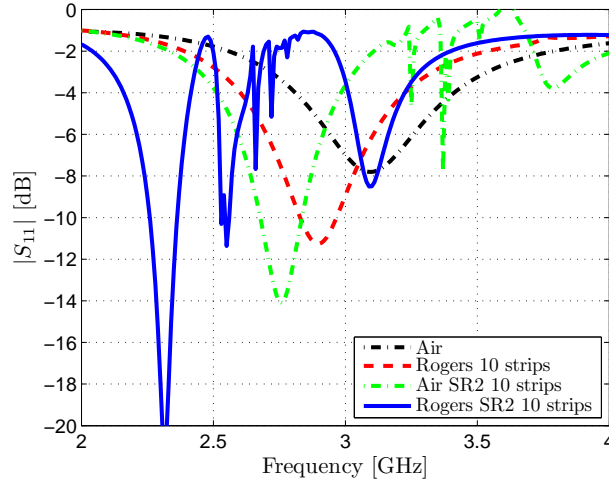
Figure 6.25: Simulated S_{11} results for the patch antenna filled with air, Rogers (only dielectric strips), SR2 (only metallic resonators), and SR2 AMM, for the feeding position 4.

Regarding the patch antenna performance, it is seen that the use of the SR2 AMM as metasubstrate decreases the operational frequency from 3.1 GHz down to 2.32 GHz, achieving a miniaturisation factor n of 1.34. Besides the patch antenna miniaturisation, the matching level is also improved when using the metasubstrate, at the expense of a FBW reduction. This FBW reduction is mainly due to the dispersive behaviour of the magneto-dielectric substrate, as stated in [102, 107]. In terms of effective parameters, the SR2 AMM substrate presents $\mu_r = 1.53$ and $\varepsilon_r = 2.66$ at 2.32 GHz; since $\varepsilon_r > \mu_r$, the antenna is miniaturised mostly due to the higher relative electric permittivity value, thus obtaining a reduced FBW, as seen before in Section 6.3.3. Detailed results for the different patch antenna loadings are listed in Table 6.7; note that in this case, since the patch antenna with the Air substrate has a minimum matching value of -8 dB, the FBW has been calculated at -6 dB for comparison purposes.

Another interesting property of the SR2 AMM metasubstrate is the small sensitivity of S_{11} to any 90° rotation angle of the spiral resonators around their axes, as seen in Figure 6.26 for the cases of 0° (SR2 S1), 90° (SR2 D1), 180° (SR2 S2), and 270° (SR2 D2). Note that a 180° rotation is equivalent to 0°, in the same way as for 90° and 270°.

This fact is also reflected in similar effective parameter results when rotating the spiral resonator, as shown in Figure 6.27 for the cases of 0° (SR2 S1) and 90° (SR2 D1);

Patch Antenna Loading	f_0[GHz]	FBW$_{-6dB}$[%]	Miniaturisation factor n
Air	3.1	10.26	1
Rogers	2.9	13.93	1.07
Air SR2	2.76	11.70	1.12
Rogers SR2	2.32	7.84	1.34

Table 6.7: Comparison of simulated results for the patch antenna with different material loadings.
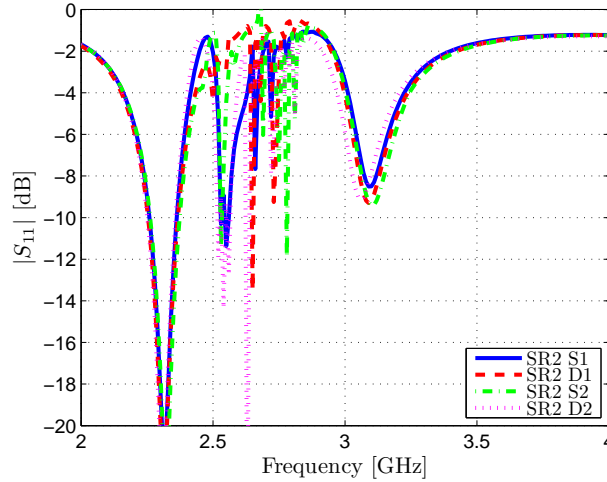
Figure 6.26: Simulated S_{11} results for the four orientations 0° (SR2 S1), 90° (SR2 D1), 180° (SR2 S2), and 270° (SR2 D2).

note that 180° rotation is equivalent to 0°, in the same way as for 270° with respect to 90°. Some minor discrepancies are observed for the relative electric permittivity ε_r results at the resonance, although they are invariant in the band of interest, in the same way as for the relative magnetic permeability μ_r and the refraction index n_r.

The patch antenna has also been simulated varying the number of metamaterial strips that compose the metasubstrate, from 0 (air) to 10 strips. This is equivalent to changing the separation between adjacent metamaterial strips. Unfortunately, a patch antenna with more than 10 metamaterial strips as metasubstrate has been unable to be simulated due to computational limitations. Simulated S_{11} results are plotted in Figure 6.28 for the case of S1 and D1 orientations, leading to very similar results for both orientations due to the aforementioned invariance to the angular rotation of the spiral resonators. The patch antenna with the metasubstrate operates at a lower frequency as the number of metamaterial strips is increased, due to the higher coupling between the spiral resonators produced when the separation g between them is reduced.

However, slightly higher FBW results are obtained for the SR2 D1 case, as noted in Table 6.8.

The effective material parameters when varying the number of metamaterial strips

N[strip]	SR2 S1 AMM				SR2 D1 AMM			
	f_0[GHz]	FBW[%]	$f2_0$[GHz]	FBW2[%]	f_0[GHz]	FBW[%]	$f2_0$[GHz]	FBW2[%]
Air	-	-	3.10	10.32	-	-	3.10	10.32
2	2.65	4.15	3.12	7.53	2.60	3.65	3.13	7.66
4	2.56	6.44	3.12	5.44	2.55	6.66	3.14	5.73
6	2.46	6.5	3.13	5.11	2.46	8.94	3.13	5.43
8	2.39	7.74	3.12	4.00	2.39	8.78	3.12	5.48
10	2.32	7.84	3.09	3.88	2.31	8.61	3.09	4.59

Table 6.8: Comparison of simulated results for the patch antenna for different number of metamaterial strips embedded in the patch antenna substrate. The bandwidths are calculated for a matching level of -6 dB.

(from 2 to 10 strips), that is, varying the separation g between spiral resonators (from 10 to 4 mm), have also been extracted for the corresponding patch antenna resonant frequency, and they are listed in Table 6.9. Note that the imaginary parts are not listed because they are close to 0. It could be concluded that the values of ε_r and μ_r are balanced at each separation g leading to an almost constant value of n_r for each patch antenna resonant frequency.

N[strip]	g[mm]	SR2 S1 AMM				SR2 D1 AMM			
		f_0[GHz]	Re$\{\mu_r\}$	Re$\{\varepsilon_r\}$	Re$\{n_r\}$	f_0[GHz]	Re$\{\mu_r\}$	Re$\{\varepsilon_r\}$	Re$\{n_r\}$
2	10	2.65	2.30	1.74	1.92	2.60	1.91	2.02	1.84
4	8	2.56	1.81	1.83	1.75	2.55	1.91	2.21	1.92
6	6	2.46	1.66	2.04	1.82	2.46	1.70	2.35	1.91
8	5	2.39	1.53	2.21	1.82	2.39	1.56	2.44	1.88
10	4	2.32	1.53	2.45	1.90	2.31	1.53	2.66	1.96

Table 6.9: Comparison of the extracted effective parameter results $(\varepsilon_r, \mu_r, n_r)$ for different number of metamaterial strips embedded in the patch antenna metasubstrate. The values have been extracted at the correspondent frequency of operation f_0 in each case.

From the results listed in Table 6.9, it could also be extracted that the metasubstrate composed of SR2 resonators behaves like a magneto-dielectric substrate with $\varepsilon_r > \mu_r$ at the patch antenna resonant frequency. This implies that no FBW improvement would be achieved with such metasubstrate. This fact is reflected in Figure 6.29 where the S_{11} results have been plotted for different homogeneous fillings operating around 2.32 GHz, the operational frequency of the patch antenna with the SR2 S1 metasubstrate composed of 10 strips. The metasubstrate has been compared with different patch antenna substrates operating at 2.32 GHz, such as an homogeneous dielectric substrate (Eps) with $\varepsilon_r = 3.2$, a magnetic substrate (Mu) with $\mu_r = 2.6$, and with a magneto-dielectric (MD) substrate with $\varepsilon_r = 2.1$ and $\mu_r = 1.5$.

The metasubstrate SR2 S1 provides the worst FBW result computed at -10 dB, with a value of 4.48%. On the other hand, the best FBW result is achieved for the dielectric only substrate (Eps), with a value of 7.67%, followed by the magneto-dielectric case

(MD), with a value of 6.55%, whereas the FBW result for the magnetic subtrate (Mu) could not be computed at -10 dB because its minimum matching level is about -4.5 dB only. These S_{11} results have been computed considering a reference impedance Z_{ref} = 50Ω. The input impedance of the patch antenna in the presence of the different fillings is plotted in Figure 6.30, and it is observed that the Eps, MD and SR2 S1 subtrates have a resistance R_0 value close to 50Ω at the resonant frequency 2.32 GHz, whereas the magnetic substrate (Mu) presents a higher resistance at the resonance, thus producing a mismatch in the S_{11} result, as commented before.

However, the maximum FBW could also be computed using the Yaghjian and Best formulation (6.9) over the whole frequency range, as shown in Figure 6.31 considering a matching level of -10 dB. The magnetic (Mu) substrate achieves the maximum FBW value around 2.25 GHz, at the expense of a reference impedance different than 50Ω (i.e. 180Ω). In addition, the patch antenna with the metasubstrate SR2 S1 has a maximum FBW value less or equal to the dielectric only case (Eps), and does not improve the maximum FBW results computed for any other patch antenna filling over the whole frequency range, except around 3.1 GHz, which corresponds to the Air case frequency.

The maximum FBW values computed at 2.32 GHz using (6.9) are listed in Table 6.10. The maximum FBW of the magnetic (Mu) substrate is 15.63%, which confirms the potential increase in FBW when the reference impedance is different to 50Ω. The metasubstrate SR2 S1 has a maximum FBW of 4.52%, smaller than the 7% obtained by the dielectric (Eps) substrate. The non-dispersive MD substrate achieves a FBW value of 9.61%. It could be concluded that the SR2 S1 metasubstrate could be used to miniaturise patch antennas, although the achievable maximum FBW would not be high due to weak magnetic response $\mu_r < 2$ and $\mu_r < \varepsilon_r$, and to the dispersive behaviour of the metasubstrate.

Patch antenna substrate	Type	Re$\{\varepsilon_r\}$	Re$\{\mu_r\}$	$Z_{ref} = 50\Omega$		$Z_{ref} = R_0$	
				Z_{ref}	FBW[%]	Z_{ref}	FBW$_{max}$[%]
Eps	Homogeneous	3.1	1	50	7.67	40.2	6.99
Mu	Homogeneous	1	2.6	50	-	181.3	15.63
MD	Homogeneous	2.1	1.5	50	6.55	72.4	9.61
SR2 S1	Dispersive	2.66	1.53	50	4.48	46.2	4.52

Table 6.10: Comparison of FBW results for different patch antenna fillings, when considering $Z_{ref} = 50\Omega$ and $Z_{ref} = R_0$.

(a) Relative electric permittivity ε_r

(b) Relative magnetic permeability μ_r

(c) Refraction index n_r
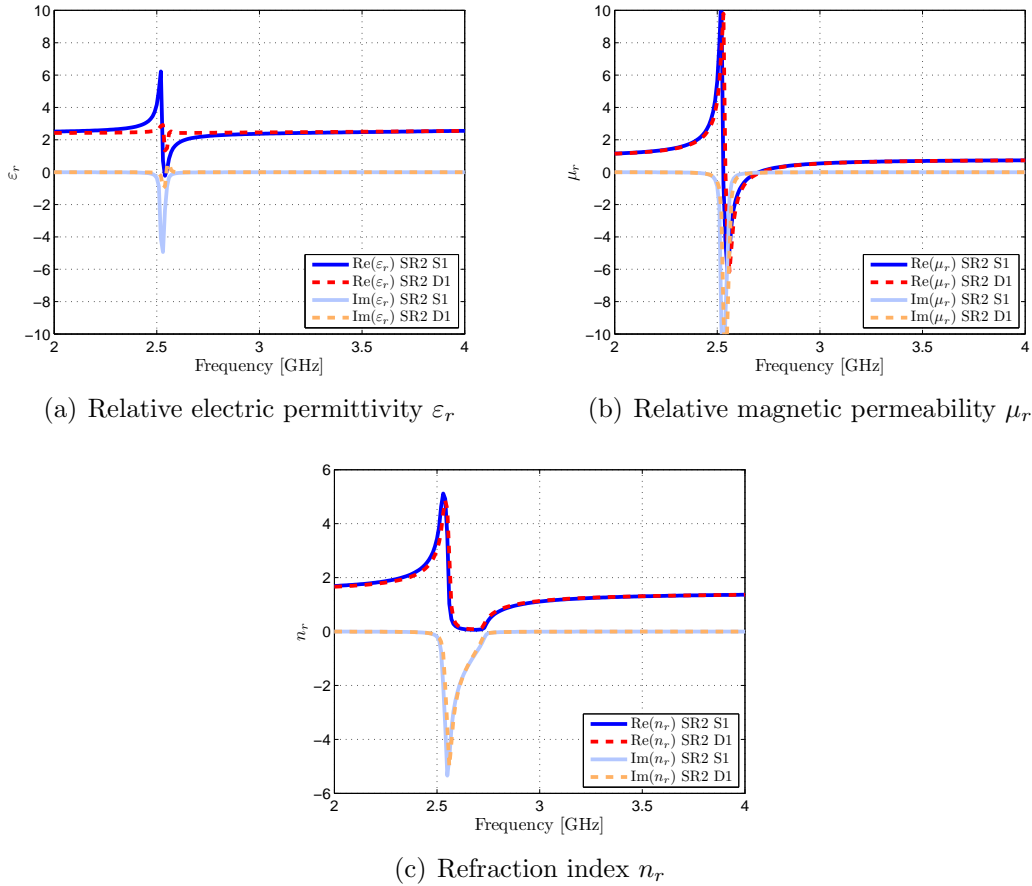
Figure 6.27: Computed relative electric permittivity ε_r, magnetic permeability μ_r and refraction index n_r of the SR2 AMM design for a rotation angle of $0°$ (SR2 S1) and $90°$ (SR2 D1).

(a) SR2 S1

(b) SR2 D1
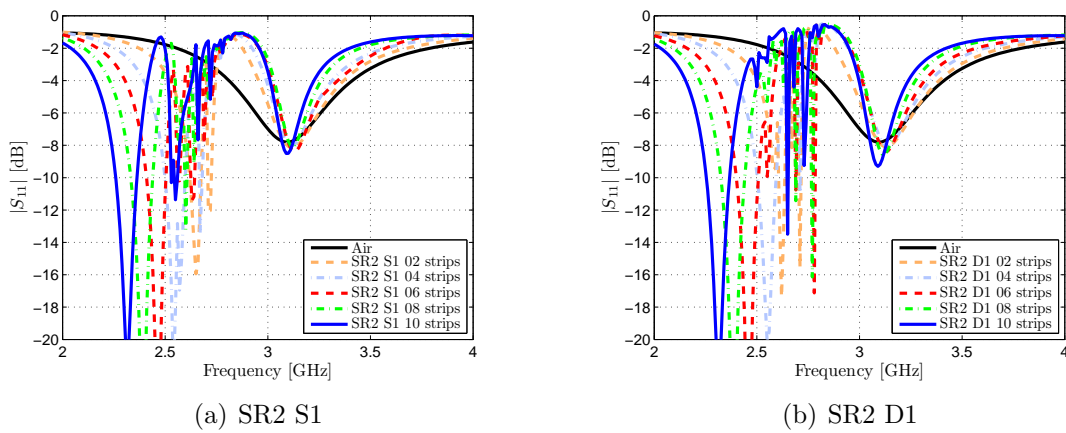
Figure 6.28: Simulated S_{11} results for the SR2 S1 and D1 while varying the number of metamaterial strips from 0 to 10.
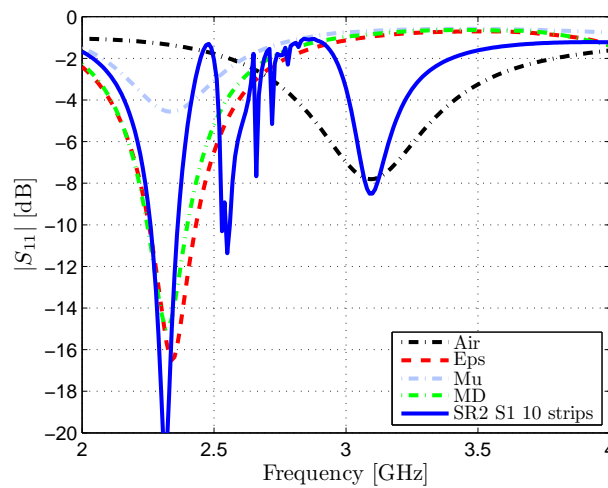
Figure 6.29: Comparison of S_{11} results for different patch antenna fillings.
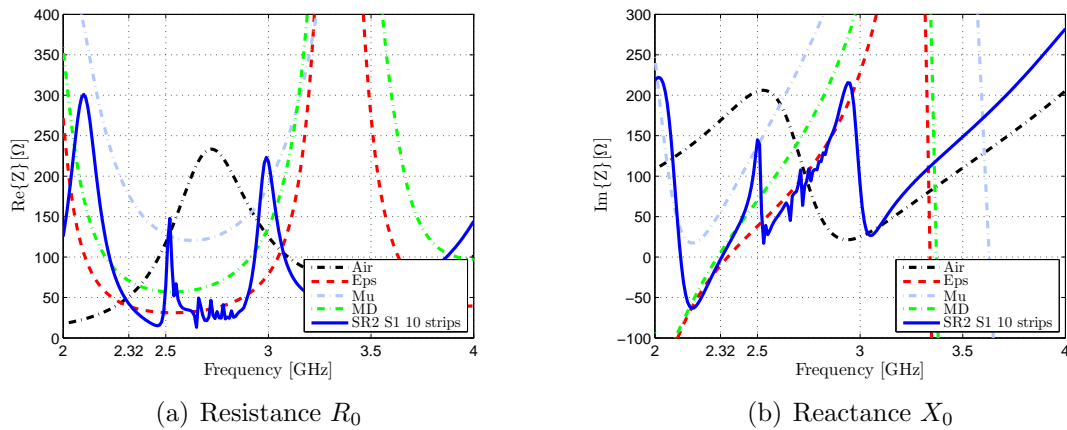
(a) Resistance R_0

(b) Reactance X_0

Figure 6.30: Comparison of real and imaginary parts of the input impedance Z results for different patch antenna fillings.
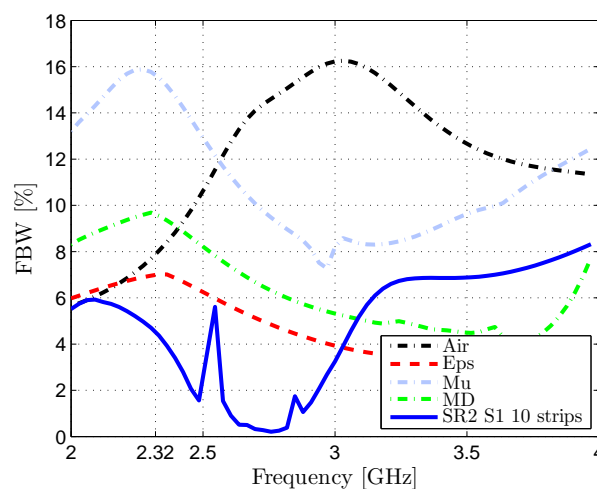
Figure 6.31: Comparison of FBW results for different patch antenna fillings computed with Yaghjian and Best formulation for a matching level of -10 dB.

6.4.3   Fabrication of Patch Antennas with AMM Metasubstrates

The SR2 AMM slab to be used as patch antenna metasubstrate has been fabricated at our facilities using standard photo-etching techniques, in order to assess the validity of the numerical results. Each of the fabricated SR2 metasubstrates are composed of 6 or 10 strips which are 40 mm long and 10 mm wide, containing 4 square spiral resonators etched on 0.8 mm thick strips of Rogers RO4003C dielectric substrate ($\varepsilon_r = 3.38$, and $\tan\delta = 0.0027$). Some fabricated SR2 S1 and D1 strips are shown in Figure 6.32.

(a) SR2 S1   (b) SR2 D1
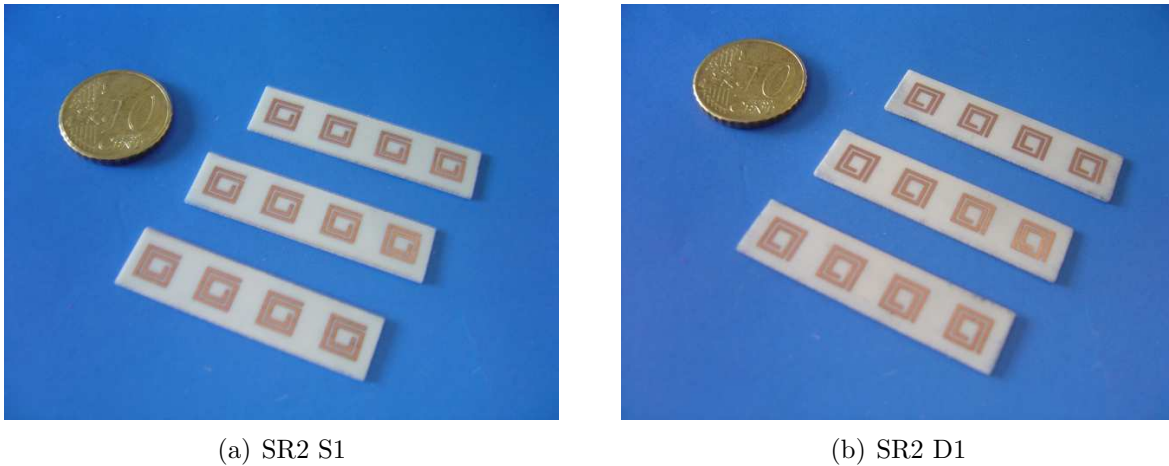
Figure 6.32: Fabricated SR2 S1 and D1 samples.

The metamaterial samples are then embedded in a Styrofoam board which is used as supporting board. This fact is observed in Figure 6.33, for the case of 6 metamaterial strips in a Styrofoam board. Additional supporting boards have been also realised for the case of 10 metamaterial strips. Despite the different number of metamaterial strips, the dimensions of the SR2 metasubstrates are 40 mm × 40 mm × 10 mm.

The patch antenna itself is made from a copper sheet with dimensions of 40 × 40 mm^2, placed 10 mm above an aluminium metal sheet of 330 × 330 mm^2. The patch antenna is coaxially fed, and the feed is set at the feeding position number 4, which has been already used in the numerical simulations because it provided better matching and bandwidth results. The fabricated patch antenna with the metasubstrate is shown in Figure 6.34.

<div align="center">
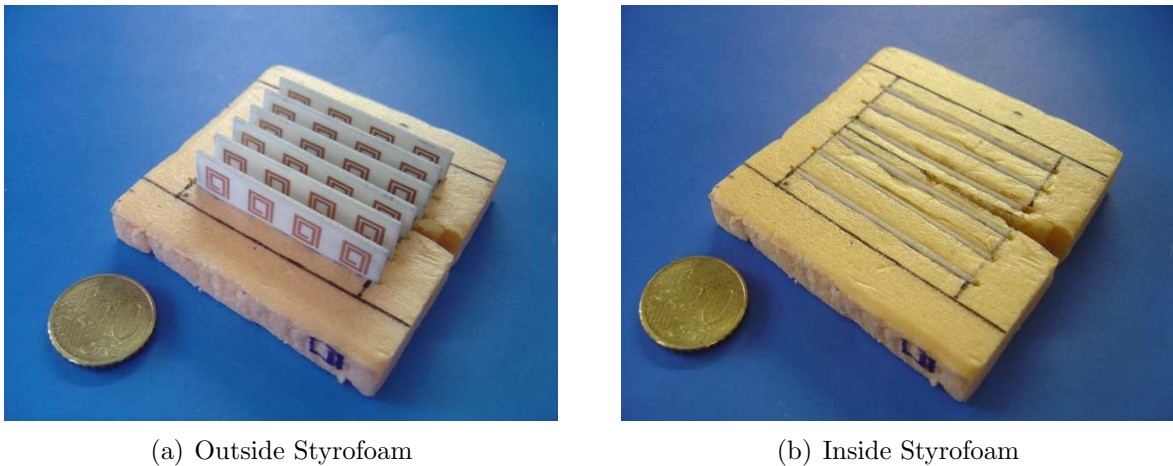
(a) Outside Styrofoam   (b) Inside Styrofoam

</div>

Figure 6.33: Fabricated SR2 samples showing their position in the Styrofoam.
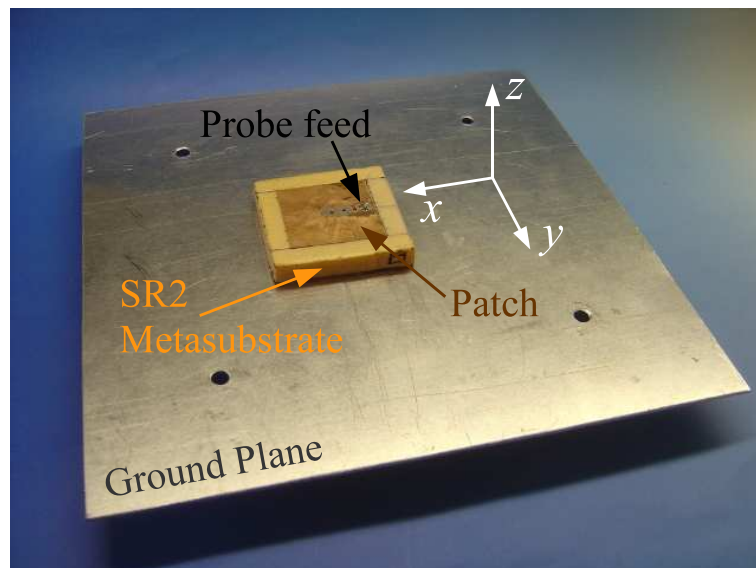
Figure 6.34: Fabricated patch antenna with a SR2 AMM metasubstrate.

6.4.4 Measurement of Patch Antennas with AMM Metasubstrates

An Agilent E8362B VNA has been used to carry out the S-parameters and the impedance Z measurements of the fabricated patch antenna with air as substrate and with the SR2 metasubstrates. The matching S_{11} of the patch antenna has been measured for the case of Air (no substrate) and for the case of the metasubstrate, which is composed of 6 and 10 metamaterial strips in the aforementioned S1 and D1 orientations. Measured and simulated results are plotted in Figure 6.35 for comparison purposes.

A slight frequency shift is observed for the resonant frequency of the patch antenna in Air, from 3.1 down to 3.0 GHz, when compared with the simulated results. This

(a) SR2 S1   (b) SR2 D1
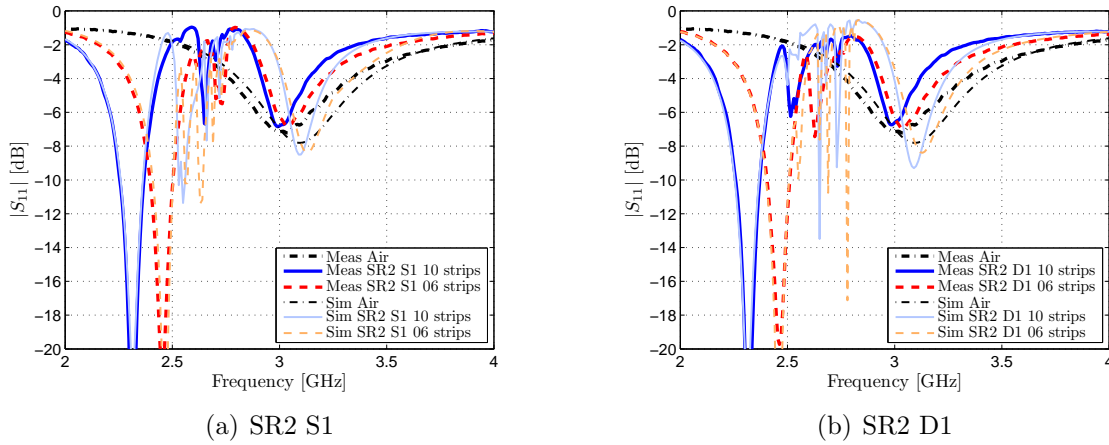
Figure 6.35: Comparison of measured and simulated S_{11} results for the SR2 S1 and D1 for 6 and 10 metamaterial strips in the metasubstrate.

discrepancy may be due to the proximity of the feeding probe to the edge of the patch antenna, resulting in higher fringing fields. However, a very good agreement has been achieved between simulated and measured matching results at the resonant frequency of the patch antenna with the metasubstrates composed of 6 and 10 metamaterial strips. The patch antenna with the metasubstrate operates at 2.32 GHz with a FBW$_{-10dB}$ of 4.82%, and at 2.46 GHz with a FBW$_{-10dB}$ of 4.36%, for the case of 10 and 6 metamaterial strips, respectively. Complete results are listed in Table 6.11. Note that the different spiral resonator orientation, that is, S1 or D1, has little effect in the results.

Patch antenna substrate	Type	f_0[GHz]	FBW$_{-10dB}$[%]
Air	Measured	3.03	-
	Simulated	3.10	-
SR2 S1 06 strips	Measured	2.45	4.36
	Simulated	2.46	3.46
SR2 D1 06 strips	Measured	2.46	4.31
	Simulated	2.46	4.39
SR2 S1 10 strips	Measured	2.32	4.82
	Simulated	2.32	4.48
SR2 D1 10 strips	Measured	2.32	4.87
	Simulated	2.31	4.89

Table 6.11: Comparison of FBW results for different patch antenna fillings.

The patch antenna impedance is easily found from the S-parameter results as follows:

$$Z = Z_{ref}\frac{1 + S}{1 - S}, \tag{6.15}$$

where $Z_{ref} = 50\Omega$, and S is the S_{11} parameter.

The measured impedance Z of the patch antenna in air and with the metasubstrates is plotted in Figure 6.36.

(a) SR2 S1   (b) SR2 D1
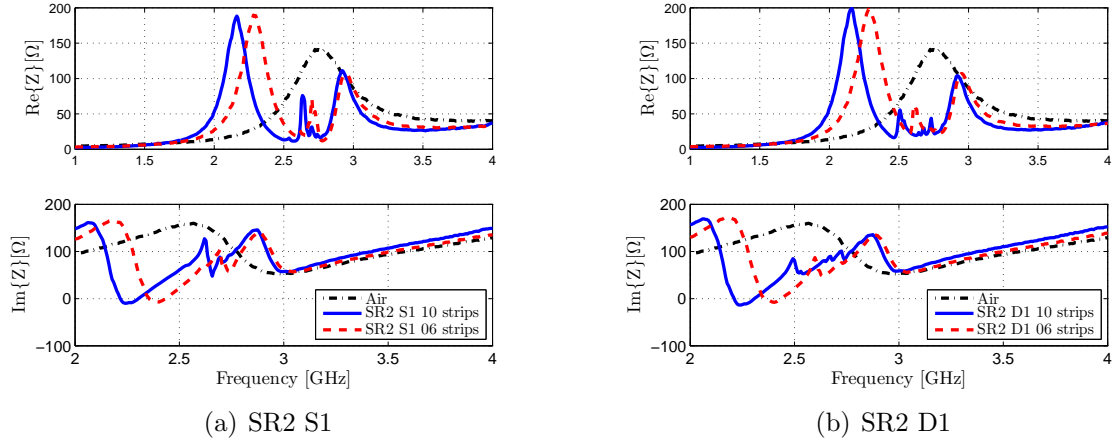
Figure 6.36: Measured Z results for the SR2 S1 and D1 for 6 and 10 metamaterial strips in the metasubstrate.

The maximum FBW is then retrieved from the measured impedance results by using Yaghjian and Best formulation (6.9). The FBW results for the case of Air and the SR2 metasubstrate are plotted in Figure 6.37. It is confirmed from the results that the use of a metasubstrate could not improve the maximum FBW results obtained for the Air case. In addition, it is remarkable that the metasubstrate composed of 6 metamaterial strips could provide a better maximum FBW than the one composed of 10 strips. This may be due to the slightly higher μ_r value at the resonance for the 6 strips case compared to the 10 strips case, which results in higher FBW, as stated before in Table 6.9.

(a) SR2 S1   (b) SR2 D1
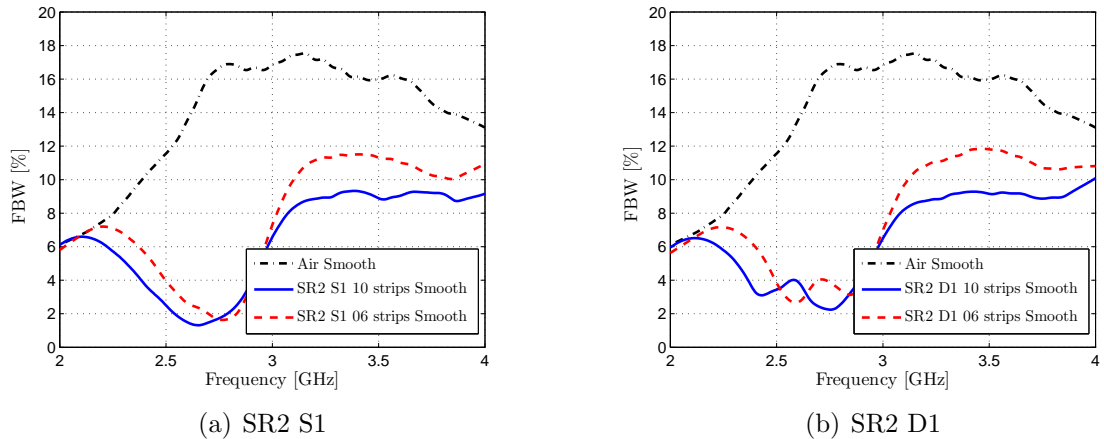
Figure 6.37: Computed maximum FBW results considering a smooth factor of 10% over the results.

Although not shown here, a smoothing factor of 10% has been applied to these

FBW results. Since the measured S_{11} suffers from electrical noise, this undesired effect is propagated and dramatically affects the FBW computation, due to the derivative of the impedance that is present in the denominator of the FBW formulation (6.9).

6.4.4.1 Radiation Efficiency

The radiation efficiency η_{rad} is used to estimate the losses of an antenna. Among others, the radiation efficiency could be easily measured with the well-known Wheeler cap method [114], although this is a narrowband solution. A broadband method based on the Wheeler cap method was presented by Johnston-Geissler in [115, 116], although some limitations have been overcome in [117], leading to the modified Johnston-Geissler method (JGM).

A metallic cap is inserted on the ground plane in order to short-circuit the antenna placed inside, as shown in Figure 6.38. The antenna resistance R_{ant} is composed of a radiation resistance R_{rad} and a loss resistance R_{loss}. Therefore, when the antenna is short-circuited, the R_{rad} tends to 0, whereas the R_{loss} remains.

Figure 6.38: Measurement of the radiation efficiency with a Wheeler cap using an Agilent E8362B VNA.

The modified JGM has been applied to the measured results to retrieve the radiation efficiency of the patch antenna with the SR2 metasubstrates over the whole frequency range, that is, from 1 to 4 GHz. The computed results are plotted in Figure 6.39.

The patch antenna has a radiation efficiency of 95.7% (at 3 GHz) when Air is used as substrate. The insertion of the SR2 metasubstrate does not significantly decrease the performance of the patch antenna, achieving a radiation efficiency of 86.5% (at 2.46 GHz) and 93.5% (at 2.32 GHz) for the metasubstrate composed of 6 and 10 metamaterial strips, respectively. Moreover, a radiation efficiency $\eta_{rad} > 80\%$ is obtained not
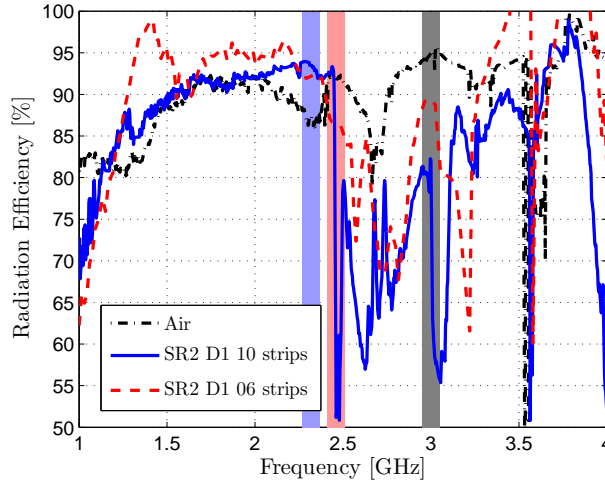
Figure 6.39: Computed radiation efficiency for the patch antenna in Air and with the SR2 metasubstrate.

only at the resonant frequency of each case, but also over a wide frequency range. This means that the use of a metasubstrate has little effect on the patch antenna losses. Detailed results are listed in Table 6.12.

Patch antenna substrate	f_0[GHz]	η_{rad}[%]
Air	3.03	95.7
SR2 D1 06 strips	2.46	86.5
SR2 D1 10 strips	2.32	93.5

Table 6.12: Computed radiation efficiency of the patch antenna with the metasubstrate applying the modified JGM.

6.4.4.2   Radiation Patterns

The patch antenna with the SR2 metasubstrate has been placed in the D3-UPC anechoic chamber in order to measure the radiation patterns, as presented in Figure 6.40. A broadband ridged horn antenna has been used as the probe antenna.

The realised gain radiation patterns have been measured at 3 GHz for the Air case, and at 2.46 GHz and 2.32 GHz for the case of SR2 metasubstrates composed of 6 and 10 metamaterial strips. The E-plane ($\phi = 0°$) and the H-plane ($\phi = 90°$) results for the three cases are plotted in Figure 6.41 and in Figure 6.42, respectively, according to the reference system coordinates of Figure 6.34. The radiation patterns for each case have been normalised to their maximum values.

The use of the SR2 metasubstrates does not change the radiation properties of a patch antenna. Thus, the radiation patterns of the patch antenna with the SR2 metasubstrates are similar to those of a patch antenna in Air. Although cross-polar
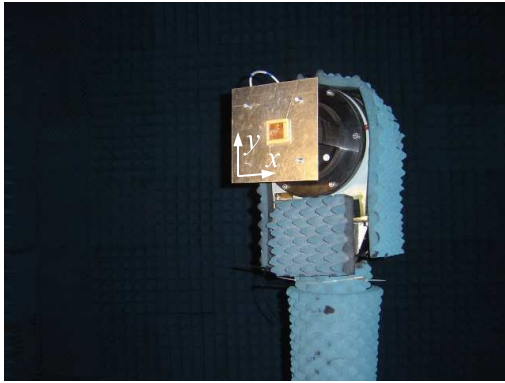
(a) Patch antenna with metasubstrate
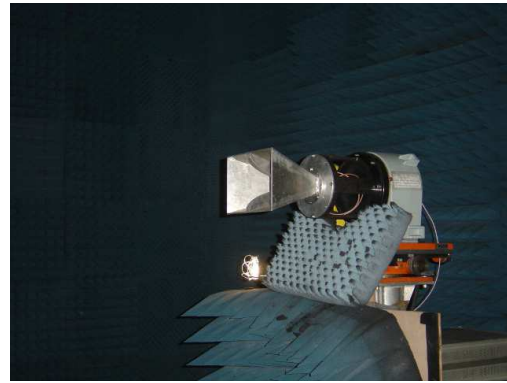
(b) Ridged horn as probe antenna

Figure 6.40: Patch antenna with the SR2 metasubstrate placed in the D3-UPC anechoic chamber.
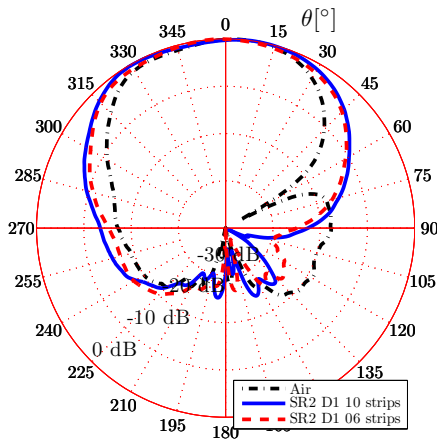
(a) E-plane co-pol
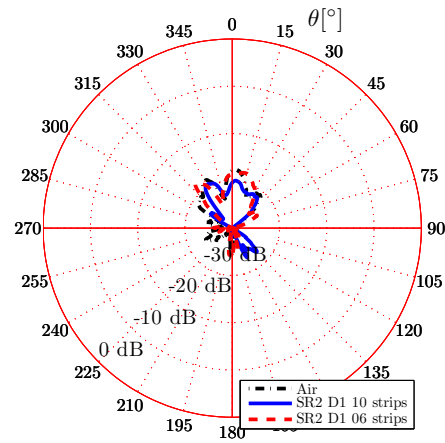
(b) E-plane cross-pol

Figure 6.41: Measured co-polar and cross-polar E-plane cuts of the patch antenna in Air, and with the SR2 metasubstrates.

results are high for all cases in the H-plane, they are 30 dB lower than the co-polar level in the broadside direction.

6.5   Chapter Conclusions

In this chapter, the performance of patch antennas with different metamaterial substrates has been studied in terms of FBW and antenna size miniaturisation. For the case of homogeneous non-dispersive metamaterial substrates, patch antennas are significantly miniaturised by using high-ε_r material substrates, but they offer a reduced FBW response. High FBW is achieved with high-μ_r ($\mu_r > 1$) and ENZ ($0 < \varepsilon_r < 1$) substrates. However, efficient antenna miniaturisation, that is, high FBW and patch

(a) H-plane co-pol
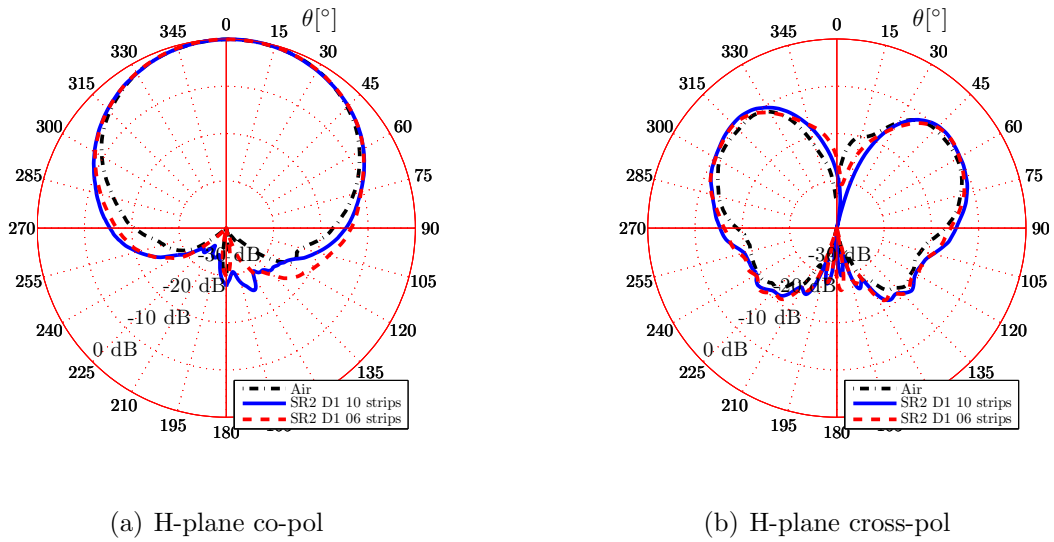
(b) H-plane cross-pol

Figure 6.42: Measured co-polar and cross-polar H-plane cuts of the patch antenna in Air, and with the SR2 metasubstrates.

antenna miniaturisation, is only achieved with the use of high-μ_r substrates. The use of magneto-dielectric substrates with $\varepsilon_r = \mu_r$ values offers a moderate increase in FBW while the antenna is still miniaturised. These FBW performances are shown in Figure 6.43.
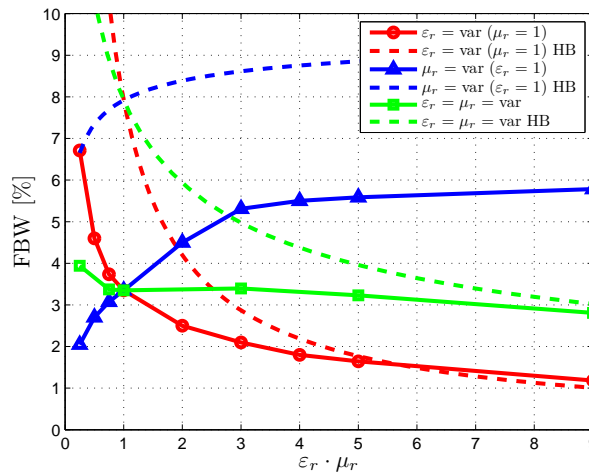
Figure 6.43: Computed FBW as a function of $\varepsilon_r \mu_r$, showing the regions of interest for higher BW patch antenna applications.

Such non-dispersive homogeneous substrates do not exist in nature. Nevertheless, a metamaterial substrate composed of spiral resonators (SR AMM slab) is characterised by its μ-dispersive behavior, and hence, provides a high-μ response. Therefore, the SR AMM slab has been investigated as a patch antenna substrate, the so called metasubstrate.

Initial simulated results state that the patch antenna with the SR2 metasubstrate operates at 2.32 GHz with a maximum FBW of 4.52%. This results in a miniaturisation factor n of 1.3, when compared with the air filled patch antenna. However, the maximum FBW for the SR2 metasubstrate is smaller than the 6.99% obtained by the dielectric (EPS) filled patch antenna, the 9.61% obtained by the MD filled patch antenna, and the 15.63% obtained by the magnetic (mu) filled patch antenna. This means that the patch antenna with the SR2 metasubstrate leads to a patch antenna size reduction, although the maximum achievable FBW is small due to the dispersive behaviour and a weak magnetic response of the SR2 metasubstrate at the frequency of operation.

The patch antenna with the SR2 metasubstrate has been fabricated and tested at our facilities. Measured antenna matching S_{11} and maximum FBW results agree with the simulated results. The measured radiation efficiency of the patch antenna is 95.7% for the air case, and 93.5% with the SR2 metasubstrate; this means that the SR2 metasubstrate does not increase the losses in the patch antenna substrate. Finally, the radiation patterns obtained with the SR2 metasubstrate are similar to those of the air filled patch antenna. Therefore, although efficient patch antenna miniaturisation could not be fulfilled due to the dispersive behaviour of the metasubstrates, these results confirm the feasibility of patch antennas with magneto-dielectric substrates for miniaturisation purposes.

Chapter 7

Leaky Wave Antennas with AMM Mu-Near-Zero Slabs

7.1 Introduction

Leaky wave antennas (LWAs) are typically wideband operation antennas that radiate a narrow beam whose direction varies with the frequency, or with the phase delay [3]; this fact means that a desired radiation angle is satisfied only for an specific frequency. Some LWA designs could radiate a highly directive beam at broadside from a point source placed inside a host medium, like a double dielectric surface [92], a partially reflecting surface (PRS) [93], or a metamaterial slab [94]. These antennas are characterised by the use of only one or few simple sources to obtain a highly directive beam, and they are often realised in planar technologies, that is, combining dielectric and metallic layers. On the other hand, some drawbacks are found in their poor matching and narrow bandwidth at which the desired radiation condition is satisfied. The principle of operation of this kind of LWAs is depicted in Figure 7.1, where a point source is embedded in a grounded material slab.

In such a situation, electromagnetic waves propagate from the point source in the radial ρ direction of the partially-open waveguide, with a complex wave-number $k_\rho = \beta - j\alpha$, producing the excitation of a pair of weakly attenuated modes, one TE and one
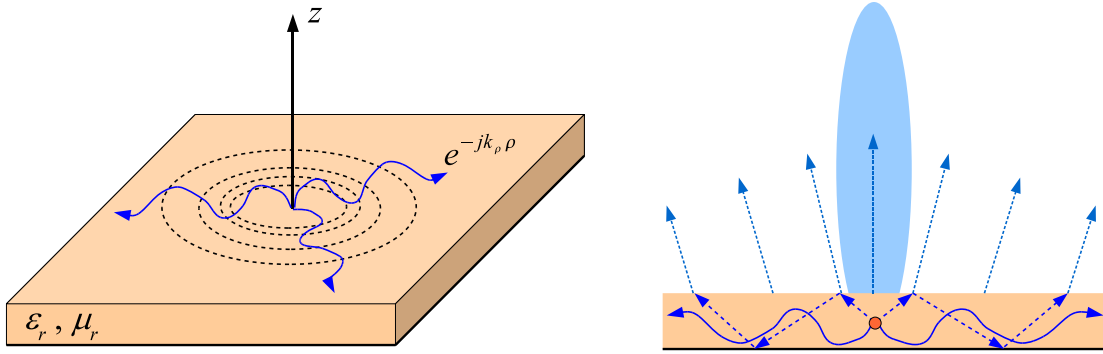
Figure 7.1: Principle of operation of a dipole source embedded in a grounded slab operating as LWA.

TM, with respect to the broadside direction $+z$. Thus, properly excited leaky wave modes contribute to the far-field pattern producing a highly directive beam.

LWAs could also be designed with metamaterial slabs, by taking advantage of their dispersive behaviour, and hence, the different values of electric permittivity ε_r and magnetic permeability μ_r they could present. For instance, an electric source embedded in a grounded low electric permittivity ($0 < \varepsilon_r < 1$, epsilon-near-zero or ENZ) substrate like the wire-medium is able to produce a highly directive beam at broadside [40]. Broadside power enhancement is achieved for an ENZ slab thickness of $h = m\lambda_1/2$ ($m = 1, 2, \ldots$), where $\lambda_1 = \lambda_0/n_r$ and $n_r = \sqrt{\mu_r\varepsilon_r}$, and by placing the electric dipole source at $h_s = h/2$, as it was also presented in Section 2.3 (Figure 2.14). This property could also be extended to magnetic dipole sources, such as loops or slots, embedded in grounded low magnetic permeability ($0 < \mu_r < 1$, mu-near-zero or MNZ) substrates [94]. In this case, the optimum metamaterial slab thickness wuld be $h = (2m-1)\lambda_1/4$ ($m = 1, 2, \ldots$), and the optimum source location is $h_s = 0$ or $h_s = h$.

The SR AMM slab presented in Chapter 3 (Figure 3.14) is characterised by its mu-dispersive behaviour, and hence, it presents a MNZ band. In this situation, the SR MNZ slab could be used as a superstrate to increase the broadside radiation of a magnetic dipole source, such as a slot antenna placed in the ground plane, forming a LWA, as stated in [94].

In this chapter, the MNZ application of the SR AMM slab will be studied. Most results have been basically obtained experimentally, because the full wave numerical simulation of the whole structure is not feasible due to memory and computation resource limitations, whereas the numerical simulation of an effective MNZ slab, by using the ε_r and μ_r parameters of the SR AMM slab, does not in principle provide fair results due to the inaccuracies found in the effective material retrieval methods.

7.2 MNZ slabs for broadside radiation improvement

The unit cell design of the SR AMM slab described in Chapter 3 (Figure 3.14) is composed of a two-turn square spiral resonator, with a major width of 5.6 mm, which is printed on a Rogers RO4003C dielectric substrate (thickness is 0.8 mm, ε_r is 3.38, and $\tan \delta$ is 0.0027). As shown before, the resonant frequency f_0 of the single layer SR AMM slab is found at 2.6 GHz, and the magnetic plasma frequency f_p is found around 3.18 GHz. Thus, the MNZ region is expected above this f_p frequency, that is, from 3.2 GHz up to about 6 GHz. This region is seen in Figure 7.2, where the extracted effective parameters (ε_r, μ_r and n_r) are plotted according to Li method.

(a) ε_r

(b) μ_r

(c) n_r
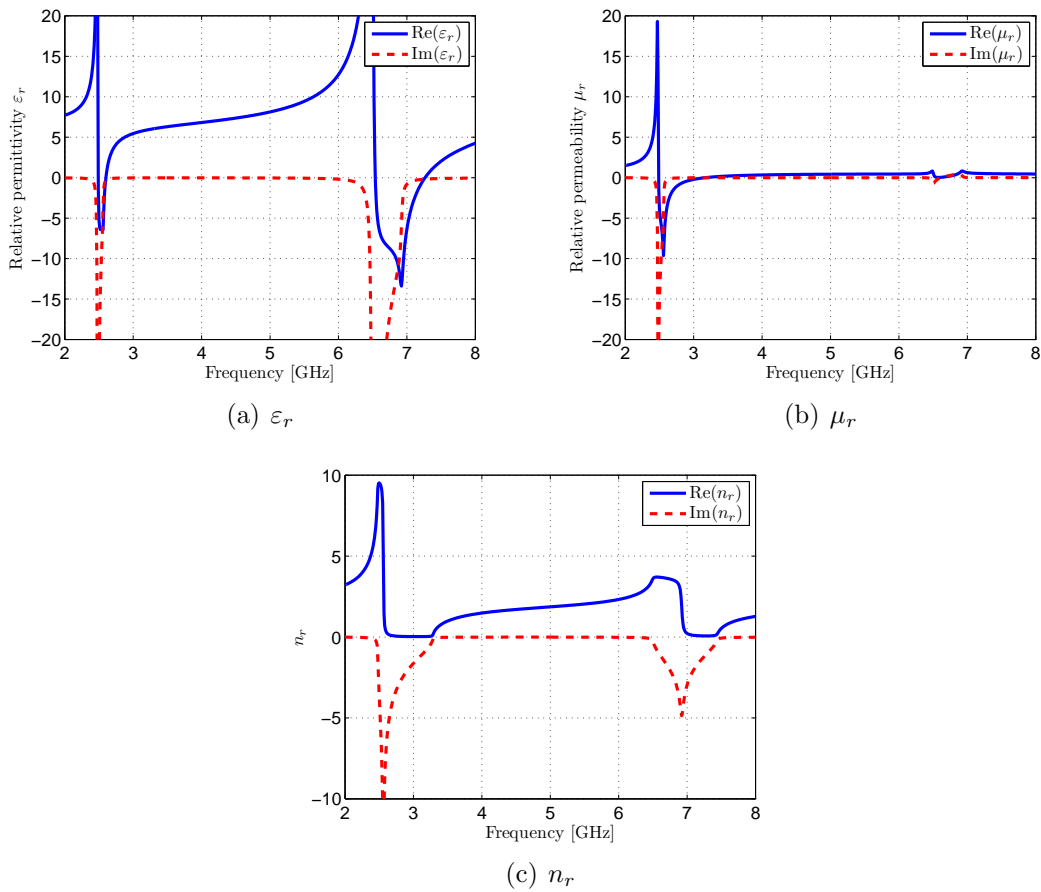
Figure 7.2: Retrieved effective material parameters of the SR AMM slab.

According to [94], the optimal thickness of an homogeneous metamaterial slab with a MNZ property to have a broadside radiation improvement is defined as:

$$h_{opt} = (2m - 1)\frac{\lambda_1}{4} = (2m - 1)\frac{\lambda_0}{4\,n_r} \tag{7.1}$$

being $m = 1, 2, \ldots$ are the resonances where maximum radiation occurs, n_r the index of refraction, and λ_0 the free space wavelength. Thus, the h_{opt}/h factor has been retrieved

to estimate the frequencies where the maximum broadside radiation may occur, that is, the height h of the MNZ substrate is equal to the optimal height h_{opt} ($h_{opt}/h = 1$). The results for $m = 1$ and $m = 2$ are plotted in Figure 7.3 for different values of metamaterial slab thickness h, that is, from 6 to 48 mm, which correspond to a SRR AMM slab of 1 layer up to 8 layers, respectively.

(a) $m = 1$ (b) $m = 2$
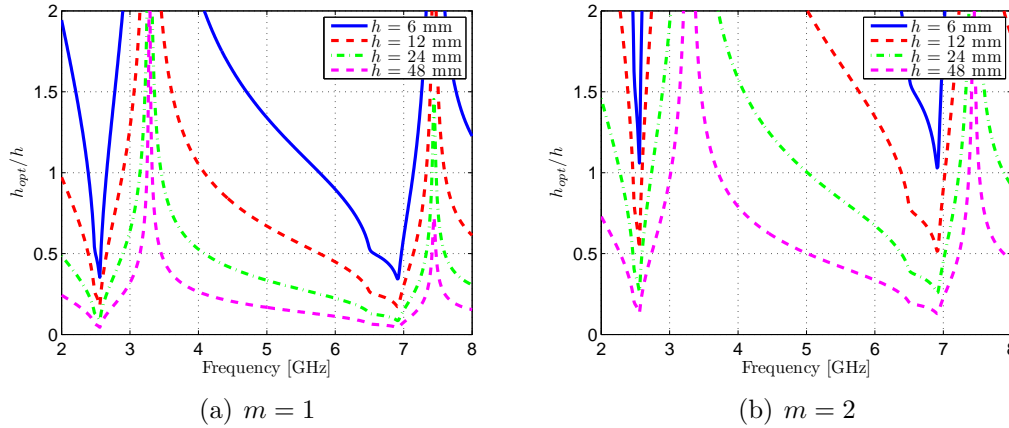
Figure 7.3: Broadside radiation improvement by h_{opt}/h factor.

The results of interest are found in the figures from 3 to 6 GHz, where the line plots related with different MNZ substrate thickness cross the $h_{opt}/h = 1$ axis. However, for better comprehension, the frequencies where the h_{opt}/h factor equals 1 have been gathered in Table 7.1 for the cases of $m = 1$ (first resonance) to $m = 4$ (fourth resonance). For the case $m = 1$, it is seen that the frequency where the maximum radiation is expected decreases as the MNZ slab thickness is increased, although a saturation is found for high thickness slabs due to their proximity to the frequency where $\mu_r = 0$, where optimal results may be found. Hence, a 6 mm slab (single layer SR MNZ) is expected to behave as optimal around 5.76 GHz, whereas a 24 mm slab (four layer SR MNZ) around 3.46 GHz. In addition, several maxima may be found as the number of SR AMM layers increases. For instance, for a slab thickness of 24 mm, the maximum broadside radiation may be found at 3.46 GHz, 5.01 GHz, and 6.19 GHz.

h	$h_{opt}/h = 1\|_{m=1}$	$h_{opt}/h = 1\|_{m=2}$	$h_{opt}/h = 1\|_{m=3}$	$h_{opt}/h = 1\|_{m=4}$
6 mm	5.76 GHz	-	-	-
12 mm	4.09 GHz	6.38 GHz	6.85 GHz	-
24 mm	3.46 GHz	5.01 GHz	6.19 GHz	6.47 GHz
48 mm	3.32 GHz	3.71 GHz	4.54 GHz	5.43 GHz

Table 7.1: Frequencies where broadside radiation maxima occur as a function of the MNZ slab thickness, and for $m = 1, 2, 3, 4$.

From these results, it would be interesting to design a magnetic dipole antenna

operating from 3 to 6 GHz in order to verify the possible broadside radiation increase produced by the SR AMM slab operating in the MNZ region.

7.3   Slot Antenna Design for MNZ Applications

A slot embedded in a ground plane has been designed as the magnetic dipole antenna to be used as a grounded MNZ slab. A rectangular shaped slot, with dimensions 2 mm × 30 mm, has been considered at the centre of a 400 mm × 400 mm metallic ground plane. The slot antenna is fed by a SMA-to-waveguide transition with a cut-off frequency around 3 GHz. The slot antenna has been designed to be tuned around 4.9 GHz, that is, within the MNZ band of the metamaterial slab.

The SR AMM slab (MNZ slab) would then be placed just above the slot antenna as a superstrate, with the strips containing the SRs aligned in the direction of the E-plane (x-direction) of the slot antenna, in order to properly excite the SR AMM slab. A sketch of the slot antenna alone is depicted in Figure 7.4 (a), and the same design in presence of a single layer SR MNZ slab is depicted in Figure 7.4 (b).

(a) Slot antenna alone   (b) Slot antenna with SR MNZ superstrate
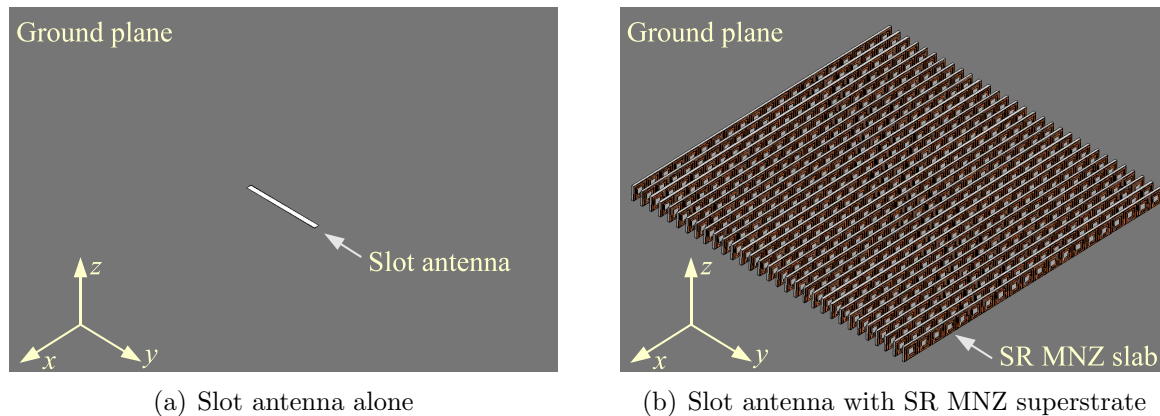
Figure 7.4: Sketch of the slot antenna embedded in the ground plane, and in presence of a single layer SR MNZ superstrate.

The slot antenna design has been simulated with HFSS. The return loss S_{11} of the slot antenna is plotted in Figure 7.5. The slot antenna is tuned at 4.86 GHz, and has a FBW$_{-10dB}$ of 5.55%.

In addition, the normalised power radiation patterns of the slot antenna have been plotted in Figure 7.6, showing the E and H planes results at 4.86 GHz. The H-plane results are slightly more directive than the E-plane ones, as expected for a slot antenna with such a configuration.
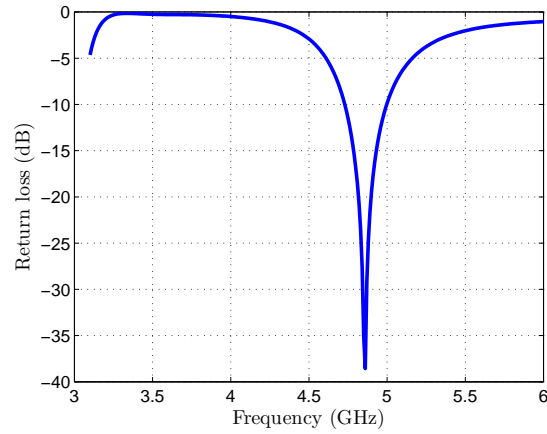
Figure 7.5: Simulated return loss results of the slot antenna.
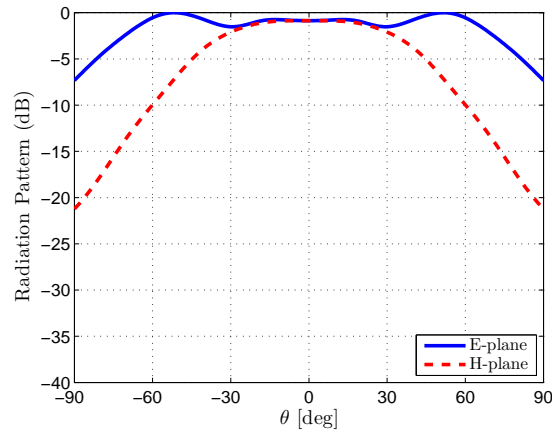
Figure 7.6: Simulated radiation patterns of the slot antenna at 4.86 GHz.

7.4   Fabrication of the MNZ Slot Antenna System

Two SR MNZ superstrates with different thickness have been fabricated in order to test the radiation and directivity enhancements of the slot antenna. The single-layer SR AMM superstrate, referred to from now on as MNZ1, is composed of 31 strips (with 20 SRs printed in each one), with a separation of 4 mm between adjacent strips, forming a 120 mm × 120 mm × 6 mm MNZ slab. On the other hand, the four-layer SR AMM superstrate, referred to as MNZ4, is identical to the single-layer one, but it contains 4 SRs layers, with an overall height of 24 mm, forming a 120 mm × 120 mm × 24 mm MNZ slab. The fabricated SR MNZ superstrates, the single-layer MNZ1 and the four-layer MNZ4, are shown in Figure 7.7. Note that two nylon endless screw rods and washers have been used for supporting purposes in order to properly align and maintain the 31 strips with the spiral resonators at a fixed separation. This fabrication solution makes the metamaterial slab more robust and accurate, in terms of

metamaterial strips position and alignment, than the previous designs where Styrofoam was used as a supporting board.

(a) MNZ1   (b) MNZ4
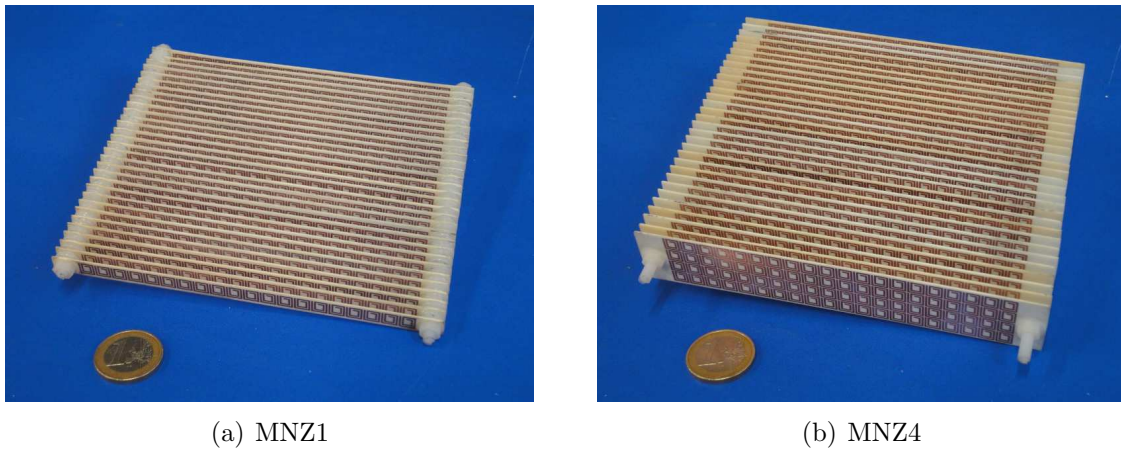
Figure 7.7: Fabricated single and four layer SR MNZ superstrates.

The whole antenna system comprising the slot antenna on the ground plane and the SR MNZ superstrates is shown in Figure 7.8.
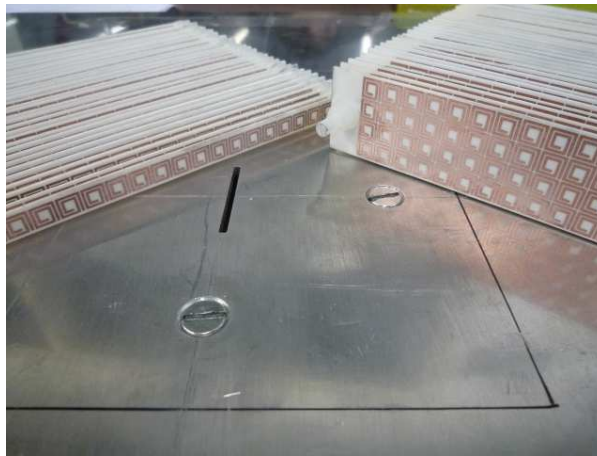
Figure 7.8: Fabricated SR MNZ superstrates and slot antenna.

7.5   Measurements of the MNZ Antenna

7.5.1   Return Loss

The return loss S_{11} of the whole antenna system has been measured from 2 to 6 GHz with an Agilent E8362 VNA, as shown in Figure 7.9, for the three cases under study: the slot antenna alone (Air), the slot antenna with the single-layer MNZ substrate (MNZ1), and the slot antenna with the four-layer MNZ substrate (MNZ4).
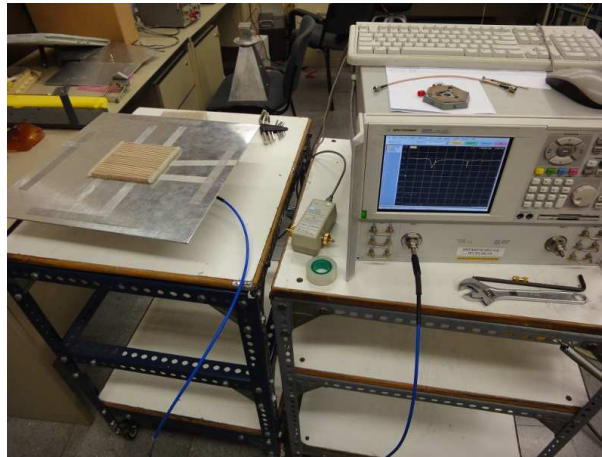
Figure 7.9: Measurement setup for the S_{11} measurements with an Agilent E8362 VNA.

The measured S_{11} results are plotted in Figure 7.10. The slot antenna is matched at 4.84 GHz with a fractional BW of 6.4%, but the matching level is significantly decreased in presence of the MNZ superstrates. The minimum matching level of the MNZ1 and MNZ4 superstrates is -5 and -8 dB, respectively. These matching minimum dips could be seen as a frequency of operation of the LWA in each case. Then, the frequency of operation is shifted towards lower frequency as the number of SR MNZ layers is increased from one to four, that is, from 4.84 GHz down to 3.46 GHz, leading to a miniaturisation factor of about 28%.
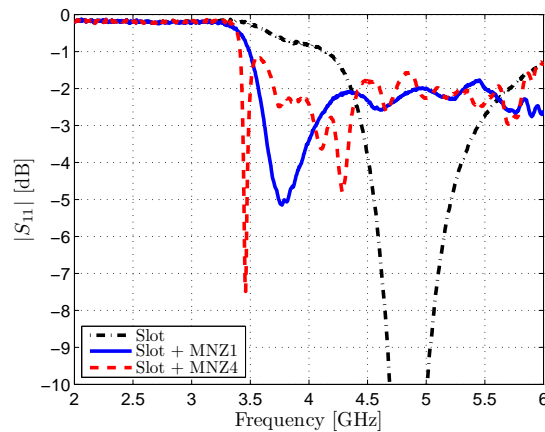
Figure 7.10: Measured S_{11} results for the slot antenna in free space and with the MNZ1 and MNZ4 superstrates.

7.5.2 Radiation Patterns

The radiation performance of the slot antenna with the SR MNZ superstrates has been tested in the D3 UPC anechoic chamber, as shown in Figure 7.11. Due to the

larger size of the ground plane with respect to the MNZ superstrates, a microwave absorber has been placed around the MNZ superstrates in order to minimise the surface waves and the unwanted diffraction effects produced by the ground plane.
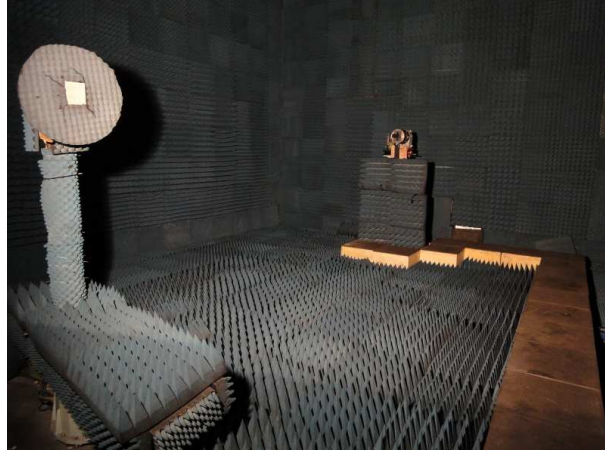
Figure 7.11: Measurement setup for the radiation pattern measurements in the anechoic chamber.

The received/radiated power at broadside ($\theta = 0$ deg), the so called power balance (PB), has been measured in the anechoic chamber, and the results for the three cases under study from 2 to 6 GHz are plotted in Figure 7.12.
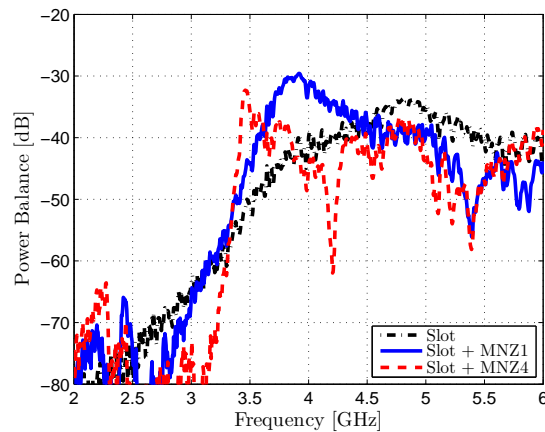
Figure 7.12: Measured power balance (PB) results for the slot antenna in free space and with the MNZ1 and MNZ4 superstrates.

It is observed that the slot antenna has its maximum radiated power around 4.8 GHz, whereas the MNZ1 and the MNZ4 have their maxima around 3.9 GHz and 3.5 GHz, respectively. When using the MNZ superstrates, the received power at broadside is increased with respect to the slot case around several frequency bands. For instance, at 3.46 GHz where the power enhancement was expected for the MNZ4 case, the received power is increased in about 13.1 dB in presence of the MNZ1, and in about 19.1 dB in

presence of the MNZ4, with respect to the slot antenna in free-space. However, note
that the radiated power maxima for each case correspond to their matched frequencies,
as expected. Therefore, to observe a potential increase in directivity, the power balance
should be normalised by a $1/(1 - |S_{11}|^2)$ factor, in order to compensate the loss due to
the mismatch of the slot antenna when using the MNZ superstrates. The normalised
power balance $(\overline{PB})$ is then plotted in Figure 7.13.
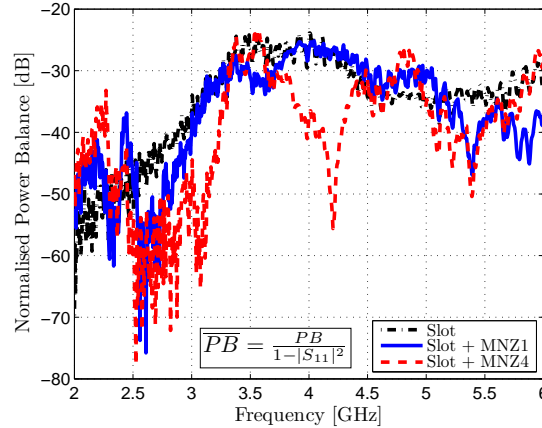
Figure 7.13: Measured corrected power balance $(\overline{PB})$ results for the slot antenna in
free space and with the MNZ1 and MNZ4 superstrates.

The normalised received power $(\overline{PB})$ at broadside when using the MNZ superstrates
is found to be higher than the result for the slot antenna, mainly around 4.8 GHz, where
the MNZ1 and MNZ4 superstrates outperform the received power of the slot antenna
in free-space. This is reflected in the measured E and H plane cuts at 4.8 GHz, where
more than 5 dB power enhancement is measured when using the SR MNZ4 superstrate.
These results are shown in Figure 7.14. Note that the E plane cut of the slot antenna
corresponds to xz-plane in the slot antenna design, whereas the H plane cut corresponds
to yz-plane.

Moreover, these radiation patterns could be referred to their maximum values. These
radiation patterns are plotted in Figure 7.15. In such a situation, a directivity enhance-
ment is observed for the E plane results at 4.8 GHz as the number of MNZ layers is
increased. On the other hand, there is no directivity improvement for the H plane at
this frequency.

The radiation patterns could also be seen over the whole frequency range. This is
shown in Figure 7.16, where the normalised E and H planes results are plotted from
2 to 6 GHz for the three cases: Air, MNZ1 an MNZ4. It is seen that the use of
MNZ superstrates leads to a narrower radiation patterns, thus increasing the overall
directivity of the slot antenna, in spite of the apparition of diffraction lobes.

In general, the directivity enhancement is mainly evidenced in the E plane results

(a) E-plane   (b) H-plane
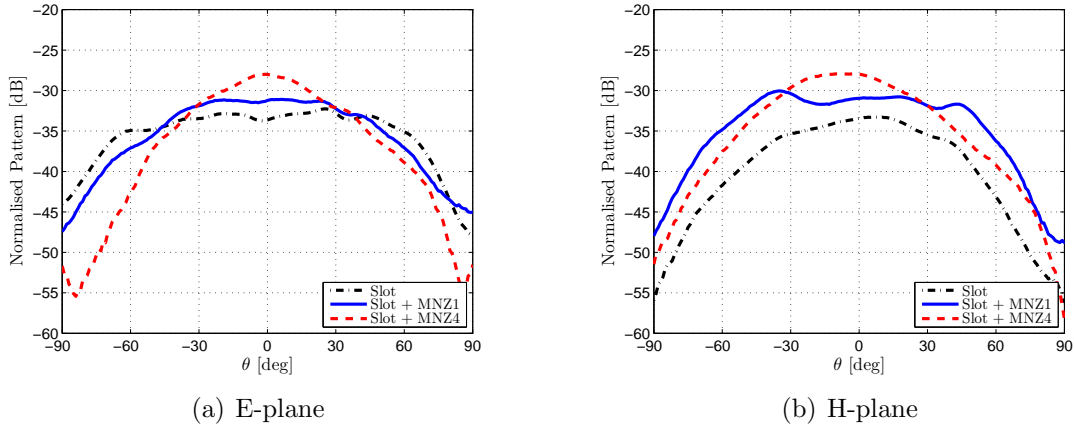
Figure 7.14: Measured E and H planes cuts at 4.80 GHz of the slot antenna in presence of the SR MNZ superstrates.

(a) E-plane   (b) H-plane
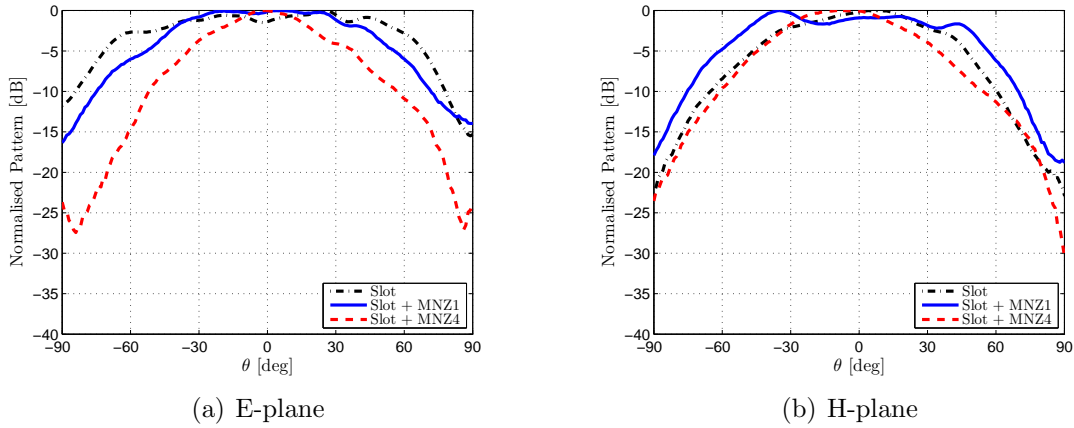
Figure 7.15: Measured E and H planes cuts at 4.80 GHz of the slot antenna in presence of the SR MNZ superstrates referred to their maximum values.

due to the excitation of the spiral resonators [96, 97]. The slot antenna presents an almost omnidirectional pattern in the E plane over the whole frequency range, and a narrower pattern in the H plane, as expected. When the MNZ superstrates are used, the radiation pattern is smooth until the grating lobes appear, which is the point where the radiation patterns are narrower, and hence, higher directivity is expected. Other directivity maxima are expected as the grating lobes evolve and broadside main lobe appear again. For the case of the MNZ1, the grating lobes appear above 4.95 GHz in the E plane results, whereas for the case of the MNZ4, they are found above 3.65 GHz. The grating lobes are also found in the H plane results, although the narrower patterns may not be found at the same frequencies as the E plane ones.

The half-power beam-width (HPBW) has been retrieved from the measured radiation patterns in order to make an initial estimation of the directivity of the slot and MNZ superstrates as the radiation pattens. The HPBW results are plotted in Figure

(a) E-plane Air

(b) H-plane Air

(c) E-plane MNZ1

(d) H-plane MNZ1

(e) E-plane MNZ4

(f) H-plane MNZ4
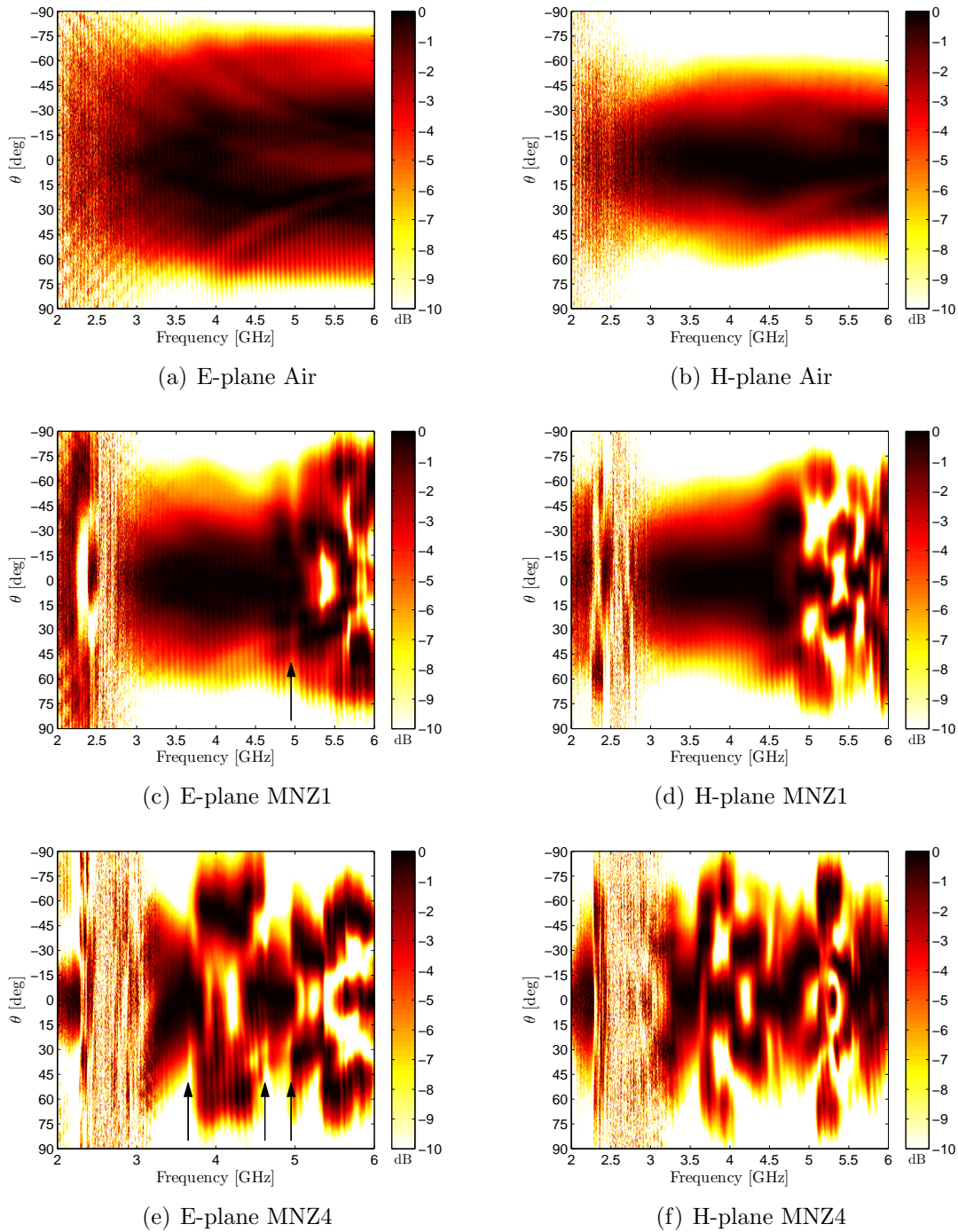
Figure 7.16: Measured normalised E and H planes of the slot antenna in the presence of the SR MNZ superstrates.

7.17 from 2 to 6 GHz. The use of the MNZ1 superstrate strongly reduces the HPBW in the E plane results of the slot antenna in free-space almost over the whole frequency range, whereas the use of the MNZ4 superstrate even outperforms the MNZ1, but around several frequencies only. In addition, the HPBW in the H plane results is only improved with the use of the MNZ4 superstrate, whereas the MNZ1 reports similar

results to those of the slot antenna alone.

(a) E-plane
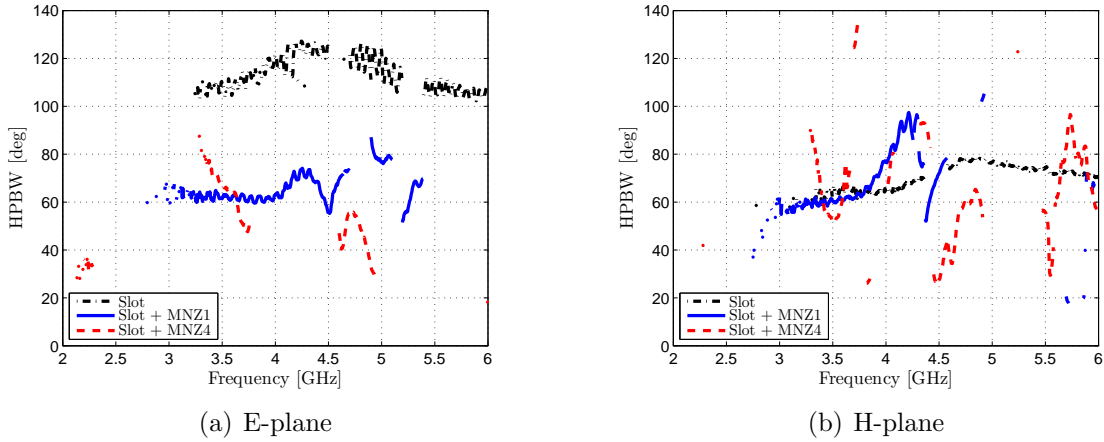
(b) H-plane

Figure 7.17: Measured HPBW for the E and H planes of the slot antenna in presence of the SR MNZ superstrates.

The directivity of an antenna is expressed as (7.2), where $t(\theta, \phi)$ is the normalised radiation pattern:

$$D = \frac{4\pi}{\int\limits_{0}^{\pi} \int\limits_{0}^{2\pi} t(\theta, \phi)\, sin\theta d\theta d\phi} \tag{7.2}$$

The directivity of the slot antenna and the SR MNZ superstrates has been computed according to (7.2) from the measured complete radiation patterns at the frequencies where the minimum HPBWs were found. The computed directivity results are plotted in Figure 7.18 for the three cases, and they are compared with the effective directivity D_{eff} produced by an uniform aperture A_{eff} of the same size as the MNZ superstrates, that is, 120 mm × 120 mm. The effective directivity D_{eff} is defined as (7.3):

$$D_{eff} = \frac{A_{eff}\, 4\pi}{\lambda^2} \tag{7.3}$$

The directivity of the slot antenna alone is found to be about 8 dB, and it is observed that the use of MNZ superstrates slightly increases the directivity of the slot antenna. As observed in the HPBW results, the MNZ4 superstrate offers a better performance than the MNZ1, in spite of fewer frequencies of operation. For instance, at 4.80 GHz, the directivity of the slot antenna is 8.36 dB, whereas the directivity for the MNZ1 and MNZ4 are 9.75 and 11.07 dB, respectively. Although these results are found about 4-5 dB below the effective directivity D_{eff}, a directivity enhancement of about 2.7 dB is obtained for the MNZ4 case.
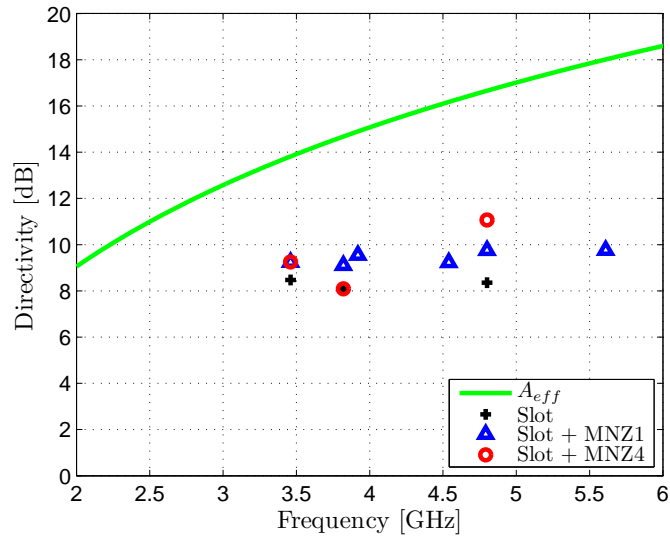
Figure 7.18: Measured directivity results for the slot antenna in free space and with the MNZ1 and MNZ4 superstrates. The effective directivity is computed using (7.3) for a square aperture A_{eff} with size 120 mm $\times$ 120 mm.

7.6   Chapter Conclusions

The broadside radiation power and directivity improvements of a MNZ cover above a slot antenna have been experimentally verified. Two different SR AMM slabs have been used as MNZ superstrates for a slot antenna, achieving a broadside power and directivity increase of about 5 dB and 3 dB, respectively.

Chapter 8

Conclusions

8.1 Main conclusions

The focus of this doctoral thesis has been the investigation of the the potentials and limitations of planar and volumetric magnetic metamaterials to be used in different antenna applications operating at the GHz frequencies.

In this way, the spiral resonator (SR) has been chosen as the magnetic inclusion to be used as the artificial magnetic material (AMM) due to its reduced size unit cell dimensions. The measured reflecting results of the fabricated AMM slab confirmed its predicted PMC performance around the resonant frequency, although the PMC response has been found in a narrow (but sufficient) frequency band of operation. Then, such AMM slab has been successfully applied to realise an AMC reflector, leading to a low profile dipole antenna, while overcoming and considerably reducing the required $\lambda/4$ antenna reflector distance.

The designed single layer AMM slabs are characterised by a dual PEC/PMC response, that is, one side of the slab reflects like a PMC, whereas the opposite side reflects like a PEC. However, the smart combination of two single layer AMM slabs, with their PMC sides facing outwards, has resulted in a bidirectional AMC slab that has been successfully applied to design a compact antenna system composed of two monopole antennas. By using a bidirectional AMC spacer between the monopole an-

tennas, the antennas are decorrelated, that is, each antenna is simultaneously matched (S_{11} < -10 dB) and decoupled (S_{21} < -10 dB). This fact is also confirmed by the measured quasi-orthogonal radiation patterns of the monopole antennas. Although this application has been developed with monopole antennas, the concept may be applied to other antenna types, leading to the design of smaller and more compact antenna systems composed of two or more antennas.

Another interesting application of the AMC reflectors is the transpolarisation property. A 90° polarisation conversion in reflection can be easily achieved by having a reflecting surface with a reflection phase difference of ±180° between two orthogonal directions, thus achieving a polarisation rotation of 90° in the resulting reflected wave. Such cross-polarising surfaces allow linear-to-linear, linear-to-circular, and circular-to-circular (with same handedness) polarisation conversions. The cross-polarisation has been initially tested by combining the SR AMM slab (reflecting with a phase of 0°) with an array of strips (reflecting with a phase of ±180°. Measured results confirmed the transpolarisation effect around the PMC frequency of the SR AMM slab. In addition, the transpolarisation has been exploited by means of a planar metamaterial design fabricated with a single dielectric layer, due to its ease of fabrication and reduced thickness. This planar design has been successfully applied to realise a modified trihedral corner reflector with a high cross-polar response at the designed frequency of operation. The fabricated prototype has been measured in the anechoic chamber, but also in field measurements at Campus Nord UPC with the help of a X-band GB-SAR system, confirming its suitability for passive polarimetric synthetic aperture radar (PolSAR) calibration purposes.

Besides the AMC applications of the designed SR AMM slabs, it has been seen that the magnetic inclusions (i.e. spiral resonators) present a relative magnetic permeability (μ_r) with a dispersive response. The PMC response of the SR AMM slab is found in the frequency band where μ_r is negative, that is, after the resonance, thus confirming the non-propagating blocking/reflecting response for the AMC applications. In addition, μ_r has values above 1 in the frequency band below the resonance. In this case, the SR AMM has been applied to miniaturise patch antennas by taking advantage of its magneto-dielectric response. Antenna miniaturisation has been achieved albeit with a narrow bandwidth; this may be due to the fact that the theoretically derived μ_r is lower than the relative permittivity ε_r in that frequency band, and also due to the dispersive response and bianisotropy effects of the SR inclusions. The last application for the SR AMM metamaterial has been found in the frequency range after its resonance where μ_r presents near zero values (MNZ), that is, $0 < \mu_r < 1$. In that case, a leaky wave antenna (LWA) can be realised by placing the SR AMM slab as the MNZ cover of a slot antenna, devoted to increasing the radiated power and directivity of the antenna

system. The measured results showed an increase in the radiated power and directivity at broadside, and they confirmed the LWA response.

As a general conclusion, the investigation on the SR AMM metamaterial has led to different antenna applications due to the exploitation of the dispersive relative magnetic permeability property of this magnetic inclusion. Therefore, such AMM metamaterials are seen as multifunctional designs because they present a different response depending on the frequency of operation, leading to the realisation of the aforementioned different applications, even though the SR AMM metamaterial is probably not the optimal metamaterial design to be used in each application presented. In addition, the dispersion and bianisotropy effects, intrinsic in most loop like magnetic inclusions, decrease the overall performance of the AMM metamaterial in the antenna application. This fact results in a narrow bandwidth of operation, although it is sufficient in most applications.

Finally, in spite of some drawbacks, Metamaterials can play an important role in trade-offs between design specifications and requirements, by introducing a different perspective on EM, as well as design and optimisation of antennas.

8.2   Future research lines

Looking at the future of metamaterials for antenna applications, we have seen the potentials of the multifunctional SR AMM metamaterials. However, such loop-like magnetic inclusions suffer from unwanted bianisotropic effects. This fact could be overcome by using non-bianisotropic magnetic inclusions, such as single layer symmetric magnetic resonators, or double sided magnetic inclusions. This results in two interesting properties:

- A non-bianisotropic AMM metamaterial lacks internal cross-polarising effects, and hence, the desired metamaterial response is substantially improved. This could be the case of the SR AMM slab used as an AMC reflector, where a small portion of the incident electric field is not reflected back, and is propagated inside the AMC slab through the SR inclusions.

- A symmetric magnetic inclusion inherently presents a double-sided PMC response. This fact may lead to the design of thinner bidirectional AMC spacer, thus leading to more compact multiple antenna systems.

The second research line starts from the design of the compact two-antenna system with the AMC spacer. Although the AMC spacer has successfully decorrelated the two monopole antennas, a performance assessment from a Telematics point of view is

required. This has been partially investigated in a Master Thesis by Marc Imbert [139], developed from the main work of this thesis. The designed optimised AMC spacer at 2.45 GHz is used as a node in a wireless ad hoc network. The measured data transmission (capacity) results in a realistic multi-channel scenario showing that the AMC spacer present by far the best results, when compared to other type of spacers placed in between two close antennas. However, due to the volumetric size of the required spacer, this solution is not compatible with current trends in Electronics designs, where all the components in a Tx/Rx system are placed over the same dielectric board, including the antennas. In such a case, some AMC designs would still be feasible if they were etched around the antennas in the dielectric substrate.

A third research line could be devoted to the optimisation of the modified trihedral corner reflector that produces a high cross-polar response. This device is of interest to the Geoscience community for the calibration of polarimetric synthetic aperture radar (PolSAR) systems due to its ease of fabrication in planar dielectric technology, and because it is a passive device which can be placed anywhere without an electrical connection, representing a unique advantage for passive calibration of airborne or satellite PolSAR platforms. After the preliminary field results with a ground based SAR (GB-SAR) system, these field measurement campaigns could be extended to current PolSAR satellite missions like the European Space Angency (ESA) Sentinnel-1.

Appendix A

RCS Measurements in Anechoic Chamber and Time-Domain Gating Method

A simple scheme of the time-domain (TD) gating method [133, 134] for the RCS measurements in the anechoic chamber is presented in Figure A.1.

The gating method is applied to the measured results of the transpolarising surface. The initial measured results are plotted in Figure A.2.

The time-domain gating method is applied to the initial measured data in several steps that are described as follows:

1. Empty chamber

   The empty chamber response is obtained when measuring the scenario without the presence of the antenna under test (AUT), or in our case, without the transpolarising surface. This result is useful to reduce the inherent reflections due to the environment present in the measured data. When the empty chamber correction is applied, initial measured data appear more clarified, and the transpolarisation response is seen around 10 GHz, as it is shown in Figure A.3. However, measured data is still affect by the couplings between antennas.
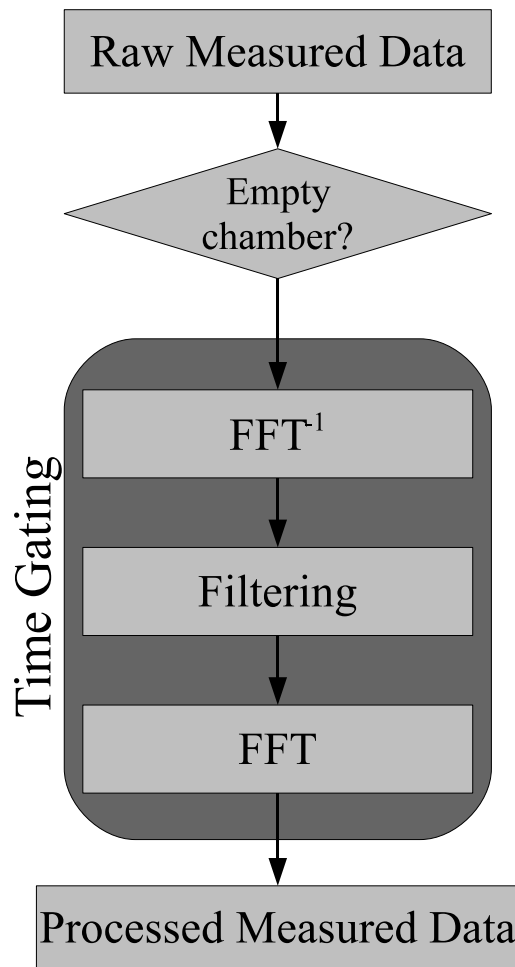
Figure A.1: Time gating method scheme.

2. <u>Frequency-to-time</u>

Once the empty chamber correction is applied, measured data are converted from frequency domain (FD) to time domain (TD). As it is shown in Figure A.4, several peaks appear above a distance of 5 m; the first and highest peak is due to the response of the transpolarising surface, because is found around 5.35 m, which corresponds to the separation between the antennas and the transpolarising surface. Some peaks appear above 5.35 m, which may be due to the metallic parts of the rotor.

3. <u>Gating window</u>

A gating window is then applied to the time domain measured data. The window is centred at the distance where the maximum peak occurs, due to the response of the transpolarising surface, and the maximum width is limited by the following peak, which is due to the metallic parts of the rotor. In this way, the time domain response of the transpolarising surface is filtered, as it is shown in Figure A.5. In
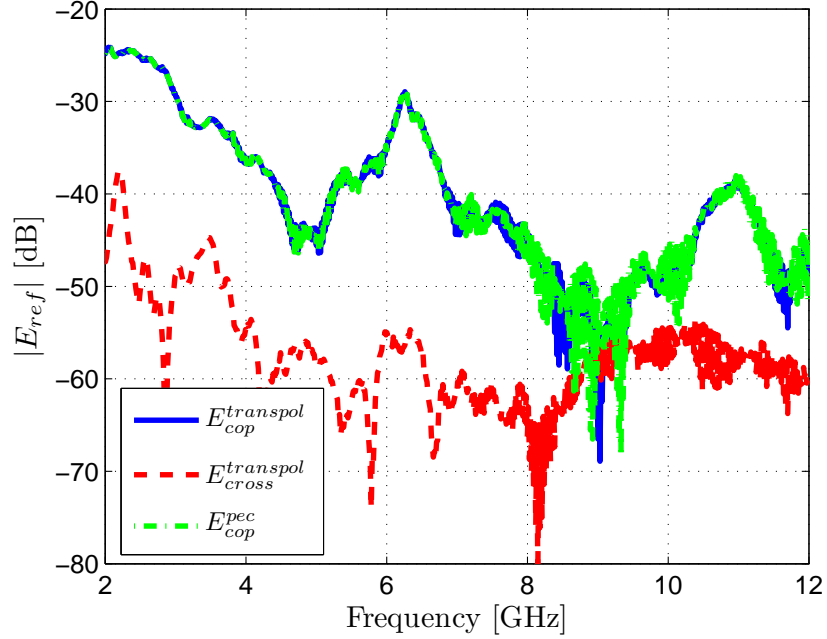
Figure A.2: Measured reflected co-polar ($E_{cop}^{transpol} \equiv E_x$) and cross-polar ($E_{cross}^{transpol} \equiv E_y$) components of the transpolarising surface, and the co-polar (E_{cop}^{pec}) component of the metallic surface.

this case, a hanning window has been applied as the gating window.

4. Time-to-frequency

Finally, the time domain measured data is transformed back to frequency domain. After this transformation, measured data presents a smoother shape, so the undesired effects caused by the couplings between the antennas have been removed. This fact is evidenced in Figure A.6.

Processed measured data need to be normalised by the co-polar response of the metallic surface, by applying expressions defined in (5.5). After this normalisation, the co-polar and cross-polar response of the transpolarising surface have a maximum value of 0 dB, as it is shown in Figure A.7. In Figure A.8, the final processed measured data is presented in logarithmic scale from 8 to 12 GHz. After the application of the time gating method, the transpolarisation response is clearly revealed around 9.8 GHz. The linear scale representation of the measured data is plotted in Figure A.9. The phase of the co-polar and the cross-polar components is plotted in Figure A.10. The phase difference between both components is $\pm 90°$ along the whole frequency range, as it was pointed out in the numerical simulations.
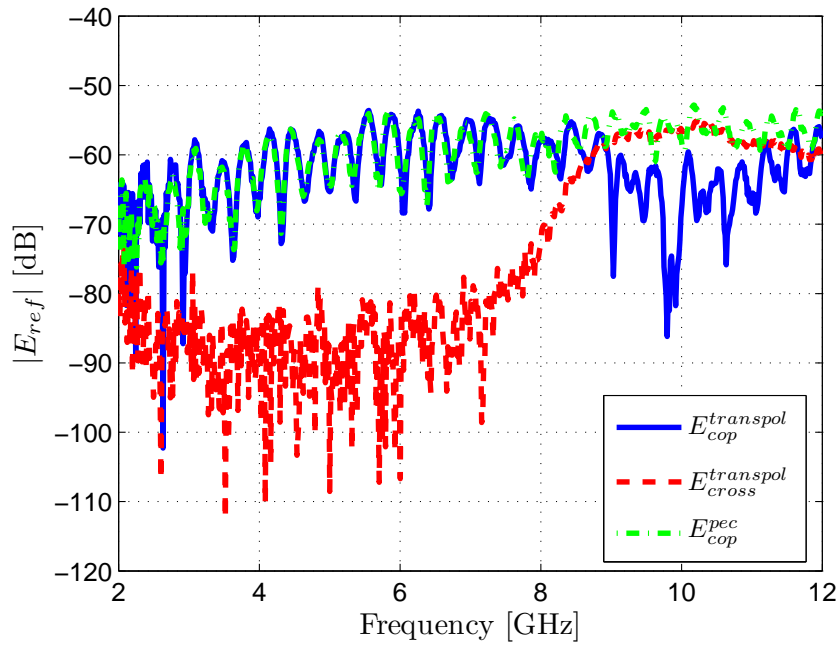
Figure A.3: Measured data after applying empty chamber correction.
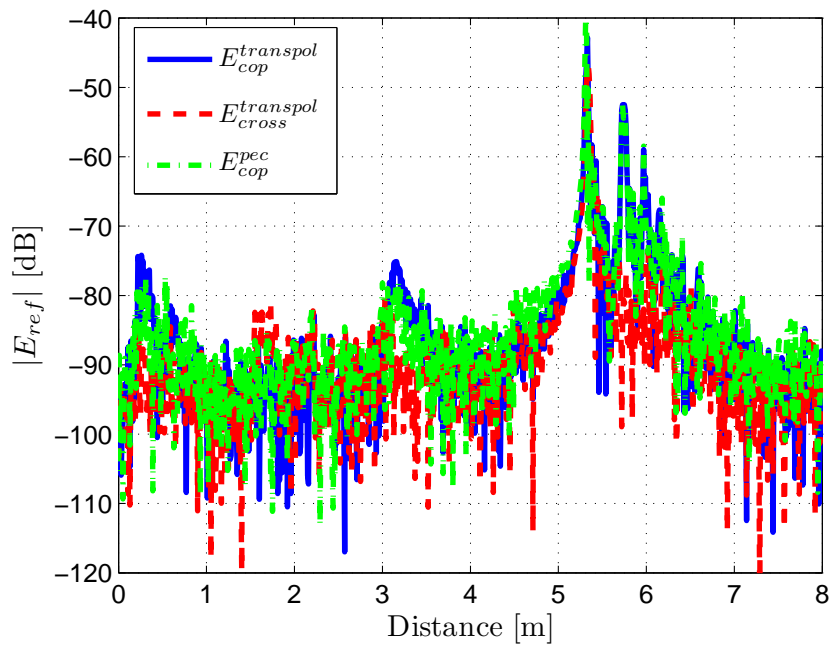
Figure A.4: Measured data in time domain.
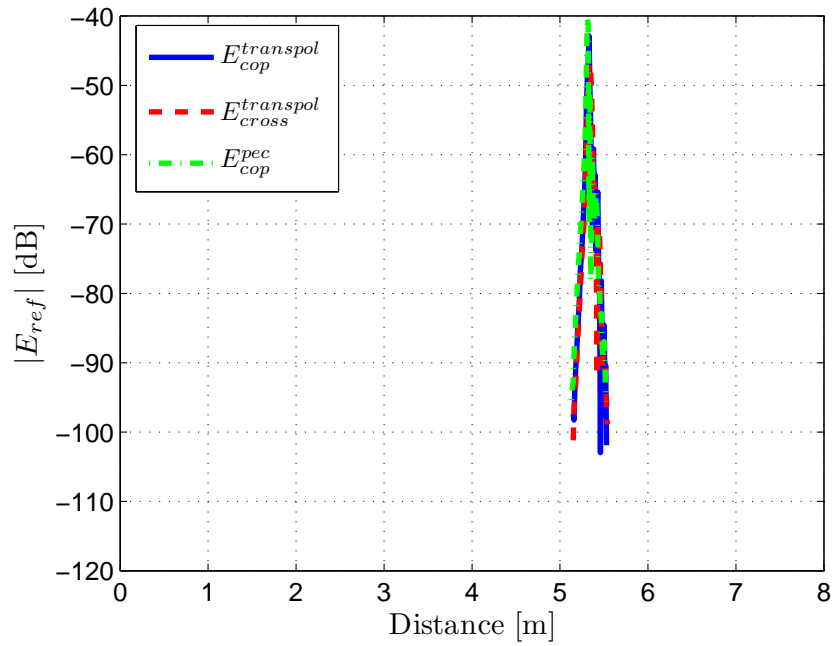
Figure A.5: Measured data in time domain after applying the gating window.
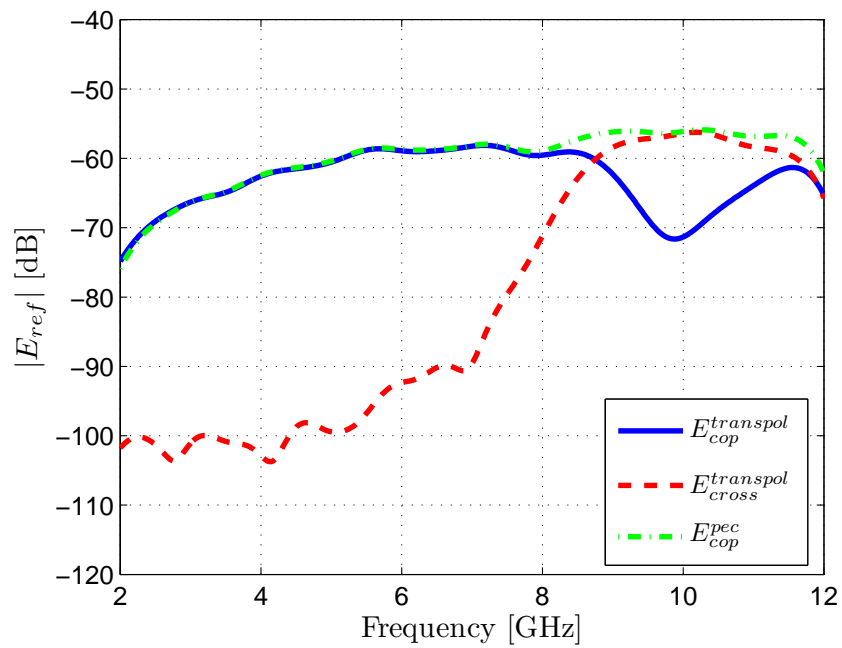
Figure A.6: Measured data in frequency domain after applying the gating window.
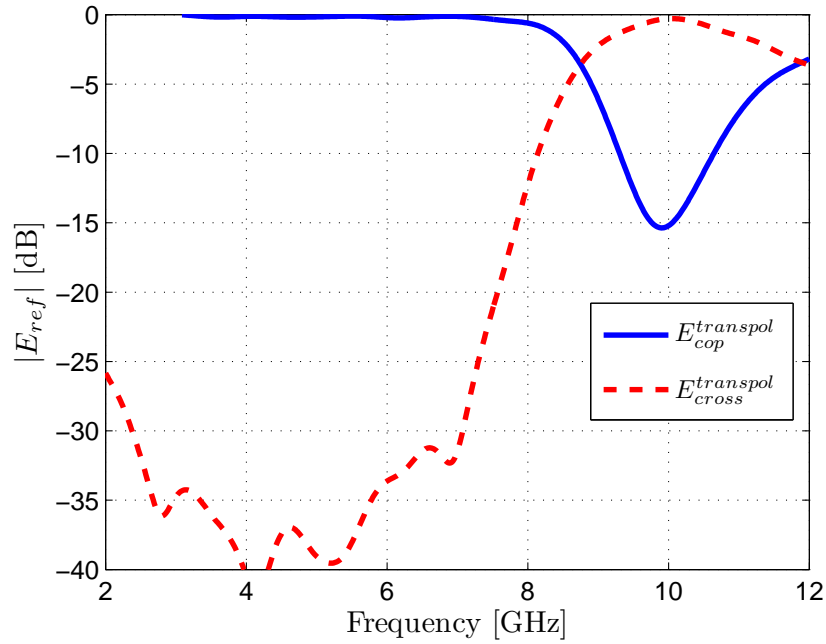
Figure A.7: Measured data in frequency domain after applying the metallic surface response normalisation.
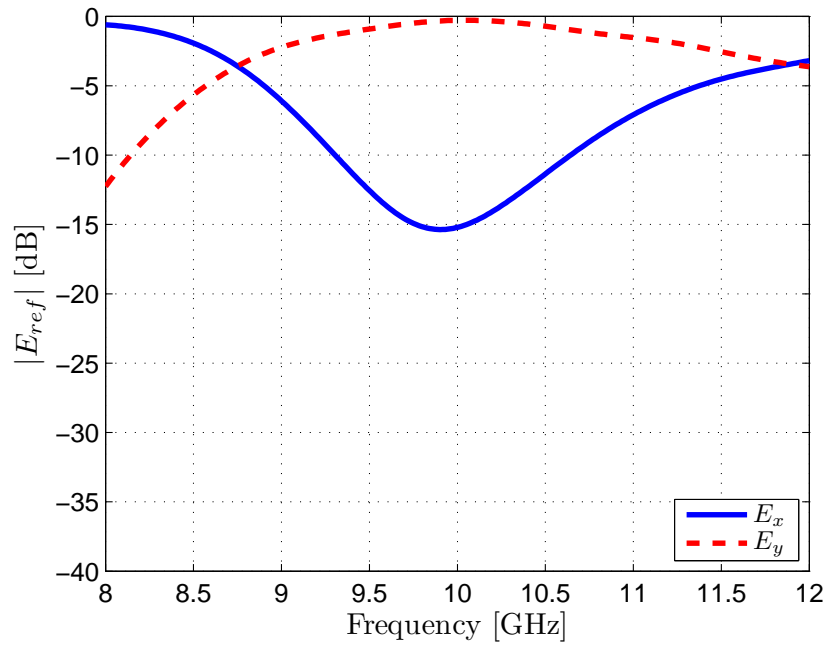
Figure A.8: Measured reflected co-polar (E_x) and cross-polar (E_y) components for normal incidence in logarithmic scale.
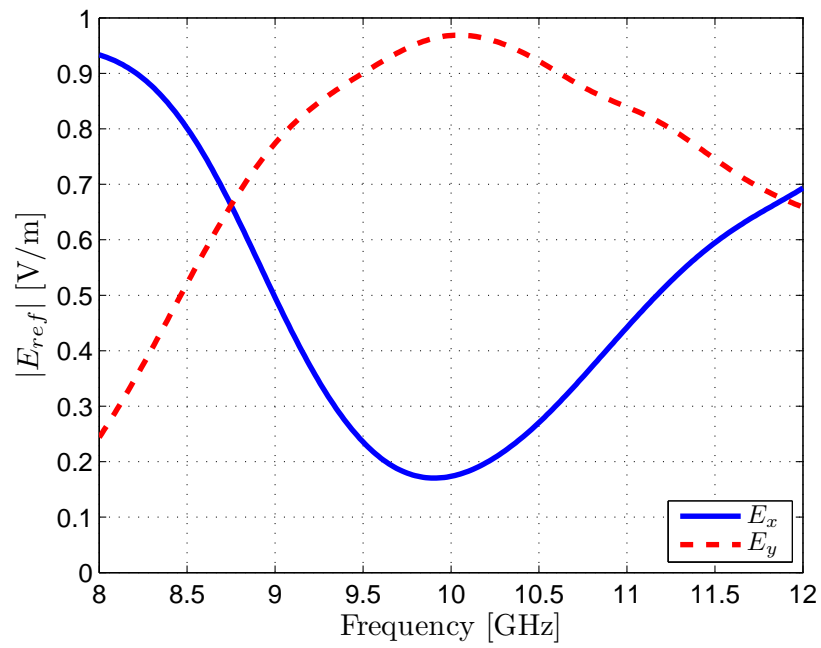
Figure A.9: Measured reflected co-polar (E_x) and cross-polar (E_y) components for normal incidence in linear scale.
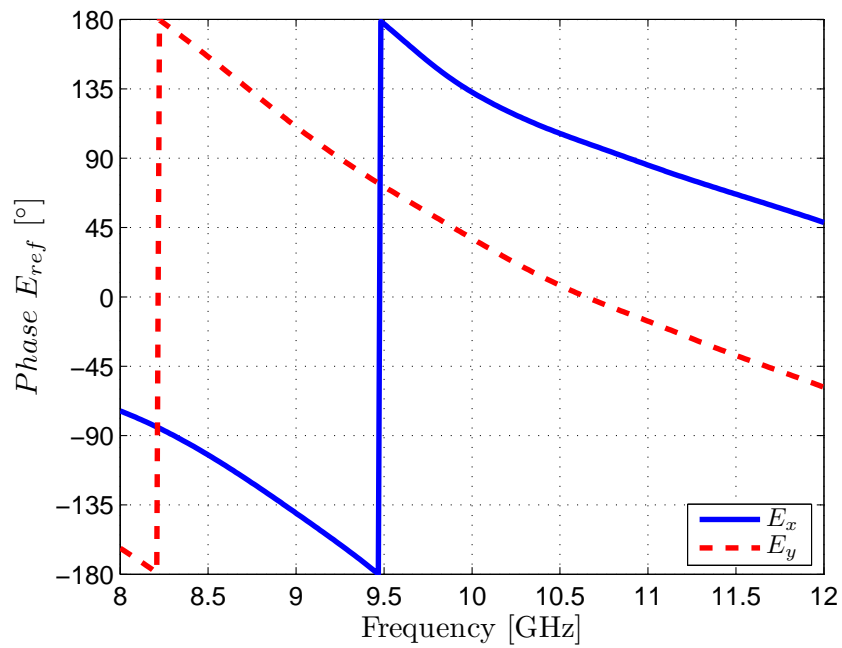
Figure A.10: Measured reflected co-polar (E_x) and cross-polar (E_y) phase components for normal incidence.

Appendix B

List of Publications

The work presented in this thesis has contributed to the publication of several international peer-reviewed article and conference papers.

Book Chapters

1. P.J. Ferrer, J.M. González-Arbesú, J. Romeu, J. Parrón, G. Junkin, and R. Villarino, "Small and Multiband MNG Resonators: Spiral, Pre-fractal and Other Geometries", *Handbook on Artificial Materials*, F. Capolino, Ed., CRC Press, 2009.

Journals

1. P.J. Ferrer, B. Kelem, and C. Craeye, "Design of Broadband Transpolarising Surfaces", *Microwave and Optical Technology Letters*, vol. 48, no. 12, pp. 2606-2611, Dec. 2006.

2. P.J. Ferrer, J.M. González-Arbesú, J. Romeu, and A. Cardama, "Bidirectional Artificial Magnetic Reflectors at Microwave Frequencies", *Microwave and Optical Technology Letters*, vol. 49, no. 8, pp. 1949-1953, Aug. 2007.

3. P.J. Ferrer, J.M. González-Arbesú, and J. Romeu, "Decorrelation of two closely spaced antennas with a Metamaterial AMC Surface", *Microwave and Optical Technology Letters*, vol. 50, no. 5, pp. 1414-1417, May 2008.

4. P.J. Ferrer, C. López-Martínez, A. Aguasca, L. Pipia, J.M. González-Arbesú, X. Fabregas, and J. Romeu, "Transpolarising Trihedral Corner Reflector Characterisation Using a GB-SAR System", *IEEE Geoscience and Remote Sensing Letters*, vol. 8, no. 4, pp. 774-778, Jul. 2011.

5. M. Imbert, P.J. Ferrer, J.M. González-Arbesú, and J. Romeu, "Assessment of the Performance of a Metamaterial Spacer in a Closely Spaced Multiple-Antenna Syste", *IEEE Antennas and Wireless Propagation Letters*, pp. 720-723, Jun. 2012.

Conferences

1. B. Kelem, P.J. Ferrer, and C. Craeye, "Design of Broadband Transpolarising Surfaces", *Proceedings of 3rd Workshop Metamaterials 2006*, Roma (Italy), 30-31 March 2006.

2. P.J. Ferrer, J.M. González-Arbesú, and J. Romeu, "Design and measurement of a Spiral-Cell PMC for Metamaterial Applications", *Proceedings of the IEEE AP-S/URSI 2006 International Sysmposium (AP-S 2006)*, Albuquerque (USA), 9-14 Jul. 2006.

3. P.J. Ferrer, F. Fortuny, J.M. González-Arbesú, and J. Romeu, "Desings for Bifrequency and Bidirectional AMC Surfaces", *Proceedings of the 1st European Conference on Antennas and Propagation (EuCAP 2006)*, Nice (France), 6-10 Nov. 2006.

4. P.J. Ferrer, J.M. González-Arbesú, and J. Romeu, "Bidirectional Metamaterial Separator for Compact Antenna Systems", *Proceedings of the IEEE Antennas and Propagation Symposium (AP-S 2007)*, Honolulu (USA), 9-15 June 2007.

5. P.J. Ferrer, C. López-Martínez, X. Fàbregas, J.M. González-Arbesú, J. Romeu, A. Aguasca, and C. Craeye, "Transpolarizing Surfaces for Polarimetric SAR Systems Calibration", *Proceedings of the IEEE International Geoscience and Remote Sensing Symposium (IGARSS 2007)*, Barcelona (Spain), 23-28 Jul. 2007.

6. P.J. Ferrer, J.M. González-Arbesú, J. Romeu, and C. Craeye, "Design and Fabrication of Transpolarising Surfaces", *Proceedings of the 14th International Student Seminar (ISS 2007)*, Belfast (UK), August 2007.

7. P.J. Ferrer, J.M. González-Arbesú, and J. Romeu, "Metamaterial slabs with double side PMC response", *Proceedings of the 1st International Congress on Advanced Electromagnetic Materials in Microwaves and Optics (Metamaterials'07)*, Roma (Italy), 22-26 Oct. 2007.

8. P.J. Ferrer, J.M. González-Arbesú, J. Romeu, and C. Craeye, "Design and Fabrication of a Cross-polarising AMC Surface", *Proceedings of the 2nd European Conference on Antennas and Propagation (Eucap 2007)*, Edinburgh (UK), 11-16 Nov. 2007.

9. P.J. Ferrer, J. Romeu, J.M. González-Arbesú, and J. Parrón, "Broadside Radiation Enhancement Using MNZ Substrate", *Proceedings of the 2nd Young Scientist Meeting on Metamaterials 2008 (YSMM'08)*, Barcelona (Spain), 5-8 Feb. 2008.

10. P.J. Ferrer, J. Romeu, J.M. González-Arbesú, J. Parrón, F. Capolino, F. Bilotti, L. Vegni, G. Lovat, and P. Burghignoli, "Broadside Radiation Enhancement Using a Spiral Resonator MNZ Metamaterial Substrate", *Proceedings of the IEEE Antennas and Propagation Symposium (AP-S 2008)*, San Diego, CA (USA), 5-11 Jul. 2008.

11. P.J. Ferrer, I. Calafell, J.M. González-Arbesú, and J. Romeu, "Bandwidth and Size Behaviour Study for Patch Antennas using Metamaterial Fillings with Positive Permittivity and Permeability", *Proceedings of the 2nd International Congress on Advanced Electromagnetic Materials in Microwaves and Optics (Metamaterials'08)*, Pamplona (Spain), 21-26 Sept. 2008.

12. P.J. Ferrer, J.M. González-Arbesú, C. Craeye, and J. Romeu, "Transpolarizing surfaces and potential applications", *Proceedings of the European Microwave Conference (EuMC 2008)*, Amsterdam (The Netherlands), 27-31 Oct. 2008.

13. P.J. Ferrer, J. Romeu, J.M. González-Arbesú, A. Aguasca, L. Pipia, C. López-Martínez, and X. Fàbregas, "Transpolarizing Trihedral Measurement Using UPC X-BAND GBSAR", *Proceedings of the IEEE International Geoscience and Remote Sensing Symposium (IGARSS 2009)*, Cape Town (South Africa), 12-17 Jul. 2009.

14. P.J. Ferrer, J.M. González-Arbesú, and J. Romeu, "Spiral resonator Mu-Near-Zero Substrates for Grounded Slot Antennas", *Proceedings of the European Conference on Antennas and Propagation (Eucap 2010)*, Barcelona (Spain), 12-16 April 2010.

15. I. Calafell, P.J. Ferrer, J.M. González-Arbesú, and J. Romeu, "Microstrip Patch Antenna Design Using Artificial Material Loadings", *Proceedings of the European Conference on Antennas and Propagation (Eucap 2010)*, Barcelona (Spain), 12-16 April 2010.

16. M. Imbert, P.J. Ferrer, J.M. González-Arbesú, and J. Romeu, "Design of a Bidirectional Metamaterial Spacer at 2.45 GHz", *Proceedings of the European Conference on Antennas and Propagation (Eucap 2010)*, Barcelona (Spain), 12-16 April 2010.

Invited Talks

1. P.J. Ferrer, J.M. González-Arbesú, and J. Romeu, "Metamaterial Applications to Antenna Design", *Workshop on Aplicaciones de los Metamateriales en circuitos, antenas y subsistemas de microondas, milimétricas y fotónicos*, XXII URSI, Tenerife, 19-21 Sep. 2007.

2. P.J. Ferrer, J.M. González-Arbesú, and J. Romeu, "Review on Artificial Magnetic Materials for Antenna Applications", *Proceedings of the 3rd Young Scientist Meeting on Metamaterials 2009 (YSMM'09)*, Leganés (Spain), 6-8 July 2009.

Supervised Master Thesis

1. I. Calafell, "Microstrip patch antenna design with artificial material loadings", ETSETB, TSC, UPC, Feb. 2009.

2. M. Imbert, "Disseny d'una pantalla bidireccional AMC per a un sistema compacte d'antenes a 2.45 GHz", ETSETB, TSC, UPC, May 2010.

Appendix C

List of Acronyms

AEC   Artificial Electric Conductor

AER   Artificial Electric Reflector

AMC   Artificial Magnetic Conductor

AMM   Artificial Magnetic Material

AMR   Artificial Magnetic Reflector

B   Bruderhedral

BC   Boundary Condition

BC-SRR   Broadside-Coupled SRR

BW   Bandwidth

CLL   Capacitively Loaded Loop (resonator)

CP   Circular Polarisation

CRLH-TL   Composite Right-Left-Handed Transmission Line

DCR   Dihedral Corner Reflector

DGS	Defected Ground Structure
DM	Direct Maximum FBW Method
DNG	Double Negative (resonator/medium/media)
DPS	Double Positive (resonator/medium/media)
ENG	Epsilon Negative (resonator/medium/media)
ENZ	Epsilon-Near-Zero (resonator/medium/media)
FBW	Fractional Bandwidth
GB-SAR	Ground-Based SAR
HIS	High Impedance Surface
HPBW	Half Power Beam-Width
ISM	Industrial, Scientific and Medical radio band
JGM	Johnston-Geissler Method
LHM	Left-Handed medium/media
LH-TL	Left-Handed Transmission Line
LP	Linear Polarisation
LWA	Leaky Wave Antenna
MD	Magneto-Dielectric
MDPA	Magneto-Dielectric Patch Antenna
MEA	Multiple Element Antenna
MIMO	Multiple Input Multiple Output
MNG	Mu Negative (resonator/medium/media)
MNZ	Mu-Near-Zero (resonator/medium/media)
MSRR	Multiple SRR
MTM	Metamaterial
MPA	Microstrip Patch Antenna

PARC	Polarimetric Active Radar Calibrator
PEC	Perfect Electric Conductor
PMC	Perfect Magnetic Conductor
PRS	Partially Reflecting Surface
PolSAR	Polarimetric SAR
RCS	Radar Cross Section
RHM	Right-Handed medium/media
SAR	Synthetic Aperture Radar
SR	Spiral Resonator
SRR	Split Ring Resonator
TCR	Trihedral Corner Reflector
TTCR	Transpolarising Trihedral Corner Reflector
TUT	Trihedral Under Test
VSWR	Voltage Standing Wave Ratio
YBM	Yaghjian and Best Maximum FBW Method
VNA	Vector Network Analyser

Bibliography

[1] S.A. Tretyakov, "Analytical Modeling in Applied Electromagnetics", *Artech House*, 1st Edition, 2003.

[2] G.V. Eleftheriades, and K.G. Balmain, "Negative Refraction Metamaterials. Fundamental Principles and Applications", *IEEE Press - John Wiley & Sons*, 2005.

[3] C. Caloz, and T. Itoh, "Electromagnetic Metamaterials. Transmission Line Theory and Microwave Applications", *John Wiley & Sons*, 2006.

[4] N. Engheta, and R.W. Ziolkowski, "Metamaterials. Physics and Engineering Explorations", *IEEE Press - John Wiley & Sons*, 2006.

[5] A.K. Sarychev, and V.M. Shalaev, "Electrodynamics of Metamaterials", *World Scientific*, 2007.

[6] R. Marqués, F. Martín, and M. Sorolla, "Metamaterials with Negative Parameters. Theory, Design and Microwave Applications", *John Wiley & Sons*, 2008.

[7] F. Capolino, "Metamaterials Handbook. Vol 1. Theory and Phenomena of Metamaterials", *CRC Press*, 2009.

[8] F. Capolino, "Metamaterials Handbook. Vol 2. Applications of Metamaterials", *CRC Press*, 2009.

[9] Y. Hao, and R. Mittra, "FDTD Modeling of Metamaterials. Theory and Applications", *Artech House*, 2009.

[10] L. Solymar, and E. Shamonina, "Waves in Metamaterials", *Oxford University Press*, 2009.

[11] B.A. Munk, "Metamaterials. Critique and Alternatives", *John Wiley & Sons*, 2009.

[12] S. Zouhdi, A. Shivola, and A.P. Vinogradov, "Metamaterials and Plasmonics: Fundamentals, Modelling, Applications", *Springer*, 2009.

[13] S.A. Ramakrishna, and T.M. Grzegorczyk, "Physics and Applications of Negative Refractive Index Materials", *Spie Press - CRC Press*, 2009.

[14] T.J. Cui, D.R. Smith, and R. Liu, "Metamaterials. Theory, Design and Applications", *Springer*, 2010.

[15] W. Cai, and V. Shalaev, "Optical Metamaterials. Fundamentals and Applications", *Springer*, 2010.

[16] I.V. Shadrivov, M. Lapine, and Y.S. Kivshar, "Nonlinear, Tunable and Active Metamaterials", *Springer*, 2015.

[17] V.G. Veselago, "The electrodynamics of substances with simultaneously negative values of ε and μ", *Sov. Phys. Uspekhi*, 10(4), pp. 509-514, 1968.

[18] J.B. Pendry, A.J. Holden, D.J. Robbins, and W.J. Stewart, "Magnetism from Conductors and Enhanced Nonlinear Phenomena", *IEEE Transactions on Microwave Theory and Techniques*, vol. 47, no. 11, pp. 2075-2084, Nov. 1999.

[19] D.R. Smith, W.J. Padilla, D.C. Vier, S.C. Nemat-Nasser, and S. Schultz, "Composite Medium with Simultaneously Negative Permeability and Permittivity", *Physical Review Letters*, vol. 84, no. 18, pp. 4184-4187, May 2000.

[20] R.A. Shelby, D.R. Smith, S.C. Nemat-Nasser, and S. Schultz, "Microwave transmission through a two-dimensional, isotropic, left-handed metamaterial", *Applied Physics Letters*, vol. 78, no. 4, pp. 489-491, Jan. 2001.

[21] R.V. Craster, and S. Guenneau, "Acoustic Metamaterials. Negative Refraction, Imaging, Lensing and Cloaking", *Springer*, 2013.

[22] P. Deymier, "Acoustic Metamaterials and Phononic Crystals", *Springer*, 2013.

[23] A. Cardama, L. Jofre, J.M. Rius, J. Romeu, S. Blanch and M. Ferrando, "Antenas", *Edicions UPC*, 2nd Edition, Barcelona, 2002.

[24] W. Rotman, "Plasma Simulation by Artificial Dielectrics and Parallel Plate Media", *Transactions of the IRE, APS*, vol. 10, no. 1, pp. 82-95, Jan. 1962.

[25] A. Vallecchi, F. Capolino, and A.G. Schuchinsky, "2-D Isotropic Effective Negative Refractive Index Metamaterial in Planar Technology", *IEEE Microwave and Wireless Components Letters*, vol. 19, no. 5, pp. 269-271, May 2009.

[26] J.F. Wang, Sh.B. Qu, Zh. Xu, J.Q. Zhang, Y.M. Yang, H. Ma, and Ch. Gu, "A candidate three-dimensional GHz left-handed metamaterial composed of coplanar magnetic and electric resonators", *Photonics and Nanostructures - Fundamentals and Applications*, vol. 6, issue 3-4, pp. 183-187, Dec. 2008.

[27] R.A. Shelby, D.R. Smith, and S. Schultz, "Experimental Verification of Negative Index of Refraction", *Science Magazine*, vol. 292, pp. 77-79, Apr. 2001.

[28] J.B. Pendry, and D.R. Smith, "Reversing Light with Negative Refraction", *Physics Today*, vol. 57, no. 6, pp. 37-43, Jun. 2004.

[29] J.B. Pendry, D. Schurig, and D.R. Smith, "Controlling Electromagnetic Fields", *Science Magazine*, vol. 312, pp. 1780-1782, 2006.

[30] D. Schurig, J.J. Mock, B.J. Justice, S.A. Cummer, J.B. Pendry, A.F. Starr and D.R. Smith, "Metamaterial Electromagnetic Cloak at Microwave Frequencies", *Science Magazine*, vol. 314, pp. 977-980, 2006.

[31] D.F. Sievenpiper, L. Zhang, R.F.J. Broas, N.G. Alexópolous, and E. Yablonovitch, "High-Impedance Electromagnetic Surfaces with a Forbidden Frequency Band", *IEEE Transactions on Microwave Theory and Techniques*, vol. 47, no. 11, pp. 2059-2074, Nov. 1999.

[32] A. Feresidis, G. Goussetis, S. Wang, and J.C. Vardaxoglou, "Artificial Magnetic Conductor Surfaces and Their Application to Low-Profile High-Gain Planar Antennas", *IEEE Transactions on Antennas and Propagation*, vol. 53, no. 1, pp. 209-215, Jan. 2005.

[33] L. Li, X. Dang, L. Wang, B. Li, H. Liu, and C. Liang, "Reflection Phase Characteristics of Plane Wave Oblique Incidence on the Mushroom-like Electromagnetic Band-Gap Structures", *Proc. Asia-Pacific Microw. Conf.*, 2005.

[34] A. Erentok, P.L. Luljak, and R.W. Ziolkowski, "Characterization of Volumetric Metamaterial Realization of an Artificial Magnetic Conductor for Antenna Applications", *IEEE Transactions on Antennas and Propagation*, vol. 53, no. 1, pp. 160-172, Jan. 2005.

[35] E. Sáenz, I. Ederra, R. Gonzalo, and P. de Maagt, "Enhancement of the power radiated by a dipole antenna at boresight by means of a left handed superstrate", *IEEE International Workshop on Antenna Technology Small Antennas and Novel Metamaterials*, pp. 9- 12, Mar. 6-8, 2006.

[36] K. Buell, H. Mosallaei, and K. Sarabandi, "Metamaterial Insulator Enabled Superdirective Array", *IEEE Transactions on Antennas and Propagation*, vol. 55, no. 4, pp. 1074-1085, Apr. 2007.

[37] R.W. Ziolkowski, and A. Erentok, "Metamaterial based efficient electrically-small antennas"', *IEEE Transactions on Antennas and Propagation*, vol. 54, no. 7, pp. 2113-2130, Jul. 2006.

[38] A. Alù, N. Engheta, A. Erentok, and R.W. Ziolkowski, "Single-Negative, Double-Negative, and Low-Index Metamaterials and their Electromagnetic Applications", *IEEE Antennas and Propagation Magazine*, vol. 49, no. 1, pp. 23-36, Feb. 2007.

[39] R.B. Greegor, C.G. Parazzoli, J.A. Nielsen, M.H. Tanielian, D.C. Vier, S. Schultz, C.L. Holloway, and R.W. Ziolkowski, "Demonstration of Impedance Matching Using a mu-Negative (MNG) Metamaterial", *IEEE Antennas and Wireless Propagation Letters*, vol. 8, pp. 82-95, Apr. 2009.

[40] G. Lovat, P. Burghignoli, F. Capolino, D.R. Jackson, and D.R. Wilton, "Analysis of Directive Radiation From a Line Source in a Metamaterial Slab With Low Permittivity", *IEEE Transactions on Antennas and Propagation*, vol. 54, no. 3, pp. 1017-1030, May 2006.

[41] M. Kärkkäinen, and P.M.T. Ikonen, "Patch antennas with stacked split-ring resonators as an artificial magneto-dielectric substrate", *Microwave and Optical Technology Letters*, vol. 46, no. 6, pp. 554-556, Sep. 2005.

[42] H. Iizuka, and P.S. Hall, "Left-Handed Dipole Antennas and Their Implementations", *IEEE Transactions on Antennas and Propagation*, vol. 55, no. 5, pp. 1246-1252, May 2007.

[43] C. Caloz, and T. Itoh, "Array Factor Approach of Leaky-Wave Antennas and Application to 1-D/2-D Composite Right/Left-Handed (CRLH) Structures", *IEEE Microwave and Wireless Components Letters*, vol. 14, no. 6, pp. 274-276, Jun. 2004.

[44] M.A. Antoniades, and G.V. Eleftheriades, "A Broadband Series Power Divider Using Zero-Degree Metamaterial Phase-Shifting Lines", *IEEE Microwave and Wireless Components Letters*, vol. 15, no. 11, Nov. 2005.

[45] R. Islam, F. Elek, and G.V. Eleftheriades, "Coupled-line metamaterial coupler having co-directional phase but contra-directional power flow", *Electronics Letters*, vol. 40, no. 5, pp. 315-317, Mar. 2004.

[46] F. Martín, F. Falcone, J. Bonache, R. Marqués, and M. Sorolla, "Split ring resonator based left handed coplanar waveguide", *Appl. Phys. Lett.*, vol. 83, pp. 4652-4654, Dec. 2003.

[47] F. Falcone, F. Martin, J. Bonache, R. Marqués, and M. Sorolla, "Coplanar waveguide structures loaded with split ring resonators", *Microwave Opt. Tech. Lett.*, vol. 40, pp. 3-6, Jan. 2004.

[48] F. Falcone, T. Lopetegi, J.D. Baena, R. Marqués, F. Martín, and M. Sorolla, "Effective negative-ε stop-band microstrip lines based on complementary split ring resonators", *IEEE Microwave Wirel. Comp. Lett.*, vol. 14, pp. 280-282, Jun. 2005.

[49] F. Falcone, F. Martín, J. Bonache, M.A.G. Laso, J. García-García, J.D. Baena, R. Marqués, and M. Sorolla, "Stop band and band pass characteristics in coplanar waveguides coupled to spiral resonators", *Microwave Opt. Tech. Lett.*, vol. 42, pp. 386-388, Sep. 2004.

[50] J. Kim, C.S. Cho, and J.W. Lee, "CPW bandstop filter using slot-type SRRs", *Electronics Letters*, vol. 41, no. 24, pp. 1333-1334, Nov. 2005.

[51] I. Gil, J. García-García, J. Bonache, F. Martín, M. Sorolla, and R. Marqués, "Varactor-loaded split ring resonators for tunable notch filters at microwave frequencies", *Electronics Letters*, vol. 40, no. 21, pp. 1347-1348, Oct. 2004.

[52] J.D. Baena, R. Marqués, and F. Medina, "Artificial magnetic metamaterial design using spiral resonators", *Physical Review B*, vol. 69, p. 014402, 2004.

[53] J.S. Derov, B.W. Turchinetz, E.E. Crisman, A.J. Drehman, S.R. Best, and R.M. Wing, "Free space measurements of negative refraction with varying angles of incidence", *IEEE Microwave Wireless Components Letters*, vol. 15, no. 9, pp. 567-569, Sep. 2005.

[54] C.R. Simovski and S. He, "Frequency range and explicit expressions for negative permittivity and permeability for an isotropic medium formed by a lattice of perfectly conducting Ω particles", *Physics Letters A*, vol. 311, 254, 2003.

[55] R. Marqués, F. Medina, and R. Rafii-El-Idrissi, "Role of bianisotropy in negative permeability and left-handed metamaterials", *Physical Review B*, 65, pp. 144440, 2002.

[56] H. Zhao and T.J. Cui, "A double-spiral resonator structure to realize left handed material with lower resonant frequency", *Microwave and Optical Technology Letters*, vol. 48, no. 5, May 2006.

[57] H. Chen, L. Ran, J. Huangfu, X. Zhang, K. Chen, T.M. Grzegorczyk, and J.A. Kong, "Metamaterial exhibiting left-handed properties over multiple frequency bands", *Applied Physics Letters*, 96, 9, 2004.

[58] R.W. Ziolkowski, "Design, Fabrication, and Testing of Double Negative Metamaterials", *IEEE Transactions on Antennas and Propagation*, vol. 51, no. 7, pp. 1516-1529, Jul. 2003.

[59] Ansoft's HFSS (FEM EM numerical method). Website: *www.ansoft.com/hfss/* (last visited, June 2009).

[60] R. Remski, "Analysis of Photonic Bandgap Surfaces Using Ansoft HFSS", *Microwave Journal*, vol. 43, no. 9, pp. 190-198, Sep. 2000.

[61] R. Marqués, J. Martel, F. Mesa, and F. Medina, "Left-Handed-Media Simulation and Transmission of EM Waves in Subwavelength Split-Ring-Resonator-Loaded Metallic Waveguides", *Physical Review Letters*, 89, 18, Oct. 2002.

[62] G. Lubkowski, C. Damm, B. Bandlow, R. Schuhmann, M. Schüßler and T. Weiland, "Broadband transmission below the cutoff frequency of a waveguide loaded with resonant scatterer arrays", *IET Microwave, Antennas and Propagation*, vol. 1, no. 1, pp. 160-169, Jan. 2007.

[63] F. Bilotti, A. Toscano, and L. Vegni, "Design of Spiral and Multiple Split-Ring Resonators for the Realization of Miniaturized Metamaterial Samples", *IEEE Transactions on Antennas and Propagation*, vol. 55, no. 5, pp. 2258-2267, Aug. 2007.

[64] D.R. Smith, S. Schultz, P. Markos, and C.M. Soukoulis, "Determination of effective permittivity and permeability of metamaterials from reflection and transmission coefficients", *Physical Review B*, vol. 65, 195104, Apr. 2002.

[65] D.R. Smith, D.C. Vier, Th. Koschny, and C.M. Soukoulis, "Electromagnetic parameter retrieval from inhomogeneous metamaterials", *Physical Review E*, vol. 71, 036617, Mar. 2005.

[66] L.L. Hou, J.Y. Chin, X.M. Yang, X.Q. Lin, R. Liu, F.Y. Xu, and T.J. Cui, "Advanced parameter retrievals for metamaterial slabs using an inhomogeneous model", *Journal of Applied Physics*, vol. 103, 064904, Mar. 2008.

[67] X. Chen, T.M. Grzegorczyk, B.-I. Wu, J. Pacheco Jr., and J.A. Kong, "Robust method to retrieve the constitutive effective parameters of metamaterials", *Physical Review E*, vol. 70, 016608, Jul. 2004.

[68] X. Chen, B.-I. Wu, J.A. Kong, and T.M. Grzegorczyk, "Retrieval of the constitutive parameters of bianisotropic metamaterials", *Physical Review E*, vol. 71, 046610, Apr. 2005.

[69] V.V. Varadan, and R. Ro, "Unique Retrieval of Complex Permittivity and Permeability of Dispersive Materials From Reflection and Transmitted Fields by Enforcing Causality", *IEEE Transactions on Antennas and Propagation*, vol. 55, no. 10, pp. 2224-2230, Oct. 2007.

[70] Z. Li, K. Aydin, and E. Ozbay, "Determination of the effective constitutive parameters of bianisotropic metamaterials from reflection and transmission coefficients", *Physical Review E*, vol. 79, 026610, Feb. 2009.

[71] X. Chen, T.M. Grzegorczyk, and J.A. Kong, "Optimization approach to the retrieval of the constitutive parameters of a slab of general bianisotropic medium", *Progress in Electromagnetics Research*, vol. 60, pp. 1-18, 2006.

[72] G. Lubkowski, R. Schuhmann, and T. Weiland, "Extraction of Effective Metamaterial Parameters by Parameter Fitting of Dispersive Models", *Microwave and Optical Technology Letters*, vol. 49, no. 2, pp. 285-288, Feb. 2007.

[73] J. McVay, A. Hoorfar, and N. Engheta, "Extraction of effective permittivity and permeability of dispersive double-negative slabs using evolutionary programming", *Proceedings of the IEEE Antennas and Propagation International Symposium, AP-S 2007*, pp. 2893-2896, Honolulu (HW), USA, Jun. 9-15, 2007.

[74] W. Xu, L.-W. Li, H.-Y. Yao, and T.-S. Yeo, "Extraction of constitutive relation tensor parameters of SRRs structures using transmission line theory", *Journal of Electromagnetic Waves and Applications*, vol. 20, no. 1, pp. 13-25, Jan. 2006.

[75] H. Chen, L. Ran, J. Huangfu, T.M. Grzegorczyk, and J.A. Kong, "Equivalent circuit model for left-handed metamaterials", *Journal of Applied Physics*, vol. 100, 024915, Jul. 2006.

[76] E. Saenz, P.M.T. Ikonen, R. Gonzalo, and S.A. Tretyakov, "On the definition of effective permittivity and permeability for thin composite layers", *Journal of Applied Physics*, vol. 101, 114910, Jun. 2007.

[77] L. Yousefi, H. Attia, and O.M. Ramahi, "Broadband experimental characterization of artificial magnetic materials based on a microstrip line method", *Progress in Electromagnetics Research*, vol. 90, pp. 1-13, 2009.

[78] A.D. Scher, and E.F. Kuester, "Extracting the bulk effective parameters of a metamaterial via the scattering from a single planar array of particles", *Metamaterials*, vol. 3, pp. 44-55, Feb. 2009.

[79] J.-M. Lerat, N. Malléjac, and O. Acher, "Determination of the effective parameters of a metamaterial by field summation method", *Journal of Applied Physics*, vol. 100, 084908, Oct. 2006.

[80] R. Mittra, "To Use or Not to Use the Effective Medium Approach for Designing Performance-Enhanced Small Antennas - That is the Question", *International Workshop on Antenna Technology: Small Antennas and Novel Metamaterials, IWAT 2008*, pp. 55-58, Chiba (Japan), Mar. 4-6, 2008.

[81] S.A. Tretyakov, and C.R. Simovski, "Metamaterial effective material parameters: Are two tensors enough?", *International Congress on Advanced Electromagnetic Materials in Microwave and Optics, Metamaterials 2008*, Pamplona (Spain), Sep. 23-26, 2008.

[82] Deliverable D1.1, "State-of-the-art and most promising analytical and numerical characterization techniques for bulk metamaterial lattices", *ECONAM 7th Framework Programme*, T0+9, pp. 1-12, Feb. 2009.

[83] H. Mosallaei, and K. Sarabandi, "Reply to Comments on Design and Modelling of Patch Antenna Printed on Magneto-Dielectric Embedded-Circuit Metasubstrate", *IEEE Transactions on Antennas and Propagation*, Vol. 10, pp. 2936-2937, Oct. 2007.

[84] F. Yang, and Y. Rahmat-Samii, "Reflection Phase Characterizations of the EBG Ground Plane for Low Profile Wire Antenna Applications", *IEEE Transactions on Antennas and Propagation*, vol. 51, no. 10, pp. 2691-2703, Oct. 2003.

[85] J.R. Sohn, K.Y. Kim, H.-S. Tae, and J.-H. Lee, "Comparative Study on Various Artificial Magnetic Conductors for Low-Profile Antenna", *Progress in Electromagnetics Research*, vol. 61, pp. 27-37, 2006.

[86] A. Erentok, D. Lee, and R.W. Ziolkowski, "Numerical Analysis of a Printed Dipole Antenna Integrated With a 3-D AMC Block", *IEEE Antennas and Wireless Propagation Letters*, vol. 6, pp. 134-136, 2007.

[87] H. Mosallaei, and K. Sarabandi, "Antenna Miniaturization and Bandwidth Enhancement Using a Reactive Impedance Substrate", *IEEE Transactions on Antennas and Propagation*, vol. 52, no. 9, pp. 2403-2414, Sep. 2004.

[88] G.J. Foschini and M.J. Gans, "On Limits of Wireless Communications in a Fading Environment when Using Multiple Antennas", *Wireless Personal Communications*, vol. 6, no. 3, pp. 311-335, Mar. 1998.

[89] S. Blanch, J. Romeu and I. Corbella, "Exact representation of antenna system diversity performance from input parameter description", *Electronics Letters*, vol. 39, no. 9, pp. 705-707, May 2003.

[90] S. Dossche, S. Blanch and J. Romeu, "Optimum antenna matching to minimise signal correlation on a two-port antenna diversity system", *Electronics Letters*, vol. 40, no. 19, pp. 1164-1165, Sep. 2004.

[91] S. Dossche, S. Blanch and J. Romeu, "Optimum antenna matching to minimise signal correlation on a two-port antenna diversity system", *Proc. IEEE/ACES Wireless Comp. and Appl. Comput. Elctromagnetics Int. Conference*, Hawaii (USA), 2005.

[92] D. R. Jackson, and N. G. Alexopolous, "Gain enhancement methods for printed circuit antennas", *IEEE Transactions on Antennas and Propagation*, vol. 33, no. 9, pp. 976-987, Sep. 1985.

[93] T. Zhao, D. R. Jackson, J. T. Williams and A. A. Oliner, "General formulas for 2-D leaky-wave antennas", *IEEE Transactions on Antennas and Propagation*, vol. 53, no. 11, pp. 3525-3533, Nov. 2005.

[94] G. Lovat, P. Burghignoli, F. Capolino, and D. R. Jackson, "Combinations of low/high permittivity and/or permeability substrates for highly directive planar metamaterial antennas", *IET Microwaves, Antennas and Propagation*, vol. 1, pp. 177-183, Feb. 2007.

[95] P.J. Ferrer, J.M. González-Arbesú, J. Romeu, and A. Cardama, "Bidirectional artificial magnetic reflectors at microwave frequencies", *Microwave and Optical Technology Letters*, vol. 49, no. 8, pp. 1949-1953, Aug. 2007.

[96] B.-I. Wu, W. Wang, J. Pacheco, X. Chen, J. Lu, T. Grzegorczyk, J.A. Kong, P. Kao, P.A. Theophelakes, and M.J. Hogan, "Anisotropic metamaterials as antenna substrate to enhance directivity", *Microwave and Optical Technology Letters*, vol. 48, no. 4, pp. 680-683, Apr. 2006.

[97] Y. Yuan, L. Shen, L. Ran, T. Jiang, J. Huangfu, and J.A. Kong, "Directive emission based on anisotropic metamaterials", *Physical Review A*, vol. 77, no. 053821, May 2008.

[98] C.A. Balanis, "Antenna Theory: Analysis and Design", *Wiley*, 2nd Edition, New York, 1997.

[99] R.C. Hansen, and M. Burke, "Antennas with magneto-dielectrics", *Microwave and Optical Technology Letters*, vol. 26, no. 2, pp. 75-78, Jul. 2000.

[100] S. Yoon, and R.W. Ziolkowski, "Bandwidth of a microstrip patch antenna on a magnetodielectric substrate", *Proceedings of the IEEE Antennas and Propagation International Symposium, AP-S*, pp. 297-300, Columbus (Ohio, USA), Jun. 22-27, 2003.

[101] H. Mosallaei, and K. Sarabandi, "Magneto-dielectrics in Electromagnetics: Concept and Applications", *IEEE Transactions on Antennas and Propagation*, vol. 52, no. 6, pp. 1558-1567, Jun. 2004.

[102] P.M.T. Ikonen, K.N. Rozanov, A.V. Osipov, P. Alitalo, and S.A. Tretyakov, "Magnetodielectric Substrates in Antenna Miniaturization: Potential and Limitations", *IEEE Transactions on Antennas and Propagation*, vol. 54, no. 11, pp. 3391-3399, Nov. 2006.

[103] H. Mosallaei, and K. Sarabandi, "Design and modelling of patch antenna printed on magneto-dielectric embedded-circuit metasubstrate", *IEEE Transactions on Antennas and Propagation*, vol. 55, no. 1, pp. 45-52, Jan. 2007.

[104] A.D. Yaghjian, and S.R. Best, "Impedance, bandwidth and Q of antennas", *IEEE Transactions on Antennas and Propagation*, vol. 53, no. 4, pp. 1298-1324, Apr. 2005.

[105] R.V. Petrov, A.S. Tatarenko, G. Srinivasan, and J.V. Mantese, "Antenna Miniaturization with Ferrite-Ferroelectric Composites", *Microwave and Optical Technology Letters*, vol. 50, no. 12, pp. 3154-3157, Dec. 2008.

[106] P.M.T. Ikonen, and S.A. Tretyakov, "On the advantages of Magnetic Materials in Microstrip Antenna Miniaturization", *Microwave and Optical Technology Letters*, vol. 50, no. 12, pp. 3131-3134, Dec. 2008.

[107] P.M.T. Ikonen, S.I. Maslovski, C.R. Simovski and S.A. Tretyakov, "On Artificial Magnetodielectric Loading for Improving the Impedance Bandwidth Properties of

Patch Antennas", *IEEE Transactions on Antennas and Propagation*, vol. 54, no. 6, pp. 1654-1662, Jun. 2006.

[108] W. Abdouni, A.-C. Tarot, and A. Sharaiha, "Simple manufacturing process of an artificial magneto-dielectric substrate applied to planar antennas", *International Congress on Advanced Electromagnetic Materials in Microwaves and Optics (Metamaterials 2008)*, Pamplona (Spain), Sep. 21-26, 2008.

[109] K. Buell, H. Mosallaei, and K. Sarabandi, "A Substrate for Small Patch Antennas Providing Tunable Miniaturization Factors", *IEEE Transactions on Microwave Theory and Techniques*, vol. 54, no. 1, pp. 135-146, Jan. 2006.

[110] F. Bilotti, A. Alù, and L. Vegni, "Design of Miniaturized Metamaterial Patch Antennas with μ-Negative Loading", *IEEE Transactions on Antennas and Propagation*, vol. 56, no. 6, pp. 1640-1647, Jun. 2008.

[111] L. Yousefi, and O.M. Ramahi, "Miniaturized wideband antenna using engineered magnetic materials with multi-resonator inclusions", *International Workshop on Antenna Technology: Small and Smart Antennas Metamaterials and Applications, IWAT07*, Cambridge (UK), pp. 1885-1888, Mar. 21-23, 2007.

[112] I.S. Nefedov, A.-C. Tarot, and K. Mahdjoubi, "Wire media - ferrite substrate for patch antenna miniaturization", *International Workshop on Antenna Technology: Small and Smart Antennas Metamaterials and Applications, IWAT07*, pp. 101-104, Cambridge (UK), Mar. 21-23, 2007.

[113] Y. Lee, and Y. Hao, "Characterization of Microstrip Patch Antennas on Metamaterial Substrates Loaded with Complementary Split-Ring Resonators", *Microwave and Optical Technology Letters*, vol. 50, no. 8, pp. 2131-2135, Aug. 2008.

[114] H.A. Wheeler, "The radian sphere around a small antenna", *Proceedings of the IRE*, vol. 47, pp. 1325-1331, Aug. 1959.

[115] R.H. Johnston, and J.G. McRory, "An Improved Small-Antenna Radiation Efficiency Measurement Method", *IEEE Antennas and Propagation Magazine*, vol. 40, no. 5, pp. 40-48, Oct. 1998.

[116] M. Geissler, O. Litschke, D. Heberling, P. Waldow, and I. Wolff, "An improved method for measuring the radiation efficiency of mobile devices", *Proceedings of the IEEE Antennas and Propagation International Symposium (APS2003)*, vol. 4, pp. 743-746, Jun. 2003.

[117] P. Miškovský, J.M. González-Arbesú, and J. Romeu, "Antenna Radiation Efficiency Measurement in an Ultra-Wide Frequency Range", *IEEE Antennas and Wireless Propagation Letters*, vol. 8, pp. 72-75, 2009.

[118] I.V. Lindell, S.A. Tretyakov, and M.I.Oksanen, "Conductor-backed Tellegen Slab as Twist Polariser", *Electronics Letters*, vol. 28, no. 3, pp. 281-282, Jan. 1992.

[119] D.S. Lerner, "A wave polarization converter for circular polarization", *IEEE Transactions on Antennas and Propagation*, vol. 13, no. 1, pp. 3-7, Jan. 1965.

[120] J.D. Hanfling, G. Jerinic, and L.R. Lewis, "Twist reflector design using E-type and H-type modes", *IEEE Transactions on Antennas and Propagation*, vol. 29, no. 4, pp. 622-629, Jul. 1981.

[121] R. Kastner, and R. Mittra, "A spectral-iteration technique for analyzing a corrugated-surface twist polarizer for scanning reflector antennas", *IEEE Transactions on Antennas and Propagation*, vol. 30, no. 4, pp. 673-676, Jul. 1982.

[122] P. Hannan, "Microwave antennas derived from the Cassegrain telescope", *IRE Transactions on Antennas and Propagation*, vol. 9, no. 2, pp. 140-153, Mar. 1961.

[123] K.C. Hwang, "Optimisation of broadband twist reflector for Ku-band application", *Electronics Letters*, vol. 44, no. 3, pp. 210-211, Jan. 2008.

[124] F. Yang, and Yahya Rahmat-Samii, "Polarization-dependent electromagnetic band gap (PDEBG) structures: designs and applications", *Microwave and Optical Technology Letters*, vol. 41, no. 6, pp. 439-444, Jun. 2004.

[125] Dunbao Yan, Qiang Gao, Chao Wang, Chang Zhu, and Naichang Yuan, "A novel polarization convert surface based on artificial magnetic conductor", *Microwave Conference Proceedings (APMC)*, vol. 3, , Dec. 4-7, 2005.

[126] P.J. Ferrer, B. Kelem, and C. Craeye, "Design of Broadband Transpolarizing Surfaces", *Microwave and Optical Technology Letters*, vol. 48, no. 12, pp. 2606-2611, Dec. 2006.

[127] Fan Yang, and Yahya Rahmat-Samii, "A low profile single dipole antenna radiating circularly polarized waves", *IEEE Transactions on Antennas and Propagation*, vol. 59, no. 9, pp. 3083-3086, Sep. 2005.

[128] V.F. Fusco, and S.W. Simms, "Reflected circular polarisation conservation using textured surface", *Electronics Letters*, vol. 43, no. 18, pp. 962-963, Aug. 2007.

[129] D.R. Sheen, E.L. Johansen, and L.P. Elenbogen, "The gridded trihedral: A new polarimetric SAR calibration reflector", *IEEE Transactions on Geoscience and Remote Sensing*, vol. 30, no. 6, pp. 1149-1153, Nov. 1992.

[130] A. Macikunas, and S. Haykin, "Trihedral twist-grid polarimetric reflector", *IEE Proceedings-F Radar and Signal Processing*, vol. 140, no. 4, pp. 216-222, Aug. 1993.

[131] D.G. Michelson, and E.V. Jull, "Depolarizing Trihedral Corner Reflectors for Radar Navigation and Remote Sensing", *IEEE Transactions on Antennas and Propagation*, vol. 43, no. 5, pp. 513-518, May 1995.

[132] P.J. Ferrer, C. López-Martínez, X. Fàbregas, J.M. González-Arbesú, J. Romeu, A. Aguasca, and C. Craeye, "Transpolarizing Surfaces for Polarimetric SAR Systems Calibration", *Proceedings of the IEEE International Geoscience and Remote Sensing Symposium (IGARSS 2007)*, Barcelona (Spain), Jul. 23-28, 2007.

[133] G.A. Burrell, and A.R. Jamieson, "Antenna radiation pattern measurement using time-to-frequency transformation (TFT) techniques", *IEEE Transactions on Antennas and Propagation*, vol. 21, no. 5, pp. 702-704, Sep. 1973.

[134] Y.-T. Hsiao, Y.-Y. Lin, Y.-C. Lu, and H.-T. Chou, "Applications of time-gating method to improve the measurement accuracy of antenna radiation inside an anechoic chamber", *Proceedings of the IEEE Antennas and Propagation International Symposium, AP-S*, vol. 3, pp. 794-797, Columbus (Ohio, USA), Jun. 22-27, 2003.

[135] A. Aguasca, A. Broquetas, J.J. Mallorquí, and X. Fàbregas, "A Solid State L to X-band Flexible Ground-based SAR System for Continuous Monitoring Applications", *Proceedings of the IEEE International Geoscience and Remote Sensing Symposium (IGARSS 2004)*, Anchorage (Alaska, USA), Sep. 2004.

[136] J.D. Silverstein, and R. Bender, "Measurements and Predictions of the RCS of Bruderhedrals at Millimeter Wavelengths", *IEEE Transactions on Antennas and Propagation*, vol. 45, no. 7, pp. 1071-1079, Jul. 1997.

[137] A. Freeman, Y. Chen, and C.L. Werner, "Polarimetric SAR calibration experiment using active radar calibrators", *IEEE Transactions on Geoscience and Remote Sensing*, vol. 28, pp. 224-240, Mar. 1990.

[138] L. Pipia, X. Fàbregas, A. Aguasca, C. López-Martínez, and J.J. Mallorquí, "A Subsidence Monitoring Project using a Polarimetric GB-SAR Sensor", *Proceedings of the PolInSAR 2007*, ESA ESRIN, Frascati (Italy), Jan. 22-26, 2007.

[139] M. Imbert, "Disseny d'una pantalla bidireccional AMC per a un sistema compacte d'antenes a 2.45 GHz", *Master Thesis*, ETSETB - TSC - Universitat Politècnica de Catalunya (UPC), May 2010.